



García de Quirós Nieto, Francisco Javier (2018) *Analysis of radiofrequency-based methods for position and velocity determination of autonomous robots in lunar surface exploration missions*. PhD thesis.

<http://theses.gla.ac.uk/75063/>

Copyright and moral rights for this work are retained by the author

A copy can be downloaded for personal non-commercial research or study, without prior permission or charge

This work cannot be reproduced or quoted extensively from without first obtaining permission in writing from the author

The content must not be changed in any way or sold commercially in any format or medium without the formal permission of the author

When referring to this work, full bibliographic details including the author, title, awarding institution and date of the thesis must be given

Enlighten: Theses

<https://theses.gla.ac.uk/>
research-enlighten@glasgow.ac.uk

Analysis of Radiofrequency-based Methods for Position and Velocity Determination of Autonomous Robots in Lunar Surface Exploration Missions



University
of Glasgow

Francisco Javier García de Quirós Nieto

Submitted in fulfilment of the requirements for the Degree of
Doctor in Philosophy

Faculty of Engineering

University of Glasgow

June, 2018

© Francisco Javier García-de-Quirós Nieto, 2018

Abstract

The use of distributed systems has been disruptive in almost any industrial sector, from manufacturing to processing plants from environmental monitoring to vehicle control, and many more. It is therefore natural to assess the benefits that such an advantageous engineering paradigm could bring to space exploration. In recent years, we have been witness to the emergence of concepts such as fractionated satellite systems, formation flying, megaconstellations, and femtoswarms. Most of these space missions have evolved from the idea of a decentralization of processes that were formerly performed in platforms conceived as monolithic systems.

The application of this concept to robotic systems is not new, and a great deal of scientific contributions on multi-robot systems exists, focusing on different aspects such as cooperative robotics, behavioural or reactive control, distributed artificial intelligence, swarm multi-agent systems etc. The intrinsic advantages of distribution (improved reliability and efficiency, higher robustness, etc.) has been boosted by the exponential growing of computational power density and a simultaneous miniaturization of technology, leading to smaller and more powerful robotic platforms, which could make a distributed robotic system, made of small robotic agents, a powerful substitute to classical large robotic platforms.

This thesis proposes, in the framework of multi-robot systems, a localization method for robotic agents in planetary surface exploration scenarios based on RF range and Doppler frequency shift analysis. The relevance of spatial localization awareness in agents belonging to a distributed robotic system is defined in the context of the advantages of robotic exploration. Different range determination techniques and, specifically, the advantages of including Doppler Effect in the determination of the relative position within the robotic system deployed are considered and the strengths and weaknesses analysed accordingly. Special attention is devoted to the noise sources present in the lunar environment, related to a practical (i.e. non-ideal) implementation architecture and its influence on the system performance. From this point of view, we develop a theoretical model for localization accuracy estimation, generated from power spectrum characteristics, in accordance with the system architecture proposed, and consolidated with numerical simulations and a parametrical assessment on a set of real references of components playing a key role in the overall performance.

The selected system architecture is then implemented in a representative set-up and tested under laboratory conditions. Algorithms used for carrier frequency generation and frequency measurement are developed, applied and tested in the hardware-on-the-loop breadboard. The results show that Doppler frequency component can be measured with the proposed architecture, yielding a high sensitivity in the determination of relative speed even at standard communication frequencies (UHF), and improving significantly at higher bands (S, C, etc.). This enables the possibility of adding relative speed to relative position determination via sensor fusion techniques, improving the response time and accuracy during navigation through the exploration scenario.

Table of Contents

Abstract	1
List of Tables	4
List of Figures	5
Acknowledgement	9
Author’s Declaration	10
Abbreviations	11
Chapter 1. Survey of the State-of-the-art	13
1.1. DILEMMA OF SPACE EXPLORATION: HUMANS VS. ROBOTS.	13
1.2. DISTRIBUTED VS. CENTRALIZED ROBOTICS: CHALLENGES IN DISTRIBUTED COOPERATIVE SYSTEMS.....	17
1.3. THE PROBLEM OF SELF-LOCATION AND NAVIGATION IN SMALL PLATFORMS.	22
1.4. THESIS OBJECTIVES: TOWARDS ROBOTIC COLONIZATION.	25
1.5. THESIS CONTRIBUTIONS.....	27
1.6. THESIS OUTLINE. WORK DEVELOPED.	28
Chapter 2.- Methods for Localization	30
2.1. INTRODUCTION.....	30
2.2. THE MOON ENVIRONMENT.....	31
2.3. METHODS FOR POSITION DETERMINATION.	36
2.4. FORMULATION OF THE LOCALIZATION PROBLEM.	45
2.4.1. INTRODUCTION.	45
2.4.2. FORMULATION OF THE MULTILATERATION PROBLEM.	50
2.4.3. FORMULATION OF THE DOPPLER SHIFT AND ITS RELATION WITH VELOCITY.	52
2.4.4. DETERMINATION OF VELOCITY VECTOR FROM THE DOPPLER FREQUENCY SHIFT.....	57
2.5. FINAL REMARKS.....	58
Chapter 3.- System Architecture Considerations	63
3.1. INTRODUCTION.....	63
3.2. FREQUENCY DOMAIN CONSIDERATIONS FOR LOCATION MESSAGE STRUCTURE.....	66
3.3. RF SYSTEM ARCHITECTURE.	70
3.4. ANALYSIS OF FREQUENCY AND TIME CRITICAL PARAMETERS.	73
3.5. ANALYSIS OF NOISE MODEL FOR THE MOON EXPLORATION SCENARIO.	86
3.6. RANGE AND DOPPLER SIGNALS IMPROVEMENT BY FILTERING.....	103
3.7. SUMMARY.	106
Chapter 4.- Implementation Case Analysis.	107
4.1. INTRODUCTION.....	107
4.2. IMPLEMENTATION APPROACH DESCRIPTION.....	108
4.3. FUNCTIONAL DESCRIPTION.....	115
4.4. SUMMARY.	122
Chapter 5.- Experimental Methods and Results.	123
5.1. INTRODUCTION.....	123
5.2. COMPONENTS AND METHODOLOGIES.....	125
5.3. ANALYSIS OF RESULTS.	133
5.4. SUMMARY.	137
Chapter 6.- Conclusions.	138
6.1. INTRODUCTION.....	138
6.2. CONCLUSIONS OVERVIEW.....	138
6.3. FUTURE LINES OF WORK.....	140

List of References	142
Bibliography	150
Appendix 1. - Electric Diagrams and Interface Description.....	151
Appendix 2. – MATLAB Functions Code.....	160
Appendix 3. – Oscillators Performance Tables.....	174

List of Tables

Table 2.4.1.- Robotic rovers sent to exploration mission from the beginning of Space Era till to date with distance covered (¹ Update 11/04/2018, ² Update 27/04/2018).....	49
Table 3.5.1.- Calculated Jitter values for a set of selected oscillators. (See Appendix 3 for more information).....	88
Table 3.5.2.- Calculated phase noise for a One-Way range measurement system utilizing a Rakon LNO-100 OCXO after applying successive averaging for 1000 to $20 \cdot 10^6$ cycles.	88
Table 3.5.3.- Frequency drifts for One-Way operation mode, for three different cases obtained combining Rakon TE300 TCXO in the Mobile Node and RK410 in the Main Station.	89
Table 3.5.4.- The frequency and subsequent Doppler shift is presented for both TE300 TCXO and RK410 from RAKON considering the Two-Ways scenario.....	90
Table 3.5.5.- One-Way total time noise variance for range and Doppler Frequency shift measurement.	92
Table 3.5.6.- Two-Ways total time noise variance for range and Doppler Frequency shift measurement.	94
Table 3.5.7.- One-Way total time noise variance for range and Doppler Frequency shift measurement with Time measurement stage based in Texas Instruments TDC7201 ($T_s=55ps$).....	101
Table 4.2.1.- Number of switches related with redundant configuration of RF subsystems.	111
Table 4.2.2.- Tracking Station RF system parts selection with mass budget estimation	113
Table 4.2.3. Mobile Node RF system parts selection with mass budget estimation ..	114
Table 5.2.1.- The control registers of the PLL.	126
Table 5.2.2.- The command data for the experimental control application and FPGA IP cores running within the Mobile Node and Tracking Station.	127

List of Figures

Figure 1.1.1- An artist conception of in-situ resource utilization robots collecting Martian material. Image credits: Pat Rawlings/NASA Family.....	14
Figure 1.1.2- Family photography of NASA Mars exploration rovers, from left to right: the small Sojourner (1997), Spirit/Opportunity (2004) and Curiosity (2012); an example of scalability for an incremental exploration plan.	15
Figure 1.1.3- Artistic recreation of a human settlement in Mars. The concept, created by ZA Architects [ZAA-2013] represents the paradigm of Human-robot cooperation in an incremental exploration plan. In this concept, robots are sent to Mars previously with the mission of building an underground human habitat. A robotic community specialized in geologic sample and drilling chooses autonomously the right location and digs the construction that is furtherly finished and conditioned by human explorers in cooperation with the robotic system	16
Figure 1.2.1- ALSEP Experimental Set-Up deployed in Lunar surface during Apollo 16 Mission.....	20
Figure 2.2.1- (Left) Near and (Right) Far side pictures of the Moon.	31
Figure 2.2.2- Picture obtained during Apollo 17 mission showing Mare Imbrium and Copernicus Crater seen almost edge-on near the horizon at the center. Credit: NASA,1972.....	31
Figure 2.2.3- Apollo 11 astronaut, Buzz Aldrin, stands in front of a seismometer instrument. The Lunar Landing Module stands in the front. The landing site, Mare Tranquilitatis was chosen because of the geological characteristics of Maria, including a smooth and leveled surface, very suitable for landing and the foreseen surface operations. Credit: NASA,1969.	32
Figure 2.2.4- A fragment of Moon regolith. The typical highly irregular form with sharp edges of regolith grains can be appreciated in this example. Credit: David S. McKay, NASA/JSC.	33
Figure 2.2.5- An Apollo 14 astronaut deploys the ALSEP power source (foreground) whilst the ALSEP's Central Station is placed nearby connected by a cable (background). It can be appreciated that the power source is totally covered by dust. The ALSEP included as a part of its Central Station an instrument specifically designed for dust analysis, since at that time, concerns about the effect of dust both in the equipment and in the crew increased. Credit: NASA/JSC.....	34
Figure 2.2.6- Lunar soil layers structure by [Kring,D.-2006], based in information from [Hörz, F.-1991].....	35
Figure 2.2.7- Lunar soil Reflectivity coefficient ρ vs. theta angle ($^{\circ}$) of incidence of radiofrequency wave with the ground for $\epsilon=1.5$ to 4 , $\sigma=0.18 \cdot 10^{-3}$ Siemens.....	35
Figure 2.3.1- Diagram of Multilateration localization method.	38
Figure 2.3.2- Diagram of Multiangulation localization method.	39
Figure 2.3.3- Location determination of a node in case of uncertainty for (Right) Multilateration and (Left) Multiangulation localization methods. The regions of uncertainty are represented as red areas.....	39
Figure 2.3.4- Multilateration based in Received Signal Strength methods. The distance from mobile node 1 to the tracking stations T_1 to T_3 can be calculated from the difference between the signal transmitted by the node and received on each tracking station T_i , or ΔP_{i1} , which can be expressed as $\Delta P_{i1} = P_{T1} - P_{Ri1}$	41
Figure 2.3.5- Multilateration based in time measurement methods. The distance from mobile node 1 to the tracking stations T_1 to T_3 can be calculated from the time elapsed	

since the transmission of the signal T_0 to the instant of reception on each tracking station T_i , or T_{i1} , which can be expressed as $\Delta T_{i1} = T_0 - T_{i1}$.	41
Figure 2.3.6- Multilateration based in Frequency Shift measurement methods. The mobile node velocity can be determined using the Doppler shift measured in the received signal frequency, which can be expressed as $\Delta f_D = f_{RX} - f_{TX}$.	42
Figure 2.4.1- Vector representation of a mobile node position and velocity.	46
Figure 2.4.2- Representation of tangent and normal velocity components of a mobile node velocity vector.	47
Figure 2.4.3- Representation of different position vectors for different coordinate systems corresponding to the different tracking stations T_1 to T_3 .	48
Figure 2.4.4- Representation of exploration rovers considering the relation between the distances traveled and the corresponding rover mass (Mars rovers in red, Moon rovers in blue).	49
Figure 2.4.5- Determination of position by Multilateration, based on the ranges from the mobile node to the tracking stations, which are located at known positions with respect to the coordinate system centered in T_1 .	50
Figure 2.4.6- Diagram of different cases for Doppler shift, when emitter approaches the receiver (Left) and when emitter and receiver get away each other (Right).	53
Figure 2.4.7- Sign of dot product to obtain the vector projection of v_1 on P_1 in order to obtain v_{1r} (Left) when the vector v_{1r} is aligned to P_1 and (Right) when they are opposite.	54
Figure 2.4.8- Linear trajectory travel scenario for a Mobile rover in an exploration area with three tracking stations T_1 to T_3 .	55
Figure 2.4.9- Doppler frequency shift values for a linear trajectory ($x=X_0$) for different mobile node velocities and different X_0 values (10m, 20m, 40m and 80m).	56
Figure 2.4.10- Doppler frequency shift and distance of Mobile node to tracking station versus position of mobile node in Y axis, when the mobile node moves along a linear trajectory $x=X_0$ from $y= -100m$ to $y= +100m$ at $v=1m/s$.	56
Figure 2.4.11- Radial velocity components from the different tracking stations, as it would be determined by the Doppler frequency shift measured.	57
Figure 2.4.12- Process for the determination of position and velocity vector for a mobile node according to the assumed exploration scenario.	59
Figure 2.4.13- Simulation results for mobile node trajectory for the scenario described in Figure 2.4.14.	60
Figure 2.4.14- Process for the determination of range and Doppler shift, and the further determination of the position and velocity vector for a mobile node according to a cinematic set of parameters and associated MATLAB functions.	61
Figure 3.1.1.- One-Way (up) and Two-Ways (Bottom) RF ranging (Time of Transit) and Doppler measurement methods.	64
Figure 3.2.1.- Two-Ways Doppler sensitivity $S_f, 2W$ (Hz/ (m/s)) as a function of frequency.	67
Figure 3.2.2.- Proposed location data frames structure of range and Doppler shift acquisition process. Each frame starts with a preamble consisting in a tone at fixed frequency with a number of signal cycles.	68
Figure 3.2.3- RF carrier preamble proposed for the determination of Doppler Frequency shift, starting each localization message frame (see Figure 3.2.2).	69
Figure 3.3.1- One-Way Operation Mode proposed architecture.	70
Figure 3.3.2- Two-Ways operation Mode proposed architecture.	71
Figure 3.4.1.- Jitter representation in a digital signal and aspect of the statistical distribution.	76
Figure 3.4.2.- Power spectrum of a carrier tone with phase noise which produces a stretching of the spectrum around the central frequency f_0 (Source Analog Devices [Kester.W-2009]).	78

Figure 3.4.3.- Jitter power spectrum as specified by a crystal oscillator manufacturer, and estimation of RMS jitter. [Kester.W-2009].....	80
Figure 3.4.4.- Multipath propagation case for the exploration scenario, considering the mobile node and a tracking station.	82
Figure 3.4.5. - Difference between direct and reflected path for a tracking station at 2m and the mobile node antenna at a height of 20cm (blue) and 50cm (red).....	83
Figure 3.4.6.- Normalized RF 400MHz signal without interference (blue) and with reflected interference (red) at the arrival at tracking station receiver after a difference between direct and reflected paths of 7,8cm.	83
Figure 3.4.7.- Delay τ in received signal introduced by multipath interference for a range of reflectivity coefficient values from $\rho=1$ (total reflection) to $\rho=0,2$. (Ground Distance D is represented in logarithmic scale).....	84
Figure 3.5.1.- One-Way time noise model.	91
Figure 3.5.2.- Two-Ways noise model.	92
Figure 3.5.3.- Cramer-Rao lower bound limit for thermal noise (red) and quantization noise (blue) plots.	95
Figure 3.5.4.- Process for the determination of range and Doppler shift introducing Gaussian time noise with a given variance, and the further determination of the position and velocity vector for a mobile node according to a cinematic set of parameters and associated MATLAB functions.	97
Figure 3.5.5.a- Range and Doppler signals with Position and Velocity reconstruction from noisy signal with noise in range $\sigma_{T1W2} = 0.156 \text{ ns}^2$ and Doppler $\sigma_{T1W2} = 1.56 \cdot 10^{-5} \text{ ns}^2$. Measured at $f_{IF}=1 \text{ MHz}$	98
Figure 3.5.5.b- Statistical analysis of Range and Doppler frequency shift error signals E_{r1l} and E_{d1l} for noise in range $\sigma_{T1W2} = 0.156 \text{ ns}^2$ and Doppler $\sigma_{T1W2} = 1.56 \cdot 10^{-5} \text{ ns}^2$. Measured at $f_{IF}=1 \text{ MHz}$	98
Figure 3.5.6.a- Range and Doppler signals with Position and Velocity reconstruction from noisy signal with noise in range $\sigma_{T1W2} = 0.156 \text{ ns}^2$ and Doppler $\sigma_{T1W2} = 1.56 \cdot 10^{-4} \text{ ns}^2$. Measured at $f_{IF} = 100 \text{ KHz}$	99
Figure 3.5.6.b- Statistical analysis of Range and Doppler frequency shift error signals E_{r1l} and E_{d1l} for noise in range $\sigma_{T1W2} = 0.156 \text{ ns}^2$ and Doppler $\sigma_{T1W2} = 1.56 \cdot 10^{-4} \text{ ns}^2$. Measured at $f_{IF} = 100 \text{ KHz}$	99
Figure 3.5.7.a- Range and Doppler signals with Position and Velocity reconstruction from noisy signal with noise in range $\sigma_{T2W2} = 5.011 \cdot 10^{-4} \text{ ns}^2$ and Doppler $\sigma_{T2W2} = 4.55 \cdot 10^{-8} \text{ ns}^2$. Measured at $f_{IF}= 1 \text{ MHz}$	102
Figure 3.5.7.b- Statistical analysis of Range and Doppler frequency shift error signals E_{r1l} and E_{d1l} for noise in range $\sigma_{T2W2} = 5.011 \cdot 10^{-4} \text{ ns}^2$ and Doppler $\sigma_{T2W2} = 4.55 \cdot 10^{-8} \text{ ns}^2$. Measured at $f_{IF}=1 \text{ MHz}$	102
Figure 3.6.1.- Sinus signal with additive Gaussian noise (blue) and filtered signal (red) extracted with Kalman filtering using <i>Ekalman()</i> MATLAB function.	104
Figure 3.6.2.- Range and Doppler signals with Position and Velocity reconstruction and filtered by Extended Kalman Filter from noisy signal with noise in range $\sigma_{T1W2} = 0.156 \text{ ns}^2$ and Doppler $\sigma_{T1W2} = 1.56 \cdot 10^{-4} \text{ ns}^2$. Measured at $f_{IF}=100 \text{ KHz}$	105
Figure 3.6.3- Range and Doppler signals with Position and Velocity reconstruction and filtered by Extended Kalman Filter from noisy signal with noise in range $\sigma_{T2W2} = 5.011 \cdot 10^{-4} \text{ ns}^2$ and Doppler $\sigma_{T2W2} = 4.55 \cdot 10^{-8} \text{ ns}^2$. Measured at $f_{IF}=1 \text{ M KHz}$	105
Figure 4.2.1.- Tracking Station RF system layout	109
Figure 4.2.2.- Mobile Node RF system layout.....	110
Figure 4.3.1.- Main Station Control Unit logic architecture	116
Figure 4.3.2.- Mobile Node Control Unit logic architecture.....	117
Figure 4.3.3.- Tracking Station Block logic flow diagram	119
Figure 4.3.4.- DSP Logic block diagram.	120
Figure 4.3.5.- Frequency measurement of the IF reception signal.....	121

Figure 4.3.6.- Mobile Node Control Block Logic Flow Diagram.	122
Figure 5.1.1.- Tracking Station (Top) and Mobile Node (Bottom) RF System architecture corresponding to the Breadboard implementation.	124
Figure 5.1.2.- Experimental Set-Up layout.	125
Figure 5.2.1.- Experimental Laboratory Set-Up implemented for performance analysis.	126
Figure 5.2.2.- Phase samples wheel for a Direct Digital Synthesis-based (DDS) frequency modulation procedure.	128
Figure 5.2.3.- Frequency shift measurement signal.	129
Figure 5.2.4.- DDS modulated tone over 400MHz main carrier, the detail is of the sub-carrier only, main carrier and image do not appear in the plots. The captures show the DDS sub-carrier tone centered at: (Top-Right) 24,999 KHz, (Bottom-Left) 25,000 KHz and (Bottom-Right) 25,001 KHz. The Top-Left plot corresponds to a detail of the main 400MHz carrier generated by the SKY72310 PLL.	130
Figure 5.2.5.- D1 (Doppler signal at T ₁ Station) signal measured (blue), Filtered (red) vs theoretical sequence of Doppler shift values (green). IF=100kHz. Kalman Filter constant a=1.22	131
Figure 5.2.6.- D1 (Doppler signal at T ₁ Station) measured error distribution (vs Theoretical sequence of values). IF=100kHz. Kalman Filter constant a=1.22.....	131
Figure 5.2.7.- D1 (Doppler signal at T ₁ Station) signal measured (blue), Filtered (red) vs theoretical sequence of Doppler shift values (green). IF=100kHz, Kalman Filter constant a=1.04	132
Figure 5.2.8.- D1 (Doppler signal at T ₁ Station) signal measured (blue), Filtered (red) vs theoretical sequence of Doppler shift values (green). IF=25kHz, Kalman filter constant a=1.04	132
Figure 5.2.9.- D1 (Doppler signal at T ₁ Station) measured error distribution (vs Theoretical sequence of values). IF=25kHz, Kalman filter constant a=1.04.....	133
Figure 5.3.1.- Mobile Node RF architecture with double IF carrier modulation up-converter scheme to reject image tone in transmitted pulse.	134
Figure 5.3.2.- Mobile node RF architecture with I/Q up-converter modulator to reject image tone in transmitted pulse. The addition of the quadrature components (I and Q) results in only one tone (Q) since the I components are cancelled by addition of conjugated phasors.	135

Acknowledgement

First and foremost, I would like to express my deepest gratitude to my thesis supervisor Dr. Gianmarco Radice, and to the staff of Aerospace Sciences Research group, without whose help, continuous support and advice along these almost eight years, this work would have not been possible.

Thanks also to my friend and colleague Dr. José Antonio Carrasco, Professor at Universidad Miguel Hernández and CEO of EMXYS. His professionalism and talent has always been a great inspiration for me.

Last but not least, I wish to wholeheartedly thank my family, my wife Sonia, my son Javier and my daughter Carolina, and of course my parents Francisco and Ángela, for their infinite patience during the endless work days, always awaiting for me with love and dedication. Your encouragement and motivation has been vital for me.

Author's Declaration

This thesis presented a work that was carried out under the supervision of Dr.Gianmarco Radice, School of Engineering, during the period between March 2008 and May 2016.

I declare that this thesis is entirely my own work and it has not been previously submitted for any other degree or qualification in any university.

Francisco Javier García de Quirós Nieto

Glasgow, June 2018.

Abbreviations

ALSEP	Apollo Lunar Surface Experiments Package.
ASIC	Application-Specific Integrated Circuit.
BER	Bit Error Rate.
CMOS	Complementary Metal-Oxide Semiconductor.
CORDIC	COordinate Rotation DIGital Computer (also Volder's algorithm).
CPLD	Complex Programmable Logic Device.
CW	Continuous Wave.
DDS	Direct Digital Synthesis.
DSP	Digital Signal Processing/Processor.
EDAC	Error Detection and Correction.
EKF	Extended Kalman Filter.
ESA	European Space Agency.
FDOA	Frequency Difference-Of-Arrival.
FM	Frequency Modulation.
FPGA	Field Programmable Gate-Array.
GPS	Global Positioning System.
ISM	Industrial, Scientific and Medical (radiofrequency band).
IC	Integrated Circuit.
IF	Intermediate Frequency.
I/F	Interface
IP	Intellectual Property (here concerning logic blocks designed in VHDL).
LIDAR	Light Detection And Ranging.
LNA	Low Noise Amplifier.
LO	Local Oscillator.
MEMS	Micro-Electro Mechanic System.
MN	Mobile Node.
MS	Main Station.
NASA	National Aeronautics and Space Administration (U.S.A.)
OBC	On-Board Computer.
OCXO	Oven-Controlled Crystal Oscillator.
PC	Personal Computer.
PCB	Printed Circuit Board.
PD	Pulse Doppler.
PLL	Phase-Locked Loop.
PM	Phase Modulation.
ppm	Parts Per Million.
PTFE	Polytetrafluoroethylene (synthetic fluoropolymer material, Teflon).
RAM	Random Access Memory.
RF	Radio Frequency.
RMS	Root-Mean Square.
RSSI	Received Signal Strength Indication.
SAW	Surface Acoustic Wave.
SNR	Signal to Noise Ratio.
SMA	Sub-Miniature version A (RF coaxial connector).
TDOA	Time-Difference-Of-Arrival.
TOA	Time-Of-Arrival.
TCXO	Temperature Compensated Crystal Oscillator.

TOF	Time-Of-Flight.
TS	Tracking Station.
UART	Universal Asynchronous Reception & Transmission.
UHF	Ultra High Frequency.
USB	Universal Serial Bus.
UWB	Ultra-Wide Band.
VCO	Voltage Controlled Oscillator.
VCXO	Voltage Controlled Crystal Oscillator.

Chapter 1. Survey of the State-of-the-art

1.1. Dilemma of Space exploration: Humans vs. Robots.

Robotic systems have become the de-facto standard in space exploration missions. The benefits of robots in different versions like probes or rovers, versus human explorers, have been considered extensively in different studies and reports [Crawford,I.-2012] [Osborne,J.R.-2012] [White,R.J.-2001] [NASA-SP-2009-566]. Despite the intrinsic limitations of robots in terms of mobility, autonomy and initiative compared to human beings, the prohibitive costs and complexity associated with manned, remote space exploration have dictated the pathway following the Apollo programme.

The above mentioned studies have contributed to the discussion of human or robotic approach for the strategic lines of future space exploration, and which paradigm to choose is still an ongoing and open decision process for most space agencies. There is however a consensus of what the strengths and weaknesses of these two different approaches are:

In case of human exploration, there are a number of notable advantages:

- Autonomy and Mobility are much greater than what could be achieved with the State-of-the-Art robotics. A human being is able to navigate along unstructured scenarios and manage unexpected situations and obstacles much better than any existing robotic system. In fact, during Apollo 17 mission, 35.7 km were traversed in three days by the crew, whilst Mars exploration rover Opportunity has taken almost eight years from 2004 to 2011 to cover a similar distance (34.4 km).
- Higher Dexterity and handling capabilities compared with their robotic counterparts. The human's natural skills for collecting, discriminating and transport of geological samples are superior to robotic grippers and automated sampling systems currently available. A notable figure in line with this argument are the 382 kg of samples returned by the Apollo program compared with the 0,32 kg returned by the Russian robotic sample and return mission Lunas, the less than one milligram of samples returned to Earth by Hayabusa (some thousands of 10-100 μ m grains) and the lack of material samples returned up to date by several Mars exploration missions. Furthermore, in order to accomplish the exploration mission's goals related to search for life, intensive field research has to be performed; nowadays, it is not possible to substitute humans in their ability to recognize and evaluate the scientific value of the samples collected or the place of work by robots, but at the cost of complex telepresence systems.
- Decision taking processes powered by powerful reasoning mechanisms. Expert knowledge and initiative makes possible to re-configure mission objectives in-situ, with low or no intervention by experts back on the Earth. This leads to being finally more efficient in time and resources, since the communication are not dimensioned to transmit a vast information to Earth to allow the technicians and scientists in the ground control to carry out sound analysis of the situations. In fact, the Apollo missions were controlled through radio-communication links with a very limited performance and at a much lower data rate compared with the modern

communication networks connecting Mars rovers with the Earth ground stations. Despite that, the scientific return of Apollo missions was significant.

On the other hand, there is a list of significant disadvantages for human exploration:

- The huge increment of mission costs associated to the transport of a human crew, not only related directly with life support systems, but health monitoring systems and conditioning of the vehicle to external factors, such as radiation, that may be harmful for humans. According to [White, R.J.-2001], three important challenges are faced by space voyagers: (1) important changes in the physical forces their bodies are subjected to, driving the human physiology mechanisms to far from nominal operation conditions, (2) impacting psycho-social conditions related with long term confinement and isolation and (3) radiation environment, which could involve severe doses like those associated with the neighborhood of Jupiter. However, according to the aforementioned study, those factors are possible to be counteracted with further research and integrative studies leading to individualized human body models for each of the crew members that, combined with suitable technologies would protect the crew members as well as predict future health troubles.
- Moreover, transport of human crew makes the mission less energy efficient: humans need more space for its transport in long periods of time than is required to store their bodies for physiological and psychological reasons. The human crew must be energized (i.e. consuming nutrients and water) at any time, even sleeping and, still, the energy required for humans to survive in space is based on nutrients that, at present, cannot be totally produced in space, adding more mass and volume requirements to the launcher.
- Finally, the social cost of losing human lives in unsuccessful space exploration missions is so high, that the quality assurance and safety procedures are never enough, which adds an extra cost to the mission.



Figure 1.1.1- An artist conception of in-situ resource utilization robots collecting Martian material. Image credits: Pat Rawlings/NASA Family.

On the other hand, robots have intrinsic advantages:

- Dramatic reduction of mission costs due to the elimination of life support systems required by human crews for space travel. Moreover, robots are operational under extreme temperature conditions and in a severe radiation environment, thus, the characteristics of vehicles that should be necessary to condition them for manned space travel are not necessary anymore, eliminating heavy and bulky equipment.
- Higher Energy efficiency. Despite human crews, robots are powered from the same energy source than the rest of the space vehicle sub-systems: solar energy, but do not require any additional charge of food and water. Moreover, robotic systems can travel along vast distances in deep sleep un-powered status, reducing to a minimum the energy required during the travel. Furthermore, robots can be stored in very compact and volume efficient configurations, allowing a reduction of requirements of launch vehicle. Smaller vehicles can enable complex robotic exploration missions.
- Due to the capability mentioned above of having robotic systems in power-off state during long-time journeys, distant targets for exploration are within our reach with the current State-of-the-art. Bodies such as Jupiter moon Europa or Saturn's moon Enceladus are now within our scope because complex robotic probes can be sent in a mid term with the current technology state-of-the-art and under moderate budgets. Such missions will be neither feasible or affordable with human crews unless a dramatic improvement of the current space travel technologies is achieved, involving so many aspects like life support, propulsion, space habitats, in-situ resources utilization, etc.
- An important factor for robotics exploration missions is scalability. Missions with a reduced exploratory scope require simpler and smaller probes than missions with complex scientific goals. This allows a rational approach to the object under research, reducing risks trough incremental exploration programs: early missions can be budget constrained, involving smaller robotic rovers and, once the technology is mature and the experience is accumulated, larger investments can be afforded in more and more ambitious missions. As opposite, sending human to space involves a high costs baseline related with life support and protection of crew independently of the mission objectives.

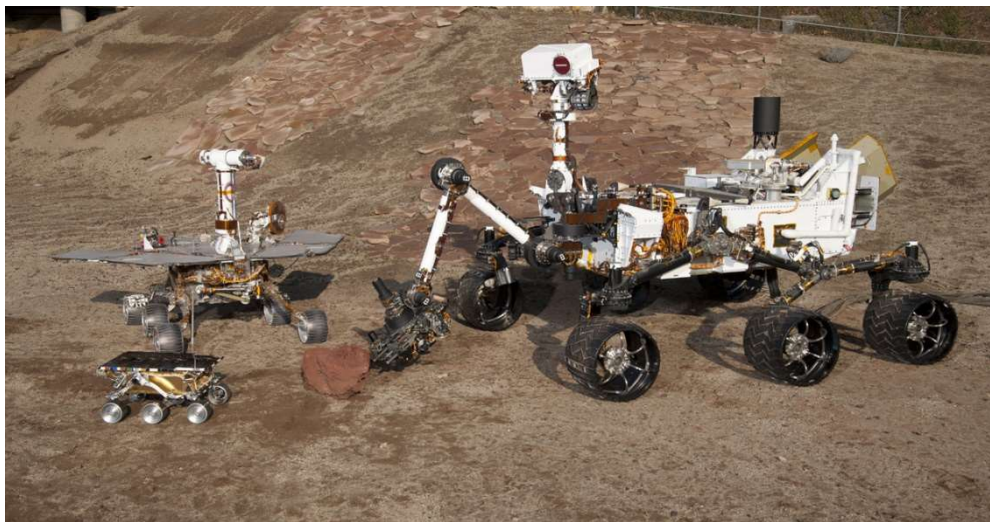


Figure 1.1.2- Family photography of NASA Mars exploration rovers, from left to right: the small Sojourner (1997), Spirit/Opportunity (2004) and Curiosity (2012); an example of scalability for an incremental exploration plan.

and significant disadvantages:

- Very limited mobility and navigation capabilities across unstructured unknown scenarios compared with human explorers. A study carried out by NASA Space Architecture Team (formerly the NASA NEXT team) aiming to determine NASA's Exploration priorities and the technologies necessary to accomplish the expected objectives ([Pedersen,L.-2003]) includes a comparative analysis of human and robotic exploration in terms of robustness. In such study, robustness is defined as "the property of a system to continue to function in the presence of faults and anomalous, unexpected conditions". Undoubtedly, the adaptability of humans to uncertainty compared with the most sophisticated robotic platforms is still very high, therefore the levels of robustness in the accomplishment of the mission objectives with human explorers are out of the reach of current robotics technology.
- Very limited planning capabilities compared with humans, and no initiative and improvisation, which are necessary to manage autonomously uncertainties and unexpected events. Robotic missions are subsequently very prone to failures due to those factors, which require a very careful and detailed planning for each single step.
- Very limited decision taking and learning capabilities compared with humans.
- Above mentioned reasons imply the requirement of a frequent supervision of ground operators that require high-performance communication channels in order to gather information enough for right decision making, which increases the infrastructure and power required for the mission.

In conclusion, advantages and drawbacks of human and robotic exploration strategies can be roughly summarized in performance vs. efficiency [Alibay,F.-2014] [Navarro-2015] [Novara,M.-1998] [Kubota,T.-2003]. Robotics applied to space exploration allows highly efficient use of the technology and resources to reach exploration targets with a significant scientific performance. On the other hand, the human presence in such bodies, like Mars or Jupiter's moon Europa, would yield outstanding research materials and knowledge, but at a huge cost.

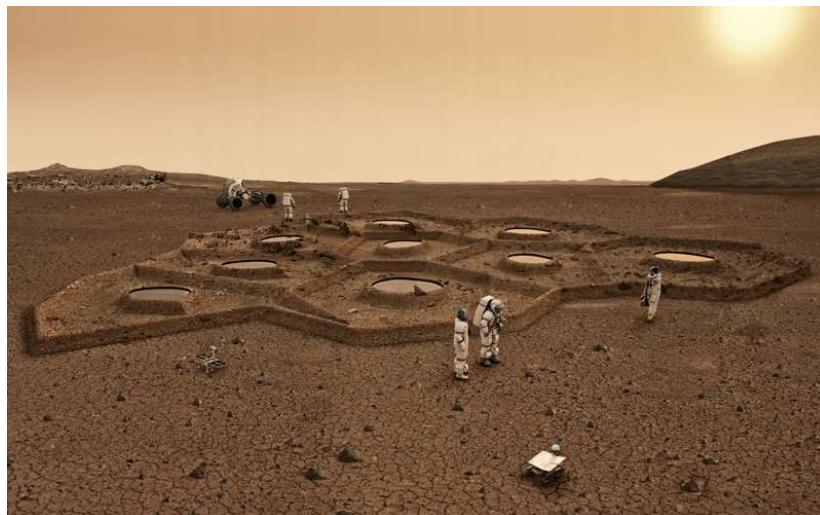


Figure 1.1.3- Artistic recreation of a human settlement in Mars. The concept, created by ZA Architects [ZAA-2013] represents the paradigm of Human-robot cooperation in an incremental exploration plan. In this concept, robots are sent to Mars previously with the mission of building an underground human habitat. A robotic community specialized in geologic sample and drilling chooses autonomously the right location and digs the construction that is furtherly finished and conditioned by human explorers in cooperation with the robotic system

Due to the reasons previously explained, the Space agencies associated to the ISECG (International Space Exploration Coordination Group) have agreed [GER-2013] in assuming a mixed model in which humans will keep playing a main role in Space exploration missions, but evolving from tele-operation to supervision, providing to robotic systems the mission objectives at high level, and relying on on-board intelligent agents for the accomplishment of short term goals. Further down the line, the cooperation between robots and humans may extend to in-situ operation, this way, human explorers may rely on robots for hazardous tasks or for those requiring accuracy and reliability a manual operation may not achieve. Works carried out as early as in 1995 [Nechyba,M.C.-1995) proposed such approach for in-Space operations during extra-vehicular activities.

Later contributions like [Osborne,J.R.-2012], develop this concept more in-depth proposing a Moon colonization plan based in a series of robotic and mixed human-robotic missions that implement, in a progressive and incremental way, the necessary infrastructures to establish a permanent exploration settlement on the moon, taking advantage of the advantages of both robots and humans by means of a cooperative work strategy. The three different mission scenarios proposed (human-controlled robotics, unpressurized crew mobility rover and pressurized crew mobility rover) contemplate robotic rovers with autonomous operation cooperating with humans in the realization of scientific experiments and maintenance works.

1.2. Distributed vs. Centralized Robotics: Challenges in Distributed Cooperative Systems.

Distributed robotics is defined as a new paradigm in the organization of robotic systems, imitating the distribution of computing processes along a network of homogeneous or heterogeneous computers. [Dudek,G.-1997] associates the concept of distributed robotics to multi-agent robotics, meaning the distribution of computational tasks among a number of intercommunicated robots, which collectively perform the task that, in a traditional monolithic approach, should be assigned to a unique and more complex robot. The author introduces the terms of “swarm” or “colony” to refer to the group of robots in order to highlight the cooperative nature of their mutual relationship.

[Parker L.-2007] presents an overview of the Distributed Intelligence concept, as well as its application to robotic communities. According to the author, “Distributed Intelligence refers to systems of entities working together to reason, plan, solve problems, think abstractly comprehend ideas and language, and learn”, where the term “entity” means any autonomous intelligent process or system such as a software or robotic agent, or even a human, a smart sensor, etc. In this sense, Distributed Intelligence paradigms are better justified in applications that are inherently distributed in space, time or functionality, such as in the case of robotic systems applied to exploration of unknown scenarios, in this case the parallelization of data processing boosts the overall performance compared with a monolithic execution, and also provides improvements in terms of reliability and robustness in case some type of redundancy is implemented. The paper continues highlighting the fact that the sort of interaction between agents are a key factor to define categories of distributed Intelligence, although other aspects like whether the goals are individual or shared (i.e.

collective) are also relevant. According to this, distributed intelligence systems could be categorized in Collective, Cooperative, Collaborative and Coordinative.

[Parker L.-2007] defines a Collective interaction as the existing in a system where the different entities (robotic agents for instance) are not aware of the existence of the other individuals of the team, although they share goals and the individual actions are beneficial to the other team components in the achievement of their respective goals. These sort of robotic systems are featured by simple controls laws (or behaviors) in the agents, which, combined in a system, emerge in a complex behavior at system level.

In the case of Cooperative interaction, the entities are aware of the existence of the others, they share goals and their respective actions contribute to the achievement of their counterparts' goals. In this sense, the robotic agents are able to define and plan their objectives considering the capabilities or chances of success of the other agents in the system.

The third category of interaction, Collaborative, implies not only mutual awareness of the agents, but that each agent tasks include to support teammates in the accomplishment of their respective goals. In this case, Collaboration means to work proactively to support others in the achievement of their goals.

Finally, the fourth type of interaction defines a distributed intelligence system as Coordinative when the agents do not have a shared goal and the individual actions are not oriented to the goals of other members of the team.

[Dudek,G.-1997] also explains the hints in relation to the differences between distributed and collective or collaborative robotics. In this sense, the term “distributed” encompass a wider scope of configurations including the case of having a central robot surrounded by telecontrolled robotic appendages, which could be understood as a single robot with distributed instruments and actuators. On the other hand, the terms “collaborative”, “collective”, “swarm”, or “colony” suggest the existence of strong interaction between the robotic agents that induces a collective behavior, with higher complexity than the behavior of the individual agents.

[Ahmad,A.-2013] highlights the exchange of information between robotic agents in a distributed community as a key value for the solution of complex problems such as the location of both static and dynamic landmarks. This way, the information exchange between agents is not only useful for their individual operation but also to address system-level computing challenges.

[Roumeliotis,I.-2002] reports a particular case of distributed robotics focusing in the problem of robots localization, defining as “collective localization” the process of solving the location determination of the different robotic agents by sharing self-location information among Kalman filters run on single robot, just as a decentralized calculation of an equivalent single Kalman estimator. In this specific case, the objective of this distribution of computational tasks is the reduction of uncertainties in the calculation of a given magnitude (such as the self-location of the position of a landmark) fusing the data obtained by a set of independent (i.e non-correlated) measurements performed by different agents by means of an estimator such as a Kalman Filter. The specific contribution of [Roumeliotis,I.-2002] is centered in the distribution of the Kalman Filter equations among the different agents in a way that the numerical process is parallelized for a more efficient execution.

[Burgard,W.-2005] proposes the problem of exploring an unknown environment using a community of cooperative robots. The key aspect of this research is to assign efficiently the targets to each robotic agent in order to cover the exploration scenario with the minimum exploration time. For this purpose, effective communication strategies must be implemented to allow the different agents share their location information, with the objective of plan the exploration targets and the paths towards them.

[Gouveia,B.D.-2015] describes the distribution of computational tasks among robotic agents in a system for Simultaneous Localization and Mapping (SLAM) problems solving. The paper uses the concept of “Robotic Cluster”, previously introduced by [Marjovi,A.-2012], referring to the segmentation and distribution of computational tasks among a number of robotic nodes, just like in computer clusters. Growing complexity of modern navigation, localization and mapping algorithms motivate the increase of computational power onboard autonomous robots; however, this factor impacts dramatically in power demand, what, in turn, affects other design parameters such as operation temperature, mass, cost, etc. Considering multi-robot systems, the availability of a number of low capacity computation nodes onboard each individual robot enables the application of computer network concepts to face complex computations instead of using a monolithic processing unit.

The advantages associated with Distributed Robotics for exploration missions compared to centralized systems have been analyzed intensively in literature, mostly due to the increment in the research intensity motivated in part by the advancement achieved in technologies related with computational power, wireless communications and sensing [Nagatani,K.-2007], [Bayindir,L.-2007], [Arai,T.-2002]. Nowadays, powerful robotic platforms endowed with impressive computational and communication capabilities in small formfactors, can be implemented at competitive costs, this enabled a totally new paradigm consisting of small robotic entities interacting to achieve a common goal: Cooperative robotics.

The intrinsic advantages of distributed versus centralized systems are:

- Scalability: allowing the incremental implementation of the system, thus minimizing the risks and enabling hybrid or technological upgrades in the process of the system completion. This factor is important in Space engineering where the development plans extend over several years and the investments are so high that missions become affordable only if the operational life is sufficiently long. Therefore, during an incremental implementation, newer and more sophisticated robots coexist with older but still operative units.
- Reliability: since the failure of one robot can be compensated by the combined operation of other units. Therefore, multi-robot cooperation leads to reliable redundant schemes.
- Robustness: as communication mechanisms between autonomous robots inside a multi-robot community allow the robotic systems to deal with uncertainty and non-planned events or difficulties in more efficient way, Moreover, distributed approach removes the threat of single point failures, a traditional concern in centralized architectures.

Moreover, other studies such as [Schenker,P.-2003] highlight as an additional but important advantage the fact that autonomous robots can cooperate to achieve goals that are not feasible for a single robot, such as deploying large structures such as solar power plants, containers, human habitats etc.

Considering this approach as advantageous for space exploration, it is clear that the accomplishment of an effective multi-robot cooperative mechanism is a complex, multi-disciplinary task.

Among the many challenges associated with cooperative robotic systems, the cooperation [Dudek,G.-1997] presented a classification of Multi-agent robotic systems in form of a taxonomy intended to establish a rationale to guide system-level and architecture design efforts. In such study, the application of multiple robot systems, formed by simpler robotic cooperative units, is already reported as advantageous against single rover approaches considering robustness, reliability, scalability and economy factors. This taxonomy aims to extend its scope to two implementation extremes, consisting in either a community of totally autonomous robotic agents or a system formed by a set of distributed peripherals communicating with a central unit in charge of the main data processing and control procedures, which leads to a sort of single but distributed robot.

Although both approaches could be considered collective systems, the advantage related with the intrinsic parallelism comes with the first extreme; nevertheless, the advantages concerning scalability and economy of implementation also apply to the second case. As an example, ALSEP concept (Apollo Lunar Surface Experiments Package) comprised, according to [NASA RP-1036], of a set of scientific instruments placed by the astronauts at the landing site of each of the five Apollo missions to land on the Moon following Apollo 11 (Apollos 12, 14, 15, 16, and 17) consisted basically in a set of distributed experimental set-ups connected by wires to a central power and telemetry station.



Figure 1.2.1- ALSEP Experimental Set-Up deployed in Lunar surface during Apollo 16 Mission

In order to be able to gain the advantages of the collectivity in terms of reliability and robustness, it is necessary that a cooperative behavior appears resulting of the combination of the operation of small and simple robots, with simpler goals and functionalities, in a way that the collective goals are equivalent to those expected to be achieved by single large robots. For this to happen, it is indispensable that efficient interaction mechanisms exist.

Within this context, and considering a space exploration application, where the scenario of operation is unstructured and uncertain by nature, and where the topological location is always a data of key scientific interest, interaction refers inevitably to intercommunication and mutual-self localization. In fact, topological organization is a key property a robotic community since most of the tasks a multi-robot system must face is defined in space, so it is considered as a basic parameter in the taxonomy defined in [Dudek,G.-1997]. Contributions like [Franchi,A.-2009] consider mutual localization in multi-robot systems with a Relative Mutual Localization (RML) approach instead of Absolute Mutual localization (AML). RML methods rely on data fusion via estimators like Kalman Filters to approximate the location of each single rover in a reference frame given by the robots themselves whilst the AML strategies rely in geometric methods to calculate the position of each individual robot within an absolute spatial reference frame.

In other study [Arai,T.-2002], an overview of the research than is being performed in distributed mobile robot systems is presented. In a first approach, seven research categories are distinguished: biological inspirations, communication, robotic architectures, navigation strategies (including localization, mapping and exploration), object transport and manipulation methodologies, motion coordination and reconfigurable systems. However, the research in cooperative multi-robotic systems is relatively recent (first works are dated in the late 80's) therefore none of the areas of research associated with the topic mentioned above can be considered mature.

Specifically, [Arai,T.-2002] reports that communications between robots in a multi-robot system have been intensively studied in both implicit (i.e. communication through the effects of different interactions) and explicit (i.e. produced by mechanisms specifically established for such purpose) mechanisms. In any case, the literature references reported in this contribution conclude that even simple interaction mechanisms enhance the system performance in appreciable levels.

[Premvuti,S.-1996] emphasizes the relevance of relative location in multi-robot system in order to take advantage of its distributed nature. Instead of relying in centralized location systems, this work proposes a relative positioning system based in individual optical range sensors based on rotating laser beams. Each robot can detect, by means of a linear photodetector, the speed of the beam swept over the detector and, since the linear speed depends on the radius when the laser beam rotates at a constant known angular speed, radial distance can be determined and, consequently, a map of individual locations can be obtained by triangulation. Although the solution approached is robust (as a decentralized system) the complexity of the emitter and detector is significant compared with the rest of the robot in a way that, localization takes a significant proportion of the robot resources in terms of payload capacity. Moreover, arbitration mechanisms (necessary to solve collision situations like when two robots are located from a third one simultaneously) have to be still implemented, which will take a significant amount of computational resources.

In a totally different approach, [Oliveira,S.-2016] proposes the use of stationary base stations called “anchors”, placed at known positions, to determine the location of each single robot. The study focuses on the implementation of accurate and efficient methods for location determination, since efficiency (from the computational point of view) is a key factor for the

successful implementation of such mechanism in small mobile robotic platforms. According to the previously mentioned study, the determination of self-location in Swarm Robotic Systems is not only necessary for performing scientific objectives, incorporating spatial information to data gathered by a network of distributed sensors for example, but also to provide the basis of those mechanisms that characterized some of the main advantages of Swarm Robotic Systems such as cooperative navigation, self-assembly and formation navigation, mutual support and healing, etc.

The algorithms proposed in [Oliveira,S.-2016] , some of them based on bio-inspired methods, demonstrate a scalar nature in the improvement of the localization accuracy. Within an interconnected swarm, location error improves dramatically when the number of main stations (or “anchors”, as denominated in the contribution) increases, whilst an increment in the population of the swarm improves the area along which the range can be determined.

This last aspect is implied in the spatial propagation characteristics of radiofrequency signals. Depending on the configuration of the location determination radio system, the operation range will be more or less limited by signal attenuation due to distance (i.e. propagation loss), obstacles and its influence within the Fresnel zone of the link, multipath interferences, etc. Considering those aspects, Swarm configurations for robotic systems provide significant advantages when the communication mechanisms provide networked topologies like mesh communication, having the capability of forwarding communication packets or location information in a way that far robotic agents can determine its location within the scenario with the support of the location information of their neighbor agents.

[García,C.-2011] contributes with a design and modeling of a distributed robotic system whose agents are legged robots, with the objective of enabling cooperative operation. The study insists in the potential of distributed robotic system as a paradigm for Distributed Artificial Intelligent (DAI) systems for highly efficient problem solving. According to this study, the integration of Multi-Agent systems relies on three key pillars: communication, cooperation and coordination mechanisms, whilst communication mechanisms provide the substrate for the distributed system operation, cooperation and coordination provide the fundamentals for tasks sharing and goals distribution for the benefit of the whole system.

Furthermore, navigation, involving localization (meaning again mutual as well as self-localization), mapping (meaning characterization of the near environment, unstructured by nature) and exploration (involving path planning and motion control) takes a great deal of research effort, being a critical ability for robotic communities to perform exploration tasks in a reliable way.

1.3.The problem of Self-Location and Navigation in Small Platforms.

As mentioned above, self and mutual localization are key capabilities in multi-robot communities in order to achieve an efficient spatial organization, which is of the outmost importance in planetary exploration. In such missions, scientific objectives are commonly associated with specific locations, selected by the scientific community through in depth studies in order to ensure the mission will yield results of the maximum scientific interest whilst providing a minimum density of obstacles, thus minimizing the uncertainty of the unstructured scenario the robot must navigate. Therefore, a great deal of research has been

performed by the robotics community in order to propose different alternatives for localization in a robotic community.

Regarding navigation strategies, [Arai,T.-2002] highlights the evolution in the research of this topic from the extension of algorithms and methods initially intended for single rovers to a community of interacting robots, to the development of totally new distributed methodologies. An example of this approach is the work reported in [Roumeliotis,I.-2002], where a method for robot localization within a group of mobile units is approached fusing the self-localization information of every single robot with the localization data of its neighbors by means of an estimator based on a Kalman Filter. Furthermore, the work categorizes the location methods as based on landmarks, scan matching and or graphs.

[Loevsky,I.-2010] defines “landmarks localization” as a method based on the estimation of the localization measuring the robot the distance to specific static elements that can be identified by the robot and thus associated to absolute positions in the scenario. The robot estimates its localization inside the scenario by a variety of methods and algorithms using the information consisting in the set of distances to different landmarks and their (known) absolute positions.

According to [Bengtsson,O.-2003], the “scan-matching algorithms” are based on the determination of specific distances from the robot by means of range sensors (like those based in laser) once the robot has reached a specific position (that can be calculated via Dead-Reckoning algorithms) and thus updating the estimated position with the position calculated from this range measurements in order to reduce the accumulative error Dead-Reckoning methods are prone to. This method, as mentioned in [Bengtsson,O.-2003], is very suitable for industrial environments with a predictable and structured scenario, which according to [Xiaorui,Z.-2017] means that the environment is built on geometrically regular structures, but complex to implement in unstructured or dynamic environments. In the case of multi-robot systems, the possible interferences produced by neighbor robotic individuals add a dynamic character that this method is not able to compensate for.

Graph based algorithms are complementary to the above mentioned methods. In general, graph-based probabilistic methods have been intensively used in the estimation of relative position within a multi-robot community. [Indelman,V.-2014] proposes an approach consisting in a distributed probabilistic method that estimates the position of each robot fusing the information shared by each individual concerning its relative position and the localization of references the absolute frame, yielding an estimation of both relative and global localization of each robot. The references could be acquired either from defined elements (such as landmarks) or via scan-matching methods.

[Fox,D.-2000] considers that the localization problem can be distributed within two categories: Position Tracking problems, consisting in the compensation of accumulative error during the estimation of the localization during a route, and Global Self-Localization, which is related with the determination of absolute localization with no previous information. The contribution proposes a probabilistic approach based in the sharing of sensor information between robots in a robotic community in order to make the localization estimation problem a distributed one.

As an interesting aspect, [Fox,D.-2000] refers to the convenience of implementing a sensor information sharing capability in order to optimize in cost the robotic system. In this way, a few rovers could carry more sophisticated sensors than those forming the majority of the population of the robotic community. By means of an efficient communication infrastructure, this information related with communication could be shared among the

robotic individuals and processed in a distributed manner and fused with less accurate but massive localization information yielding more precise and rich mapping details. This way, the communication infrastructure the multi-robot system is equipped with, becomes a key asset in for the determination of self and mutual localization.

[Wang,L.-2016] makes an interesting analysis about the convenience of combining self-location internal procedures (here denominated as proprioceptive) with externally driven self-location methods (or exteroceptive) in Multi-Agent robotic systems operating in situations where communication capabilities could not be guarantee, what is usual in real scenarios like natural or urban canyons (where external means like GPS are unavailable).

The solution proposed consists in using a hierarchical architecture categorizing the agents in two levels: the measuring agents, which have the capability of obtaining self-location information by means of high precision instrumental resources (here GPS) and non-measuring agents, which obtain the own location information from the measuring ones by means of some mechanisms internal to the distributed robotic system. The survey also suggests the idea of including the agents in one category or another depending not just on functional aspects but also on mission objectives: those agents not requiring (due to the nature of the tasks assigned) a high positioning precision) can obtain the location information with higher update time period and through less accurate procedures, enabling the implementation of agents with lower hardware and software requirements and, thus, incrementing the population of the system which should result in an increment of overall efficiency.

Although the study denotes that cooperative localization has already been intensively investigated through several estimation techniques (including Extended Kalman Filtering – EKF-, Particle Filtering, Parameter Estimation, etc.). EKF method provide the resources to balance computational load (demanded by the number of necessary iterations) and accuracy, enabling the implementation of an efficient localization estimator with a minimum hardware footprint when communications stage simplicity is a primary design parameter.

Concerning specific implementation methods for localization mechanisms, [Carroll,P.-2016] suggests a method for mobile nodes based in Doppler frequency shift determination. The method is proposed for underwater mobile systems, such as Unmanned Underwater Vehicles (UUV), and supported underwater acoustic communications, though the principles proposed are applicable to electromagnetic radio signals propagation substituting the speed of sound in water by the speed of light. As this analysis explains, many localization methods rely only on time measurement associated to messages transmission, like Time-Of-Fight, Time-Of-Arrival, etc. in combination with filtering and estimation techniques for tracking purposes. The incorporation of Doppler frequency shift information enhances the overall accuracy of position estimation adding relative speed information. Furthermore, the study evaluates the efficiency of the localization estimation method using estimation techniques like Kalman Filtering and Probabilistic Data Association.

The contribution gives an approach very similar to system architectures proposed by the aforementioned [Oliveira,S.-2016] and [Wang,L.-2016], suggesting the use of a Distributed Antenna System (DAS) instead a central localization antenna in a way that, besides communication, the parameters measured along the different reception antennas could be “fused” to obtain localization information. This concept is supported by a former contribution from the same authors [Carroll,P.-2012] dealing with underwater localization and tracking of mobile systems based in a distributed system composed by a network of interconnected surface buoys. A mechanism of message broadcasting was proposed through which, measuring the time difference between two messages coming from different senders,

the mobile system could determine its relative position in the reference framework associated to the surface nodes. The advantage of the system is that floating buoys can be more hardware intensive and have the capability of receiving GPS signal, therefore absolute position information is available with high resolution. In the same way, synchronization between these reference base stations or (“anchors” as defined in [Oliveira,S.-2016]) is also guaranteed by GPS infrastructure. The paper proposes mechanisms not only for self-localization but also for relative position information propagation for further nodes that could be out range.

In general, [Carroll,P.-2016] demonstrates that a Doppler frequency component-supported method improves the efficiency of position estimation over simple time-delay based methods, despite a more complex estimation algorithm. Nevertheless, current microcontrollers and embedded microprocessors make possible the implementation of highly complex algorithms in some cases (like those implemented in logic devices like FPGAs) with high parallelism, reasons that make this approach very feasible in space exploration scenarios.

1.4.Thesis Objectives: Towards Robotic Colonization.

The trade-off performed along this chapter shows that when small robots are intended to work in a cooperative community for planetary surface exploration, navigation and inter-nodes communication aspects become a critical issue for the success in a real mission scenario. For this paradigm to succeed, it is necessary however to deploy the required infrastructure for the robotic community to achieve efficient self-location as well as relative positioning and effective communications between nodes.

In this thesis, an exploration mission concept in which two cooperative robotic systems co-exist is presented. This paradigm hinges on the advantages of a community of robots that provide support in terms of communication and navigation to a second robotic community that is devoted to the exploration goals. This way, a progressive robotic colonization may take place in order to simplify the robotic settlement, not only for future scientific exploration mission but also for other purposes such as human settlement, in-situ resources utilization and improvement of existing missions.

This thesis focuses on the role of the robotic community dedicated to the support and, more specifically, on the aspects concerning the analysis of the different position and velocity determination methods, which are combined with the communication services.

Most of the space exploration missions have just one main single scientific goal and are hence designed to meet this primary objective. There would be multiple benefits from both the scientific and technical points of view if it would be possible to have a stable infrastructure on the Moon dedicated to give support to exploratory mission, besides those related to the distributed nature of the system. Some of the benefits would be:

- A higher cost efficiency per mission. Some of the subsystems in current exploration rovers like those related with telemetry, navigation, power supply are not so prone to obsolescence as more sophisticated elements related with instrumentation like chemical detectors, image sensors etc. New missions could rely on in-situ power and communications infrastructures instead of replicating those sub-systems from mission to mission.

- Incremental improvement of past missions with the growing of the support robotic community. When the support multi-robot system grows to cover the needs of future missions, the existing robots take advantage of these new resources. This is not possible with the current monolithic approach.
- The use of specific support robotic platforms forces the industry to keep compatibility from mission to mission in aspects like mechanical and electrical interfaces, communication protocols etc. This induces the need for standards to be adopted that, in long term, enhance the robustness of the solutions adopted by maturation of technology that inevitably imply to costs reduction through industrial competitiveness.

As was explained above, the ALSEP instrumentation system used during Apollo missions could be considered as a precedent of a distributed and scalable scientific research set-up. Nevertheless, such a concept has never been proposed in a robotic equivalent, and with the purpose of becoming a modular and wirelessly scalable and distributed system aiming to give support to a variety of mission goals, not only scientific, but also exploratory or even for future human colonization. Such a robotic system could be designed to provide storage systems for rovers, a communication relay, navigation and localization services or energy. To be novel, such support robotic stations would need to be built up in an intelligent, reconfigurable and modular manner, to be able to adapt to different scientific scenarios.

Since the paradigm is complex and strongly multidisciplinary, involving engineering disciplines such as power systems, communications, navigation, motion control and path planning, etc. this thesis focuses in the aspects related to RF navigation and, more specifically, localization.

An analysis of the different methods for position and velocity calculation in combination with presently used RF communication standards in planetary exploration is presented, considering different methods and basic technologies in the context of the lunar surface exploration scenario, which will be properly studied in order to identify the main physical characteristics that will condition the selection of localization methods and technologies.

Once the method and related technologies for position and velocity determination are selected for the application under consideration, a complete mathematical formulation of the localization process will be developed, as well as a complete numerical model in order to make possible the simulation of different conditions in the acquisition of position and velocity of a mobile robot travelling across an exploration area.

Following, an analysis about the noise sources as well as the main limiting factors for precision and resolution, such as phase and frequency noise in RF reference carriers or long term drift mechanisms such as thermal drift and aging will be performed, and those instability factors will be introduced in the model in order to make simulations considering different noise scenarios. This way, the effect of carrier frequency instability due to phase noise is categorized in different contributing noise sources, and their impact in the overall localization performance is considered both in the position and in the relative speed determination points of view. Furthermore, considerations about possible filtering techniques used to obtain position and velocity from RF noisy signals are also presented and mathematically formulated.

Finally, a real hardware implementation of a prototype implementing the proposed localization concept will be proposed and key metrics in terms of mass and power consumption of the required payload hardware are also assessed. An experimental phase will be performed to consolidate with laboratory measurements the methods and

mathematical formulations developed along the thesis, and further analysis and conclusions will be elaborated from the experimental results.

1.5. Thesis Contributions.

The main contributions of the thesis can be summarized in the following list:

- A method for tracking the location of a mobile robot from a set of reference stations has been developed, considering the specific aspects of lunar landscape. A survey of the lunar environment has been performed followed by a tradeoff of different localization methods suitable for the case of lunar robotic exploration. The method proposed suits the characteristics of the environment and its implementation with minimum power consumption.
- The localization method has been formulated and a complete mathematical model implemented including noise sources in order to make possible the simulation of different exploration scenarios.
- A hardware architecture for the implementation of the localization method is presented, and its associated noise model defined and introduced in the numerical model. Different simulations are performed and analyzed, and a filtering technique proposed for the mitigation of time-domain noise is implemented in the model and tested.
- The localization method proposed has been conceived to ensure a minimum hardware implementation signature, in order to enable its application for small robotic platforms. This feature will enable exploration robots in small mass and volume still with resources to power research payloads aiming to expand the ambition of the lunar mission. A detailed analysis of the time-domain instability contributors, both in short term (i.e. noise) and long term (i.e. bias drift) is performed considering real components and their impact in the overall performance on a hypothetical implementation.
- The localization tracking method is based in a time domain principle that will resolve the Doppler with low complexity, enabling tolerance of RF impairments such as those related with phase noise in the up and down conversion process. Moreover, the effect of practical (i.e. real world) effects such as main clock frequency drift related with temperature and aging, as mentioned above, or phase noise, have been explained and considered in the analysis of impact in the localization accuracy,
- Finally, the thesis consolidates the contributions with an experimental working demonstration platform.
- To study noise compensating techniques in different aspects of the localization method to achieve a precise location and velocity determination in noisy environments operating at UHF band (400MHz), identifying the key parameters in the location method that would improve accuracy and SNR, together with filtering.
- Analysis of a redundant topology in the physical implementation architecture in order to improve power consumption and reliability whilst considering hardware signature and power consumption etc.

As a result of the work involved of this thesis, a number of publications have been generated:

- Garcia-de-Quirós, F., Radice, G. and Carrasco, J. (2018). FDOA-based method to enhance TOF method for Position Determination of Lunar Exploration Rovers. In: European Planetary Science Congress EPSC2018-1143. (Presentation).

- Garcia-de-Quiros, F. and Radice, G. (2018). A Radiofrequency Based Navigation Method for Cooperative Robotic Communities in Surface Exploration Missions. In: 20th International Conference on Space Robotics. (Presentation).
- Garcia-de-Quiros, F., Radice, G. and Carrasco, J. (2011). Hybrid Robotic community Strategies For Lunar Surface Exploration. In: 62nd International Astronautical Congress. Cape Town. (Poster).
- Garcia-de-Quirós, F., Radice, G. and Carrasco, J. (2019) “Influence of Oscillator Phase Noise in Frequency-Based Location Methods for Mobile Exploration Robots” EUCASS 2019 (Presentation).
- Garcia-de-Quirós, F., Radice, G. and Carrasco, J., (2019) “Analysis of Phase Noise Effects on Doppler-shift Measurements used for the Determination of Position and Velocity of Surface Exploration Robots” European Planetary Science Congress EPSC2019 (Accepted for Poster).
- Garcia-de-Quirós, F., Radice, G. and Carrasco, J., (2019) “Theoretical Estimation of Lunar Soil Reflection coefficients in Radiofrequency Communication Bands”, IEICE Transactions on Communications” (manuscript accepted for publication on March 2020 - Vol.E103-B, No.3).

1.6. Thesis Outline. Work Developed.

The first part of this work consisted in an analysis of the advantages and drawbacks of robotic exploration, in particular considering distributed robotic systems in opposition of classical strategies based in monolithic architectures involving single (though complex) rovers. An analysis of the State-of-the-Art through relevant literature about the topic has been performed along chapter one, as well as a consideration about the technological hurdles to reach an effective implementation of this strategy that could unleash its intrinsic advantages. The relevance of self-location awareness for the operation of a population of mobile autonomous robots has been highlighted and justified.

In Chapter 2, the problem of self-location is analysed in the context of a Lunar exploration scenario defined by the assumption of the deployment of a distributed robotic system composed by a number of small autonomous mobile rovers (Mobile Nodes) supported by a few of larger units (Tracking Stations, which could be stationary or also mobile) in charge of providing radiofrequency network communications infrastructure and (eventually) power supply. The Tracking stations are conceived as larger robotic systems concentrating the data relay capacity (communications from Lunar surface to an eventual satellite communicating with Earth) and power conditioning systems. The concept behind this approach is based in the model of concentrating the more complex and bulky systems (large batteries, solar panels, power conditioning units, Lunar surface-to-orbit communication systems and related antennas) in Tracking Stations whilst the Mobile nodes, more light and simpler, are intended to perform the navigation to pursue the science objectives, navigating through the exploration scenario, and collecting data and material samples. Different techniques and procedures for self-location determination based in radiofrequency signal transmission are presented and discussed, and key parameters and performance limiting factors are identified and analyzed. Finally, a specific and representative exploration scenario is defined on a justified analysis of previous robotic exploration missions, and a complete mathematical formulation is developed to model all the phases in the location and velocity determination of mobile nodes across an exploration area delimited by a number of Tracking Stations.

In Chapter 3, an implementation architecture is presented, considering development aspects involving real space hardware design guidelines. The objective is to propose and analyze a system architecture able to execute the operation described in Chapter 2 that could be implemented in a spaceborne version, that is, whose main constituent parts would be available in space quality versions or could be directly implemented with parts of this class. Practical criteria such as volume and mass budget as well as power consumption were considered to define the system architecture. Along this chapter, a complete analysis of the different noise and drift sources are analyzed, contrasted with real components information, a mathematical noise model is defined and combined with the mathematical model designed in Chapter 2, in a way that different simulations with noise are performed and the results analyzed. A filtering technique to compensate the influence of noise, based in an adaptation of Kalman Filtering, is proposed and the results of its application in the noise models analyzed.

In Chapter 4, a prototype implementing the proposed architecture is presented and discussed. Specific design aspects both from the hardware and logic layers are presented and discussed. Redundancy scheme in the proposed implementation is presented and justified in accordance with its suitability for a potential real application.

Along Chapter 5, different experiments carried out with the prototypes are presented and analyzed in comparison with the model simulations discussed in Chapter 3. The results yielded are analyzed in the context of a potential application in a real exploration mission.

Finally, the general conclusions generated by the thesis work are presented in Chapter 6, together with a proposal of possible continuation work lines that could become the topic for future thesis.

Chapter 2.- Methods for Localization

2.1. Introduction

Although there are different methods and technologies to determine the position of autonomous agents in a given environment, the decision about which of these methods to implement is not trivial as it is a key factor to guarantee the success of the mission.

In order to choose the appropriate paradigm, environmental factors must be considered, in order to adapt the robotic system to the peculiarities of the scenario in which the robots must operate in order to fulfill their mission objectives. As explained in [Schilling, K.-1996], environmental factors help to define the optimum architecture for any mobile robotic system in any ground application such as mining, search & rescue, research, reconnaissance, etc. However, in space exploration missions, the same tasks must be performed under a more constrained set of requirements determined by the harsh environmental conditions (vacuum, extreme temperatures, energy available, etc.) as well as the limitations imposed by space missions such as limited mass or payload volume available, and the long hibernation periods the system must face during the transfer to the objective.

[Schilling, K.-1996] reviews specific design constraints of different rovers from Europe, USA and Soviet Union used for planetary surface exploration. Specifically, the set of requirements in these applications are influenced by, as mentioned above, extreme temperatures, but also by the operational scenarios for which poor or no information is available about basic environmental properties such as soil composition or mechanical properties, lower gravity that combined with a different (or none at all) atmosphere causes unforeseen interaction with the dust generated by the movement of the robot over the surface. Moreover, the significant latency in communications combined with the limited on board processing and data storage capabilities only add more constraints to the autonomy of the mobile robots in case of unexpected situations.

The review performed here also includes navigation procedures and methods developed for the MARSNET mission scenario for ESA. In this mission, a robotic system consisting of a simple rover that deploys several scientific instruments over the Martian surface at locations that are far from the landing site is proposed. The IDD (Instrument Deployment Device) carries a payload consisting of manifold research instrumentation and intended to egress the lander, while linked to the power and communication central system by a tether, and with some navigation capabilities to traverse the terrain in order to take samples and make measurements of different parameters of the Mars soil. For IDD, two main navigation approaches were considered: navigation by reference and Dead-Reckoning techniques. As mentioned in chapter 1, referenced navigation is based on self-positioning by measuring the distance from selected land marks, which define the frame of reference within which the robot moves. Should landmarks not be available then the position is determined by integration of the path with respect to a starting point. This approach, known as *Dead Reckoning* is highly susceptible to accumulative errors, but has the intrinsic advantage of being independent of external references and therefore usually employed in combination with external referenced systems that are used both to compensate integration errors

providing information about the absolute position and to add a redundant positioning mechanism to improve overall reliability.

In order to provide the reader with the appropriate context we will start first introduce the unique characteristics of the Moon environment, highlighting the aspects that are of relevant impact in the design of a multi-robot distributed system intended to operate on its surface. This will be followed by a review of the State-of-the-Art in position determination methodologies, including both optical and radiofrequency based approaches and finally a proposed architecture is discussed.

2.2. The Moon Environment.

The Moon is the better known of the extraterrestrial environments, mainly thanks to the Apollo program missions, but this does not simplify the task of sending a robotic probe to perform autonomous exploration missions to its surface.

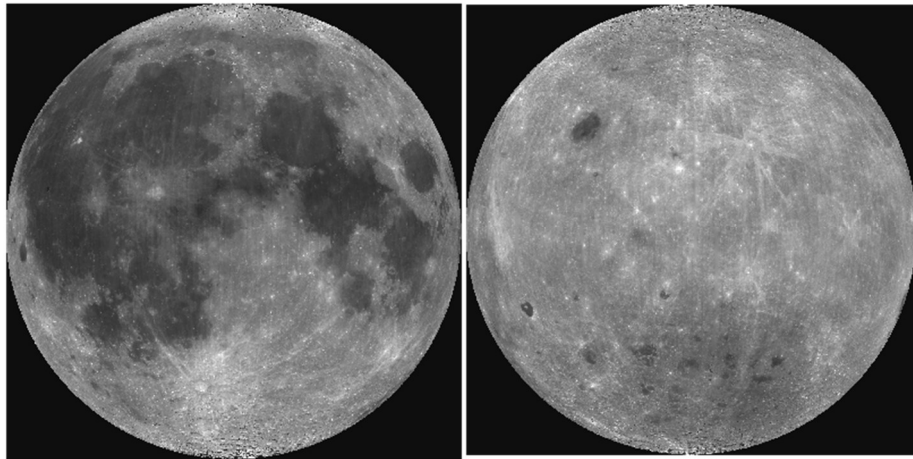


Figure 2.2.1- (Left) Near and (Right) Far side pictures of the Moon.

The geography of the Moon's surface according to [Seedhouse ,E.-2008] is comprised of three main elements: craters, maria, and highlands. When observing the moon surface, the most noteworthy aspect is the strong difference in color tone of the terrain, with dark grey zones surrounded by lighter, almost white areas. Such light areas are called lunar highlands, or Terrae and different in composition from the Maria



Figure 2.2.2- Picture obtained during Apollo 17 mission showing Mare Imbrium and Copernicus Crater seen almost edge-on near the horizon at the center. Credit: NASA,1972.

Maria soil is of basaltic nature, a product of early volcanic activity of the Moon, is very rich in iron and titanium, mostly present in the mineral Ilmenite. The lava produced by volcanic eruptions flowed to impact basins, filling the area and causing the Maria soil to have its distinctive aspect. It is important to mention that, although low lands usually coincide with Maria areas, there are exceptions like the South Pole-Aitken basin, a huge crater impact in the far side of the moon. The unbalanced volcanic activity of the moon, produced in part by the tidal forces caused by the proximity of the Earth, meant that low lands on the near side were filled by lava more than the regions with the same characteristics on the far side.

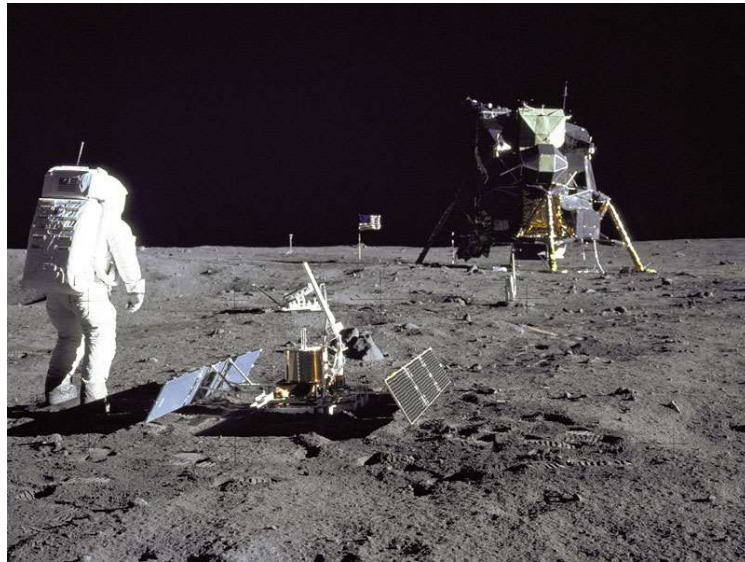


Figure 2.2.3- Apollo 11 astronaut, Buzz Aldrin, stands in front of a seismometer instrument. The Lunar Landing Module stands in the front. The landing site, Mare Tranquilitatis was chosen because of the geological characteristics of Maria, including a smooth and leveled surface, very suitable for landing and the foreseen surface operations. Credit: NASA,1969.

The highlands, are composed mainly of anorthosites, the pristine rocks considered to be the oldest rocks on the Moon, with high Aluminum and Calcium composition [Khan-Mayberry, N.-2008], and containing Potassium, Phosphorous and Pyroxene. The soil characteristic of this area, covers 83% of the total lunar area, is considered the nearest form to the original Moon crust.

Impact craters originate from meteoric activity in the early periods of the Moon's life. The absence of atmosphere increased the impact energy, causing huge craters like the South Pole-Aitken Basin as well as smaller ones. Due to the lack of erosion agents, most craters are still very clearly defined, with sharp rims whilst others present steep inner walls or terraces produced by slipping of the soil material. When a meteorite impacts at hypervelocity, the higher albedo materials are ejected, forming the crater and the characteristic ray pattern. The main constituent of the craters soil are impact breccias, rocks made by compaction and solidification of different rocks produced by the impact. These rocks were formed and shattered and compacted again by the extremely high temperatures ensuing the impact and therefore the composition is highly irregular in these areas, including grains of very different sizes and shape.

An important category of lunar soil is the so-called lunar regolith, which is formed by a mixture of iron-rich rock debris of all kinds, including dust and volcanic ash. Lunar regolith, [Khan-Mayberry, N.-2008], was agreed during Apollo program, to encompass all broken and impact resultant rocks fragments and minerals or glass grains spread out on the lunar surface. Although lunar regolith and lunar soil are sometimes synonymous, the term regolith only refers to the fraction of soil corresponding to sub-centimeter grains, therefore, everything bigger than one centimeter is officially classified as a rock. As a subset of regolith, “dust” refers to particles in the range of $< 20\mu\text{m}$. Due to its very small size, lunar dust was a source of problems both to the crew and hardware during the Apollo missions.

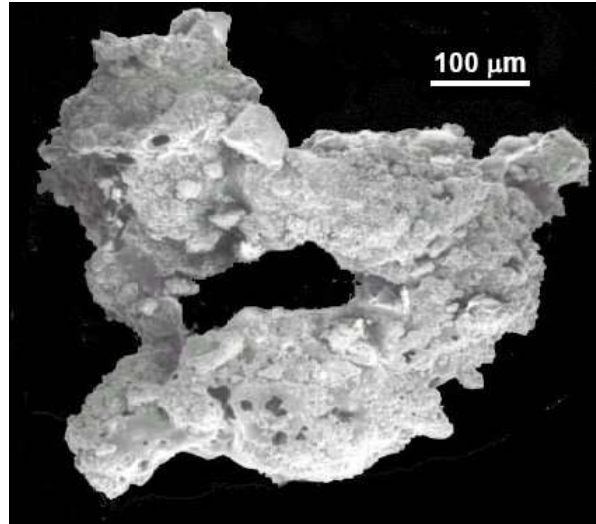


Figure 2.2.4- A fragment of Moon regolith. The typical highly irregular form with sharp edges of regolith grains can be appreciated in this example. Credit: David S. McKay, NASA/JSC.

Moreover, horizon glow effects were noticed by astronauts [Stubbs, T.J.-2005], and later demonstrated to be caused by a layer of $5\text{-}6\ \mu\text{m}$ particles dust in suspension up to 1 m above the Moon surface. Transport phenomena of electrostatically charged dust particles in alternating cycles (positive and negative) during day and night cause the existence of a layer of dust in suspension, significant up to 1 m but also existing at higher altitudes although with smaller particles.

The problems associated with dust interference on the exploration activities have been intensively studied [Stubbs, J.-2005]. Astronauts participating in Apollo program reported a wide range of problems such as adhering to clothes and equipment, reducing visibility during rover driving or landing causing breathing difficulties and other health troubles, already discussed in [Khan-Mayberry, N.-2008]. The problems associated with dust are caused by the following factors:

- The grain size is $70\ \mu\text{m}$ average, too small to be perceived by human eye.
- The shape of lunar dust grains is highly variable and can present extremely sharp sides, even in an elongated shape. This factor makes lunar dust highly abrasive and, therefore, potentially harmful for mechanical moving structures.
- The electrical conductivity of the grain is very low, and consequently it is susceptible to be electrostatically charged. This effect produces adhesion of dust to different items such as space suits, solar panels, roving vehicle parts, etc. hindering system operations and requiring constant maintenance actions.

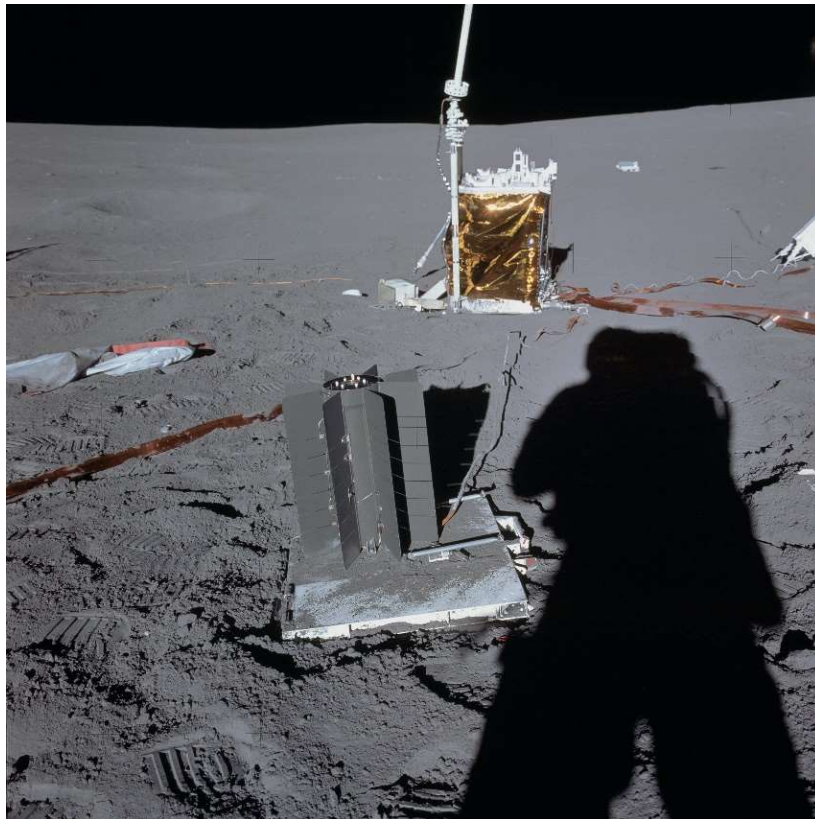


Figure 2.2.5- An Apollo 14 astronaut deploys the ALSEP power source (foreground) whilst the ALSEP's Central Station is placed nearby connected by a cable (background). It can be appreciated that the power source is totally covered by dust. The ALSEP included as a part of its Central Station an instrument specifically designed for dust analysis, since at that time, concerns about the effect of dust both in the equipment and in the crew increased. Credit: NASA/JSC.

Another important physical property of the Moon is its gravity. Gravity on the moon is only one-sixth of that of the Earth, and this must be considered when designing the mobility sub-system of the roving robots.

Finally, the lunar environment is characterized by a strong variation of surface temperatures spanning from -153°C to $+107^{\circ}\text{C}$ and a hard vacuum, where solar radiation reaches the surface in form of both electromagnetic and ionizing radiation. The advantage given by the availability of sunlight for power generation is compensated by the strong ionizing dose contained high-energy electrons, protons and heavy nuclei that must be considered in the design of the robotic subsystems.

Concerning the electrical properties of the lunar soil, which is a critical aspect from the point of view of the propagation of radiofrequency signals on the surface of the moon, several studies have contributed to the characterization of conductivity and permittivity of the lunar soil layers, based in analysis performed on Apollo program Lunar soil samples.

Figure 2.2.6 shows the structure of the different layers of lunar soil, having each layer different densities and mechanical properties and, thus, different electrical behavior.

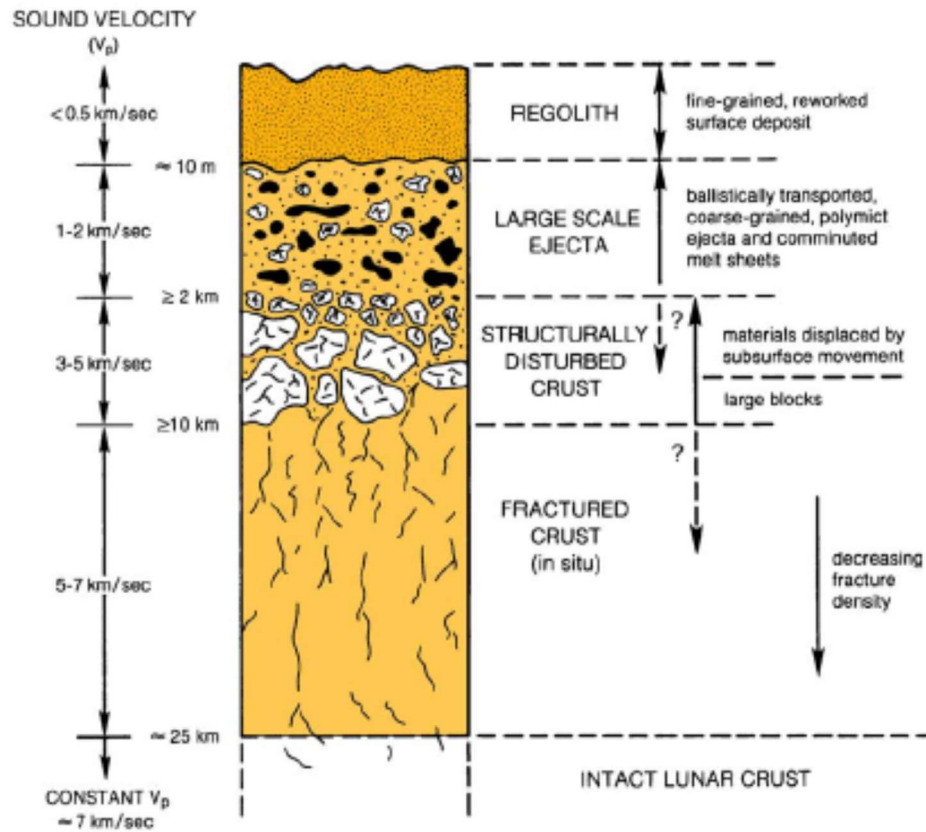


Figure 2.2.6- Lunar soil layers structure by [Kring,D.-2006], based in information from [Hörz, F.-1991]

The electrical behaviour of a soil is modelled by its electrical conductivity and permittivity, which real part is known as dielectric constant [ITU-1990]. In this sense [Anderson,R.-2005] reports measurements of the permittivity of the lunar soil (regolith and ejecta in Figure 2.2.6) ranging from 1.5 to 4 depending on the density of the samples, whilst 2.2 to 2.3, whilst [Olhoeft,G.-1974] report values from 2.2 to 2.3. Concerning conductivity, [Anderson,R.-2005] reports values around $0.15 \cdot 10^3$ Siemens for frequencies higher than 1MHz.

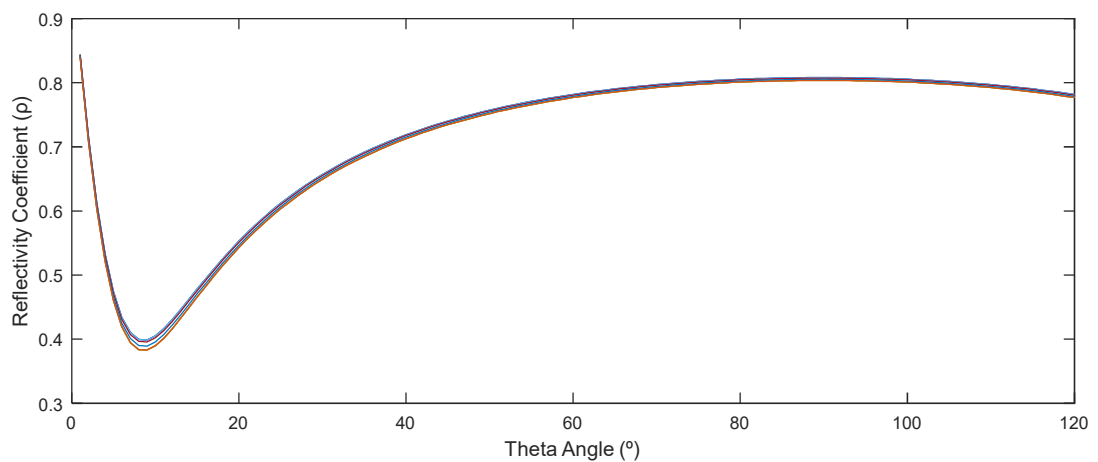


Figure 2.2.7- Lunar soil Reflectivity coefficient ρ vs. theta angle ($^\circ$) of incidence of radiofrequency wave with the ground for $\epsilon=1.5$ to 4, $\sigma=0.18 \cdot 10^{-3}$ Siemens.

Figure 2.2.7 represents the RF reflectivity coefficient ρ as a function of the angle of incidence in the ground surface, obtained with the MATLAB function *Reflectance()*, which was coded according with the standard formulation of $\rho = \rho(\sigma, \epsilon)$ [ITU-1990] [McClanning, K.-2011]. As it can be appreciated in such figure, the reflectivity coefficient range from 0.4 to 0.8 for angles from 15° to $>100^\circ$, reaching the minimum at the Brewster angle (14°).

2.3. Methods for Position Determination.

Localization can be defined as “the process through which (sensor) nodes in a network are associated with their physical location rather than a network address” [Lanzisera-2006]. In this sense, the problem of self and mutual positioning, has been extensively discussed in many studies concerned with ground robotic navigation, as mentioned in chapter 1, as well as multi-robotic distributed systems like the swarm or flock operations. Moreover, the measurement of relative positioning is not limited to robotics; other contributions like [Thorbjornsen, N.-2010], [Amundson, I.-2009], [Lanzisera-2006] or [Sanz, D.-2013] address this same challenge for a different application consisting in the distribution of wireless sensor nodes across the area of exploration interest. Again, the main advantage of this type of instrumentation deployment is that, despite the complexity of distributing the sensors, with this method a large area can be covered by instrumentation without the robustness and reliability required for a single rover covering and sampling the entire area, at a much lower cost and mission time. Specifically, [Sanz, D.-2013] mentions that the idea behind this concept consist in deploying a number of self-organizing sensor nodes forming a wireless networked architecture to provide a distributed instrument for the study and exploration of a planetary body. This study considers a number of scenarios for the application of a wireless sensor network, including fixed (i.e. anchored) or mobile sensor nodes, aerial or ground, intended as a distributed payload that can adapt to the characteristics of the area of interest to collect valuable information both from the sensors themselves as well as from the geographic data obtained from the location determination, which yields mapping information. [Amundson, I.-2009] highlights the interest of wireless mobile sensors network in their capability to adapt the arrangement of the nodes to dynamic events, such as those related with climatic or biologic phenomena, enabling a more accurate observation along the time.

In any case, all above mentioned references mention explicitly the determination of location (i.e. localization) as the most significant challenge when the sensor network is composed by mobile agents or when, being static) their location is not previously determined but critical for the experiment results (like for example when sensor nodes are deployed from an airplane over an area of interest) as [Amundson, I.-2009] suggests.

[Amundson, I.-2009] also provides a taxonomy of localization methods for mobile wireless sensor nodes, based in the definition of the three phases for location determination: Coordination, Measurement and Position Estimation, agreeing with [Lanzisera-2006] in the second and third phases which are defined by this reference as (1) measurement of relationships between the node and a set of reference stations and (2) calculation of location according some numerical procedure or algorithm based in the measurements obtained.

Coordination phase covers all the tasks and processes previous to the beginning of the measurement phase, such as clock synchronization, exchange of command and notification frames to start the location procedure typical in wireless communication protocols, etc. Measurement phase includes all the necessary tasks to measure the magnitudes that will be

required for the localization like ranges, angles, signal power received, etc. Finally, the Position Estimation phase encompasses all the calculations and algorithms necessary to calculate the position of the nodes out from the measurements obtained in the previous phase.

The first phase described by [Amundson,I.-2009] relies on the existing communications infrastructure operating in the robotic system. The determination of location requires preparatory processes in order to make it compatible with the rest of the tasks being executed by the exploring robots. Moreover, if the robotic agents have limited computational resources, the processes related with its localization may be incompatible with other actions such as experimental data sampling, information processing, etc. Considering this perspective, [Munir,S.A.-2007] categorizes the mobile sensor network architectures in three types: Flat, 2-Tier and 3-Tier hierarchical architectures, which are also suitable for the case of multi-robot systems.

Flat architectures, a set of both mobile and static homogeneous or heterogeneous units communicate sharing a common network. Most of basic navigation systems operate in this way [Thorbjornsen, N.-2010], [Lanzisera-2006].

Two-Tier architectures are defined by the existence of two communication layers, one intended to the transport of information among mobile nodes (experimental data in principle) and the second one for the communication with the stationary units that serve as navigation support nodes. As suggested in [Munir,S.A.-2007], this architecture becomes necessary when the mobile nodes have a significantly lower computational power than the stationary nodes, what makes sense in case of lunar exploration considering the power, mass and volume required for mobility. The communication network governing the exploration robots would be less data intensive and more focused to system-level coordination purposes. On the other hand, the communication network at the stationary stations should be focused on high data-rate communication in order to enable an efficient collection of experimental data from the mobile robots.

Finally, 3-Tier architectures are defined as an evolution of 2-Tier architectures when a third communication infrastructure is necessary to coordinate the system in case 2-Tier communications network has not such capability. For instance, if a multi-robot system expands across a wide area, the 2-Tier communication equipment may not have range enough to cover the furthest nodes. In such case, a 3-Tier network exist to enable the communication with remote stations. Considering our lunar exploration example, the existence of a communications satellite orbiting the Moon, through which distant stationary stations could communicate to keep the mobile robots under range, would define this 3-Tier communications layer.

Concerning the second phase for localization (Measurement phase), there are different methods to determine the position of a mobile node in a given exploration scenario. The convenience of a specific method depends on different aspects, not only technological, but also related with the characteristics of the navigation environment and the mobility of the robots. According to different reference surveys compiling the existing methods for localization ([Amundson,I.-2009], [Thorbjornsen,N.-2010], [Vladimorova,T.-2007], [Sha'ameri, A.-2017], [Lanzisera-2006] and [Sanz,D.-2013]), that is, for the determination of the location of an object in space, those can be categorized according to the magnitude observed during the Measurement phase:

1. **Multilateration (MLAT):** this method is based on the determination of the location of an object measuring the relative distances from the object to a number of reference stations placed at known locations (T_i stations in Figure 2.3.1). Therefore, this method is based in range as the parameter to be measured, what can be performed by several procedures that will be described below. Due to the geometrical constraints of the range parameter, which implies that the mathematical set of possible locations of an object in a two dimensions space knowing its distance is a circle which radius equals the distance, a minimum of three distances are necessary to determine a unique certain location. When the number of reference stations is three, the method is known as Trilateration (TLAT). The Figure 2.3.1 depicts the concept.

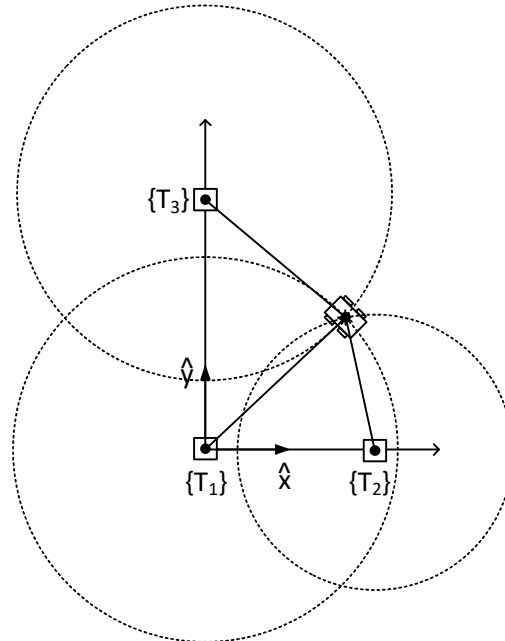


Figure 2.3.1- Diagram of Multilateration localization method.

2. **Multiangulation (MANG):** this procedure consists in the localization of an object from the angles subtended to a number of reference stations (T_i in Figure 2.3.2) situated at known locations, denominated Angle Of Arrival (AOA) or Direction Of Arrival (DOA). Since in this case the parameter to be measured is angle instead of distance, the measurement procedure is based in different mechanisms. The constraints in this case implies that the mathematical place of all possible locations forming an specific angle to a given reference station is defined by a line, therefore at least two angles are necessary to be measured from two reference stations to determine the location of a mobile target in a two dimensions space, and three angles in three dimensions. This method is well know from ancient times to determine distances and altitudes, and is called Triangulation. The Figure 2.3.2 shows this idea.

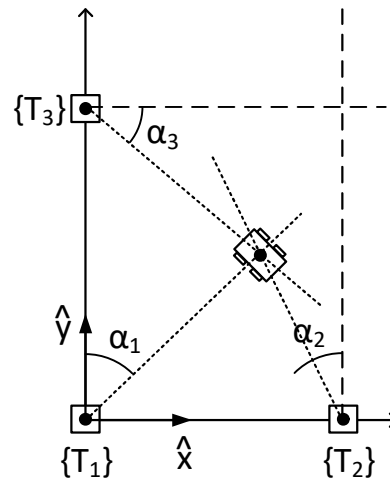


Figure 2.3.2- Diagram of Multiangulation localization method.

The figures above show a theoretical scenario in which the magnitudes are measured without error, but in real cases some uncertainty exists produced by inaccuracy or noise existing in the measurement instruments and procedures. In such cases, no unique solution exists but an infinite set of solutions constrained in a determinate area. The Figure 2.3.3 shows this case.

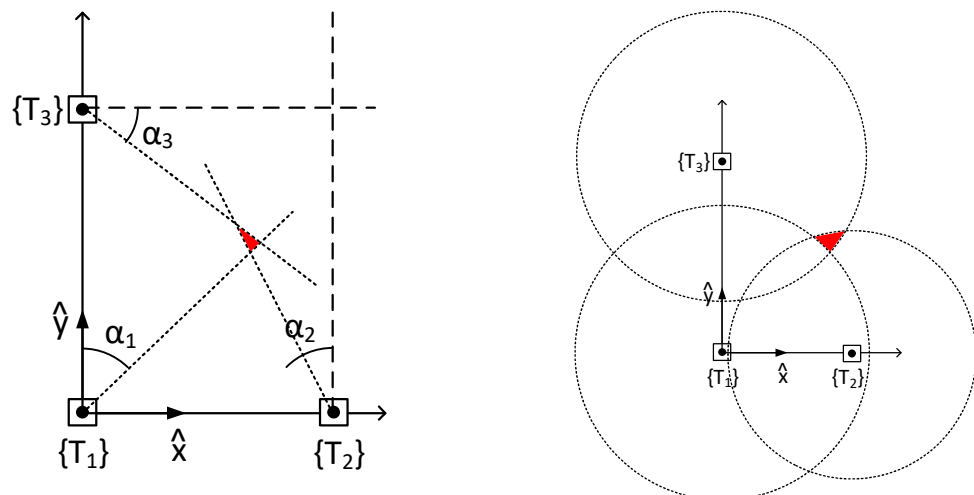


Figure 2.3.3- Location determination of a node in case of uncertainty for (Right) Multilateration and (Left) Multiangulation localization methods. The regions of uncertainty are represented as red areas.

As it can be appreciated in the Figure 2.3.3 (Left), the uncertainty in case of Multiangulation with only two reference stations leads to an error in the localization impossible to determine, the application of a third angulation reference provides a defined uncertainty area in a way that, with a representative (i.e. statistically) set of measurements, it is possible to determine the area where the real solution for the node location will be. The better the accuracy of the angle or range measurement, the smaller the uncertainty area.

[Shuzhi,S.-2006] provides a detailed analysis about the localization of robots by Multiangulation based in a land-mark based navigation method. In this application, the mobile robot detects different landmarks situated at known positions, being able to calculate

its relative position and orientation by a method of Multiangulation. In this case, the method of angle measurement is optical since the application is in-door.

[Sha'ameri, A.-2017] analyzes the quality of the position determined via Multilateration and Multiangulation for mobile emitters, being in this case aircrafts or drones approaching a sensitive zone. In this case, radiofrequency signal is used to determine both range and angle. In this reference, a review of different methods for Angle of Arrival determination is presented, based all of them in the calculation of the radiofrequency wave angle of incidence over a multiple-elements reception antenna. Obtaining the angle of incidence of the wave on the antenna surface and knowing the orientation of the antenna, the Angle of Arrival of the transmitting target can be calculated.

[Sha'ameri, A.-2017] concludes that Angle of Arrival measurement accuracy depends on SNR of the received signal and on the number of elements forming the tracking antenna. The larger (i.e. higher number of elements) the tracking antenna is, the lower the SNR must be to provide an acceptable error. On the other hand, large antennas have a limited angular span, therefore some steering mechanism is required to increase the angular detection range. Multilateration can rely on simpler reception hardware (like omnidirectional antennas) with no mechanical elements for beam steering to yield similar accuracy at reasonable SNR levels. That factor makes Multilateration methods more suitable for hardware constrained applications, like in small mobile robotic platforms. Moreover, the references confirms that Multilateration performs better at lower distances with respect to the tracking stations (<30 km at a test carrier of 2,5 GHz) whilst Multiangulation improves at longer distances (>50 km at 2,5 GHz). The angular resolution is related with the wavelength and, at such radio frequencies, the study confirms that Multilateration is a more suitable option for our application scenario.

Regarding Multilateration, different literature references such as [Thorbjornsen,N.-2010], [Ollero-2005], [Doberstein,D.-2012] define range measurement as a common problem in mobile robotics since, in general, localization of mobile robots by radiofrequency methods are usually based in Multilateration.

The techniques used for the determination of range (which is a necessary first step towards the calculation of position by Multilateration) can be categorized in the following categories:

1. **Signal Strength Methods**, such as those based in Received Signal Strength Indication (RSSI) measurements. The received signal strength is related to the distance between source and receiver, therefore it is possible to estimate distance from it. This method is popular because most commercial radio transceivers, including WiFi, Bluetooth and ISM, are able to provide RSSI measurements since it is also useful to estimate the Bit Error Rate (BER) associated to the quality of reception in the form of Signal-to-Noise Ratio (SNR). Nevertheless, although easy to implement and use, the error in the estimation is usually very high due to a number of factors, such as multipath fading, accuracy and stability in the transmitted power, etc.

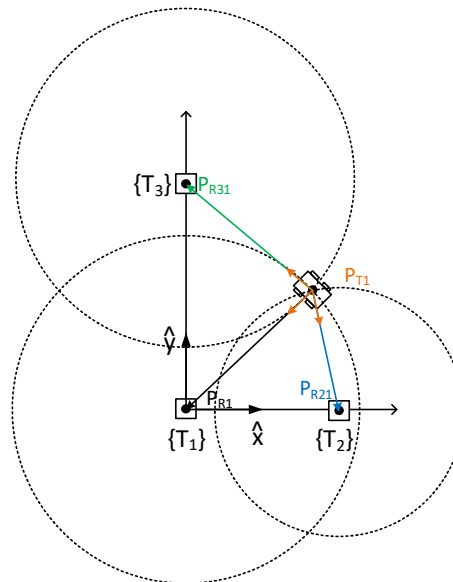


Figure 2.3.4- Multilateration based in Received Signal Strength methods. The distance from mobile node 1 to the tracking stations T_1 to T_3 can be calculated from the difference between the signal transmitted by the node and received on each tracking station T_i , or ΔP_{i1} , which can be expressed as $\Delta P_{i1} = P_{T1} - P_{Ri}$.

2. **Time Measurement based Methods:** Those methods are based on the measurement of the time a wave propagates from the emitter to the receiver, calculating the position by means of its relation with the speed of light c . These methods include traditional pulsed approaches like those measuring the Time Of Flight (TOF) or Time Of Arrival (TOA) of radiofrequency discrete frames travelling from emitter to receiver, Time Difference of Arrival (TDOA) and other techniques based in phase shift measurement of a single or multi carrier signal received at different stations

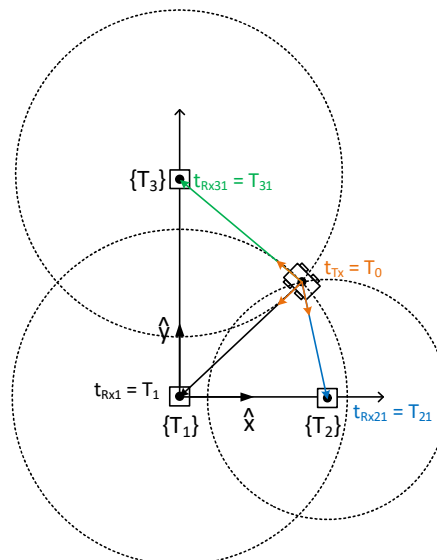


Figure 2.3.5- Multilateration based in time measurement methods. The distance from mobile node 1 to the tracking stations T_1 to T_3 can be calculated from the time elapsed since the transmission of the signal T_0 to the instant of reception on each tracking station T_i , or T_{i1} , which can be expressed as $\Delta T_{i1} = T_0 - T_{i1}$.

3. **Frequency shift-based methods.** The measurement of Doppler frequency shift (Frequency of Arrival or FOA) or Frequency Difference of Arrival (FDOA) is used to calculate information about the velocity vector of the mobile node, which can lead

to range calculation by means of time integration of the velocity vector components over a given period (i.e. Dead Reckoning). This parameter can provide instantaneous range information that, although susceptible to error accumulation, could be very convenient for navigation control applications. Alternatively, this method is used in combination with absolute position determination techniques like the above mentioned (TDOA, TOA, etc.) to increase the total accuracy introducing information about target velocity.

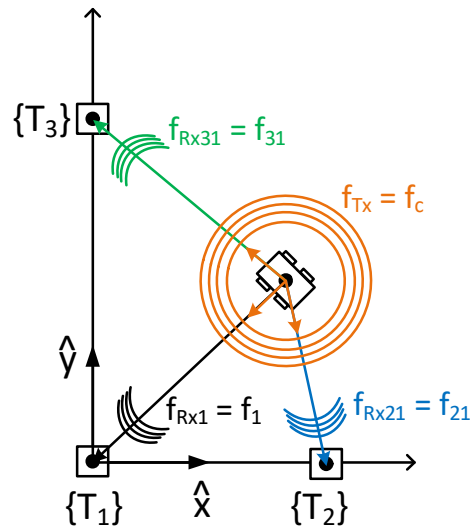


Figure 2.3.6- Multilateration based in Frequency Shift measurement methods. The mobile node velocity can be determined using the Doppler shift measured in the received signal frequency, which can be expressed as $\Delta f_D = f_{RX} - f_{TX}$.

Before considerations about the different signal processing methods for the determination of position, it is necessary to consider the two technological approaches for range measurement that are compatible with space environment: optics and radiofrequency based. Although the nature of both methods hinges on the same basic principles (electromagnetic), the difference in wavelength causes a very different behavior in terms of generation, propagation modes and detection methods.

Optical range measurement methods can be categorized in two main groups depending on the propagation mode of light involved: laser (i.e coherent) and diffuse light (i.e. non-coherent) emission. Diffuse light sensors such as photoelectric sensors operate by detecting the incidence of a light beam emitted from a non-coherent light source like a LED. The light beam can be focused or not, and can operate in visible and infrared (IR) bands. In robotics, the use of IR range detectors is extensively used in mobile platforms for obstacle detection mainly due to the simplicity and low cost of the components associated to them. [Shuzhi,S.-2006] introduces the Triangulation position determination method proposing an scenario with a mobile robot detecting optically different landmarks at placed at strategic locations in a navigation environment. The Landmarks consisted in an adhesive patch fixed in the walls and were passively detected by onboard camera sensors. In this sense, the advantage of optical detection is that ambient light can be used to illuminate the landmarks and, thus, not requiring extra power consumption for them.

The main disadvantage of diffuse light range detectors is related to energy efficiency when the distance to measure is large and there is little spatial resolution due the beam divergence, or when ambient illumination is not homogenous or very intense. In this case, the detection based on coherent light sources (laser) are more effective. The high directivity of laser beams and short wavelength spectrum makes it possible not only to measure large distances with

high precision and lower energy requirements but also to acquire spatial information with high resolution thanks to the high beam directivity. Laser ranging methods are usually categorized under LIDAR (Light Detection And Ranging) technologies, which include different methodologies for distance measurements and other applications such as 3D scenario scanning or altimetry mapping.

The energy efficiency of light-based range measurement methods coupled with the advantages due to the low complexity in generation and detection are undeniable. However, there are two key considerations that lead us to discard light-based methods for our application.

1 - The dust-rich Lunar surface [Seedhouse,E.-2008] [Stubbs,T.J.-2005] [Khan-Mayberry,N.-2008] renders range detection based on coherent light sources very unreliable. In addition to the constant accumulation of dust on the surface of the equipment and instruments as observed during the Apollo missions, hampering optical emission and detection, the existence of a layer of floating dust introduces high attenuation as well as possible erroneous reading due to the interaction (i.e. reflection) of the light beam with the dust particles in suspension.

2. - The Sun, without the attenuation effect of an atmosphere, provides a very high, background noise source on light bands. This effect is less marked in laser ranging methods due to the spatial discrimination but, when it comes to measuring the range between mobile systems, the technical complexity for laser beam capture and alignment processes makes the system less practical.

On the other hand, range measurement methods based on RF are not affected by ambient dust or dust deposited on the transmission and reception antennas. Also, the noise emitted by the sun at such lower frequencies is less intense, and does not lead to providing extra mechanisms, such as dark baffles, to shield the receivers against its influence.

Due to the above consideration, we are going to propose the use of radiofrequency ranging methods, as the most appropriate approach for Moon surface positioning. As discussed in Chapter 1, GPS is not available in the Moon, and the deployment of a system implementing such positioning methodology is not trivial. As explained in [Doberstein, D.-2012], GPS is mainly based on the principle of Time Difference-Of-Arrival (TDOA) determination which relies on a highly accurate time base and synchronization. This is achieved with ultra-precise (<1ns error) atomic clocks on board the GPS satellites, acting as reference stations and complex clock synchronization algorithms located in the receiver. The purpose of all this is to implement a global self-positioning system with minimum hardware requirements at the user's side. To be global, the system must be satellite based, but here, a very drastic limitation enters in place: the communication pathway necessary to determine position must be unidirectional (satellite to ground receiver) as bidirectional communication necessitates high power requirements from the ground in order to communicate with the orbital stations.

In order to make possible the implementation of a self-positioning system with minimum hardware footprint on GPS ground users, the system complexity should reside in the satellite stations: highly precise atomic clocks on board each satellite, all synchronized (<1ns drift) are the time references for the message frames that are broadcasted by each satellite and subsequently received by ground terminals, where a sophisticated algorithm corrects their local clock deviation with the GPS network (by means of including a fourth satellite in the algorithm) in order to make possible the total Time-Difference-Of-Arrival determination and, thus, the distance to each satellite that will allow the calculation of the geodetic position by trilateration.

The cost (not only financial but also in terms of mass, volume and power) associated with the use of atomic synchronized clocks on the ground references in an exploration scenario like the Moon should make a distributed robotic mission prohibitive. The good news is that, in the case we are envisaging, the robot to be determined its position can also participate in the location process because the distances between the agents (either other robots or land mark tracking stations) are limited by the exploration area, which is always well defined and within ranges available for point to point radio communications (from meters to a few kilometers). Considering this assumption, the location determination method can be based in radiofrequency bidirectional propagation effects associated with either the radio communications network in use (Flat architecture) or using an ad-hoc radio network specifically deployed for that purpose (for Tier-2 and Tier-3 architectures).

According to the purpose and case of application, different literature references studied consider methods that can be included in one of the above mentioned categories.

The study carried out by [Thorbjornsen, N.-2010] focuses on the consideration of methods to determine the point-to-point range as a first step to relative position determination, focusing on Time-Of-Flight based methods. A Time-Of-Arrival calculation scheme based on a method consisting of the use of two radiofrequencies is proposed. It is very interesting the distinction between range measurement procedures and range estimation methods established to determine the range between two agents, previously to the determination of location, criteria that is aligned with the two phases for location determination defined by [Lanzisera-2006]: acquisition of parameter and range calculation based in the measurements obtained. Both aspects must be studied in parallel since the methodologies for estimation of values and analysis of error source differ although both use similar statistical tools.

[Vladimorova, T.-2007] goes further by proposing the use of Commercial Off-The-Self (COTS) protocols and low cost sensors to enhance mission reliability by distributing many sensors across a spacecraft. This way, potential failures are compensated by the redundancy of having many distributed “sensor motes” that yield enough scientific and technical data.

[Sanz, D.-2013] centers the study on the organization issues in wireless sensor networks deployed for planetary exploration, and categorizes the application cases depending on the use of a ground deployment of anchored or mobile nodes, or aerial nodes able to move and redistribute under the action of winds. In this case, location of nodes is a critical function since it allows a redistribution of tasks within the network in case it is required by any reason (like loss of nodes due to lack of visibility or the need to compensate communication bottlenecks). Clearly, the solution of using a GPS-like system is not affordable at the present stages of planetary exploration. The alternative of using pseudolites (that is, pseudo-satellites or ground stations that mimic the operation of GPS satellites for small area localization) involves also high energy requirements and mass cost and a positioning of the landmarks with a centimeter level precision at. The conclusion is that, a solution based on a distributed methodology, involves minimum resources and a compact approach for an exploration scenario.

[Kusy,B.-2010] proposes a localization method based in the measurement of Doppler frequency shift in the signal received by a number of reference tracking stations from a mobile node emitting a radiofrequency carrier. The integration of the relative velocity vector yields the position though with an accumulative error. In a similar approach, [Amar,A.-2008], proposes a Differential Doppler measurement method for, in this case, determine the location of a stationary emitter, measuring the Doppler frequency shift at several stations that move at a known velocity along a known trajectory. This way, the position of the emitter

can be calculated using different mathematical estimation methods. [Amar,A.-2008] makes reference to ARGO satellite navigation system, and its emitter distance calculation method also based in Doppler shift. In this case, ARGO satellites orbiting at very well determined orbital altitude and speed receive the signal emitted by on ground mobile stations, a narrow band signal at a defined frequency. ARGO satellites measure the Doppler frequency shift in the signal received as well as the moment of zero Doppler Shift, which coincide with the Point of Closest Approach (PCA) between the ARGO satellite and the mobile node. With that information, the ARGO system can determine the position of the node in the Earth surface.

As a conclusion from the reference studies presented above, a system architecture able to implement an efficient method to determine the localization of a mobile robotic agent in a scenario like the surface of the Moon, must include a reliable method for relative range and velocity determination as a first step towards relative localization. Afterwards, numerical methods will be used to estimate location from distance and speed information with high accuracy without requiring a continuous sampling of position or high demand of computational power. These mechanisms can be implemented with techniques based on a combination of both Time and Frequency Shift measurement procedures in order to be able to determine relative range and velocity vectors within the coverage of a Flat architecture radio network. The localization method must be compatible with existing Tier-2 or Tier-3 communications systems or implement the physical layer of the communication system in order to reach a more efficient and compact implementation. This should be possible assuming narrow band radiofrequency operation, as opposed to standard Tier-2 and Tier-3 communication protocols that, to reach high data rates, are commonly implemented in broadband modulation schemes.

In [Thorbjornsen, N.-2010], a comparison between TOA and TDOA methods for sensor mobile nodes is presented. Although TDOA is widely use in long range position determination, due to the high resolution achievable, it requires a precise clock synchronization between tracking stations which, combined with the fact that the range of time values involved in TDOA are much more reduced that in TOA for small distances, TOA becomes the most suitable option for our application scenario.

2.4. Formulation of the Localization Problem.

2.4.1. Introduction.

In this section, an algebraic formulation of the Multilateration problem is developed, according to several assumptions taken according with the case of study. The formulation defines the position of a mobile node (a mobile rover, for instance) that evolves across an exploration area delimited by a number of tracking stations that play the role of reference location points or landmarks. The formulation developed here includes primary and secondary reference frameworks, as well as the algebraic nomenclature to define both position and velocity.

Special attention is dedicated to measurement magnitudes such as range and relative velocity components (radial and normal), which are necessary to consider TOA and FDOA multilateration approaches, and to the relationships between them and the location of the nodes.

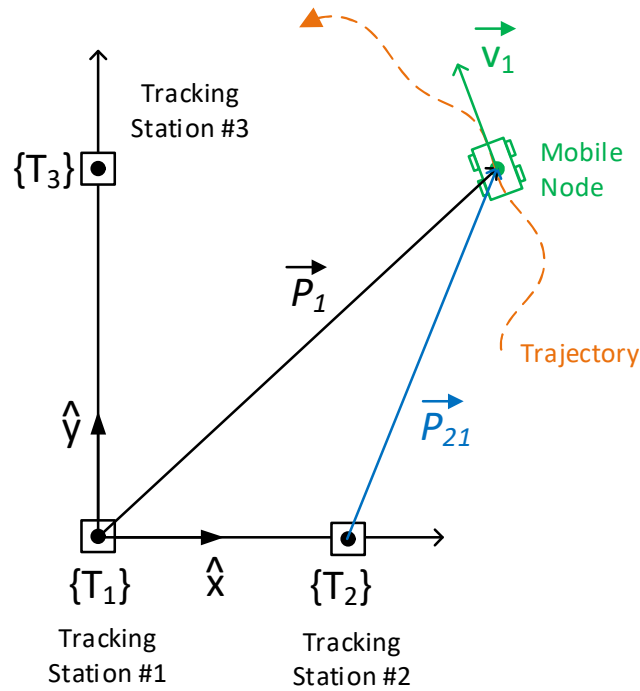


Figure 2.4.1- Vector representation of a mobile node position and velocity.

The figure above represents an exploration scenario composed by a mobile node (as a robotic rover for instance) and a number (three) of reference tracking stations defined as T_1 to T_3 . As in the cases mentioned in the section 2.3, the mobile node can have its position determined according to the coordinate framework of each of the tracking stations, which is denoted with the first subscript in the position vector. The mobile node position is, hence, determined by a vector expressed as:

$$\overrightarrow{P_{kn}} = (P_{knx} \ P_{kny} \ P_{knz})^T \quad (2.4.1)$$

Where k express the coordinate framework the position vector is referred to, and n identifies the mobile node related to the vector. In case the reference is the tracking station in the origin (T_1 in this case), the subscript k is omitted, therefore $\overrightarrow{P_{11}}$ is expressed simply as $\overrightarrow{P_1}$.

The Figure 2.4.2 represents the velocity vector for the mobile node presented in Figure 2.4.1. The velocity vector of the object being tracked can be represented by two orthogonal components related with each coordinates system, consisting on a component parallel to the position vector (Radial velocity or v_r) and another one normal to the position vector (Normal velocity or v_n). The Left superscript on both the normal and radial velocity components denote the coordinate framework in which the velocity vectors are referred.

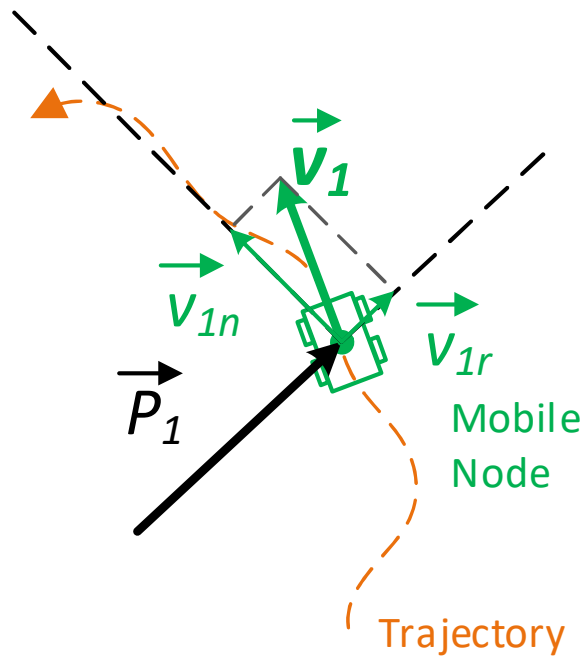


Figure 2.4.2- Representation of tangent and normal velocity components of a mobile node velocity vector.

Therefore, v_l can be expressed as:

$$\vec{v}_1 = \vec{v}_{1r} + \vec{v}_{1n} = |v_{1r}| \cdot \hat{u}_{1r} + |v_{1n}| \cdot \hat{u}_{1n} \quad (2.4.2)$$

Where \hat{u}_n and \hat{u}_r denote the unit vectors of the normal and radial velocity vectors respectively.

The position of any mobile node, referred to any tracking station coordinate framework, can be determined from any of the reference frameworks and the position vectors of the tracking stations referred to such coordinate framework. Therefore, if we have the T_2 and T_3 tracking stations positioned with respect T_1 , as represented in Figure 2.4.3, the position vectors can be expressed as:

$$\vec{P}_{kn} = \vec{P}_n - \vec{T}_k \quad (2.4.3)$$

Where k denotes the tracking station and n refers to the identification index of the mobile node. The position vectors P_{kn} represent the location of the mobile node n relative to the tracking stations k and the vectors T_k represent the position of the tracking station relative to the main one (T_1 in this case).

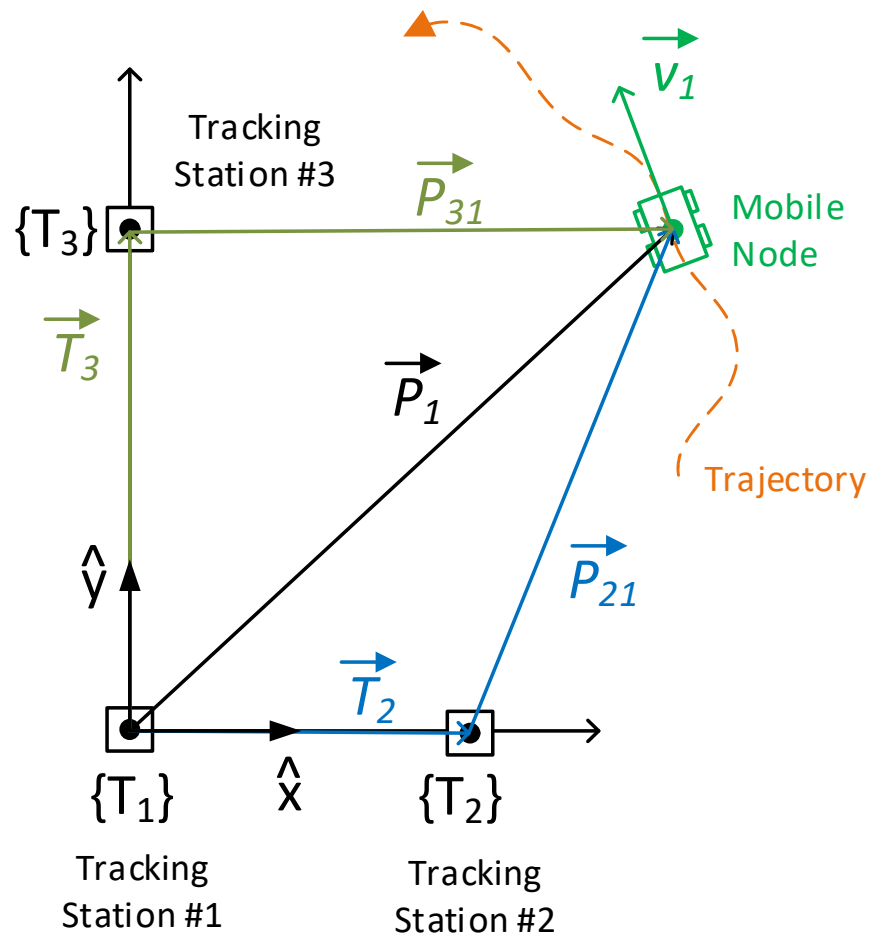


Figure 2.4.3- Representation of different position vectors for different coordinate systems corresponding to the different tracking stations T_1 to T_3 .

The assumptions observed for our case of study are:

1. Two Dimensions scenario: 2-D scenario is assumed, focusing in the problem of 2-D location in an area with not significant change in altitude (Z-axis distance) compared with range in XY plane. However, to extend the analysis to 3D is straightforward from the formulation included in this section.
2. For the experimental and numerical simulations case, an exploration area consisting in a square of 1000 x 1000 m is assumed. This assumption is based in the information obtained from previous exploration rovers used and the distance covered related with the rover mass. The table 2.4.1 shows the rovers used in exploration missions since the beginning of space exploration, including rover dry mass and distance travelled, with last update in currently active missions with information of 2015.

The table has been completed with information provided by [Tate,K.-2015], NASA Mars exploration rovers mission websites [MER-2016], [MSL-2016], [MSL-2018] and [MER-2018]; [LRO-2015] providing information about soviet Moon exploration rovers, and [Lei,Z.-2013] for the Chinese Moon rover Yutu.

Rover Name	Year	Mass (kg)	Distance Travelled (km)	Object explored
Lunokhod-1 (URSS)	1970-1971	756	10,5	Moon
Lunokhod-2 (URSS)	1973-1973	840	39	Moon
Sojourner (USA)	1997-1998	10,6	0,1	Mars
Spirit (USA)	2004-2010	185	7,7	Mars
Opportunity (USA)	2004-Present	185	45,14 ¹	Mars
Curiosity (USA)	2012-Present	899	18,85 ²	Mars
Yutu (China)	2013-2016	140	0,1	Moon

Table 2.4.1.- Robotic rovers sent to exploration mission from the beginning of Space Era till to date with distance covered (¹ Update 11/04/2018, ² Update 27/04/2018)

Considering the information included in the table, we can extract information about the relation between the mass of the rovers and the distance travelled. Moreover, if we compare such magnitudes, excluding the still active missions and the Chinese Yutu rover, which was reportedly faulty along its operational life, we can establish a linear regression showing a relation of 0,0323 km/kg ratio with an offset of 157.7m, with a coefficient of determination R^2 value of 0,612. The Figure 2.4.4 shows a graphic representation of the rover mass and the distance covered for the different robotic exploration missions.

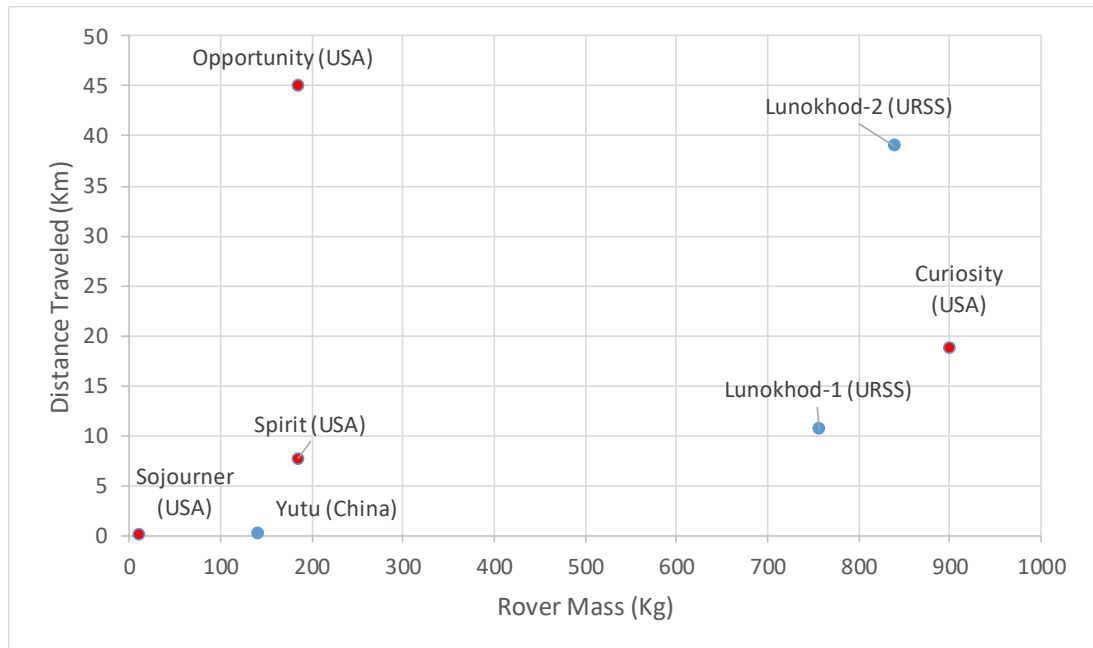


Figure 2.4.4- Representation of exploration rovers considering the relation between the distances traveled and the corresponding rover mass (Mars rovers in red, Moon rovers in blue).

Opportunity was initially scheduled for 90 Mars sols (92,15 Earth days) mission travelling a distance of 100 m/sol, thus a total travel of 9 km [MER-2017], though finally is operational after more than 13 Earth years, covering a distance over 45 km. Curiosity was planned to cover a 5 km to 20 km distance over Mars depending on the experiments performed. In any case, applying the linear relationship presented above we obtain, for a rover mass in a range

from 15 kg to 20 kg, it can be estimated a distance travelled from 642.2m to 803.7m, what is within the assumed 1000 m side square hypothetical exploration area.

3. Flat Surface: The scenario is considered flat, not geodetic, due to the area of exploration scenario compared with the Moon radius. When the distances from the tracking stations to the mobile node are comparable with the radius of the body under consideration (Earth, Moon or any other), the assumption of flat ground surface may introduce an important error, thus the shape of the body must be included in the formulation [Fang,B.-2018] [Deng,B.-2016]. This is usual, for example, in global location systems such as DECCA or LORAN-C and other proposed systems based in ground stations intending to cover large areas [Sha'ameri, A.-2017], or systems based in satellites like ARGOS, where the tracking stations [Ho,K.-1997]. In our case, a nominal distance travelled of 1000m is far from the Moon radius (equatorial radius = 1738.1 km, polar radius = 1736 km [GSF-2018]), representing a 0.006% of the radius length.
4. The tracking stations could consist on mobile or static robotic position references (just as landmarks), but for the determination of the mobile node position, the tracking stations are in fixed (i.e. constant) positions in the XY plane.
5. The tracking stations are in known positions relative to a reference station (T_1), which defines the main coordinate system origin.

2.4.2. Formulation of the Multilateration Problem.

As explained above, the first step in the determination of position with a FDOA supported TOA Multilateration method is to calculate the location of the mobile node based on the distances measured from the tracking stations to the mobile node. Many literature references exist that present the Multilateration formulation in different ways and with different sets of assumption for the application scenarios considered, like [Deng,B.-2016], [Fang,B.-2018], [Seco,F.-2009], [Ho,K.-1997], etc.

In our case of study, we consider an exploration scenario defined by the assumptions presented in section 2.4.1 and represented in the Figure 2.4.5.

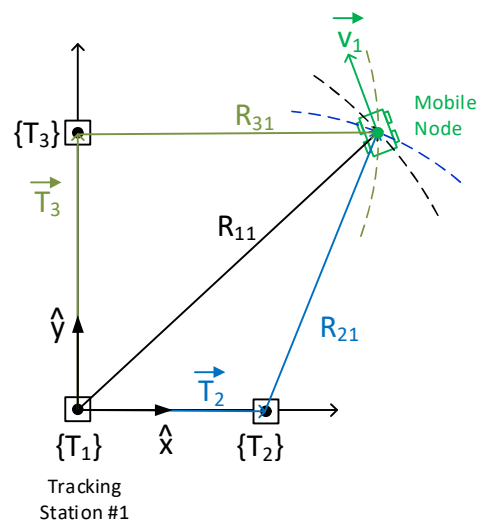


Figure 2.4.5- Determination of position by Multilateration, based on the ranges from the mobile node to the tracking stations, which are located at known positions with respect to the coordinate system centered in T_1

The distance between the mobile node and the different tracking stations is represented here by R_{kn} where k determines the tracking station considered and n denotes the mobile node under localization. The distance denoted by R_{kn} is the modulus of the vector $\overrightarrow{P_{kn}}$ (see Figure 2.4.3), which can be calculated from the position of the mobile node $\overrightarrow{P_n}$ and the position of the k tracking station $\overrightarrow{T_k}$ according with the following equation:

$$\overrightarrow{P_{kn}} = \overrightarrow{P_n} - \overrightarrow{T_k} = R_{kn} \cdot \widehat{u_{kn}} \quad (2.4.3)$$

The Time-Of-Arrival only yields information about R_{kn} , since $\widehat{u_{kn}}$ (i.e. the information about direction) is missing, the mathematical place of possible locations is a circle centred in T_2 with radius R_{kn} , as it is shown in Figure 2.3.1. From the Equation 2.4.3, the three tracking stations considered yield the following system of equations:

$$R_{11} = \sqrt{P_{1x}^2 + P_{1y}^2} \quad (2.4.4.a)$$

$$R_{21} = \sqrt{(P_{1x} - T_{2x})^2 + (P_{1y} - T_{2y})^2} \quad (2.4.4.b)$$

$$R_{31} = \sqrt{(P_{1x} - T_{3x})^2 + (P_{1y} - T_{3y})^2} \quad (2.4.4.c)$$

Where P_{1x} and P_{1y} are the unknown variables. The equations can be formulated as a two-variable quadratic system as follows:

$$R_{11}^2 = P_{1x}^2 + P_{1y}^2 \quad (2.4.5.a)$$

$$R_{21}^2 = (P_{1x} - T_{2x})^2 + (P_{1y} - T_{2y})^2 \quad (2.4.5.b)$$

$$R_{31}^2 = (P_{1x} - T_{3x})^2 + (P_{1y} - T_{3y})^2 \quad (2.4.5.c)$$

The system can be reduced to a linear equation system operating the equations of system 2.4.5 as (a)-(b) and (a)-(c) obtaining:

$$(a) - (b) = R_{11}^2 - R_{21}^2 = 2P_{1x}T_{2x} + 2P_{1y}T_{2y} - T_{2x}^2 - T_{2y}^2 \quad (2.4.6.a)$$

$$(a) - (c) = R_{11}^2 - R_{31}^2 = 2P_{1x}T_{3x} + 2P_{1y}T_{3y} - T_{3x}^2 - T_{3y}^2 \quad (2.4.6.b)$$

Which can be expressed in a matrix form as a linear equations system:

$$\begin{bmatrix} R_{11}^2 - R_{21}^2 \\ R_{11}^2 - R_{31}^2 \end{bmatrix} = \begin{bmatrix} 2T_{2x} & 2T_{2y} \\ 2T_{3x} & 2T_{3y} \end{bmatrix} \cdot \begin{bmatrix} P_{1x} \\ P_{1y} \end{bmatrix} - \begin{bmatrix} T_{2x}^2 + T_{2y}^2 \\ T_{3x}^2 + T_{3y}^2 \end{bmatrix} \quad (2.4.7)$$

In general Multilateration cases, with K tracking stations, the resulting linear equation system (2.4.7) will have $K-1$ equations of the form:

$$R_{11}^2 - R_{i1}^2 = 2P_{1x}T_{ix} + 2P_{1y}T_{iy} - T_{ix}^2 - T_{iy}^2 \quad (2.4.8)$$

For $i = 2$ to K , where K is the total number of tracking stations, leading to an overdetermined system when $K > 3$.

As it was explained in section 2.3 (Figure 2.3.3), the errors introduced in the measurement of the distances (R_{11} to R_{31} in this case) introduce an uncertainty in the determination of

location, expressed in the Figure 2.3.3 as the red areas including the possible locations of the mobile node. In order to reduce such uncertainty, more tracking stations can be included, which introduce more equations in the system (2.4.7). Such overdetermined equations systems can be solved by methods aimed to find an approximate solution when a unique solution does not exist due to an overdetermination of the equations system or when noise or error sources introduce a perturbation in the coefficients, thus leading to a linear inconsistent system [Anton,H.-2010]. The traditional approach to address this sort of problems is Least Squares method, in which given an inconsistent linear equations system of the type $\mathbf{A}\vec{x} = \mathbf{B}$ where \mathbf{A} is a $m \times n$ matrix, therefore it has m equations for n unknown variables. The Least Squares method yields a vector $\vec{x} \in R^n$ such as $e = \|\mathbf{B} - \mathbf{A}\vec{x}\|$ where $e \in R^m$ is minimum, therefore, \vec{x} obtained is the best solution possible.

One way to calculate the Least Squares solution to $\mathbf{A}\vec{x} = \mathbf{B}$ according to [Anton,H.-2010] is to calculate the orthogonal projection $Proj_W(\mathbf{A})$ of the matrix \mathbf{A} on the columns space of the matrix \mathbf{A} (W) and then solve the equation $\mathbf{A}\vec{x} = Proj_W(\mathbf{A})$. This leads to the expression:

$$\mathbf{A}^T \mathbf{A} \vec{x} = \mathbf{A}^T \mathbf{B} \quad (2.4.9)$$

Which is called ‘‘Normal Equation’’ or ‘‘Normal System’’ [Anton,H.-2010] associated with the system to $\mathbf{A}\vec{x} = \mathbf{B}$. Equations system (2.4.9) is consistent and the solution obtained \vec{x} is a Least Squares approximation, and $e = \|\mathbf{B} - \mathbf{A}\vec{x}\|$ for $e \in R^m$ is the error vector associated to the approximation \vec{x} .

The Equation (2.4.10) express the Multilateration equations system in (2.4.7) in the format $\mathbf{A}\vec{x} = \mathbf{B}$.

$$\begin{bmatrix} T_{2x} & T_{2y} \\ T_{3x} & T_{3y} \end{bmatrix} \cdot \begin{bmatrix} P_{1x} \\ P_{1y} \end{bmatrix} = \begin{bmatrix} \frac{1}{2}(R_{11}^2 - R_{21}^2) + \frac{1}{2}(T_{2x}^2 + T_{2y}^2) \\ \frac{1}{2}(R_{11}^2 - R_{31}^2) + \frac{1}{2}(T_{3x}^2 + T_{3y}^2) \end{bmatrix} \quad (2.4.10)$$

From the analytical point of view, the operation of (2.4.9) and obtaining of the error e is simple, although it could require an intensive calculation if the number of tracking stations is high. In such case, instead of calculating the inverse of $\mathbf{A}^T \mathbf{A}$, methods like the Elimination Gauss-Jordan could be used to reduce the computational load for the real-time determination of position. Alternative methods for solving Least Squares problems, when computational resources or time required for the calculation are a concern consist on numerical procedures like the LU decomposition or iterative procedures like the Gauss-Newton method. Those methods will be reviewed in chapter 3.

2.4.3. Formulation of the Doppler Shift and its Relation with Velocity.

The Figure 2.4.2 presented in the section above represents the velocity vector for the mobile node which, as explained, can be expressed by the addition of two orthogonal components, one in parallel direction to the position vector (Radial velocity or v_r) and another one in normal direction to the position vector (Normal velocity or v_n). The Doppler Effect implies, as explained, that the measurement of the radio signal transmitted by the mobile node is received in the tracking stations with a shift in frequency proportional to the relative speed

between the emitter (mobile node) and receiver (tracking station), which can be formulated as:

$$\Delta f_D = f_{measured} - f_{real} = \frac{f_c \cdot v_r}{c} \quad (2.4.11)$$

When $v_r \ll c$, where v_r is the relative velocity between transmitter and receiver, f_c is the frequency of the transmitted signal, c is the propagation speed of the signal across the medium (for radiofrequency signals in the scenario under consideration, it can be assumed as the speed of light in vacuum).

The sign of the Doppler frequency increment depends on whether the emitter and transmitter get close or away each other. The Figure 2.4.6 shows this concept.

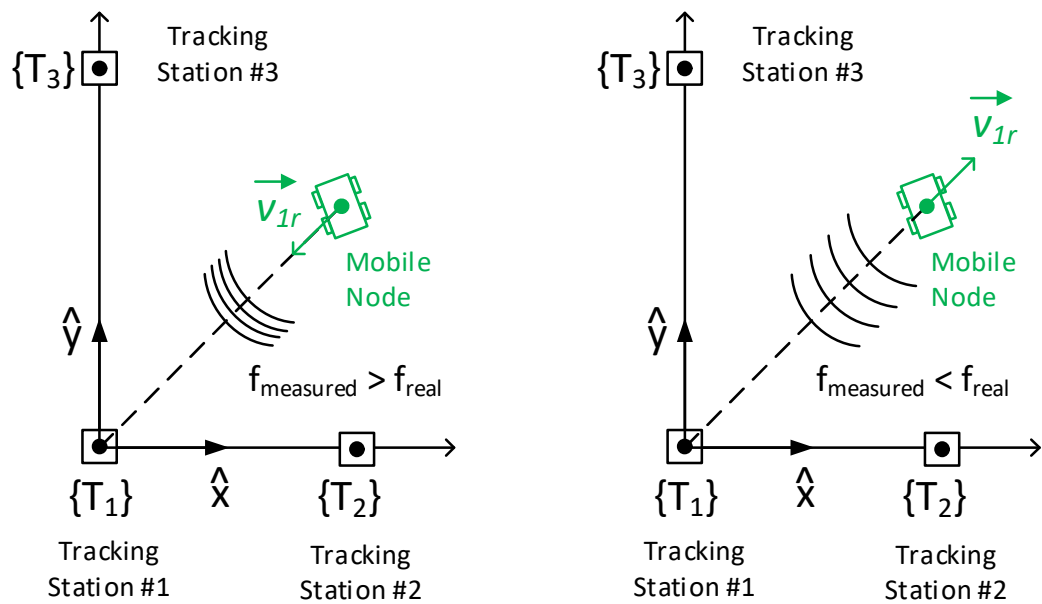


Figure 2.4.6- Diagram of different cases for Doppler shift, when emitter approaches the receiver (Left) and when emitter and receiver get away each other (Right).

As it is depicted in the Figure 2.4.6, and considering our sign criterion, when the emitter and receiver get closer, $\Delta f_D = f_{measured} - f_{real} > 0$, and when both emitter and receiver get away $\Delta f_D = f_{measured} - f_{real} < 0$. The problem here is that the sign of Doppler frequency increment must be obtained as a result of the analysis of the mobile node trajectory and not be specified in advance depending on the direction of the radial velocity.

In order to include the Doppler shift in the formulation presented in a consistent way (that is, providing information of both magnitude and sign), it must be expressed according the position vector determining the location of the mobile node, evolving Equation 2.4.11 to its vector expression.

Let us define \vec{v}_1 as the Mobile node 1 velocity referred to the main coordinates reference centred in $\{T_1\}$, according to the following expression:

$$\vec{v}_1 = \frac{d}{dt} \vec{P}_1 \quad (2.4.12)$$

Since the Doppler frequency shift depends on the modulus of the radial velocity, it can be expressed as the modulus of the Euclidean projection of \vec{v}_1 on \vec{P}_1 , that is:

$$v_{1r} = |v_{1r}| = \vec{v}_1 \cdot \hat{u}_1 = \frac{1}{|P_1|} (\vec{v}_1 \cdot \vec{P}_1) \quad (2.4.13)$$

Where \hat{u}_1 is the unit vector in the direction of \vec{P}_1 , which can be expressed as $\vec{P}_1/|P_1|$. Therefore, the Doppler frequency can be expressed in a vector-like algebraic form as:

$$\Delta f_D = f_{measured} - f_{real} = \frac{f_c \cdot v_r}{c} = - \frac{f_c}{c|P_1|} (\vec{v}_1 \cdot \vec{P}_1) \quad (2.4.14)$$

This expression yields both magnitude of Doppler frequency increment and sign, related to approximation or distancing of emitter and receiver, thanks to the introduction in the formula of the cosine of the angle between \vec{P}_1 and \vec{v}_1 , implicit in their dot product.

The negative sign in Equation 2.4.14 is necessary to make consistent the sign of the dot product with the sign criteria assumed for the Doppler frequency shift according to what was expressed above in Figure 2.4.6. In this sense, Figure 2.4.7 shows the sign of the dot product $\vec{v}_1 \cdot \vec{P}_1$, where it can be appreciated that the result of the dot product is negative when emitter and transmitter approach each other (v_{1r} in opposite direction to \vec{P}_1) and positive when emitter and transmitter move away (v_{1r} in opposite direction to \vec{P}_1). These signs are opposite to the criteria established for the Doppler increment in Equation 2.4.11 and Figure 2.4.6, therefore, it is necessary to introduce the negative sign in the calculus of Doppler frequency in Equation 2.4.14 to make the sign consistent with the Doppler Effect.

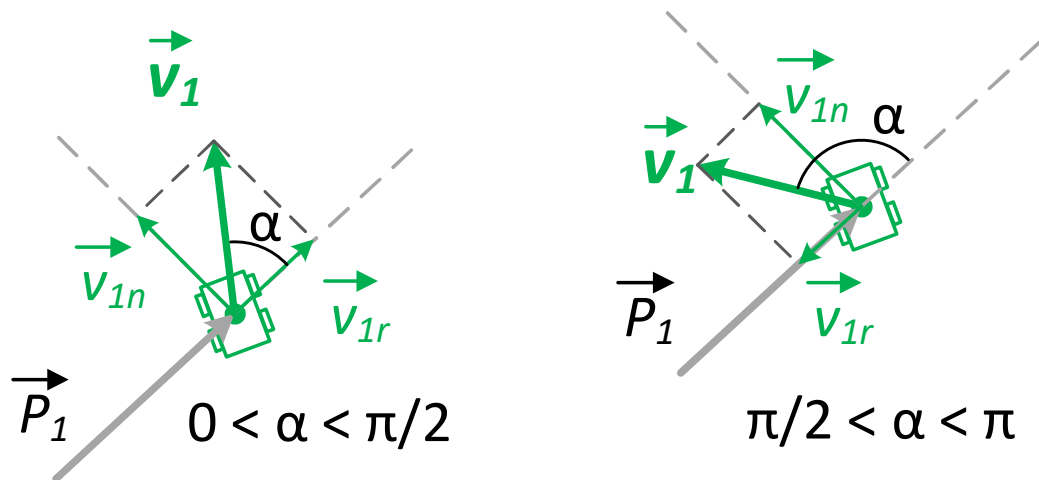


Figure 2.4.7- Sign of dot product to obtain the vector projection of \vec{v}_1 on \vec{P}_1 in order to obtain v_{1r} (Left) when the vector v_{1r} is aligned to \vec{P}_1 and (Right) when they are opposite.

As an example of application of this formulation, let us assume an exploration scenario defined by a linear trajectory like the one depicted in Figure 2.4.8.

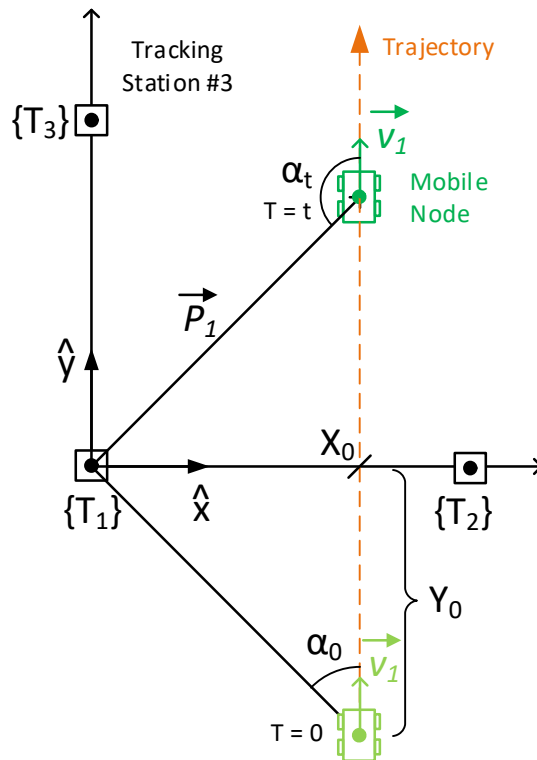


Figure 2.4.8- Linear trajectory travel scenario for a Mobile rover in an exploration area with three tracking stations T₁ to T₃.

In this scenario, the rover moves at constant velocity v_l , starting at an initial position in $T=0$ $P_0=(X_0, -Y_0)$, along a linear trajectory parallel to Y axis. Such trajectory is defined by the following position vector:

$$\vec{P}_1 = (P_{1x} \ P_{1y})^T = \begin{pmatrix} X_0 \\ v_1 t - Y_0 \end{pmatrix} \quad (2.4.15)$$

With modulus:

$$|P_1| = \sqrt{P_0^2 + v_1^2 t^2 - 2Y_0 v_1 t} \quad (2.4.16)$$

Where $P_0^2 = X_0^2 + Y_0^2$, that is, the square of the modulus of \vec{P}_0 .

The velocity vector can be calculated as:

$$\vec{v}_1 = \frac{d}{dt} \vec{P}_1 = \begin{pmatrix} 0 \\ v_1 \end{pmatrix} \quad (2.4.17)$$

Therefore, the Doppler frequency shift can be expressed as:

$$\begin{aligned} \Delta f_D &= \frac{f_c \cdot v_r}{c} = -\frac{f_c}{c|P_1|} (\vec{v}_1 \cdot \vec{P}_1) = \\ &= -\frac{f_c v_1}{c\sqrt{P_0^2 + v_1^2 t^2 - 2Y_0 v_1 t}} (v_1 t - Y_0) \end{aligned} \quad (2.4.18)$$

The Figure 2.4.9 shows the Doppler frequency shift plots assuming a value of $Y_0 = -100\text{m}$, velocities of 0.25m/s , 0.5m/s , 1m/s and 2m/s , and X_0 values of 10m , 20m , 40m and 80m .

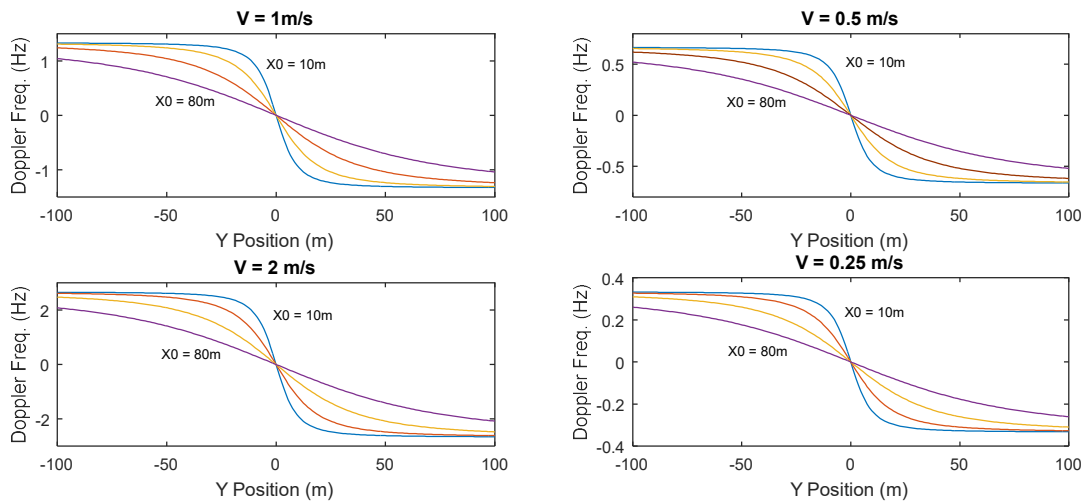


Figure 2.4.9- Doppler frequency shift values for a linear trajectory ($x=X_0$) for different mobile node velocities and different X_0 values (10m , 20m , 40m and 80m).

The Figure 2.4.9 shows the Doppler frequency shift plots obtained for different X_0 and velocity values considering the scenario described in Figure 2.4.8. The plots include the evolution of the frequency shift for different X_0 distances and, as expected, the change of the frequency shift becomes more drastic for lower values of X_0 . The Doppler Frequency measured at reception converges for both lower and higher Y values (approximation and distancing respectively) depending on the X_0 value, though the convergence value depends on the mobile node velocity.

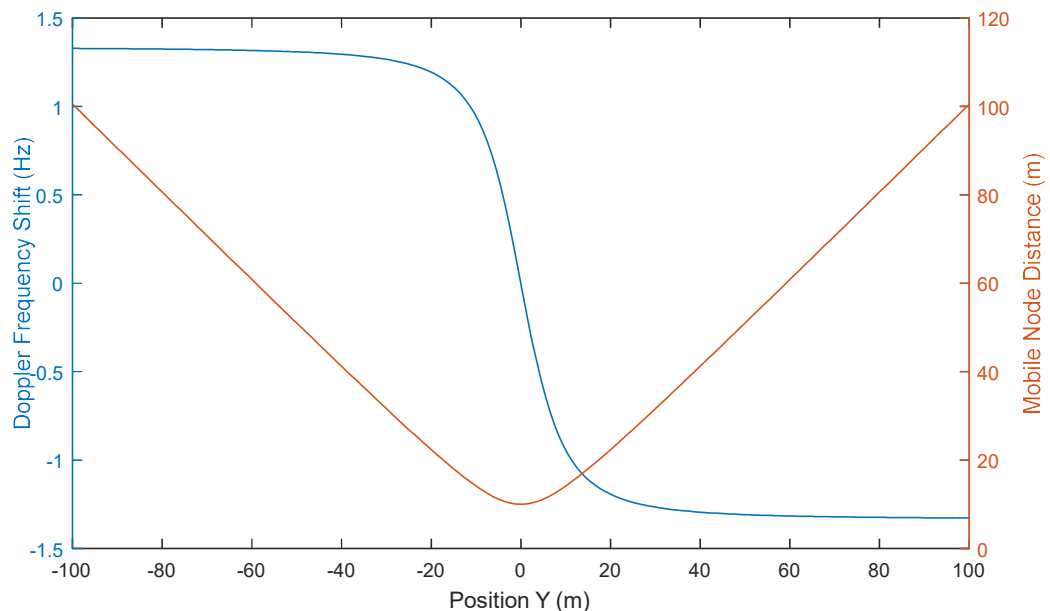


Figure 2.4.10- Doppler frequency shift and distance of Mobile node to tracking station versus position of mobile node in Y axis, when the mobile node moves along a linear trajectory $x=X_0$ from $y = -100\text{m}$ to $y = +100\text{m}$ at $v=1\text{m/s}$.

The Figure 2.4.10 shows the relation between the distance of the mobile node to the tracking station, that is, the modulus of the position vector \vec{P}_1 , and the Doppler frequency shift Δf_D versus the position in Y coordinate. As it can be appreciated in the figure, the range of positions where the radial speed appreciates the influence of the distance in X axis (X_0) is limited by Y positions values from -40m to $+40\text{m}$; out of these limits the variation of distance nearby constant and related with an almost constant Doppler Frequency component. The displacement in X axis is noticed mostly in the range from $Y=-20\text{m}$ to $Y=20\text{m}$. Therefore, this analysis implies that the sensitivity in the measurement of Doppler frequency shift will be determinant when the position of the mobile node is predominated by one of the axis. This effect will be analysed in the next chapter, along with other sources of uncertainty and noise.

2.4.4. Determination of Velocity Vector from the Doppler Frequency Shift.

The Figure 2.4.11 shows the scenario for calculation of total velocity from the radial velocity components obtained from the Doppler frequency shift Equation 2.4.11 and measured from the different tracking stations T_1 to T_3 . The components measured v_{1r} , v_{21r} and v_{31r} correspond to the projections of the main velocity vector \vec{v}_1 over the different position vectors corresponding to the different tracking stations.

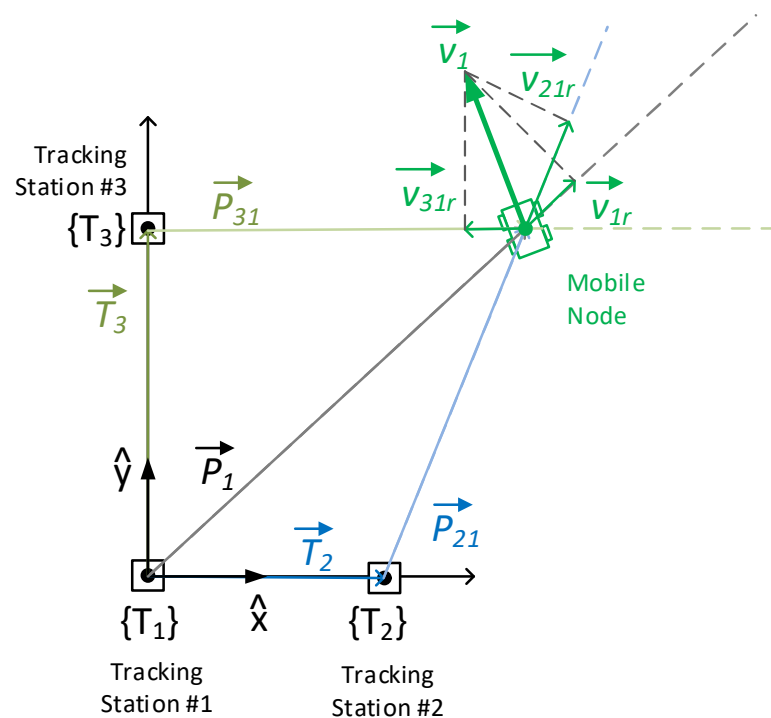


Figure 2.4.11- Radial velocity components from the different tracking stations, as it would be determined by the Doppler frequency shift measured.

The radial velocity components are related with the Doppler frequency shift by the next equation:

$$\Delta f_{Di1} = \frac{f_c \cdot v_{ri1}}{c} = - \frac{f_c}{c|P_{i1}|} (\vec{v}_1 \cdot \vec{P}_{i1}) \quad (2.4.19)$$

Where the subindex $i1$ represents the magnitude (either position or Doppler frequency shift) related to mobile node 1, considered from tracking station T_i . In the Equation 2.4.19, \vec{v}_1 is the unknown term whether the position vector \vec{P}_{i1} is known by a previous determination of position by Multilateration as defined in section 2.4.2. In our case, we are considering three tracking stations, from T_1 to T_3 , therefore, we can express an overdetermined system of three equations (one per tracking station) as follows:

$$\begin{aligned} -\frac{\Delta f_{D1}|P_1|c}{f_c} &= (\vec{v}_1 \cdot \vec{P}_1) \\ -\frac{\Delta f_{D2}|P_{21}|c}{f_c} &= (\vec{v}_1 \cdot \vec{P}_{21}) \\ -\frac{\Delta f_{D31}|P_{31}|c}{f_c} &= (\vec{v}_1 \cdot \vec{P}_{31}) \end{aligned} \quad (2.4.20)$$

Where $\vec{P}_{i1} = \vec{P}_1 - \vec{T}_i$ for $i = \text{index of tracking station (1 to 3 in our case)}$.

The system of Equations 2.4.20 can be expressed in a matrix form as an overdetermined linear system in the format $\mathbf{A}\vec{x} = \mathbf{B}$:

$$\begin{bmatrix} P_{1x} & P_{1y} \\ P_{21x} & P_{21y} \\ P_{31x} & P_{31y} \end{bmatrix} \cdot \begin{bmatrix} v_{1x} \\ v_{1y} \end{bmatrix} = \begin{bmatrix} -\frac{\Delta f_{D1}|P_1|c}{f_c} \\ -\frac{\Delta f_{D21}|P_{21}|c}{f_c} \\ -\frac{\Delta f_{D31}|P_{31}|c}{f_c} \end{bmatrix} \quad (2.4.21)$$

From the analytical point of view, the solution of (2.4.10) can be addressed using the same method based in Least Squares approximation described in section 2.4.2 for the determination of position using Multilateration method and its formulation, also leading to a linear overdetermined system.

2.5. Final Remarks.

In Figure 2.4.12, the complete process for determination of position and velocity for a mobile node exploring an area monitored by three tracking station is presented. The process takes six steps although only the four last ones are required for successive monitoring events on mobile node, since the first two processes are only required at the beginning of the mission, once the robotic system is deployed across the area of exploration.

In conclusion, the implementation of a mechanism combining distance determination based in Time-Of-Flight measurement and radial velocity based in Doppler frequency shift determination is possible with a Flat or Two-Tier architecture, using in this last case the communications network to exchange the information about position vectors of tracking stations and Doppler frequency shift components in order to centralize the calculation of position and velocity for each sampling event.

In general terms, a complete algebraic formulation for both position and velocity has been introduced in this chapter, making possible the estimation of the complexity associated to

the calculations involved with both magnitudes. According to the considerations developed in relation with the systems of equations for the calculation of \vec{P}_1 and \vec{v}_1 , which lead to a probably inconsistent and overdetermined system, the selection of the method to obtain the approximated solution is crucial to allow its implementation in a given hardware architecture.

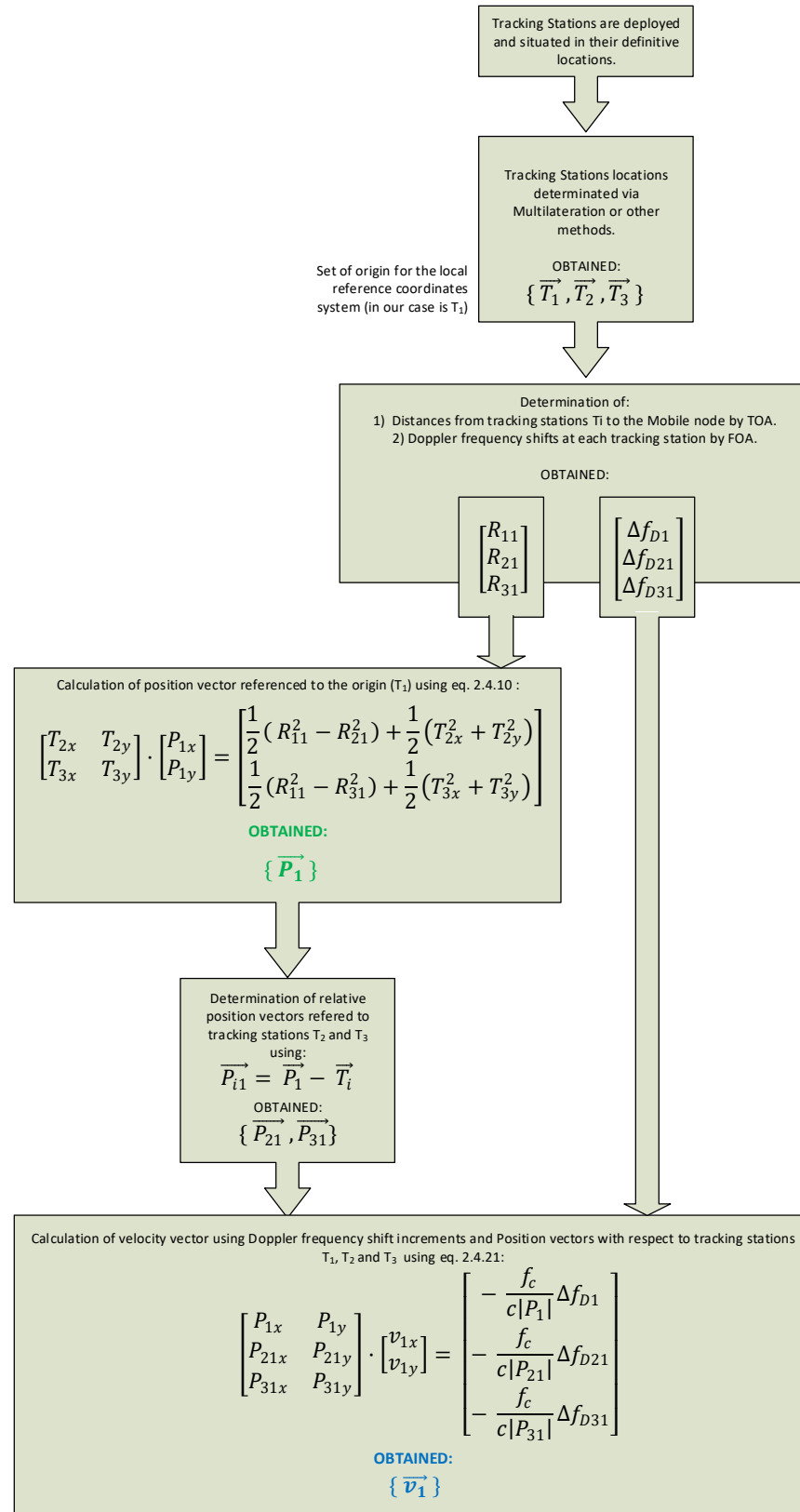


Figure 2.4.12- Process for the determination of position and velocity vector for a mobile node according to the assumed exploration scenario.

In order to implement a computational model of the abovementioned formulation, a number of MATLAB functions and scripts were developed (see appendix 2 for more details) enabling:

1. The generation of Range and Doppler frequency shift values vectors associated to a given mobile node trajectory. The exploration scenario implemented consists in the one defined in this chapter (depicted in Figure 2.4.1), formed by one mobile node and three tracking stations at specific coordinates, with the station T_1 as the origin of the reference coordinates system. The main .m code functions in this category are *RangeCalc()*, *RangeCalc_VN()* and *DopplerCalc_VN()*.
2. The reconstruction of position (P_x, P_y) and velocity (v_x, v_y) vectors for each position point from the ranges and Doppler frequency shift vectors corresponding to a complete trajectory. The main functions in this category are *PositionCalc()* and *VelocityCalc()*.

This set of functions enable the possibility to simulate a complete scenario for a mobile node moving in a linear trajectory across the exploration area, with configurable parameters (velocity, initial coordinates, initial and final time, time step, position of tracking stations, RF frequency for the ranging frames, etc.), obtaining the range and Doppler frequency shift values for each tracking station (T_1 to T_3 in our case) and, from them, re-construct the trajectory and velocity information as if it would be performed by the formulation presented above (2.4.10 and 2.4.21).

The Figure 2.4.14 shows the process for model simulation, adapting the measurement phases explained in Figure 2.4.12 to the different steps related with the mentioned MATLAB functions and its associated scripts. Figure 2.4.13 shows the simulation results.

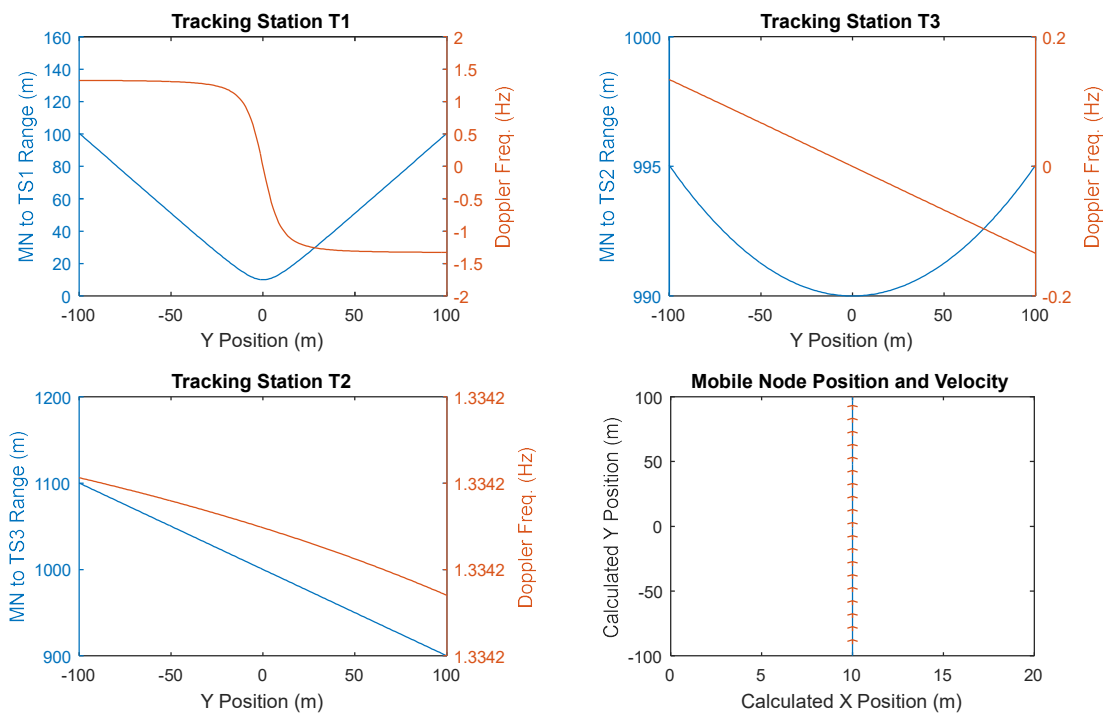


Figure 2.4.13- Simulation results for mobile node trajectory for the scenario described in Figure 2.4.14.

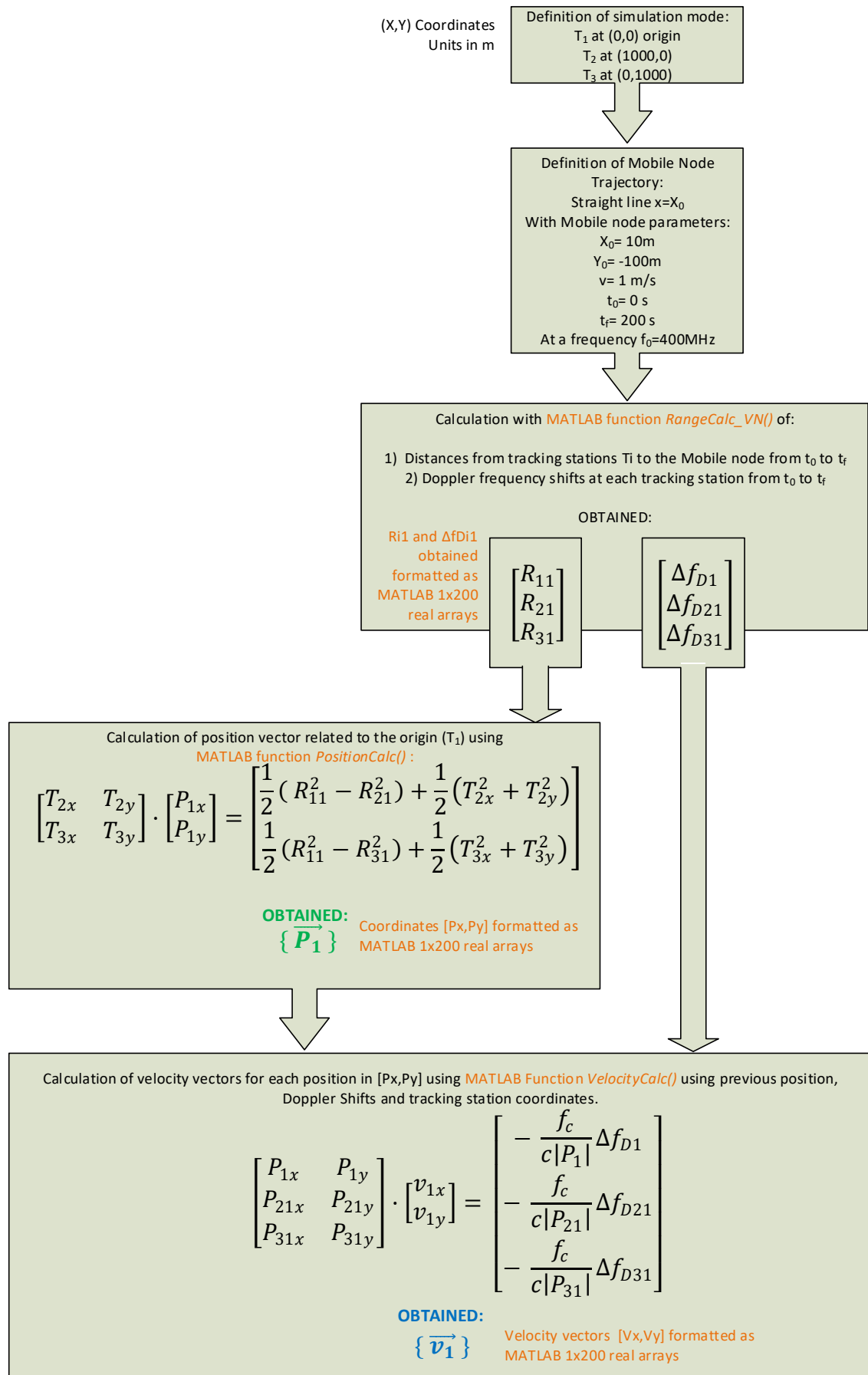


Figure 2.4.14- Process for the determination of range and Doppler shift, and the further determination of the position and velocity vector for a mobile node according to a cinematic set of parameters and associated MATLAB functions.

Along this chapter, a review of the different localization methods has been performed considering techniques suitable for radiofrequency signals, which was considered the appropriate choice considering that an optical alternative would not be compatible with the characteristics of the exploration scenario, the Moon surface in this case. The configuration of a hypothetical robotic multiagent system was proposed considering precedent missions and their track record; and a complete algebraic vector formulation specifically for the application under study was developed in order to make possible the design of mathematical models for a given tracking stations distribution and a mobile node trajectory.

In the next chapter, specific implementation issues will be considered concerning hardware details and limitations, as well as noise and uncertainty sources for the determination of position and velocity.

Chapter 3.- System Architecture Considerations

3.1. Introduction.

In this section, a performance analysis and technology trade-off is performed for a radiofrequency electronic system able to implement a localization mechanism of a mobile node, like an exploration rover, based in both TOA Multilateration and Doppler shift velocity measurement, including the complete radiofrequency chain (Tracking stations to Mobile node) considering both the One-Way and Two-Ways principles of operation.

For this purpose, the key parameters for the different RF components will be identified as well as their impact on the overall performance both at dynamic (i.e. noise) and static (i.e. drift) levels in the time frequency domains, since magnitudes such as the resolution, precision or sensibility of the instruments measuring the frequency and time separation of signals are critical when considering range and Doppler shift determination in the hypothetical exploration scenario as described in Chapter 2. The mathematical foundations of how these parameters affect the measurement performance will be described and justified as a part of the RF component models, as well as consolidated with the models introduced in Chapter 2. The system-level models are presented together and a parametric analysis of different implementation possibilities with commercial Space-Grade and Hi-Rel components. Finally, an analysis of the results obtained from the simulations is performed.

In Chapter 2, the scenario of exploration is defined as an square area of 1000m x 1000m where a multirobot system is deployed, consisting in three tracking stations T_1 to T_3 , and a mobile exploration robot defined as mobile node. In this scenario, a RF infrastructure exists allowing the determination of ranges (R_{11} , R_{21} and R_{31} considered as the distances from the mobile node to the different tracking stations T_1 to T_3) and Doppler frequency shifts at each tracking station (Δf_{D1} , Δf_{D21} and Δf_{D31}). This set of magnitude leads to the determination of the position of the mobile node in the coordinates reference framework with the tracking station T_1 as the origin, as well as its velocity vector obtained from the radial velocity components directly related with the Doppler frequency shifts, that is, the velocity vector components projected in the line from the mobile node to each of the tracking stations.

Considering the measurement of TOA and Doppler frequency shift, two possibilities exist, One-Way and Two-Ways measurement methods [Thorbjornsen,N.-2010] [Amundson,I.-2009] [Amar,A.-2008] [Lanzisera-2006]. Figure 3.1.1 present both concepts.

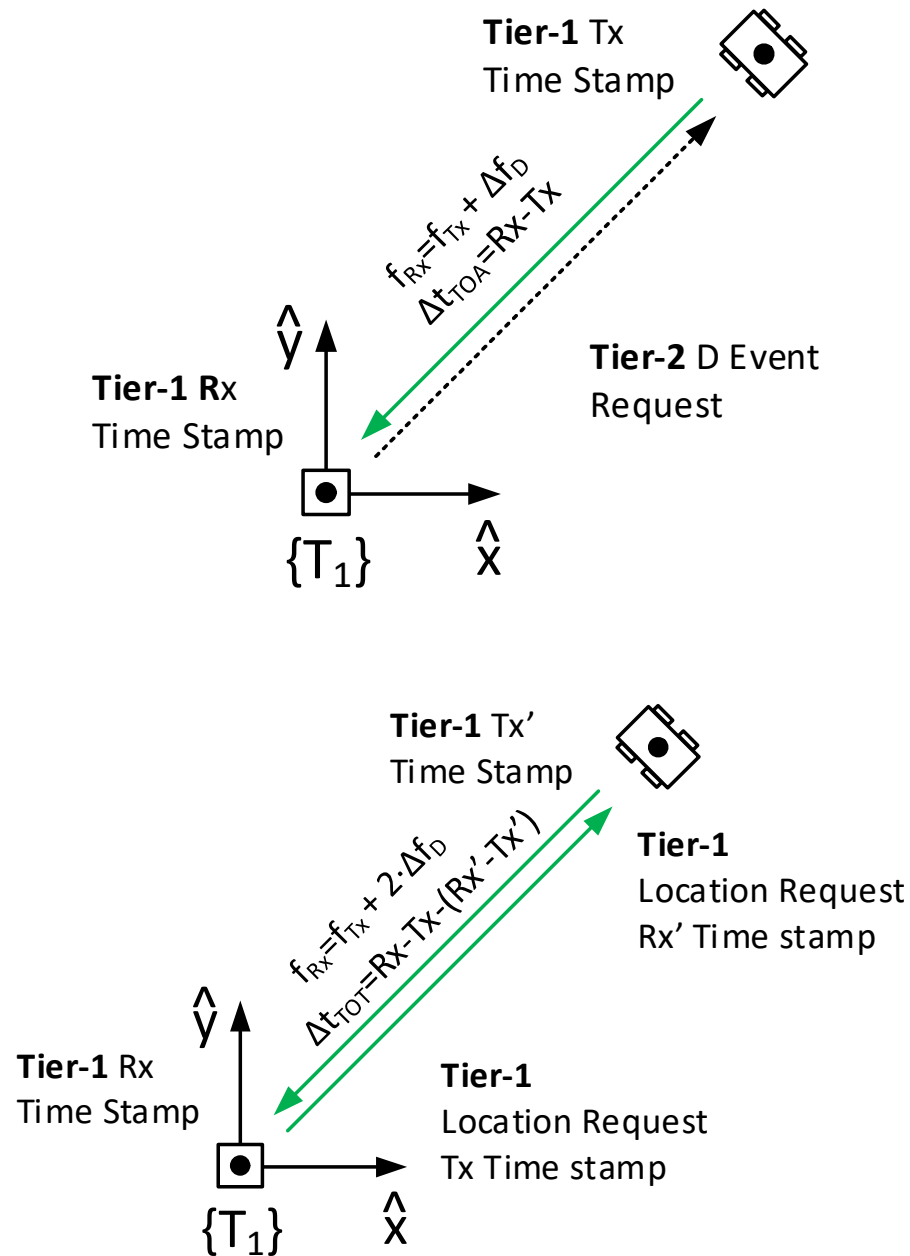


Figure 3.1.1.- One-Way (up) and Two-Ways (Bottom) RF ranging (Time of Transit) and Doppler measurement methods.

In both cases, the approach consists in obtaining the velocity by measuring the Doppler shift applied to the RF carrier signal along its travel from one robotic platform to the other, whilst time measurement between signal pulses at such carrier frequency should provide distance values via the measurement of the Time-Of-Arrival of pulses travelling along the RF path.

As it can be appreciated in Figure 3.1.1, One-Way method consists in measuring the time elapsed since the transmission of a signal from the mobile node to the reception of such signal at the tracking station. The method is simple and straightforward since, as the RF signals propagate at the speed of light in vacuum, the time increment can be translated directly to distance by $R_{i1} = c \cdot \Delta t_{i1}$ where R_{i1} is the distance from the mobile node to the tracking station T_i and $\Delta t_{i1} = t_{Rx} - t_{Tx}$ is the signal TOA, where t_{Rx} is the time stamp for the signal reception event and t_{Tx} is the time stamp for the signal transmission event. The

activation or request for position determination must be triggered either by a specific message frame in the same network or through the communications network used to exchange data (Tier-2 network in the diagram of Figure 3.1.1).

As noted in [Thorbjornsen,N.-2010], for this to work properly the time base implemented as high precision clocks must be highly synchronized among the different agents, tracking stations and mobile nodes, which is technically challenging and demanding from the point of view of the hardware, as it will be explained later, due to the different uncertainty factors affecting time base generators. In the same extent, relative velocity can be calculated from Doppler frequency shift by Equation 2.4.11. However, to calculate precisely the Doppler shift, the frequency of transmission (f_{real} in Equation 2.4.11) must be known with a high precision. Nevertheless, the transmission frequency depends on several environmental factors as well as stability issues in the RF frequency generation stage, what can introduce uncertainty to the measurement. The advantage of this method is that the underlying mechanism is simple from the point of view of the hardware and software involved, once the synchronization of clock signal generators involved is achieved, which involves a high cost at component level, but a simple system level implementation.

In case of Two-Ways method, a location request message is sent from tracking station to the mobile node. The message is time stamped at the origin by the tracking station, and retransmitted back to the tracking station with local (i.e. at mobile node) reception and transmission time stamps. The tracking station receives the signal and stamps the arrival instant. This way, the time of transit can be calculated subtracting the two time stamps at the tracking station (Rx-Tx) and afterwards subtracting the time required at the mobile node for the processing of the signal (Rx'-Tx'). The TOA can be estimated as a half of the time of transit.

Simultaneously, the signal received at the mobile node is measured in frequency. The resultant frequency value will include the Doppler shift term in the form of $f_{Rx} = f_{Tx} + \Delta f_D$, which as explained in Chapter 2 depends on the radial velocity component as well as on the original frequency of the signal and the speed of light in vacuum. This frequency is used to generate a new tone at a $f_{Rx'}$ and then retransmitted to the tracking station, which receives the tone with an additional Doppler shift increment resulting in $f_{Rx} = f_{Tx} + 2 \cdot \Delta f_D$.

The main advantage of this method (also mentioned in [Thorbjornsen,N.-2010]) is that it does not require time synchronization between tracking stations and mobile node, not even among the tracking stations themselves. The measurement of time is fully differential considering the expression included in the Figure 3.1.1 as $\Delta t_{TOT} = t_{Rx} - t_{Tx} - (t'_{Rx} - t'_{Tx}) = \Delta t_{TOA} - \Delta t_{TOP}$, where $\Delta t_{TOA} = t_{Rx} - t_{Tx}$ represents the total Time on Arrival and $\Delta t_{TOP} = t'_{Rx} - t'_{Tx}$ represents the time of process for the location signal on the mobile node. The event for location determination triggering could be implemented in Tier-1 network (at the reception of location message frame by the mobile node) or in Tier-2 communication network by the appropriate message in order to prepare the mobile node for the reception of the location message. The main disadvantage of Two-Ways method is that, as presented in Figure 3.2.6, the implementation at system level involves a higher complexity, especially at the mobile node side, where the relatively simple RF transmitter described in Figure 3.2.5 is substituted by a complex RF reception stage with frequency measurement capabilities, able to synthesize the same frequency for the transmission of the response frame message back to the tracking station.

Due to the dichotomy involved in the adoption of either One-Way and Two-Ways methods, a detailed analysis must be performed in order to understand the impact of the different uncertainty and noise generators in the position and velocity measurement performance.

Along this Chapter, the performance achieved in the position and velocity determination based in the range and Doppler frequency shift components measurement will be studied. For this purpose, a model of the system architecture proposed for robotic agents localization will be defined in detail and the key operation parameters identified. Once the operation of the proposed system is defined for both One-Way and Two-Ways methods, the main uncertainty, instability and noise sources will be identified and characterized considering real hardware components in order to make a realistic approach to the system level analysis. Finally, the impact of noise and uncertainty factors will be analysed considering the hypothetical exploration scenario defined and formulated in Chapter 2 in order to obtain relevant conclusions, both qualitative and quantitative, about the performance of the methods and architectures proposed.

3.2. Frequency Domain Considerations for Location Message Structure.

Concerning the calculation of the Doppler frequency shift as expressed in Equation 2.4.11, it can be obtained calculating the number of carrier wavelengths existing between both stations at any time. Being R the range (in m) between the Mobile Node and Main Station at a specific time, the number of wavelengths is:

$$N_{W,1W} = \frac{R}{\lambda} ; N_{W,2W} = \frac{2R}{\lambda} \quad (3.2.1)$$

For One-Way and Two-Ways respectively (see Figure 3.1.1), where λ is the carrier frequency's wavelength in m. The phase of the signal corresponding to such number of cycles can be expressed as:

$$\theta_{d,2W} = \frac{4\pi R}{\lambda} ; \theta_{d,1W} = \frac{2\pi R}{\lambda} \quad (3.2.2)$$

Where $\theta_{d,2w}$ refers to the phase of the signal in Two-Ways and $\theta_{d,1w}$ to the phase in One-Way. By differentiating the phase, we obtain the angular velocity ω_D and, from there, the frequency f_d associated with the Doppler shift:

$$\begin{aligned} \omega_{d,2W} &= \frac{d\theta_d}{dt} = \frac{4\pi}{\lambda} \cdot \frac{dR}{dt} = \frac{4\pi}{\lambda} \cdot v_{d,2W} = 2\pi f_{d,2W} \\ f_{d,2W} &= \frac{2v_{d,2W}}{\lambda} = \frac{2v_{d,2W} \cdot f_c}{c} \\ f_{d,1W} &= \frac{v_{d,1W}}{\lambda} = \frac{v_{d,1W} \cdot f_c}{c} \end{aligned} \quad (3.2.3)$$

Here c is the speed of light in vacuum (299.792.458 m/s) and f_c is the RF signal frequency, which in practice could range from UHF (400MHz) up to C (4GHz to 8GHz) bands. Equation 3.2.3 includes also the expression corresponding to One-Way Doppler frequency shift component, which corresponds to the Equation 2.4.11.

Given the Equations in 3.2.3 we could define and calculate the frequency sensitivity S_f , that is, the increment in the Doppler shift per unit of relative velocity $\Delta v_r = 1 \text{ m/s}$ for both the One-Way and Two-Ways operation modes at 400 MHz, a frequency in UHF band, as a preliminary estimation:

$$\begin{aligned} S_{f,2W} &= \Delta f_{D,2W} \Big|_{\Delta v_r=1 \text{ m/s}} = \frac{2f_c \cdot \Delta v_r}{c} = 2.6685 \text{ Hz/(m/s)} \\ S_{f,1W} &= \Delta f_{D,1W} \Big|_{\Delta v_r=1 \text{ m/s}} = \frac{f_c \cdot \Delta v_r}{c} = 1.3342 \text{ Hz/(m/s)} \end{aligned} \quad (3.2.4)$$

As expressed in Equation 3.2.4, the sensitivity is higher for the Two-ways ($S_{f,2W}$) approach since the Doppler Effect frequency increment adds twice to the total signal frequency received at the tracking station (see Figure 3.1.1). While in the One-Way approach the signal travels just one path from mobile node to tracking station, in the Two-ways approach the Mobile Node repeats the signal, adding a second (and identical) Doppler component. Figure 3.2.1 represents the Doppler shift per m/s versus frequency in a two ways configuration. As it can be appreciated, the Doppler shift sensitivity increases rapidly at higher frequencies.

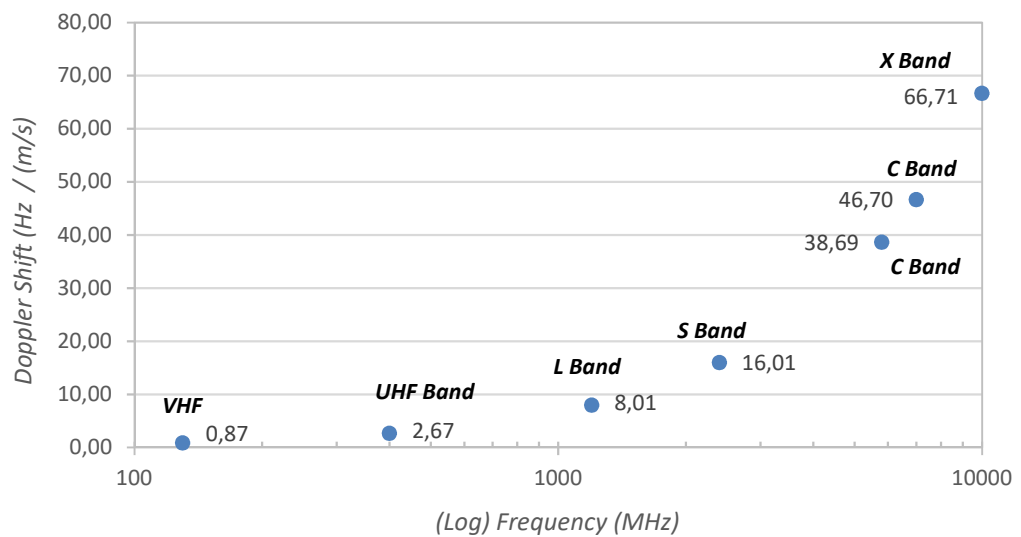


Figure 3.2.1.- Two-Ways Doppler sensitivity $S_{f,2W}$ (Hz/ (m/s)) as a function of frequency.

Considering that the resolution of frequency measurement instruments are better than 1 Hz ($<0.1\text{Hz}$ in most laboratory equipment) these numbers relate to relative speed theoretical resolutions ranging from 114cm/s in VHF up to 21,4 mm/s in C band using Equation 3.2.5, and assuming a minimum Doppler shift $\Delta f_{D,2W} = 0,1 \text{ Hz}$ determined by instruments resolution:

$$\Delta v_r = \frac{\Delta f_D}{S_f} \quad (3.2.5)$$

For robotic exploration, the relative speed resolution yielded by UHF frequency value in Figure 3.2.1 (37,45 cm/s) represents a suitable value for such application, therefore the study along this thesis will be carried out in this frequency band (UHF, in the range of 400 MHz). Furthermore, this band provides a minimum path loss for such velocity resolution, which adds another argument in support of its selection.

Despite of the considerations above, more factors must be taken into account prior to consider one of the operation modes as the most suitable for this application. The different effects that will play a relevant role for the scoring of both approaches will be discussed in depth in the following sections.

The RF signal structure is considered to operate either in Continuous Wave (CW) or in active Pulse-Doppler (aPD) modes. The CW is based on the principle of continuous and simultaneous transmission of both RF carriers (from tracking station to mobile node and vice versa), and the measurement of frequency displacement of both tones (transmitted and received) at the tracking station. In principle, the CW operation mode is considered not practical for robotic exploration applications since it requires two separate frequency channels and two independent reception and transmission RF signal paths (including transceiver circuit and antenna) for forward (tracking station to mobile node) and backward (mobile node to tracking station) RF links respectively, which duplicate the hardware requirements for the radio subsystems. On the other hand, aPD method is suitable for both configurations with a minimal impact for the Two-Ways mode thanks to its “half duplex” nature, and furthermore it enables the possibility to implement the measurement of Time Of Arrival due to its intrinsic capability of operating the RF tones on discrete message packets or frames in the time domain.

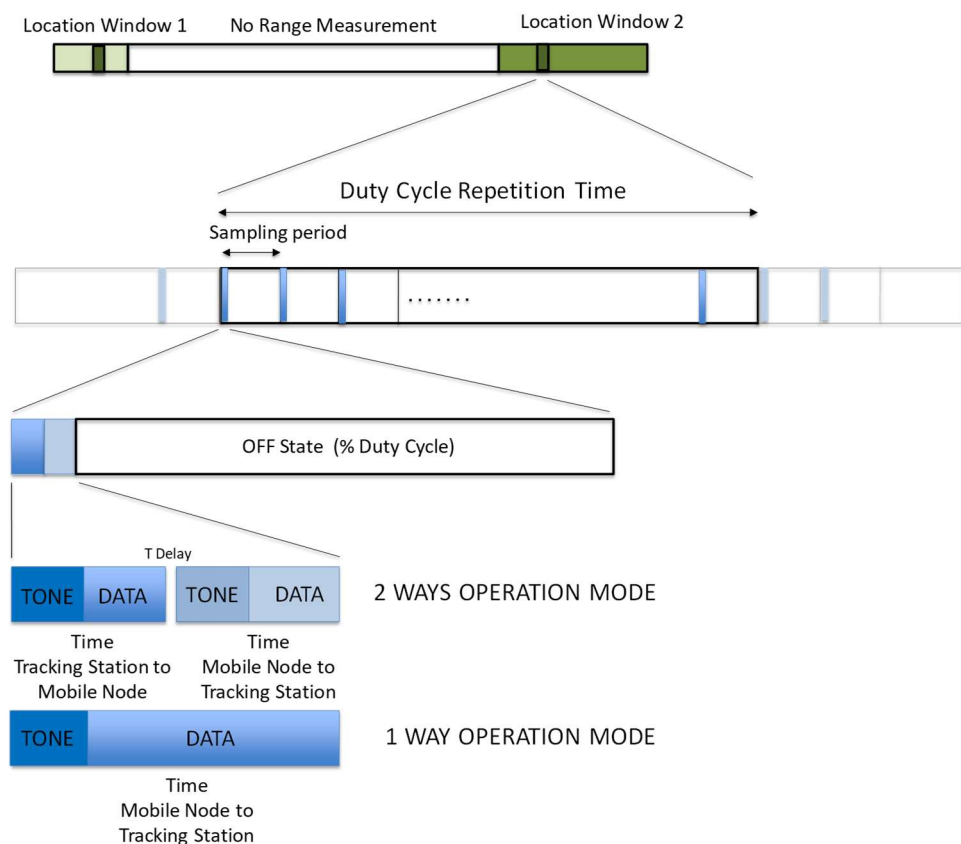


Figure 3.2.2.- Proposed location data frames structure of range and Doppler shift acquisition process. Each frame starts with a preamble consisting in a tone at fixed frequency with a number of signal cycles.

Figure 3.2.2 represents an example of time plan for the RF signal transmission proposed for range calculation based in Time Of Arrival measurement, in a generic scheme. The sampling period separates each measurement cycle consisting in the period for RF transmission, in the case of One-Way mode. For the Two-Ways mode, the period of activity is distributed over two periods for transmission from tracking station to Mobile Node, a delay intended to RF circuit switching and the same period of RF transmission from mobile node to tracking station.

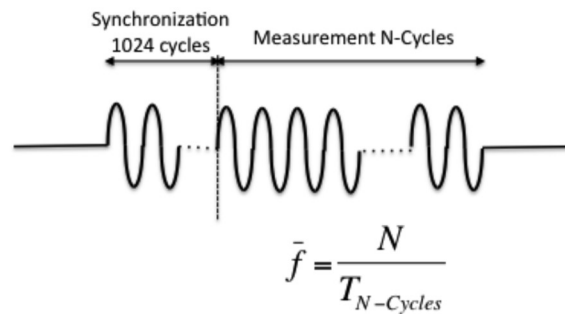


Figure 3.2.3- RF carrier preamble proposed for the determination of Doppler Frequency shift, starting each localization message frame (see Figure 3.2.2)

Figure 3.2.3 represents the structure of the RF pulse intended for range determination with Time of Arrival combined with Doppler frequency shift Measurement. It consists of a single RF pulse with 1024 + N carrier tone cycles, meaning that the first 1024 cycles are intended as a preamble for synchronization allowing to detect the pulse at the receiving station; and to check its integrity counting 1024 correct carrier cycles. The following N cycles (for N=10.000 to 100.000) are used to calculate the estimation of average period, and thus, the average frequency for that pulse. This signal corresponds to the segment labeled as “tone” in the datagram represented in Figure 3.2.2, this way, the preamble used commonly to synchronize the demodulator at reception stage can be used as well to measure the incoming frequency and, thus, obtain the Doppler shift information.

The reason for using a time-domain frequency measurement method is twofold, on one side, the electronics used to measure time between RF pulses for TOA range determination mechanisms could be used to simultaneously measure the time duration of a number of carrier cycles in each pulse as described above, saving resources and accomplishing an efficient implementation of both TOA and frequency measurement. On the other hand, an alternative mechanism based on the calculation of the frequency spectrum by means of Fast Fourier Transform (FFT) procedures requires a high sampling frequency (much higher than signal central frequency itself) [Fang,Y.-2012] [Liu,Y.-2011] [Hernandez,D.-2008] which would make the frequency measurement stage very demanding considering the necessary clock frequency and the computational resources required [Henzler,S.-2010]. Therefore, a frequency determination method based on time domain calculation is more convenient for an application being distributed among a multi-robot community composed by small robotic exploration agents.

Different values for the number of measurement cycles per pulse have been considered in the analysis of the different application cases, as will be explained below, where the noise levels of the components have had a critical impact in the resulting performance. In general, the higher the number of cycles involved in the measurement (i.e. estimation of the average), the lower the total phase noise level in the measurement, therefore, if the implementation introduces components that contribute with higher phase noise, more cycles must be averaged to reach the necessary range accuracy and, consequently, longer times will be

required for range calculation, impacting in the time constant of the system. In any case, these aspects will be justified later in this document.

3.3. RF System Architecture.

As explained in section 3.1, the two operation modes proposed above (One-Way and Two-Ways) have been considered and their performance analysed to assess their suitability to implementation by taking into consideration different parameters: power consumption, complexity, mass/volume budgets and accuracy. Figures 3.3.1 and 3.3.2 below illustrate the proposed architectures for One-Way and Two-Ways measurement operation modes.

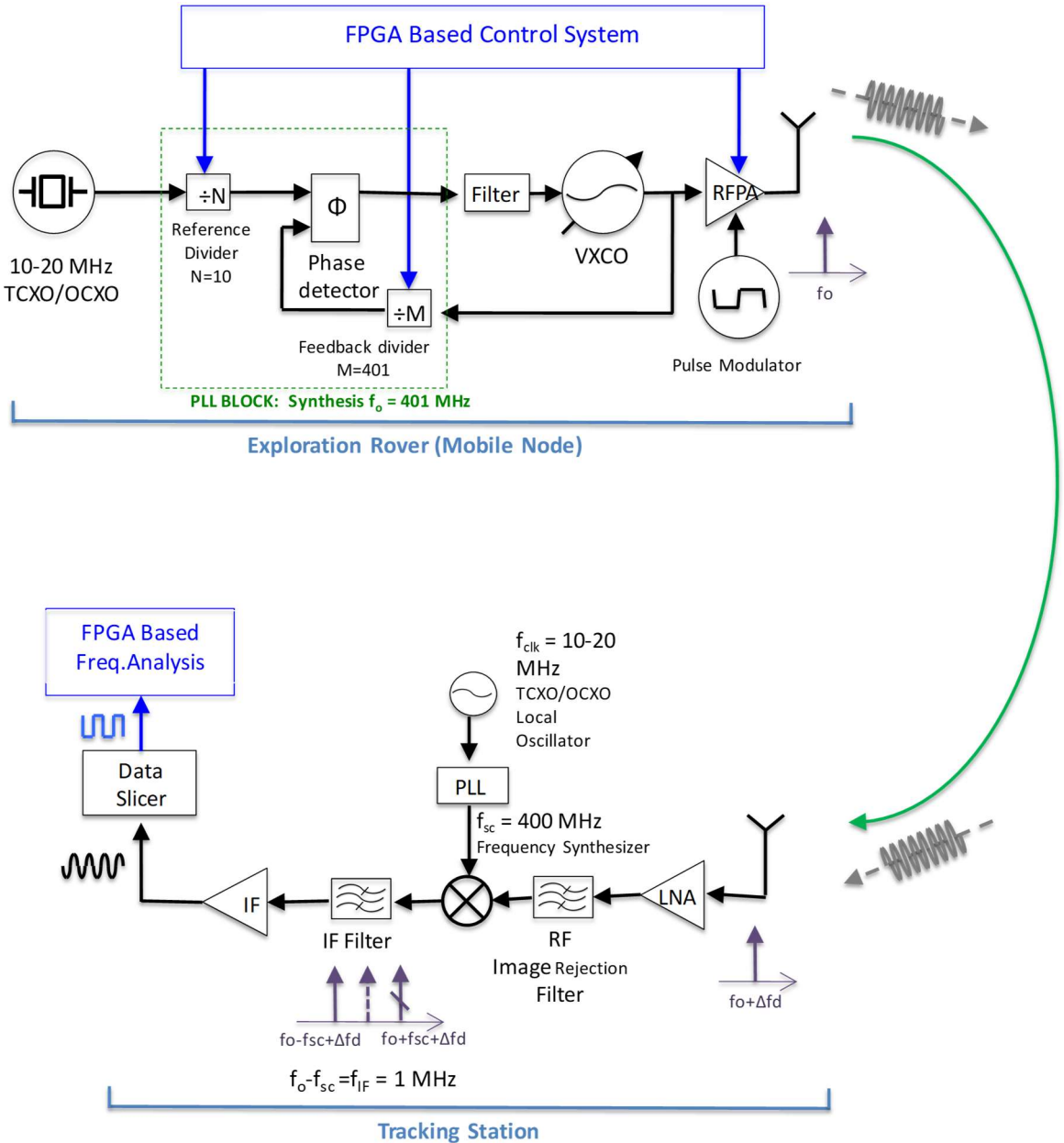


Figure 3.3.1- One-Way Operation Mode proposed architecture

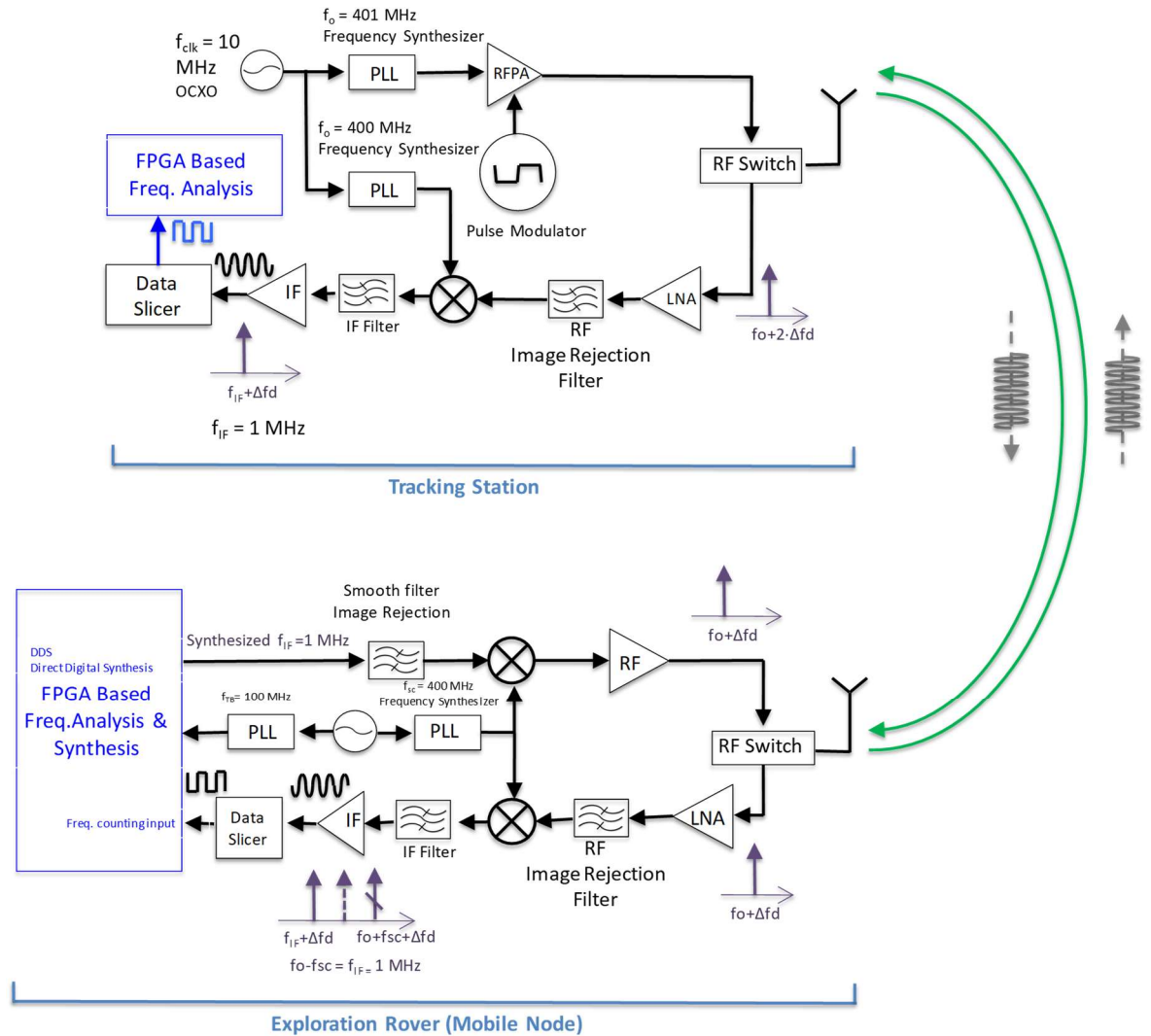


Figure 3.3.2- Two-Ways operation Mode proposed architecture

The One-Way mode is composed of an independent high-stability oscillator in the Main Station, operating in a low frequency (with a nominal range of 10MHz as nominal) and connected to a frequency synthesis stage that will up-convert this tone to the range of UHF band (401 MHz as an example for UHF application). The output signal is amplified by a RF power amplifier with a switching input able to modulate its output in On-Off Keying, thus making possible the generation of RF pulses from the logic control device: a FPGA (or other logic device) implementing the RF pulse generation logic and the logic to control the RF frequency through the PLL inputs. The receiving stage at the Mobile Node receives the incoming RF pulse, with the Doppler frequency shift increment (Δf_d) added, that is amplified through a LNA and down-converted, by means of a mixer and a 400 MHz high stability carrier, to an Intermediate Frequency (IF) in the range of the MHz (1MHz in this case). The next stage measures in the time domain the Doppler frequency component directly from the IF down-converted signal. For this purpose, a Data-Slicer stage will transform the sinusoidal signal to a squared digital signal with voltage levels being compatible with the FPGA input ports logic levels (+1,8V to +3,3V). A frequency-measurement logic block will calculate the frequency of the incoming digital signal, thus measuring the Doppler component given that the original carrier frequency is known at reception stge.

The Two-Ways approach is based on the generation of a highly stable RF carrier at the tracking station, which is transmitted to the mobile node in a pulsed fashion as for the One-Way mode. Once in the mobile node, the pulse is sent back to the tracking station where it is down-converted to an IF in the range of the MHz (1 MHz in this case) and processed afterwards to obtain the Doppler component. In this case, as the pulse is retransmitted from the Sample Container, the Doppler increment applies twice ($2 \cdot \Delta f_d$), thus doubling the sensitivity, as explained in section 2.2 (Equation 3.2.4).

By far, the strongest advantage on this Two-Ways operation mode is the coherent processing in the frequency domain of the RF pulse since the same frequency carrier generation is used both to modulate the RF outgoing pulse and to down-convert the retransmitted pulse to the IF domain, thus automatically compensating the frequency drift due to ageing and temperature in a large portion of the RF chain. Conversely the One-Way option, though simpler from the electronics point of view, introduces a non-coherent frequency operation (generation of carrier tone and down-conversion for Doppler component detection are carried out by different oscillators) that will result in the accumulation of the different drift effects due to the different oscillators involved.

In both modes, the carrier frequency synthesis is performed by means of a combination of a high-stability oscillator, such as an Oven Compensated Crystal Oscillator (OCXO) or a less accurate option based on a Temperature Compensated Crystal Oscillator (TCXO), and a Phase Locked Loop (PLL) operating as a N-Integer frequency synthesizer. The reason for this design option is the lack of high-stability crystal based oscillators available for frequencies above the range of tens of MHz.

Considering the different options for stable frequency generators, oscillators based in Quartz crystal exhibit large long term stability (against ageing and temperature drift effects) and high spectral finesse, involving low phase noise and high frequency accuracy, when compared with alternative technologies like Surface Acoustic Wave (SAW) or Micro-Electromechanical Systems (MEMS) resonators. Nevertheless, an intrinsic limitation exists for the resonance frequency of crystal-based oscillators: Quartz resonators operate depending on the crystal cut used to manufacture the crystal sheet, and its natural resonance frequency depends on such cutting technique as well as other physical parameters of the vibrating element such as thickness and the cut angle.

The most typical crystal cut techniques used are:

- **AT (0.5 to 300 MHz):** Typically used in commercial crystal-based oscillators. It can be found in crystals with resonance frequency up to 200 MHz for extended temperature (although the nominal range is below 100MHz). The thickness of the vibrating sheet is related to the fundamental frequency by a rate of 1,661 mm/MHz. Typically, the fundamental tone is 30MHz, with a 5th overtone at 150 MHz. This cut produces oscillators, which although able to reach frequencies in the range of 100MHz, are very sensitive to temperature and mechanical stress. This is the reason why the AT oscillators are found in electronic devices designed for non-demanding applications typical of consumer markets.
- **SC (0.5 to 200 MHz):** Special cut technique used for high stability oscillators. Most OCXOs (Oven Controlled Crystal Oscillators) are based on a SC cut crystal resonator. SC crystal-based oscillators exhibit lower phase noise and ageing characteristics than their AT counterparts, as well as much lower temperature sensitivity. A drawback of this technique is that the operation of SC resonators in overtone frequencies results in strong reduction of the frequency stability. Therefore, SC crystal oscillators usually only operate in their fundamental frequencies.

- **BT (0.5 to 200 MHz):** variation of AT, to increase repeatability. Up to 50MHz central frequency, with similar performance to that of AT.

There are more cut types (CT, DT, GT) but for lower frequencies (up to 1MHz) and with worse stability and phase noise characteristics.

Additionally, the frequency depends strongly on the thickness of the crystal plate comprising the vibrating structure, therefore the thinner the crystal plate, the stronger the effect of external mechanical factors is on the stability of the oscillation frequency. As a general conclusion, the oscillators for applications that require high stability and a large range of operational conditions (involving operation temperature and vibration) will require SC cuts at low frequencies, which involves a crystal plate thick enough to make the environmental (mechanical/ T°) effects negligible.

As a consequence the range of OCXOs and TCXOs available for Space Qualified and High Reliability applications are characterized by relatively low frequencies (typically 10-50MHz), and thus, the generation of a frequency in the UHF (400MHz) and higher bands (S,L,C, etc.) implies the need to use some frequency synthesis strategy. Considering this, the use of a PLL as the central element for frequency synthesis is the traditional approach. Moreover, there are PLL building blocks of space grade quality that make the option feasible of a spaceborne design feasible.

3.4. Analysis of Frequency and Time Critical Parameters.

To model the performance of the different elements of the RF chain involved both in the One-Way and Two-Ways modes; we must first identify the critical parameters that most affect the performance of the measurement of the Doppler frequency shift component and Time of Arrival.

In the frequency domain, which mainly affects to Doppler Shift measurement, the parameters under consideration must be those that affect the stability of the frequency, which could be categorize by its influence over short and long term timeframes.

1. **Long term stability:** the factors involved in the performance of frequency generator devices are mainly **ageing** and **temperature**, as well as mechanical vibrations and radiation. In this case, the mechanical vibration is negligible during the system operation, and radiation is below the dose levels required to significantly impact in the resonance frequency. In fact, the radiation dose in Moon surface spans from 38 Rad to 11 Rad [Reitz,G.-2012], when the radiation levels inducing a change comparable with the thermal drift or aging in several orders of magnitude higher, in the order of 100 kRad to 1MRad as the experimental studies concluded [Euler,F.-1980] [TAC-1998] [MML-1991] [GIT-1963] [Norton,J.-1994]. Furthermore, the electronic systems in an exploration robotic rover would be placed inside a protection case and not exposed to the outer environment; therefore, the effect of radiation would be even lesser.

Aging is usually expressed in Parts-Per-Million (ppm) specified for time periods in the order of one year to 10 years, for the value of the nominal frequency.

The temperature stability coefficient is specified in ppm of the nominal frequency, for the whole temperature operation range of the device. If an oscillator is featured as 10 ppm and it is specified to operate in the range of -20 to +80 °C, the oscillator will exhibit a stability of 10ppm/(80 -(-20))°C, therefore the thermal stability will be 0,1 ppm/°C. Using this ratio to the expected thermal excursion of the part under consideration, the estimated frequency drift due to the temperature would be calculated.

2. **Short term stability:** the most relevant contributors to the short term (i.e. fast) frequency stability is the **thermal noise** and **phase noise** of the system, where oscillators are the main phase noise contributors in a RF system. Additionally, PLL's used for RF signal synthesisers multiply the effect of phase noise generated by the oscillators, whilst adding its own phase noise, mainly produced by phase detectors nonlinearities. Finally, **Quantization errors**, introduced by the limitation in the precision of the numerical representation of the sampled measurements, is also an important contributor to short term stability, implying a significant noise generator. The quantization noise influences time-domain parameters in a similar way to frequency, so it will be explained and formulated later.

Concerning the thermal noise, the variance associated to its contribution to the uncertainty introduced in the Doppler frequency shift measurement is limited by the Cramer-Rao Lower Bound (CRLB). CRLB expresses the lower value of the variance of an unbiased estimator, like, for example, the mean of a number of uncorrelated samples. CRLB yields a very important information to dimension the minimum noise level in a measurement process since it is not possible theoretically to have a better uncertainty level than the limit established by the Cramer-Rao one. The CRB is expressed by the general equation:

$$\text{Var}(\hat{\theta}) = \sigma_{\hat{\theta}}^2 \geq \frac{1}{I_F(\theta)} = \frac{1}{-E \left[\frac{\partial^2 l(x; \theta)}{\partial^2 \theta} \right]} \quad (3.4.1)$$

Here $\hat{\theta}$ is an unbiased estimator of the statistical parameter θ obtained from the variable x like for example, the mean \hat{x} , $I_F(\theta)$ is the Fisher Information function of the estimator θ which depends on the Expectancy E of the second derivative of the natural logarithm of the likelihood function since $l(x, \theta) = \log(f(x; \theta))$.

The CRLB for Doppler frequency shift measurement has been studied previously by different authors, whose contributions differ in the signal time and frequency parameters considered due to the particular applications. [Lie Ching Cheong, P.-1993] and [Dogandzic, A.-2001] consider an application case that adapts to our exploration scenario, consisting in a pulsed RF signal composed by a number of carrier cycles that is transmitted with a given repetition rate. In this case, the CRLB associated to the measurement of Doppler frequency shift is given by:

$$\sigma_{\hat{f}_D}^2 \geq \frac{1}{\text{SNR} \cdot T_R^2 \cdot N(N^2 - 1)} \quad (3.4.2)$$

Here SNR is the Signal-to-Noise Ratio, N is the number of cycles in the pulse and T_R is the repetition period.

[Bamler, R.-1991] proposes a new expression for CRLB assuming a correlation between power spectrum of the pulse signal and the noise power spectral density yielding an approximate expression for the variance of Doppler frequency shift noise:

$$\sigma_{\hat{f}_D}^2 \geq \frac{1}{16} \cdot \left(\frac{1}{m^2} + \frac{1}{2} \right) \cdot \frac{1}{T_R^2 \cdot N} = \{m = 0.7\} = \frac{0.1588}{T_R^2 \cdot N} \quad (3.4.3)$$

As it can be appreciated in Equation 3.4.3, the assumption of certain power spectral correlation between the signal and noise impacts on the factor depending on the SNR and the number of cycles involved with the term N^2 , although there is still a dependence on the Repetition period and the number of cycles. In any case, for this thesis the formulation provided by [Lie Ching Cheong, P.-1993] and [Dogandzic, A.-2001] and corresponding with Equation 3.4.2 will be used since it is considered more suitable because of being more general, allowing the consideration of different characteristics of the signal used for Doppler shift determination.

Regarding phase noise, it consists of instabilities in the period value due to internal effects such as imperfections in the oscillator structure, electronic noise introduced by the oscillator circuit components such as Flicker and Gaussian white noise. The accumulation of all these random effects produces a variation of the time period of a signal that is supposedly periodic. When this effect is considered in the frequency domain, about it is termed phase noise; while when observed from the time domain perspective, it is known as jitter, thus, both concepts are manifestations of the same effect that is ultimately related with the spectral purity of the oscillator, as described in [Shinde.S.-2014]

Along this contribution, a detailed comparative study of the different phase noise models proposed in the literature is performed, some of them also included in the references such as [Leeson,D.B.-1966] and [Demir.A-2000]. However, the correspondence between frequency domain description of phase noise and the time domain variation in measured period (i.e. Jitter) is necessary for us to be able to estimate the uncertainty in the frequency and time measurement for both Doppler shift and TOF determination, therefore, our analysis will focus on the determination of jitter in the time domain from the set of parameters provided by oscillators manufacturers, which are usually based in the observation of the spectral response because of the simplicity on its determination.

Jitter (or phase noise) implies an uncertainty in the measurement of the signal period, and thus of its frequency, since at any specific period T_n , measure will be $T_n + \delta_n$, and therefore the frequency measurement will carry an error component, that can be modelled as δ_n , a random (i.e. noisy) time magnitude that changes along the time and different at any period T_n .

Fortunately, as the causes that contribute to the phase noise are uncorrelated to each other [Shinde.S.-2014] [Demir.A-2000] [Barnes,J.A.-1971], the Central Limit Theorem which implies that the probability distribution of the phase noise values is a Normal (Gaussian) distribution, only characterized by a mean and normal deviation value. Figure 3.4.1 shows jitter as both in time domain and as a Gaussian distribution function.

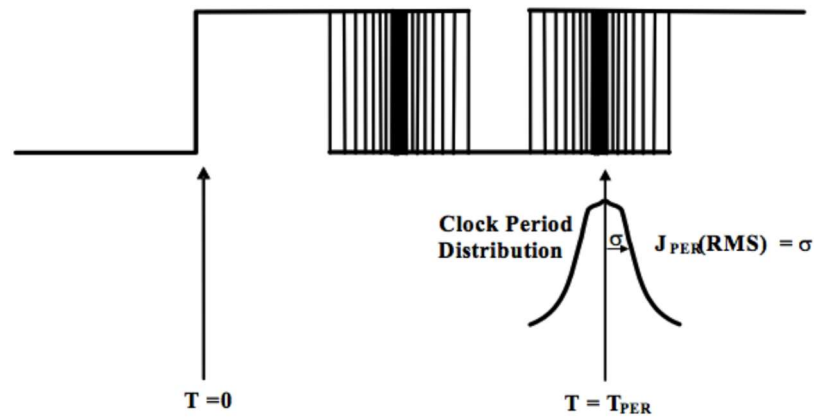


Figure 3.4.1.- Jitter representation in a digital signal and aspect of the statistical distribution

The literature [Howe,D.A.-2003] defines Cycle (or Period) Jitter as the distribution of error values for each measured period, versus the theoretical period value. The variance of this magnitude is calculated assuming the difference between the real period values and the average period (i.e. the mean value of the distribution):

$$\sigma_c^2 = \lim_{N \rightarrow \infty} \left[\frac{1}{N} \sum_{n=1}^N (T_n - T_0)^2 \right] \quad (3.4.4)$$

In [Barnes, J.A.-1971] an instantaneous frequency deviation from average is used, which corresponds to the same concept in frequency domain. This definition also corresponds to other more complex representation of phase noise, such as the one defined in [Demir.A-2000], where the cycle jitter concept is extended to an orbital perturbation in a State-space interpretation of the phase values describing an orbital trajectory along a limit cycle.

Other references, such as the famous work of [Barnes, J.A.-1971] that provides a comprehensive analysis of frequency stability issues for oscillators, make use of the Cycle-to-Cycle Jitter denomination, based on representing the jitter in each period nT as the increment in the measured value of the period over two successive period samples, yielding a variance expression of:

$$\sigma_c^2 = \lim_{N \rightarrow \infty} \left[\frac{1}{N} \sum_{n=1}^N (T_n - T_{n-1})^2 \right] \quad (3.4.5)$$

This expression is interesting from the point of view of a separate analysis of jitter from other low frequency phase variations. The successive differences remove low frequency components from the jitter magnitude, thus decoupling effects like those above mentioned (thermal drift, ageing, etc.).

An evolution of this concept is the interesting contribution of [Allan,D.W.-1966] known as Allan Variance, which is used extensively to determine phase deviation in oscillators, allowing a categorization of the impact of different phase shift contributors depending on its frequency.

$$\sigma_y^2(\tau) = \frac{1}{2} (\bar{y}_n - \bar{y}_{n-1})^2 \quad (3.4.6)$$

Here $\overline{y_n}$ represents an average of the frequency deviation along an observation period τ , and n the period where the first sample is taken. This representation of the variance is consistent with experimental observations since two average of frequency deviation estimations are compared as a function of the interval between the two samples subsets. That relation yields interesting representations of the frequency deviation depending on the time interval, which helps to isolate high frequency (random noise) and low frequency (thermal drift, ageing and random walk) effects.

For this case, we will consider cycle jitter as it is represented in Equation 3.4.6 since it allows the accumulation of different effects, not only random noise, but also ageing and thermal drift.

Considering that the jitter statistic features produce, as justified above, that the real period values are distributed around the theoretical (average when $N \rightarrow \infty$) period value according to a Gaussian distribution, it is correct to assume that the jitter mean is zero, therefore, since the variance and mean square value of a random set are related as:

$$\langle X \rangle_{MS}^2 = \tilde{X}^2 + \sigma_x^2 \quad (3.4.7)$$

In this case the variance and mean square value are equivalent, therefore, the typical deviation is:

$$\sigma_x = \sqrt{\langle X \rangle_{MS}^2} \quad (3.4.8)$$

The typical deviation of the cycle jitter is a critical parameter since it would allow us to estimate the error range in frequency measurement for a range pulse, given that a range pulse is formed by a finite number of cycles, therefore though the average of an infinite number of period values will yield the theoretic period, having a finite subset of values will produce a set of estimators yielding a lower variance.

In order to estimate the worst case jitter value for a given application case, and to find out how the Normal distribution of estimated jitter values become narrower through lower variance values for different number of cycles per pulse and different subsequent measurement samples averaged, firstly we have to find a mechanism to estimate the variance of the jitter distribution for the contributing components.

As explained in [Baran,O.-2010], both time and frequency domains are used to determine and characterize phase noise. In general, for observation (i.e. sampling) frequencies below 1 Hz, time domain is more apt, while for higher sampling rations, the frequency domain is more used mainly due to the fact that, from an experimental point of view, obtaining the spectrum response of a system is quite straightforward with common instrumentation (spectrum analyser). That is the main reason why manufacturers of oscillators and phase-sensitive components like PLLs, Up and Down-Converters, VCOs etc. provide the phase noise characteristics and contribution of their devices in frequency domain.

Many references refer to the frequency domain of phase noise and instability. [Leeson,D.B.-1966] [Howe,D.A.-2003] [Kester.W-2009] [Demir.A-2000] provided the first insight into the frequency response noise model of oscillators, defining the phase noise power spectral density as a function of the Root Mean Square of the frequency deviation (inversely related to the Cycle Jitter).

With the aim to define the phase noise of a component (usually oscillators and PLLs) the manufacturers of those components provide some values for the phase noise power spectrum at some given frequencies in a magnitude called dB_C/Hz. These values correspond to amplitude difference with the carrier spectral peak (the C in the subscript) per frequency offset from the central frequency (that is the frequency corresponding to the power spectrum peak). Figure 3.4.2 shows this concept over a simulated power spectrum corresponding to a noisy carrier centred at a frequency f_0 . The phase noise is represented by the widening of the spectral peak (a $\delta(t)$ ideally) and the red area represents the noise contributed by the noise at frequency f_m .

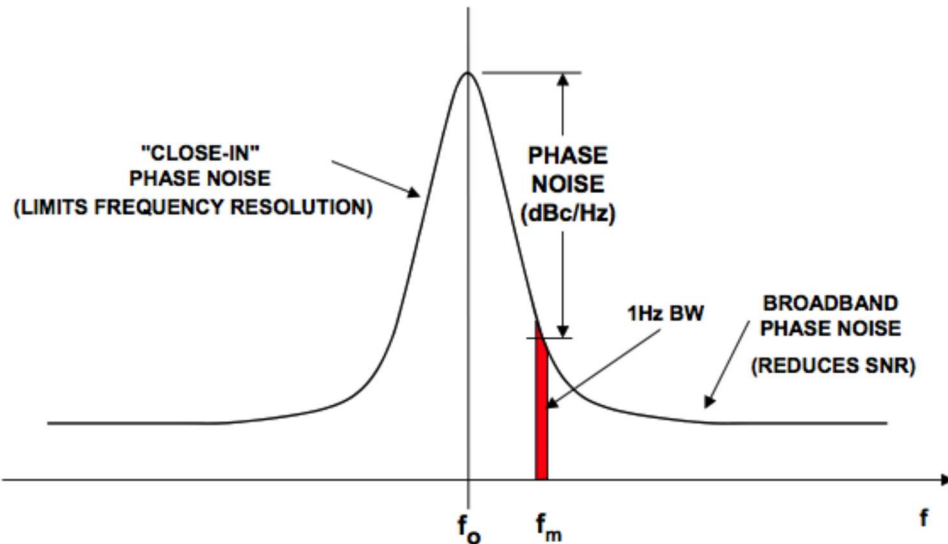


Figure 3.4.2.- Power spectrum of a carrier tone with phase noise which produces a stretching of the spectrum around the central frequency f_0 (Source Analog Devices [Kester.W-2009])

To understand the convenience of this definition, let's represent the jitter signal, $\theta(t)$, as a part of the phase of a carrier signal of amplitude A at f_c .

$$c(t) = A \cdot \sin(2\pi f_c t + \theta(t)) = A \cdot \sin\left(2\pi f_c \left(t + \frac{\theta(t)}{2\pi f_c}\right)\right) \quad (3.4.9)$$

The term $\theta(t)/2\pi f_c$ represents the period time jitter component, that is, the time that is added to each theoretical period as a consequence of the phase noise in a way that the signal repeats not at multiples of T_c (nT_c) but at $nT'_c = nT_c + \theta(nT_c)$.

We can express the signal by applying trigonometric identities as:

$$c(t) = A \cdot \sin(2\pi f_c t) \cdot \cos(\theta(t)) + A \cdot \cos(2\pi f_c t) \cdot \sin(\theta(t)) \quad (3.4.10)$$

Since the jitter phase component $\theta(t)$ is very small compared to the main phase term $2\pi f_c$ for each time t , the signal expression can be written assuming that:

$$\text{If } \theta(t) \ll \forall t \text{ then } c(t) \approx A \cdot \sin(2\pi f_c t) + A \cdot \theta(t) \cdot \cos(2\pi f_c t) \quad (3.4.11)$$

This expression is important because it denotes that, if the jitter phase shift is small, the signal can be expressed as the addition of two terms:

$$c(t) \approx x_c(t) + j(t) \quad (3.4.12)$$

Here $x_c(t) = A \cdot \sin(2\pi f_c t)$ represents the pure tone without any phase noise component and $j(t) = A \cdot \theta(t) \cdot \cos(2\pi f_c t)$ represents the jitter phase noise now modulating a tone with f_c as the central frequency. This identity has an important consequence in the frequency spectrum domain. If we consider its Fourier transform:

$$\begin{aligned} C(f) &\approx X_c(f) + J(f) \\ C(f) &\approx \frac{A}{2i} (\delta(-f_c) - \delta(f + f_c)) + \Theta(f) \\ &\quad * \frac{A}{2} (\delta(f - f_c) + \delta(f + f_c)) \end{aligned} \quad (3.4.13)$$

Here the Jitter spectrum component can be expressed, due to the convolution properties, as:

$$J(f) = \frac{A}{2} (\Theta(f - f_c) + \Theta(f + f_c)) \quad (3.4.14)$$

That is, the Fourier transform of the jitter component, multiplied by the half of the amplitude ($A/2$) and shifted to $+f_c$ and $-f_c$ because of the modulation. Considering the Power Spectral Density (i.e. Power spectrum as seen in a spectrum analyser), the Power Spectrum of $c(t)$ yields:

$$S_c(f) = \frac{A^2}{4} [\delta(f - f_c) + \delta(f + f_c)] + \frac{A^2}{4} [S_\theta(f - f_c) + S_\theta(f + f_c)] \quad (3.4.15)$$

Where $S_\theta(f)$ is the Power Spectrum of the phase signal $\theta(t)$, $S_\theta = |\Theta(f)|^2$.

On the other hand, and applying the Parseval Theorem, we can calculate the Energy of the signal known its power spectrum distribution, that in a random process equals the mean square value and, in this specific case, its variance:

$$\langle \theta(t) \rangle^2 = 2 \int_0^{\infty} S_\theta(f) df \quad (3.4.16)$$

The problem of calculating the maximum period error is solved once we have obtained the mean square of the jitter distribution, and it seems to be achievable observing the power spectrum of the phase-noisy signal since it includes information of the power spectrum of the jitter signal $\theta(t)$ in an additive way, as shown above in Equation 3.4.16.

In fact, this is the most usual method to calculate (and to characterize) phase noise in electronic oscillators since to obtain the power spectrum of $\theta(t)$, once removing the carrier frequency, is very straightforward. Just consider measuring the spectrum power amplitude from frequencies starting at f_c in order to compensate the frequency shift produced by the modulation of the phase noise component, and mixing the signal $S_c(f)$ with a high spectral purity carrier at the same frequency f_c and amplitude, and filtering the lower component we have a power spectrum corresponding with the phase noise, with frequencies referred to zero but initially offsetting the carrier frequency and compensated in amplitude by $4/A^2$, this is funded on the fact that:

$$10 \operatorname{Log} \left(\frac{A^2}{4} \cdot S_{\theta}(f') \right) = 10 \operatorname{Log} \left(\frac{A^2}{4} \right) + 10 \operatorname{Log}(S_{\theta}(f')) \quad (3.4.17)$$

Here $f' = f + f_c$.

Therefore, the spectrum related only to the jitter component can be calculated as:

$$10 \operatorname{Log}(S_{\theta}(f)) = 10 \operatorname{Log} \left(\frac{A^2}{4} \cdot S_{\theta}(f) \right) - 10 \operatorname{Log} \left(\frac{A^2}{4} \right) = L(f)_{dBc} \quad (3.4.18)$$

This spectrum is usually named $L(f)$, and given in magnitudes of dBc/Hz for (offset) frequencies separated by growing order of logarithmic magnitudes (1 Hz, 10Hz, 100 Hz, etc.). Figure 3.4.3 shows a representation of such spectrum.

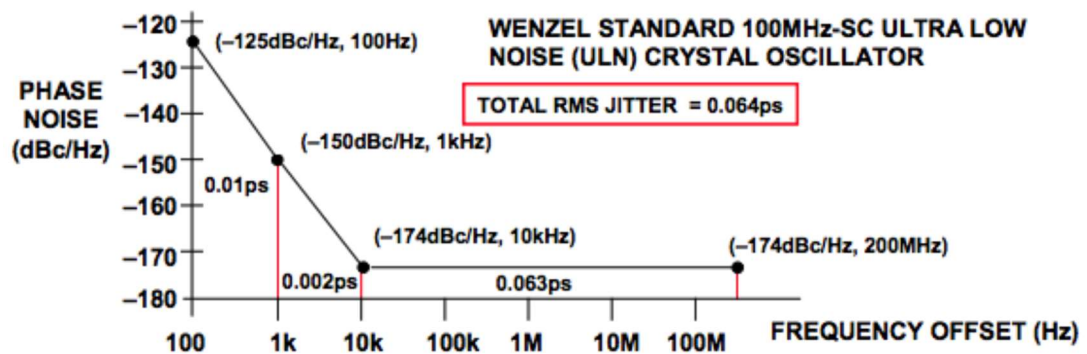


Figure 3.4.3.- Jitter power spectrum as specified by a crystal oscillator manufacturer, and estimation of RMS jitter. [Kester.W-2009].

The normal procedure is to use the phase noise spectrum to estimate the integral of the spectrum with the areas of the polygons formed by the discrete spectral values given by the manufacturer. In this way, the estimation of the RMS jitter, and hence the value of the typical deviation is obtained.

In order to approximate the worst case for the period measurement, that is the maximum error in measuring the frequency and hence the Doppler component, we consider the $3 \cdot \sigma$ value to calculate the period error, which corresponds to 99,97% of the possible error values.

Considering time-related parameters, and considering the implementation of ranging RF frames described in section 3.2 (see Figures 3.2.2 and 3.2.3), the most relevant sources of error and uncertainty in the measurement of Time-Of-Arrival are:

1. **Thermal Noise:** The influence of thermal noise as a contributor of noise in the measurement of Time-Of-Arrival both in One-Way and Two-Ways configuration has already been studied in literature references aiming to determine the CRBL for the variance of the Time-Of-Arrival of ranging RF pulses in presence of White noise [Dogandzic, A.-2001] [Lanzisera-2006] [Thorbjornsen,N.-2010].

As explained above, the CRLB expresses the lower value of the variance of an unbiased estimator, this time the Time-Of-Arrival noise variance caused by the thermal noise. Assuming that the thermal noise (White from the frequency spectrum point of view) introduce a noise source in the determination of time from edge to edge, the variance of the uncertainty in the determination of the TOA is defined [Lanzisera-2006] [Thorbjornsen,N.-2010] for a Two-Ways scenario by:

$$\sigma_{TOA}^2 \geq \frac{1}{2 \cdot (2\pi B_w)^2 \text{SNR} \cdot N} \quad (3.4.19)$$

Here B_w is the bandwidth of the RF signal travelling from tracking station to mobile node, used for Time-Of-Arrival measurement, SNR is the Signal-to-Noise ration and N is the number of samples used to calculate the TOA by averaging. The Cramer-Rao variance for range can be calculated from the TOA CRLB as $\sigma_R^2 = c \cdot \sigma_{TOA}^2$ being c the speed of light in vacuum (299.792.458 m/s).

One-Way scenario is obtained directly from Equation 3.4.19 simply multiplying by 2 the CRLB expression.

2. **Clock synchronization** between tracking stations and mobile node, the lack of synchronization would introduce errors in the measurement of the total Time-Of-Arrival as discussed in section 2.1 (see Figure 3.1.1).

As explained above, the distance from tracking station T_i to the mobile node can be determined as $R_{i1} = c \cdot \Delta t_{i1}$ where R_{i1} is the aforementioned distance and $\Delta t_{i1} = t_{Rx} - t_{Tx}$ is the Time of Flight of the pulse signal. Considering clock desynchronization, the expression for the Time of Arrival can be reformulated as:

$$\Delta t'_{i1} = t_{Rx} - (t_{Tx} + \Delta t_d) \quad (3.4.20)$$

Here Δt_d is the time phase difference between tracking station and mobile node clocks. Therefore, the TOA is the result of adding the TOF with the phase difference as a result of the desynchronization of both clock sources. In One-Way, this problem will persist unless a strong synchronization of both clock sources is implemented (i.e. with atomic clocks), which would be extremely expensive in mass and power. Some procedures or techniques can be implemented to compensate the desynchronization delay, for example [Thorbjornsen,N.-2010] proposes the use of an RF network for synchronization and the use of ultrasound waves for the range measurement, in order to use a slower signal that could be measured by longer time base. A possible method for our scenario could consist in the calibration of the Δt_d by means of the range measurement in a known position in the ground, at a known distance to the tracking stations, this way $\Delta t_{i1} = t_{Rx} - t_{Tx}$ should be known in advance and $\Delta t'_{i1} = t_{Rx} - t_{Tx} + \Delta t_d$ should yield information only about Δt_d .

In Two-Ways, the Time of Arrival could be formulated as a function of total Time-Of-Transit (TOT) for the location frame messages, including the synchronization delay Δt_d to the reception and transmission times at the mobile node side:

$$\begin{aligned} \Delta t_{TOT} &= t_{Rx} - t_{Tx} - (t'_{Rx} + \Delta t_d - t'_{Tx} - \Delta t_d) \\ &= t_{Rx} - t_{Tx} - (t'_{Rx} - t'_{Tx}) = \Delta t_{TOA} - \Delta t_{TOP} \end{aligned} \quad (3.4.21)$$

As it can be appreciated, the synchronization delay terms Δt_d disappears in the equation since the time information is fully differential, assumed by the time differences Δt_{TOA} and Δt_{TOP} , therefore the clock desynchronization has no effect in Two-Ways ranging mode.

3. **Multipath interference.** Multipath propagation can introduce a relevant error in the Time-Of-Arrival measurement since the signal received both at mobile node and tracking station is contributed by the reflected signal, which covers a longer distance. Figure 3.4.4 shows the multipath propagation case for the exploration scenario under consideration.

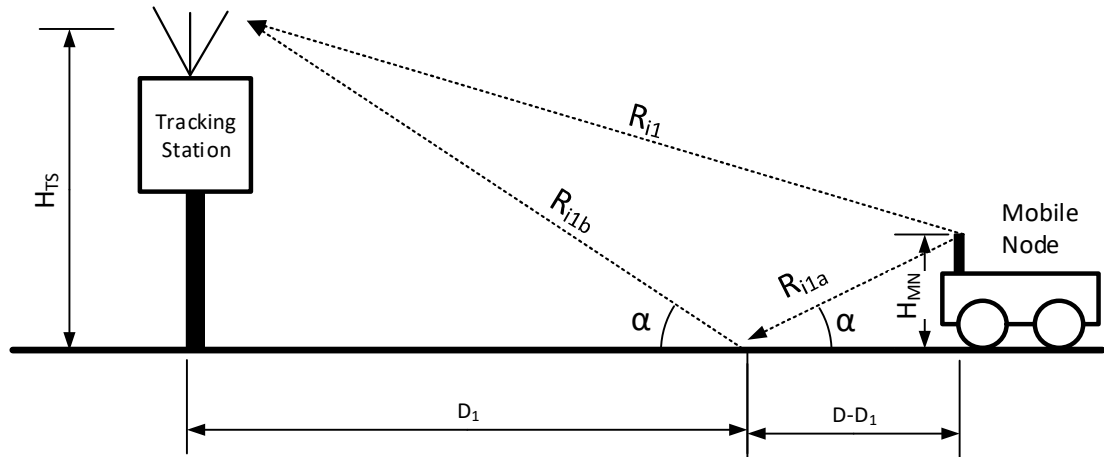


Figure 3.4.4.- Multipath propagation case for the exploration scenario, considering the mobile node and a tracking station.

As it can be appreciated in Figure 3.4.4, multipath interference is produced by the simultaneous reception of the signal travelling along its direct path (represented as R_{i1}) and the reflected one (represented by $R_{i1a} + R_{i1b}$). The reflected path is determined by the Fresnel equations of reflection which impose that the incident and reflection angle is the same (α), therefore:

$$D_1 = D \cdot \frac{H_{TS}}{H_{TS} + H_{MN}} \quad (3.4.22)$$

Having the relation between D_1 and D (obtained from the $\tan(\alpha)$) we obtain the expressions for direct (DP) and reflected (RP) path:

$$DP = R_{i1} = \sqrt{D^2 + (H_{TS} - H_{MN})^2} \quad (3.4.23)$$

$$RP = R_{i1a} + R_{i1b} = \sqrt{(D - D_1)^2 + H_{MN}^2} + \sqrt{D_1^2 + H_{TS}^2} \quad (3.4.24)$$

Figure 3.4.5 shows the impact of multipath interference, representing the difference between direct and reflected distances for an average case of having the tracking station antenna at a height of 2m and with a mobile node 20cm and 50cm height. As it can be appreciated, the higher the mobile node (incrementing the distance to ground) the higher the difference between direct and reflected, and the difference of distance (range error in the curve) decreases at a high rate when mobile node and tracking station distance each other at a

range around 50m. Further than 200 in both cases, the difference between direct and reflected path is lower than 2 cm, obtaining a relative error in distance of 0.008% for a mobile node antenna height at 20 cm and of 0.02% for a height of 50 cm.

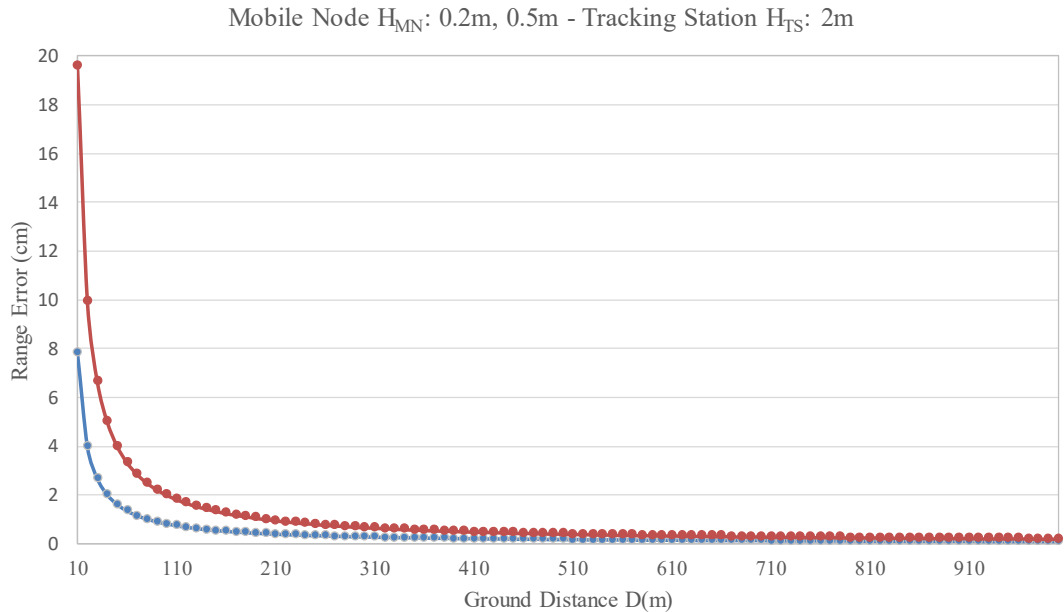


Figure 3.4.5. - Difference between direct and reflected path for a tracking station at 2m and the mobile node antenna at a height of 20cm (blue) and 50cm (red).

The Figure 3.4.6 represents a carrier signal of 400MHz and the same signal with a multipath interference considering the value in Figure 3.4.5 for a mobile node at 20cm (blue plot) at a ground distance of 10m (difference between direct and reflected path) of 7,8cm or 0.26ns time difference in the arrival at tracking station antenna.

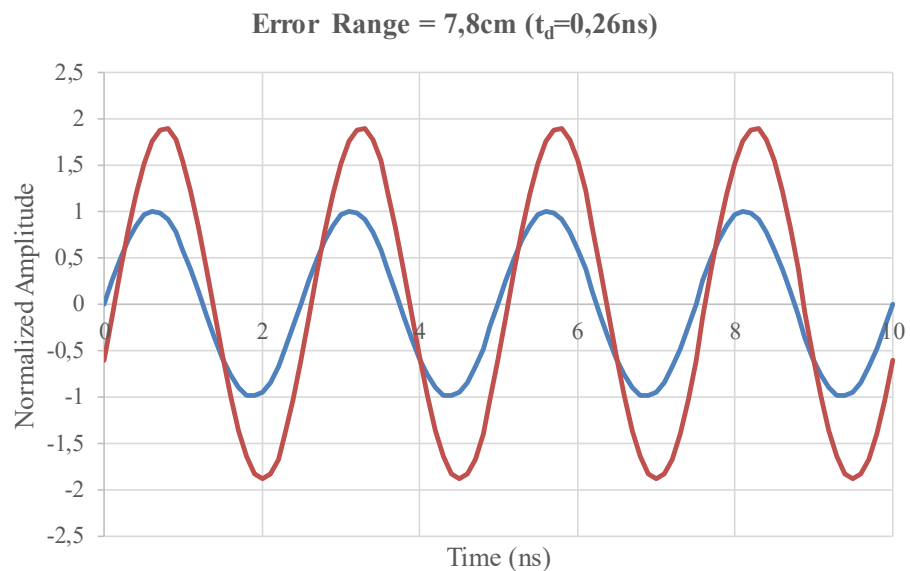


Figure 3.4.6.- Normalized RF 400MHz signal without interference (blue) and with reflected interference (red) at the arrival at tracking station receiver after a difference between direct and reflected paths of 7,8cm.

The aspect of the total signal, that is, the result of adding the direct and reflected components yields a signal corresponding with [McClanning, K.-2011] model for a Two-Rays multipath interference:

$$x_{Rx} = \cos(\omega_0 t) + \rho_1 \cdot \cos(\omega_0 t + \varphi_1) = \beta_1 \cdot \cos(\omega_0 t + \theta_1) \quad (3.4.25)$$

Here:

$$\beta_1 = \sqrt{1 + \rho_1^2 + 2\rho_1 \cos(\varphi_1)} \quad (3.4.26)$$

$$\theta_1 = \tan^{-1} \left(\frac{\rho_1 \sin(\varphi_1)}{1 + \rho_1 \cos(\varphi_1)} \right) \quad (3.4.27)$$

And $\varphi_1 = -\omega_0 \tau_1$ since the reflected signal can be expressed (as included in Equation 3.4.20) in the form $\rho_1 \cdot \cos(\omega_0(t - \tau_1))$ in order to represent the reflected signal as a signal with the same frequency but a shifted phase defined by a delay τ_1 , and with an attenuation defined by the reflectivity coefficient ρ_1 .

Taking the aforementioned model to calculate the error in the determination of the mobile node to tracking station distance, introduced by the addition of the reflected signal, we can represent the results as in the Figure 3.4.7:

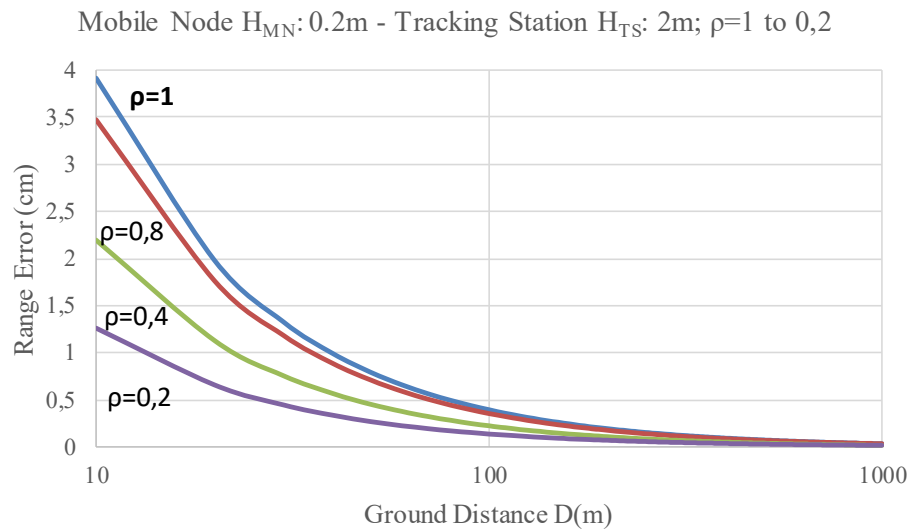


Figure 3.4.7.- Delay τ in received signal introduced by multipath interference for a range of reflectivity coefficient values from $\rho=1$ (total reflection) to $\rho=0,2$. (Ground Distance D is represented in logarithmic scale)

As it can be appreciated, the error introduced by multipath propagation on the scenario under consideration is 0.4% in worst case (maximum reflectance for $\rho=1$), rapidly decreasing to less than 0.02% after 50m. For lower values of reflectance coefficient (according with [ITU-1990] a value of $\rho=0,2$ to 0,1 corresponds to dry ground surface at an angle of incidence $\alpha=12^\circ$ that corresponds to our case when $D=10$ m), the contribution to the error falls

dramatically. Nevertheless, as reported in Section 2.6 in Chapter 2, the reflectivity angle ranges from 0.4 to 0.8 for the reported values of lunar soil characteristics.

Furthermore, it is relevant to observe in Equation 3.4.20 and Figure 3.4.6 that the multipath propagation interference does not affect to the frequency of the original signal, therefore it does not impact on the Doppler frequency shift, mostly because of the close angular separation of the two paths at low height as assumed in this scenario (see Figure 3.4.4).

4. Quantization error: the quantization error models the uncertainty introduced in the system due to the limitations of the data representation and storage of the system compared with the real signals. When the signals under consideration (for example time or frequency) are time-continuous signals, both sampling and truncation of values due to the quantization (that is, the limited representation field of the numeric system used) introduce an error that can be modeled as a White noise source, since the quantization error is strongly uncorrelated with the process under study.

The quantization error in signals is defined by truncation and round off of values due to the limitation in the representation range of numbers, which is implicitly related with the resolution in Bits used to represent the measurements [Lanzisera-2006] [Santina,M.1996] [Oppenheim, A.-2014]. According to this, the effect of signal samples quantization is usually modelled as a White noise source with a variance [Santina,M.1996] of :

$$\sigma_q^2 = \frac{2^{-2C}}{12} \quad (3.4.28)$$

Here C is length of the variables in Bits, that is, 2^C is the maximum range of representation for a word with C Bits, from 0 to 2^C-1 .

On the other hand, [Thorbjornsen,N.-2010] uses an expression of the quantization related with the sampling frequency instead of the representation range. That is correct since the sampling frequency is also directly related with the maximum difference between sampled and real values by the signal value corresponding to the Least Significant Bit (LSB) increment value [Oppenheim, A.-2014], meaning the analog increment in the signal corresponding to a an increment of +1 being:

$$\sigma_q^2 = \frac{T_s^2}{12} \quad (3.4.29)$$

In fact, to deduce the Equation (3.4.29) provided by [Thorbjornsen,N.-2010] is simple considering the normalized nature of Equation (3.4.23). Let us assume that the expression of noise variance provided by (3.4.28) can be also expressed as:

$$\sigma_q^2 = \frac{1}{12 \cdot (2^C)^2} \quad (3.4.30)$$

Here 2^C represents the full representation range for a data word of C Bits (for instance a Byte, being an 8 Bits length word, can represent $2^8 = 256$ numbers, from 0 to 255). The term 2^{-C} represents the increment for 1 LSB, that is, the +1 increment in the least significant

bit, meaning an arithmetic increment of +1 to the number represented in a word of C Bits length, when the full representation range (2^C values from 0 to 2^C-1) is distributed in a normalized value range from 0 to 1. If we need to extend the representation range to another value, for example a period of time that we can denominate T_{FS} (FS is from Full Scale), then the variance should be expressed multiplying the unitary step size by T_{FS} as:

$$\sigma_q^2 = \frac{1}{12} \cdot \left(\frac{T_{FS}}{2^C}\right)^2 \quad (3.4.31)$$

But $T_{FS}/2^C$ is the sampling period T_S , that is, the minimum time sample acquired and, thus, the limit of the precision in time measurement. If we substitute the expression as indicated, the Equation 3.4.24 will be obtained.

3.5. Analysis of Noise Model for the Moon Exploration Scenario.

In this section, the focus of the analysis will be addressed to the noise model of both One-Way and Two-Ways systems, considering the noise sources and contributors described in section 2.4. For this purpose, the different aspects of noise contributors will be analysed and adapted to a specific application case in the Moon exploration scenario under study in this thesis.

From the frequency stability point of view, the main components to be modelled are the crystal oscillators and PLLs as mentioned in the previous sections, with the following assumptions:

- Crystal oscillators base their operation on the piezoelectric and mechanical properties of a vibrating plate, prone to be interfered by electrical and mechanical artefacts, thermoelastic processes and electronic noise sources. Crystal oscillators are the main phase noise source of the system, as well as contributors to frequency shift due to aging and temperature.
- PLLs base their operation on a Voltage Controlled Oscillator (VCO) or Voltage Controlled Crystal Oscillator (VCXO). VCO and VCXOs can be considered as common oscillators, thus generating phase noise, with the peculiarity that they are in the loop of PLLs and thus, the phase noise introduced is limited since it is the gain stage of a closed control loop.
- PLL's phase detector is the main contributor to phase noise since it operates as a N-Integer synthesiser and therefore applies the same multiplying factor to the phase noise components, effectively multiplying the phase noise by the gain.
- PLLs are solid state (semiconductor based) and the ageing and thermal drift effects are negligible compared with to those typical of crystal oscillators.
- Uncorrelated noise sources add in variance, and correlated noise sources add in typical deviation. This has been taken into account to model the total phase noise of the systems.

For the oscillators, the phase noise is determined by the value of RMS jitter obtained by the method specified above (Equation 3.4.9 and method based in phase noise spectrum calculation detailed in Figure 3.4.3).

However for PLLs (a component that is in the core of most frequency synthesizers topologies) the procedure is rather more complex as there are three elements that contribute to the total phase noise within the PLL: the phase noise of the reference input, the phase noise of the VCO or VCXO, and the contribution to the phase noise produced by the internal noise of the phase detector.

In summary, and as the causes contributing to the phase noise in a PLL are uncorrelated, the total phase noise associated to a PLL is, according to:

$$\sigma_T^2 = N^2 \cdot \sigma_S^2 + \frac{N^2}{K_V^2 K_D^2} \sigma_{VCO}^2 + \frac{N^2}{K_D^2} \sigma_{PD}^2 \approx N^2 \cdot \sigma_S^2 \quad (3.5.1)$$

Here σ_T is the Total RMS Jitter, σ_S is the RMS Jitter introduced by the Voltage Controlled Oscillator (VCO), σ_{VCO} is the RMS Jitter introduced by the oscillator at the reference input, σ_{PD} is the RMS jitter introduced by the phase detector, K_V is the gain of the VCO (V/Hz), K_D is the gain of the Charge Pump at the output of the phase detector and N is the PLL multiplying factor.

Considering PLLs for low phase noise applications, such as the Space Qualified parts from Peregrine Semiconductor (PE9701) with a normalized phase detection floor better than 212 dBc/Hz, the high multiplying index involved ($N=40$ for a $F_c=10\text{MHz}$ for UHF case) and the low phase noise of VCXOs together with its low contribution lowered by a factor of $K_V^2 \cdot K_D^2$, the most important contribution to the total phase noise variance is the N^2 multiplying factor.

The contribution to phase noise by the mixers is negligible when compared to the aforementioned elements.

Considering the context of space exploration, we have focused our analysis (see Appendix 3) on space-qualified components, or in their absence, high-reliability and military specification components for the implementation of the prototype. Table 3.5.1 summarizes the preliminary selection of components that helped to define the scenario of available components and their expected performance in terms of frequency stability.

The jitter values have been calculated taking into consideration the total phase noise spectrum and 3-sigma estimation for maximum frequency error. In a first approach the values even for high quality OCXOs seem to be very high, but we have to consider that those values correspond to a statistical set and that averaging procedures have to be considered to reduce noise.

If one considers that the frequency could be determined measuring the duration of a pulse formed by a large number of cycles (N as mentioned above, which in practice could be in the range of 1,000 – 100,000 cycles), dividing this duration by the number of cycles implies a first averaging operation over a large number of samples (i.e. the number of cycles forming the pulse). If we then average a number of period samples, once calculated from successive pulses, this second overlapped averaging process will further reduce the statistical distribution of period estimation values until the target Doppler error is achieved.

Model	Manufacturer	Nominal Freq. f_c (MHz)	L(f) offset (KHz)	σ Jitter (Rad)	σ Jitter (ps)	3σ Jitter (ps)	Δf_D at 3σ (Hz)	Doppler Error ε_D at 3σ (m/s)
OCXO DS 9700	Symmetricon	10	100	3,169E-05	0,5043	1,5130	151,2950	56,4534
OCXO DS 9600QT	Symmetricon	5	100	8,924E-06	0,2841	0,8522	21,3049	7,9496
9960 TCXO	Symmetricon	10	100	0,0003805	6,0557	18,1672	1816,3858	677,7559
RK410 AV OCXO	Rakon	10	10	1,865E-05	0,2968	0,8904	89,0394	33,2236
TE400 OCXO	Rakon	40	10	0,0016964	6,7497	20,2491	32372,2704	12079,2054
LNO 100 OCXO	Rakon	100	100	3,055E-05	0,0486	0,1459	1458,5427	544,2324
TE 300 TCXO	Rakon	10	10	0,0016966	27,0019	81,0057	8094,0107	3020,1532
HT700 TCXO	Rakon	10	100	0,0016964	26,9990	80,9971	8093,1593	3019,8355
QT806-X TCXO	Q-Tech	10	100	0,0095394	151,8245	455,4735	45340,8331	16918,2213
EX209 EMXO	VECTRON	20	100	0,0001	0,7962	2,3885	955,3496	356,4737

Table 3.5.1.- Calculated Jitter values for a set of selected oscillators. (See Appendix 3 for more information)

Table 3.5.2 shows how the phase noise for One-Way utilizing, for instance, a RAKON LNO-100 OCXO improves its phase noise by applying successive averaging after calculating the cycle period from a number of 10.000 cycles sent in the transmission pulse.

Number of Cycles N in Preamble	Duration of Preamble for N cycles (ms)	σ Jitter (ps)	3σ Jitter (ps)	Freq Error (Hz)	400 MHz Synthesis (x4)	Doppler Shift (m/s)
(1= unfiltered)						(2 WAYS case)
1	0,00001	0,0486	0,1458564	1458,542728	5834,170912	2176,929445
1000	0,01	0,001537461	0,004612384	46,12382232	184,4952893	68,84152585
10000	0,1	0,000486188	0,001458564	14,5856379	58,34255159	21,7696088
100000	1	0,000153746	0,000461238	4,61238414	18,44953656	6,884155434
1000000	10	4,86188E-05	0,000145856	1,458563983	5,834255934	2,176961169
2000000	20	1,53746E-05	4,61238E-05	0,461238444	1,844953775	0,688415588
4000000	40	4,86188E-06	1,45856E-05	0,145856395	0,583425581	0,217696112
10000000	100	1,53746E-06	4,61238E-06	0,046123847	0,184495389	0,068841563
20000000	200	4,86188E-07	1,45856E-06	0,014585644	0,058342576	0,021769618

Table 3.5.2.- Calculated phase noise for a One-Way range measurement system utilizing a Rakon LNO-100 OCXO after applying successive averaging for 1000 to $20 \cdot 10^6$ cycles.

As it can be appreciated, with a pulse of 10.000 cycles (which represents a pulse duration of 0,1 ms) the Doppler 3-Sigma error falls to 21.77 m/s for UHF band frequency (400 MHz). If we consider averaging 100 values afterwards, the Doppler measurement precision falls to 2.17 m/s. Finally, for a preamble of $20 \cdot 10^6$ cycles (200ms preamble) the Doppler shift error improves down to 0.022 m/s. Such preamble duration is a normal value for many commercial UHF FSK modulation radio transceivers.

In the One-Way case, and only considering the phase noise, we observe that both RF systems (tracking station and mobile node) are uncorrelated, therefore their respective noise sources variances can be added as their cross-correlation will be zero. The expected phase noise model for One-Way will be:

$$\sigma_T^2 \approx N_1^2 \sigma_{S1}^2 + N_2^2 \sigma_{S2}^2 \quad (3.5.2)$$

Here $N_1^2 \cdot \sigma_{s1}^2$ is the phase noise contributed by the oscillator at the mobile node and $N_2^2 \cdot \sigma_{s2}^2$ is the noise contributed by the down-converting oscillator at the tracking station; being N_1 and N_2 the PLL frequency multiplication factor for mobile node and tracking station respectively.

For the Two-Ways case, considering again the phase noise, the total phase noise model introduces a second oscillator that, though not playing a role towards frequency drift introduces an additional phase noise source in a coherent way, which worsens the total phase noise balance. The expected noise model is:

$$\sigma_T^2 \approx N_1^2 \sigma_{s1}^2 + 4N_2^2 \sigma_{s2}^2 + N_3^2 \sigma_{s1}^2 = (N_1^2 + N_3^2) \sigma_{s1}^2 + 4N_2^2 \sigma_{s2}^2 \quad (3.5.3)$$

Where σ_T^2 is the total phase noise variance corresponding to Two-Ways option. $N_1^2 \cdot \sigma_{s1}^2$ and an $N_3^2 \cdot \sigma_{s1}^2$ are the two frequency synthesis stages at the tracking station (the same oscillator but different multiplication ratio to operate at an IF of 1MHz in Figure 3.3.2) and $2N_2^2 \cdot \sigma_{s2}^2$ corresponds to the contribution of the frequency synthesizer at the mobile node side. The variance in this last case is multiplied by $2 \cdot N^2$ because of the up and down conversion at the mobile node with the same multiplying factor (N), contributing twice to the total variance.

For the system level models, we will first consider the long term frequency drift models for both One-Way and Two-Ways modes. Long term frequency drift is given by an accumulation of ageing and temperature drift, as mentioned above. The frequency bias (i.e. systematic error) introduced by the tolerance of the components will be compensated by calibration and, therefore, its effect will be negligible.

Considering the **One-Way approach**, the frequency drift will be ruled by the superposition of the two drift effects on the Mobile Node and Main Station oscillators that we will name S1 and S2. Therefore, the total drift for One-Way will be:

$$\Delta f_T = N_1 \Delta f_{s1} + N_2 \Delta f_{s2} \quad (3.5.4)$$

Here Δf_{s1} is the frequency drift produced by the Mobile Node oscillator (crystal oscillator plus N_1 multiplying factor on the PLL on Sampler Container) and Δf_{s2} is the drift introduced by the Main Station oscillator.

Oscillator Tracking Station Model	Nominal Freq. f_c (MHz)	PLL Multiplication Factor	T° Drift (ppm)	T° Min (°C)	T° Max (°C)	T° Min Operation (°C)	T° Max Operation (°C)	Thermal Frequency Drift (Hz)
Tracking Station Side:								
RK410 AV OCXO	10	40	0,0002	-30	60	-20	50	0,0622
Mobile Node Side:								
HT700 TCXO	10	40	0,5	-40	85	-20	50	112,0000
Total Freq. Shift (Hz):								112,0622
Total Velocity Thermal Drift (m/s) :								83,6285

Table 3.5.3.- Frequency drifts for One-Way operation mode, for three different cases obtained combining Rakon TE300 TCXO in the Mobile Node and RK410 in the Main Station.

Table 3.5.3 represents some examples of total frequency drifts for One-Way operation mode, for 3 different cases, obtained combining Rakon TE300 TCXO in the Mobile Node and RK410 OCXO in the Main Station (both space grade): Since the drift increments are a result

of the addition of ageing and temperature drift, the calculations were made separately to differentiate between the impact of both drift sources.

For the Two-Ways operation mode, the drift model is slightly different. Since the Mobile Node does not contribute to the overall drift (the oscillator down and up-convert the signal in the same loop, cancelling its contributed drift term), the total drift is only due to the frequency conversion process introduced in the Main Station:

$$\Delta f_T = (N_1 - N_2) \Delta f_{s1} \quad (3.5.5)$$

Where Δf_{s1} is the frequency drift produced by the Main Station oscillator and, N_1 and N_2 are the up and down-conversion multiplying factors applied on the Main Station to make possible the measurement of the Doppler shift component.

In Table 3.5.4, the frequency and subsequent Doppler drift is presented for both TE300 TCXO and RK410 from RAKON considering the Two-Ways scenario, according to the model in Figure 3.5.2.

Oscillator Tracking Station Model	Nominal Freq. f_c (MHz)	PLL Multiplication Factor	Ageing Drift (ppm/Year)	Ageing Drift (Hz/Year)
Tracking Station Side:				
RK410 AV OCXO	10	40	0,01	4
Mobile Node Side:				
HT700 TCXO	10	40	1	400
Total Freq. Shift (Hz):				404
Total Velocity Thermal Drift (m/s) :				301,4925373

Table 3.5.4.- The frequency and subsequent Doppler shift is presented for both TE300 TCXO and RK410 from RAKON considering the Two-Ways scenario.

Once the details for the phase noise are considered for both operation modes (One-Way and Two Ways), a complete noise model can be proposed for each of the aforementioned modes, considering the main noise contributors, that is: phase noise, quantization error noise and thermal noise (defined by the Cramer-Rao lower bound).

In our analysis, as mentioned previously, the analysis will be focused to the short-term stability affected by the noise sources further than the long term stability issues, which can be compensated by calibration or external compensation methods as suggested above.

For the One-Way case, the noise model can be expressed by the diagram in Figure 3.5.1:

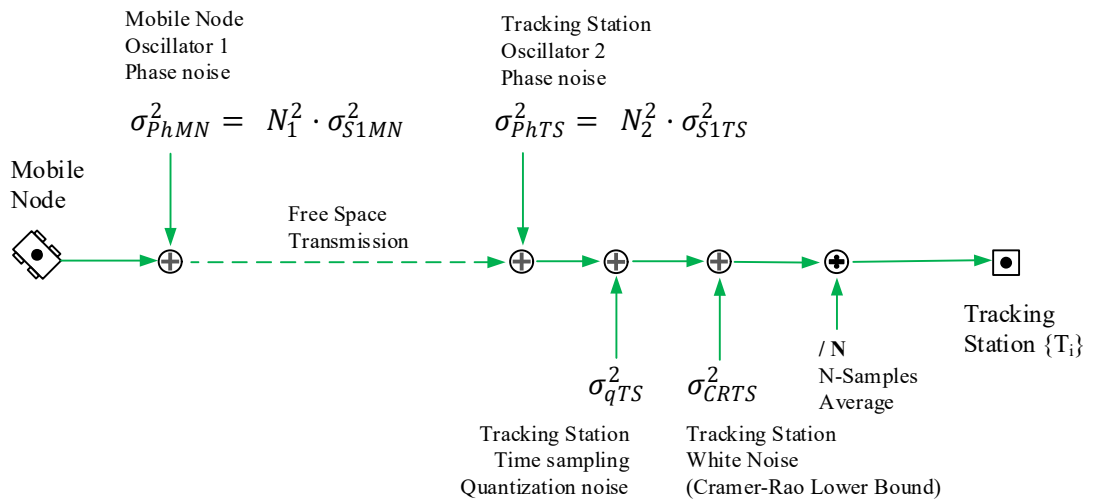


Figure 3.5.1.- One-Way time noise model.

The One-Way mode corresponds to the concept presented in Figure 3.1.1 (up). The mobile node sends a RF localization frame message preceded by a preamble consisting on a carrier signal pulse of N cycles at a specific UHF frequency (401 MHz in our example). The pulse is detected by the tracking station at its first edge and, then, the preamble is processed in order to measure the frequency of the carrier tone. After this process, TOA and frequency of the incoming signal is calculated. The frequency synthesizers at mobile node and tracking station operate at a different frequency as depicted in Figure 3.3.2 (frame signal transmitted at 401MHz from Mobile node and mixed with 400 MHz at tracking station to operate at an IF of 1MHz) therefore, the noise sources include different multiplication factors N_1 and N_2 . In the case of Doppler frequency measurement, the frequency analyzer at the tracking station FPGA measures the frequency of the preamble tone averaging all the cycles in the preamble, which clearly improves the total error variance. In the case of ranging measurement, N will consist in the number of ranging message frames received and averaged to calculate the range. The Equation 3.5.6 expresses the total noise variance corresponding of the model in Figure 3.5.1.

$$\sigma_{T1W}^2 = \frac{(\sigma_{PhMN}^2 + \sigma_{PhTS}^2 + \sigma_{qTS}^2 + \sigma_{CRTS}^2)}{N} \quad (3.5.6)$$

With:

$$\sigma_{PhMN}^2 = N_1^2 \cdot \sigma_{S1MN}^2 \quad (3.5.7)$$

$$\sigma_{PhTS}^2 = N_2^2 \cdot \sigma_{S1TS}^2 \quad (3.5.8)$$

Here: σ_{PhMN}^2 is the phase noise variance (s^2) of the mobile node frequency generator, σ_{PhTS}^2 is the phase noise variance (s^2) of the tracking station frequency generator, σ_{qTS}^2 is the quantization noise (s^2) at the tracking station frequency measurement system and σ_{CRTS}^2 is the Cramer-Rao lower limit (s^2) variance associated to the thermal noise at tracking station measurement system. The table 3.5.5 summarizes the calculation and values for the case under study, for the different terms in Equation 3.5.6, of the One-Way total variance for range and Doppler frequency shift measurement.

Equation Term	Assumptions	Variance Value
$\sigma_{PhMN}^2 = N_1^2 \cdot \sigma_{S1MN}^2$	Oscillator: TE400 TCXO (Rakon) $f_c=40$ MHz; $N_1=10.025$ $\sigma_{S1MN}^2 = 45.558$ ps ²	$\sigma_{PhMN}^2 = 4578.607$ ps ² = $4.578 \cdot 10^{-3}$ ns ²
$\sigma_{PhTS}^2 = N_2^2 \cdot \sigma_{S1TS}^2$	Oscillator: LNO100 OCXO (Rakon) $f_c=100$ MHz; $N_2=4$ $\sigma_{S1TS}^2 = 0.00236$ ps ²	$\sigma_{PhTS}^2 = 0.03776$ ps ² = $3.776 \cdot 10^{-8}$ ns ²
$\sigma_{qTS}^2 = \frac{1}{12} \cdot \left(\frac{T_{FS}}{2c}\right)^2 = \frac{T_s^2}{12}$	$f_s = 300$ MHz Sampling Freq. $T_s = 3.33$ ns	$\sigma_{qTS}^2 = 0.925$ ns ²
$\sigma_{CRTS}^2 = \frac{1}{(2\pi B_w)^2 SNR}$	$B_w = 2$ MHz SNR=40dB (experimental)	$\sigma_{CRTS}^2 = 0.63$ ns ²
N	<u>Doppler Frequency Measurement:</u> N= $100 \cdot 10^3$ cycles (samples) Preamble $T_p = 100$ ms	$N_{Doppler} = 100 \cdot 10^3$
σ_{T1W}^2	Total One-Way time noise variance for Doppler Frequency shift determination	$\sigma_{T1W}^2 = 15.610$ ps² $1,56 \cdot 10^{-5}$ ns²
N	<u>TOA Range Measurement:</u> N=10 Samples Range determ. Period= 10×100 ms= 1s	$N_{Range} = 10$
σ_{T1W}^2	Total One-Way time noise variance for range determination	$\sigma_{T1W}^2 = 1.56 \cdot 10^5$ ps² 0.156 ns²

Table 3.5.5.- One-Way total time noise variance for range and Doppler Frequency shift measurement.

The Two-Ways time noise model is represented in Figure 3.5.2.

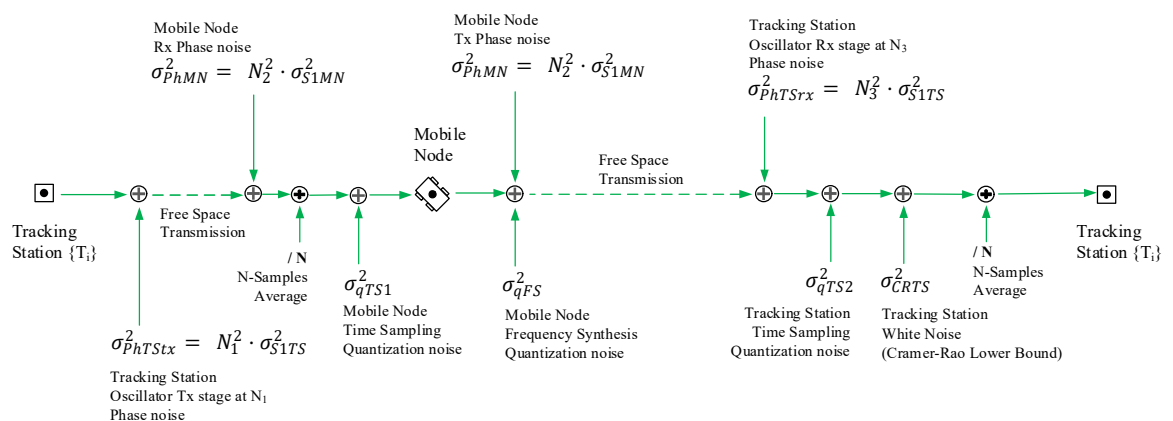


Figure 3.5.2.- Two-Ways noise model.

The Two-Ways mode corresponds to the concept presented in Figure 3.1.1 (down). In this case, the tracking station sends a RF localization frame message preceded by a preamble

consisting on a carrier signal pulse of N cycles at a specific UHF frequency (401 MHz in our example). The pulse is detected by the mobile node at its first edge, time tagged internally with the mobile node time base and the preamble is processed in order to measure the frequency of the incoming carrier tone. Afterwards, the mobile node frequency synthesizer generates the frame signal at the receiver frequency, although with the limitation of the PLL quantization resolution, which is transmitted back to the tracking station.

Once received by the tracking station, the signal is demodulated with a local oscillator frequency of 400 MHz and, once in IF (1 MHz) the frame start (first edge of the preamble) is detected and time tagged, and the incoming frequency measured again during the preamble. The mobile node processing time (difference between transmission time tag and reception time tag at mobile node) is transmitted as a part of the location frame data payload. This value is used to compute the Time-Of-Arrival from the total Time-Of-Transit that, together with the frequency shift, position and radial velocity information is obtained.

The Equation 3.5.9 expresses the total noise variance corresponding of the model in Figure 3.5.2.

$$\sigma_{T2W}^2 = \frac{\left(\frac{(\sigma_{PhTSt}^2 + \sigma_{PhMN}^2)}{N} + \sigma_{qTS1}^2 + \sigma_{PhM}^2 + \sigma_{qFS}^2 + \sigma_{PhTSr}^2 + \sigma_{qTS2}^2 + \sigma_{CRTS}^2 \right)}{N} \quad (3.5.9)$$

With:

$$\sigma_{PhTStx}^2 = N_1^2 \cdot \sigma_{S1TS}^2 \quad (3.5.10)$$

$$\sigma_{PhMN}^2 = N_2^2 \cdot \sigma_{S1MN}^2 \quad (3.5.11)$$

$$\sigma_{PhTSrx}^2 = N_3^2 \cdot \sigma_{S1TS}^2 \quad (3.5.12)$$

Here: σ_{PhMN}^2 is the phase noise variance (s^2) of the mobile node frequency generator, σ_{PhTStx}^2 is the phase noise variance (s^2) of the tracking station transmitter frequency generator, σ_{PhTSrx}^2 is the phase noise variance (s^2) of the tracking station receiver frequency generator, σ_{qTS1}^2 is the quantization noise (s^2) at the mobile node frequency measurement system, σ_{qFS1}^2 is the quantization noise (s^2) at the mobile node frequency generation system, σ_{qTS2}^2 is the quantization noise (s^2) at the tracking station frequency measurement system and σ_{CRTS}^2 is the Cramer-Rao lower limit (s^2) variance associated to the thermal noise at tracking station measurement system.

The next table summarizes the calculation and values for the case under study, for the different terms in Equation 3.5.9, of the Two-Ways total variance for range and Doppler frequency shift measurement.

Equation Term	Assumptions	Variance Value
$\sigma_{PhTStx}^2 = N_1^2 \cdot \sigma_{S1TS}^2$	Oscillator: LNO100 OCXO (Rakon) $f_c=100$ MHz; $N_1=4,01$ $\sigma_{S1MN}^2 = 0.00236$ ps ²	$\sigma_{PhTStx}^2 =$ 0.0379 ps ² = $3.795 \cdot 10^{-8}$ ns ²
$\sigma_{PhMN}^2 = N_2^2 \cdot \sigma_{S1MN}^2$	Oscillator: TE400 TCXO (Rakon) $f_c=40$ MHz; $N_2=10$ $\sigma_{S1MN}^2 = 45.558$ ps ²	$\sigma_{PhMN}^2 =$ 4555.8 ps ² = $4.556 \cdot 10^{-3}$ ns ²
$\sigma_{qTS1}^2 = \frac{1}{12} \cdot \left(\frac{T_{FS}}{2C}\right)^2 = \frac{T_s^2}{12}$	$f_s = 300$ MHz Sampling Freq. $T_s = 3.33$ ns	$\sigma_{qTS1}^2 = 0.925$ ns ²
$\sigma_{qFS1}^2 = \frac{1}{12} \cdot \left(\frac{T_{FS}}{2C}\right)^2 = \frac{T_s^2}{12}$	$f_s = 300$ MHz Sampling Freq. $T_s = 3.33$ ns	$\sigma_{qFS1}^2 = 0.925$ ns ²
$\sigma_{PhTSrx}^2 = N_3^2 \cdot \sigma_{S1TS}^2$	Oscillator: LNO100 OCXO (Rakon) $f_c=100$ MHz; $N_3=4,01$ $\sigma_{S1MN}^2 = 0.00236$ ps ²	$\sigma_{PhTSrx}^2 =$ 0.0379 ps ² = $3.795 \cdot 10^{-8}$ ns ²
$\sigma_{qTS2}^2 = \frac{1}{12} \cdot \left(\frac{T_{FS}}{2C}\right)^2 = \frac{T_s^2}{12}$	$f_s = 300$ MHz Sampling Freq. $T_s = 3.33$ ns	$\sigma_{qTS2}^2 = 0.925$ ns ²
$\sigma_{CRTS}^2 = \frac{1}{(2\pi B_w)^2 SNR}$	$B_w = 2$ MHz SNR= 40dB (experimental)	$\sigma_{CRTS}^2 = 0.63$ ns ²
N	<u>Doppler Frequency Measurement:</u> N= $100 \cdot 10^3$ cycles (samples) Preamble $T_P = 100$ ms	$N_{Doppler} = 10 \cdot 10^3$
σ_{T2W}^2	Total Two-Ways time noise variance for Doppler Frequency shift determination	$\sigma_{T2W}^2 =$ $3.409 \cdot 10^{-5}$ ns ² = 34.091 ps ²
N	<u>TOA Range Measurement:</u> N=10 Samples Range determ. Period= 10×100 ms= 1s	$N_{Range} = 10$
σ_{T2W}^2	Total Two-Ways time noise variance for range determination	$\sigma_{T2W}^2 =$ 0.341 ns ² = $3.41 \cdot 10^5$ ps ²

Table 3.5.6.- Two-Ways total time noise variance for range and Doppler Frequency shift measurement.

Both in One-Way and Two-Ways modes, the thermal (White) noise modelled by the Cramer-Rao Lower Bound limit and the quantification noise are relevant instability contributors. The main consideration here is motivated by the quantization noise dependence on the sampling frequency. The Figure 3.5.3 below illustrates the Cramer-Rao lower limit for the thermal noise for the conditions defined in the One-Way and Two-Ways cases explained above (tables 3.5.5 and 3.5.6 respectively), compared with the quantization noise related with a sampling frequency ranging from 100 MHz to 1GHz.

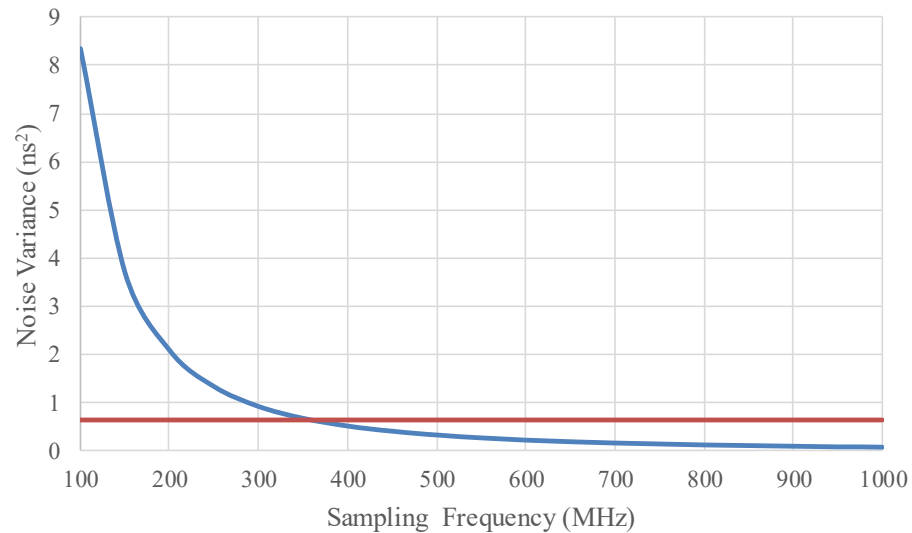


Figure 3.5.3.- Cramer-Rao lower bound limit for thermal noise (red) and quantization noise (blue) plots.

As it can be appreciated, there is a sampling frequency value from which the quantization noise is less relevant than the lower limit of thermal noise (in the plot of Figure 3.5.3, around 300 MHz). The higher the frequency band allowed for a given SNR, the lower the Cramer-Rao lower limit noise variance, but also the higher the sampling frequency required to take measures at a low quantization noise.

Following this plot, and considering Equations 3.4.19 and 3.4.24, an expression could be obtained to calculate the sampling frequency limit as the intersection of both plots in Figure 3.5.3:

$$f_s = 2\pi B_w \sqrt{\frac{SNR}{12}} \quad (3.5.13)$$

The Equation 3.5.13 can be used to calculate the limit sampling frequency for a given SNR and bandwidth of the RF signal. In particular, for the case under consideration with SNR=40dB and $B_w=2$ MHz, the minimum sampling frequency for the quantization noise to be below the Cramer-Rao lower limit is 362,75 MHz, which represents a sampling frequency quite high for most space grade components, although within the range of commercial signal sampling products, such as high speed ADCs, that reach sampling rates in the order of 1GHz.

Considering our implementation case, which will be discussed later, the logic system is based in a logic programmable device (PROASIC 3 FPGA from Microsemi), which has a maximum operation clock frequency of 400MHz. The selection of this device is motivated by the fact that it is also available in Space-Grade and Military versions, and has a strong heritage in Space mission.

Although the upper frequency limit is above the minimum sampling frequency calculated above (362.75 MHz), practical limitations pose an operation limit of 300 MHz (basically due to limitations in the internal circuitry of the logic block after routing), which is finally defined as the time sampling frequency.

Comparing the noise performance of One-Way and Two-Ways methods in the tables 3.5.5 and 3.5.6, the most noticeable fact is the impact of quantization and thermal noise in the balance compared with clock phase noise and other factors. In fact, with the proposed sampling scheme, those noise contributors are highly dominant in both methods, until the point that the noise in Two Ways is mostly incremented due to the different sampling and quantization processes, representing an increment around 55% with respect to One-Way. The impact will be much more dramatic in Doppler frequency shift measurement than in range determination due to the ratio between the time involved and the amount of noise (i.e. typical deviation).

In order to analyze the impact of noise in range and Doppler frequency shift measurement, a number of MATLAB scripts and functions have been implemented in order to complement the scripts and simulation process described in Chapter 2 Section 2.5 with the objective of adding noise to Range and Doppler Frequency shift, allowing the analysis of the impact of such noise in the determination of position and velocity.

Figure 3.5.4 shows the simulation diagram including the introduction of noise by means of the MATLAB functions *DopplerNoise()* and *RangeNoise()*. These functions use the Range and Doppler shift vectors generated by *RangeCalc_VN()*, introducing time noise with a specific variance in ns^2 . The sequence of this model has been coded in the MATLAB script *NoiseModel_script*.

An important result of the simulation of the location and velocity determination model with noise, is the one related with the analysis of the error signal E_{ri1} and E_{di1} , consisting in the error in range and Doppler frequency shifts introduced by the noise in time due to the aforementioned noise sources.

The analysis of this error sources will give relevant information about the contributors to the noise as well as some hidden parameters that are critical for the total noise in the system. The MATLAB script *NoiseModel_script* yields a statistical analysis of the noise vectors E_{ri1} and E_{di1} for $i=1$ to 3 allowing its statistical analysis as Gaussian noise (Gaussian fit and Standard Deviation).

Introducing the variances of table 3.5.5 for One-Way case, the simulation according to the model in Figure 3.5.4 yields the results presented in Figure 3.5.5.

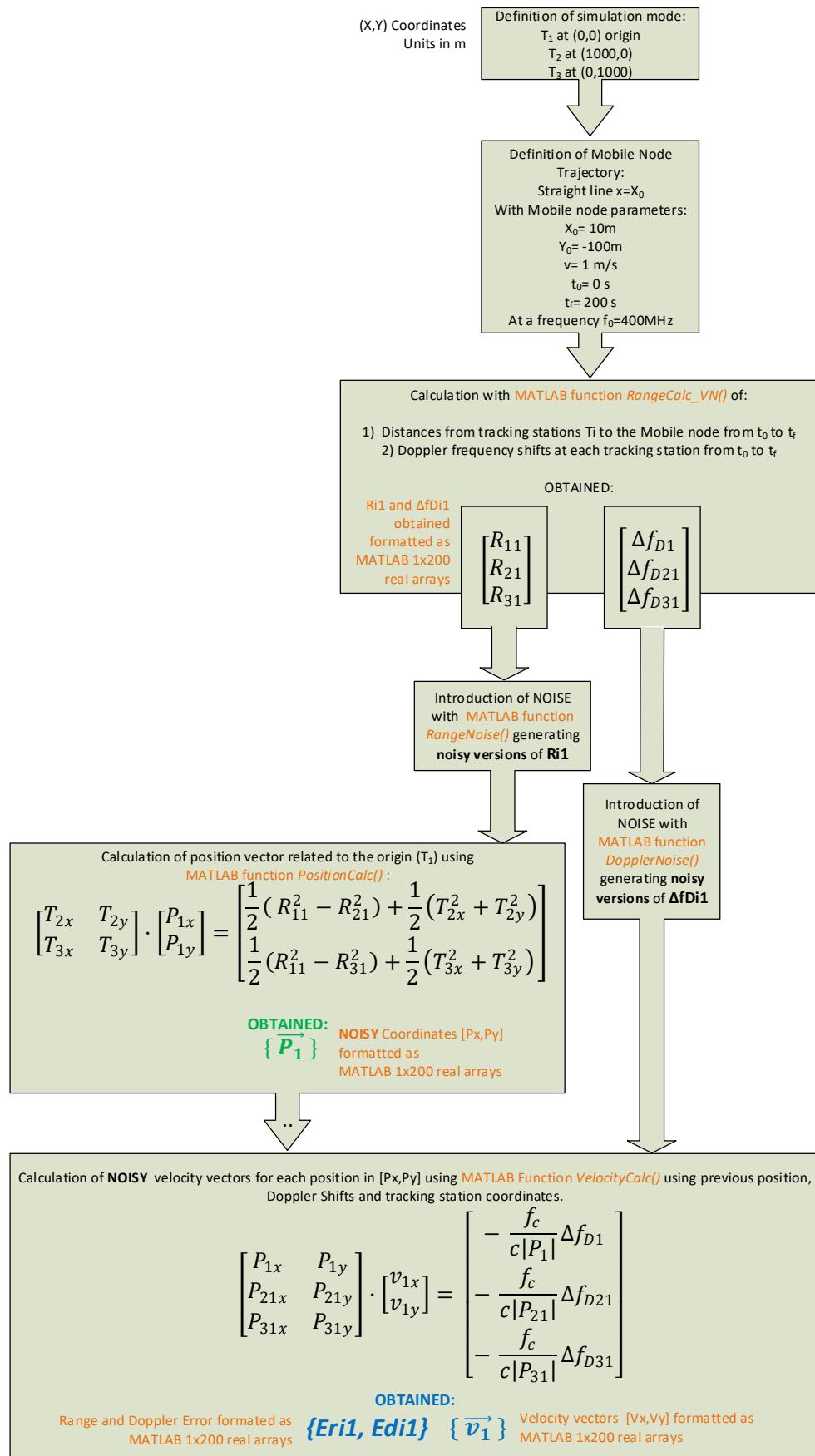


Figure 3.5.4.- Process for the determination of range and Doppler shift introducing Gaussian time noise with a given variance, and the further determination of the position and velocity vector for a mobile node according to a cinematic set of parameters and associated MATLAB functions.

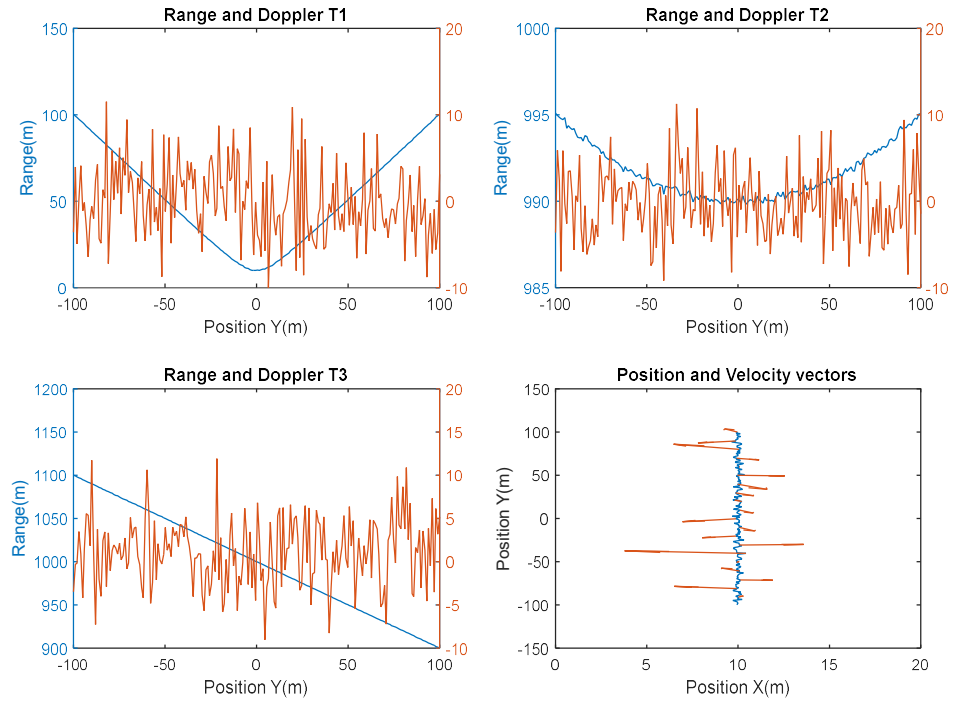


Figure 3.5.5.a- Range and Doppler signals with Position and Velocity reconstruction from noisy signal with noise in range $\sigma_{T1W}^2 = 0.156 \text{ ns}^2$ and Doppler $\sigma_{T1W}^2 = 1.56 \cdot 10^{-5} \text{ ns}^2$. Measured at $f_{IF}=1 \text{ MHz}$.

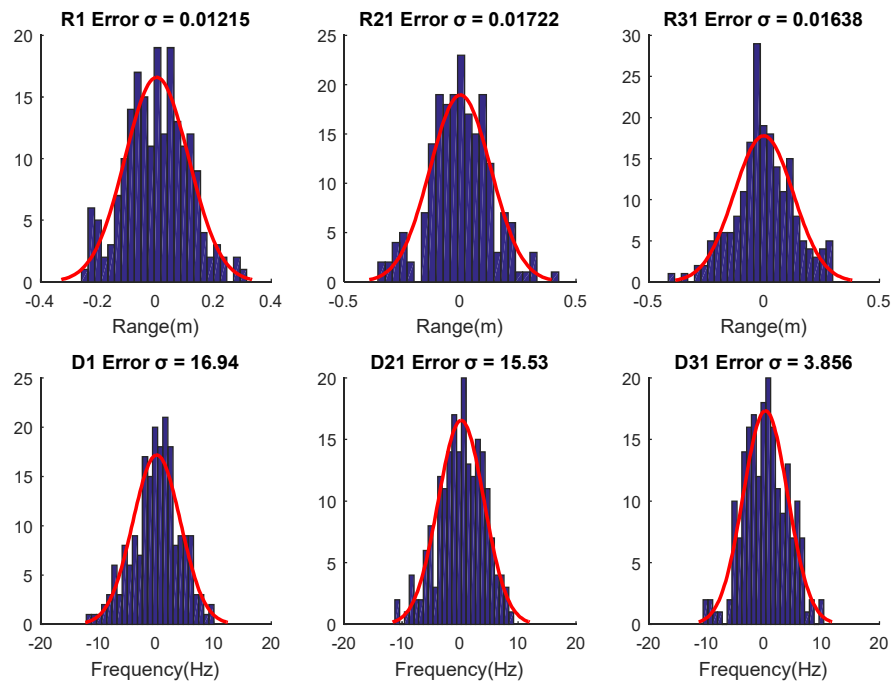


Figure 3.5.5.b- Statistical analysis of Range and Doppler frequency shift error signals E_{ri1} and E_{di1} for noise in range $\sigma_{T1W}^2 = 0.156 \text{ ns}^2$ and Doppler $\sigma_{T1W}^2 = 1.56 \cdot 10^{-5} \text{ ns}^2$. Measured at $f_{IF}=1 \text{ MHz}$.

In this sense, it would be interesting to analyze a case where the IF lowers to 100KHz though keeping the preamble time in the same value of 100ms. If with an IF of 1MHz, a number of $100 \cdot 10^3$ cycles fitted in the 100ms preamble duration, with an IF of 100ms, only 10.000 cycles will fit, therefore, the number of averaging cycles is reduced by 10 (just as the IF frequency). Applying the same simulation parameters except the new IF of 100 KHz and $N=10.000$, we obtain the results shown in Figure 3.5.6.

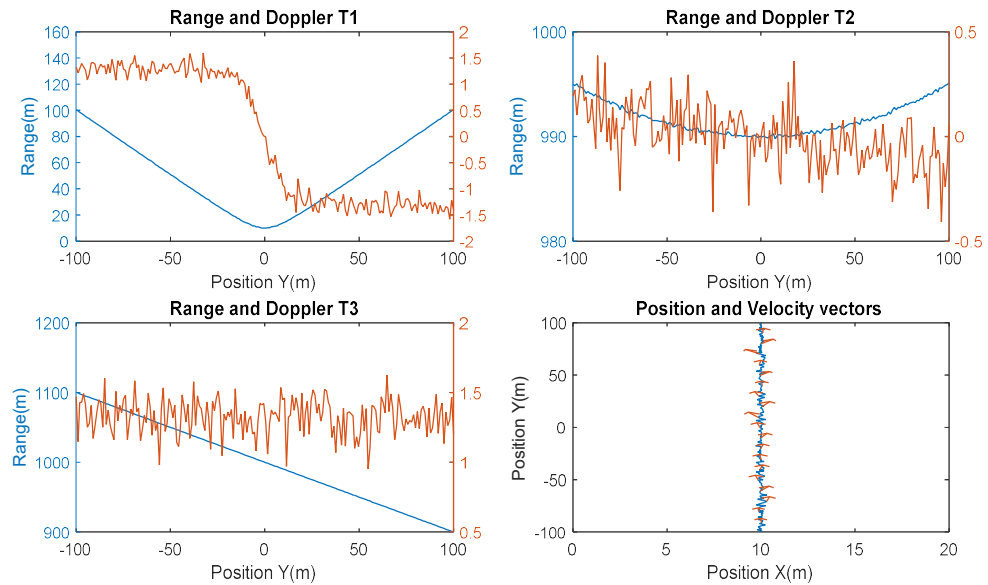


Figure 3.5.6.a- Range and Doppler signals with Position and Velocity reconstruction from noisy signal with noise in range $\sigma_{T1W}^2 = 0.156 \text{ ns}^2$ and Doppler $\sigma_{T1W}^2 = 1.56 \cdot 10^{-4} \text{ ns}^2$. Measured at $f_{IF} = 100 \text{ KHz}$.

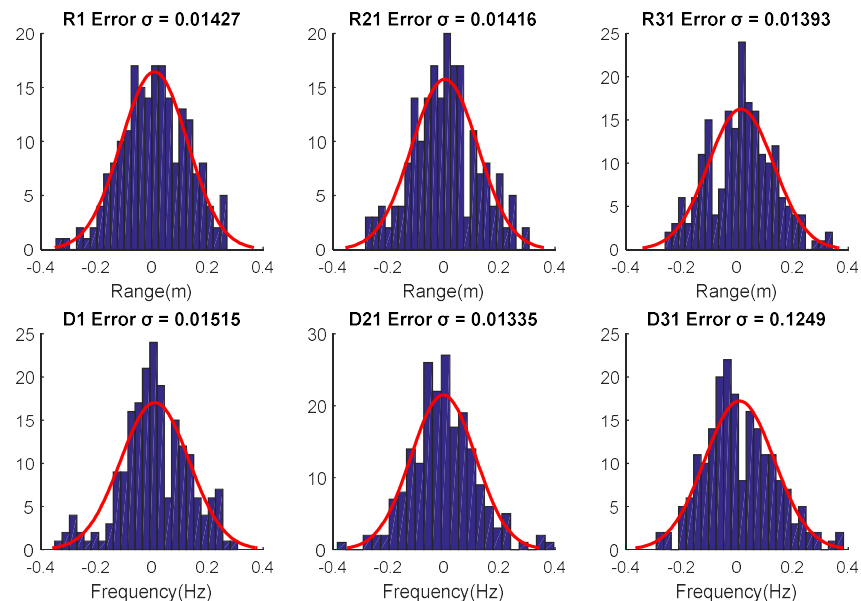


Figure 3.5.6.b- Statistical analysis of Range and Doppler frequency shift error signals E_{ri1} and E_{di1} for noise in range $\sigma_{T1W}^2 = 0.156 \text{ ns}^2$ and Doppler $\sigma_{T1W}^2 = 1.56 \cdot 10^{-4} \text{ ns}^2$. Measured at $f_{IF} = 100 \text{ KHz}$.

The improvement in the noise levels of both range and Doppler signals is very noticeable considering the ideal response depicted in Figure 2.4.13 in Chapter 2 and comparing the typical deviation values of the error distributions in Figure 3.5.6.b with the corresponding histograms in Figure 3.5.5b. The impact of the intermediate frequency might seem counterintuitive in the reduction of noise but it is crucial if we consider the additive nature of the noise sources in time and the property of frequency mixing. When the RF carrier is downshifted to IF by mixing with a local oscillator tone, the RF spectrum selected by the image rejection filter is shifted but preserving the amplitude in time of phase noise and Doppler frequency component. The point is that, the lower the IF frequency, the higher the period where the noise is added in time domain, therefore, the Signal-to-Noise Ratio in time domain is higher and, thus, the averaging much more effective.

To make this concept clear, let us assume a signal with period T_c , generated with an additive Gaussian noise ε_τ . The resulting signal has an instantaneous error frequency expressed by:

$$\varepsilon_f = \frac{1}{T_c} - \frac{1}{T_c + \varepsilon_\tau} = \frac{\varepsilon_\tau}{T_c(T_c + \varepsilon_\tau)} \approx \frac{\varepsilon_\tau}{T_c^2} \quad \{T_c \gg \varepsilon_\tau\} \quad (3.5.14)$$

In our case, T_c is the IF frequency period (added with the Doppler frequency shift, though for this example analysis about the importance of noise versus T_c , we assume it constant and zero). In both examples (Figures 3.5.6 and 3.5.5) we assumed a constant preamble period of 100 ms, therefore, the number of cycles and the IF frequency period are related by the expression $T_p = N \cdot T_c$, which we can replace in Equation 3.5.14 giving:

$$\varepsilon_f \approx N^2 \frac{\varepsilon_\tau}{T_p^2} \quad (3.5.15)$$

Therefore, if N decrements its value by a factor of 10, the noise improves with $N^2 = 100$ as maximum. Depending on the distribution and magnitude of Doppler shift, this improvement would be smaller, but in case of D_{21} and D_1 error, the improvement is applied in this order.

The main problem with this technique consists in managing a very low IF frequency since it should require a very selective and stable image rejection filter; therefore, the implementation of this option is complex in the existing architecture, requiring a more sophisticated RF stage, like an IQ demodulation stage.

The possibility of reducing the system noise increasing the sampling rate, in order to reduce the quantization noise (one of the most important contributors to the total noise) is presented in the table 3.5.7. A Time-to-Digital Converter (TDC) from Texas Instruments with reference TDC7201 is analyzed in the context of the One-Way case. The use of such component, able to sample with a resolution of 55ps, only provides an improvement of 59,3% with respect to the Doppler variance (values in table 3.5.5.)

In conclusion, the reduction of noise by increasing the sampling rate has not a strong influence if thermal noise is not reduced in a similar order. However, to keep a high SNR at a large bandwidth requires very low noise measures for the variance to reach the low levels achieved by the quantization noise once the sampling period has been set to 55ps.

Equation Term	Assumptions	Variance Value
$\sigma_{PhMN}^2 = N_1^2 \cdot \sigma_{S1MN}^2$	Oscillator: TE400 TCXO (Rakon) $f_c=40$ MHz; $N_1=10.025$ $\sigma_{S1MN}^2 = 45.558$ ps ²	$\sigma_{PhMN}^2 =$ 4578.607 ps ² = $4.578 \cdot 10^{-3}$ ns ²
$\sigma_{PhTS}^2 = N_2^2 \cdot \sigma_{S1TS}^2$	Oscillator: LNO100 OCXO (Rakon) $f_c=100$ MHz; $N_2=4$ $\sigma_{S1TS}^2 = 0.00236$ ps ²	$\sigma_{PhTS}^2 =$ 0.03776 ps ² = $3.776 \cdot 10^{-8}$ ns ²
$\sigma_{qTS}^2 = \frac{1}{12} \cdot \left(\frac{T_{FS}}{2c}\right)^2 = \frac{T_s^2}{12}$	$f_s = 18.2$ GHz Sampling Freq. (Effective) $T_s = 55$ ps	$\sigma_{qTS}^2 =$ 252.08 ps ² = $2.52 \cdot 10^{-4}$ ns ²
$\sigma_{CRTS}^2 = \frac{1}{(2\pi B_w)^2 SNR}$	$B_w = 2$ MHz SNR=40dB (experimental)	$\sigma_{CRTS}^2 =$ 0.63 ns ²
N	<u>Doppler Frequency Measurement:</u> N= $100 \cdot 10^3$ cycles (samples) Preamble $T_P = 100$ ms	$N_{Doppler} = 100 \cdot 10^3$
σ_{T1W}^2	Total One-Way time noise variance for Doppler Frequency shift determination	$\sigma_{T1W}^2 =$ 6.35 ps² $6.35 \cdot 10^{-6}$ ns²
N	<u>TOA Range Measurement:</u> N=10 Samples Range determ. Period= 10×100 ms= 1s	$N_{Range} = 10$
σ_{T1W}^2	Total One-Way time noise variance for range determination	$\sigma_{T1W}^2 =$ $6.35 \cdot 10^4$ ps² = 0.0635 ns²

Table 3.5.7.- One-Way total time noise variance for range and Doppler Frequency shift measurement with Time measurement stage based in Texas Instruments TDC7201 ($T_s=55$ ps).

Finally, Table 3.5.7 presents the simulation of the system noise considering only the noise related with oscillators phase noise, removing thermal and quantization noise for both One-Ways and Two-Ways. In One-Way case, the variance values are:

- σ_{T1W}^2 for Doppler frequency shift determination = $4.58 \cdot 10^{-8}$ ns²
- σ_{T1W}^2 for Range determination = $4.58 \cdot 10^{-4}$ ns²

And in Two Ways the variance values are:

- σ_{T2W}^2 for Doppler frequency shift determination = $4.55 \cdot 10^{-8}$ ns²
- σ_{T2W}^2 for Range determination = $5.011 \cdot 10^{-4}$ ns²

The error values are of a similar order. Figure 3.5.7 shows the simulation for the noise model with the Two-Ways case.

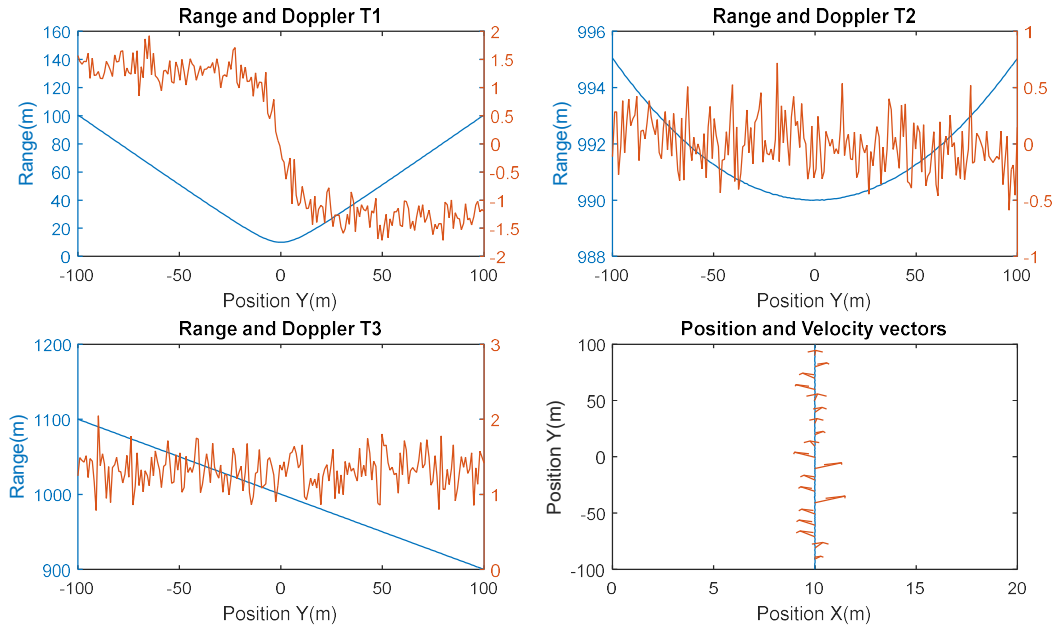


Figure 3.5.7.a- Range and Doppler signals with Position and Velocity reconstruction from noisy signal with noise in range $\sigma_{T2W}^2 = 5.011 \cdot 10^{-4} \text{ ns}^2$ and Doppler $\sigma_{T2W}^2 = 4.55 \cdot 10^{-8} \text{ ns}^2$. Measured at $f_{IF} = 1 \text{ MHz}$.

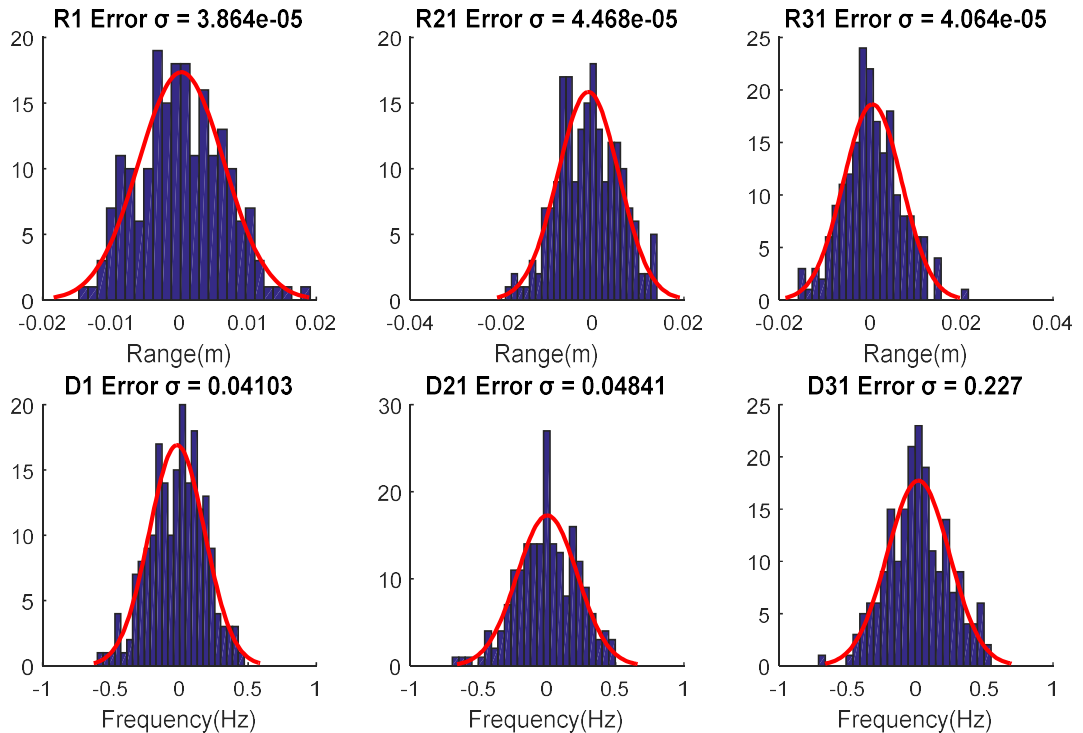


Figure 3.5.7.b- Statistical analysis of Range and Doppler frequency shift error signals E_{ri1} and E_{di1} for noise in range $\sigma_{T2W}^2 = 5.011 \cdot 10^{-4} \text{ ns}^2$ and Doppler $\sigma_{T2W}^2 = 4.55 \cdot 10^{-8} \text{ ns}^2$. Measured at $f_{IF} = 1 \text{ MHz}$.

3.6. Range and Doppler Signals Improvement by Filtering.

Although the simulations above yield quite pessimistic conclusions about the level of noise required to determine position and velocity with a minimum quality, fortunately, there are methods to filter noise from a signal or process if the statistic parameters of the noise affecting the signal under study are known.

From the different prediction techniques available, Kalman Filter (KF) is one of the most efficient from the computational point of view [Santina,M.-1996]. Extended Kalman Filter (EKF) is an enhancement of the simple Kalman Filter to deal with non-linear systems although in this case, the implementation of Kalman Filter is simple since our objective is to use this technique to filter Range and Doppler frequency shift signals.

Kalman Filter is also denominated as a Linear Quadratic Estimator (LQE), that is, a numerical algorithm that uses previous values of a signal to output estimations of future values considering the statistical characteristics of the noise and uncertainties added to the signal being measured. The main advantage of this technique is that it is possible to extract a signal buried in noise without compromising the frequency spectrum of the signal as it happens with conventional filtering [Kumar,A.-2016] [Leśniak, A.-2009]. When it deals for real time applications, the time constant of the signals coming from sensors could be critical, therefore, Kalman Filtering takes a clear application advantage in such cases like, for instance, in autonomous navigation.

Kalman filter is expressed in matrix form since it is designed to predict or estimate state vectors from linear or non-linear (EKF) systems modelled by matrix equations [Saderzadeh,A.-2009]. In our case, the problem only applies to the estimation of a single value, that is, the value of the signal (just as R_{i1} range or D_{i1} Doppler frequency shift signals) for the present state (i.e. current instant of time) from previous values and the characteristics of the noise taking part in the process.

Kalman Filtering is an algorithm applied in two phases, here formulated for one dimension signals, the phases are called Prediction:

$$\hat{x}[n] = a \cdot \hat{x}[n - 1] \quad (3.6.1)$$

$$P[n] = a^2 \cdot P[n - 1] \quad (3.6.2)$$

And Update:

$$K[n] = \frac{P[n]}{P[n] + R} \quad (3.6.3)$$

$$\hat{x}[n] \leftarrow K[n] \cdot x[n] + (1 - K[n]) \hat{x}[n - 1] \quad (3.6.4)$$

$$P[n] \leftarrow (1 - K[n]) \cdot P[n] \quad (3.6.5)$$

Here $\hat{x}[n]$ is the estimated value of $x[n]$ in instant n , $x[n]$ is the measured value in the instant n , a is the theoretic gain of the system (theoretic relation between previous value and present value), R is the variance of the noise entering in the system and $P[n]$ is the prediction error in instant n . $K[n]$ is the Kalman gain, that is, the weighting factor for the influence of the

previous value in the estimation of present one. As it can be noted in Equation 3.6.4, for $K[n]=1$ the assignment yields $x[n]$, that is, the measured value in instant n (like if there is no noise, since for that $R=0$); but for $K[n]=0$ (very noisy system since $R \rightarrow \infty$), then the assignment yields $\hat{x}[n-1]$, that is, the former prediction since there is no information to contribute to the current estimation but the previous one.

A Kalman filter algorithm for the filtering of R_{i1} range or D_{i1} has been implemented in MATLAB as the function *EKalman()*. This algorithm implements the process of Prediction-Estimate for the ranges and Doppler shift values, and afterwards, the output values used to determine position and velocity vectors with *PositionCalc()* and *VelocityCalc()* according to Equations 3.6.1 to 3.6.5. Figure 3.6.1 shows the output of the Kalman Filter implemented in the MATLAB function *EKalman()* for a sinus signal (amplitude=1) and frequency=100Hz with a Gaussian additive noise with variance $\sigma^2 = 0.5$.

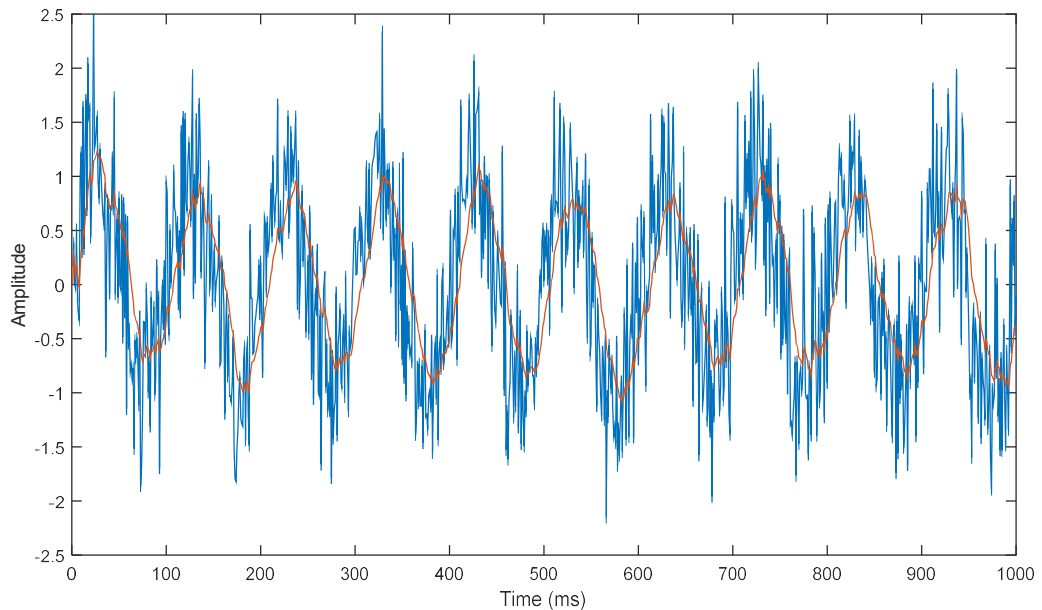


Figure 3.6.1.- Sinus signal with additive Gaussian noise (blue) and filtered signal (red) extracted with Kalman filtering using *Ekalman()* MATLAB function.

As it can be appreciated above, the Kalman filter implemented extracts the signal out of its noisy version even with a low SNR with a small prejudice of sinus amplitude, as it would happen with conventional filtering.

Figures 3.6.2 and 3.6.3 show the results of applying the Kalman Filter to the cases of One-Way with $f_{IF}=100$ KHz and the Two-Ways case at with $f_{IF}=1$ MHz considering only oscillators phase noise.

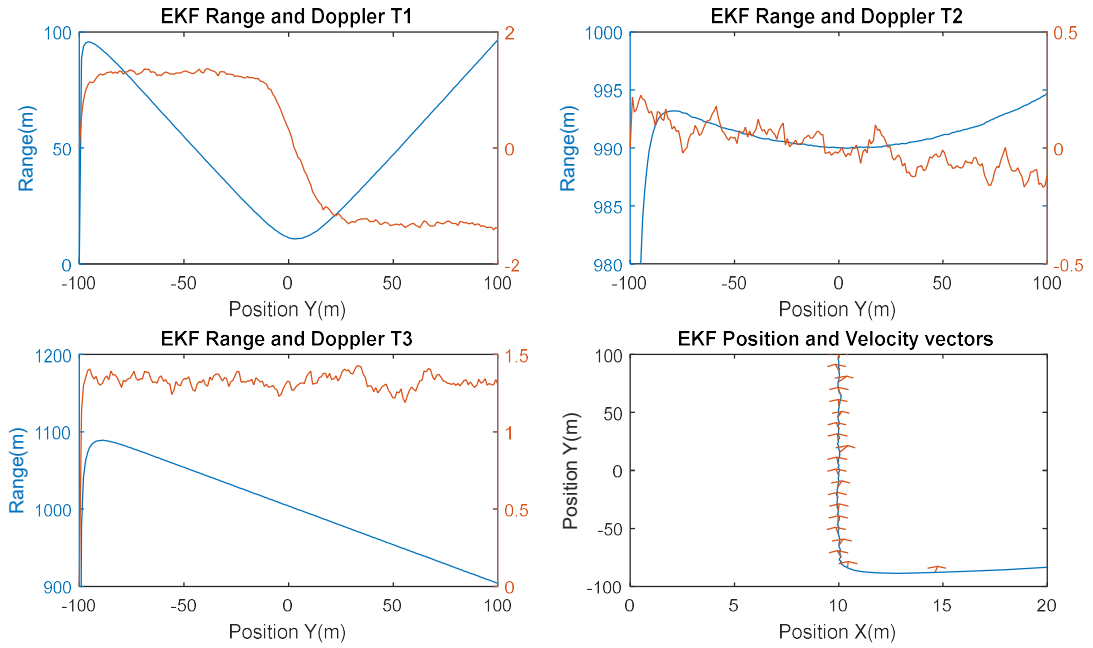


Figure 3.6.2.- Range and Doppler signals with Position and Velocity reconstruction and filtered by Extended Kalman Filter from noisy signal with noise in range $\sigma_{T1W}^2 = 0.156 \text{ ns}^2$ and Doppler $\sigma_{T1W}^2 = 1.56 \cdot 10^{-4} \text{ ns}^2$. Measured at $f_{IF}=100 \text{ KHz}$.

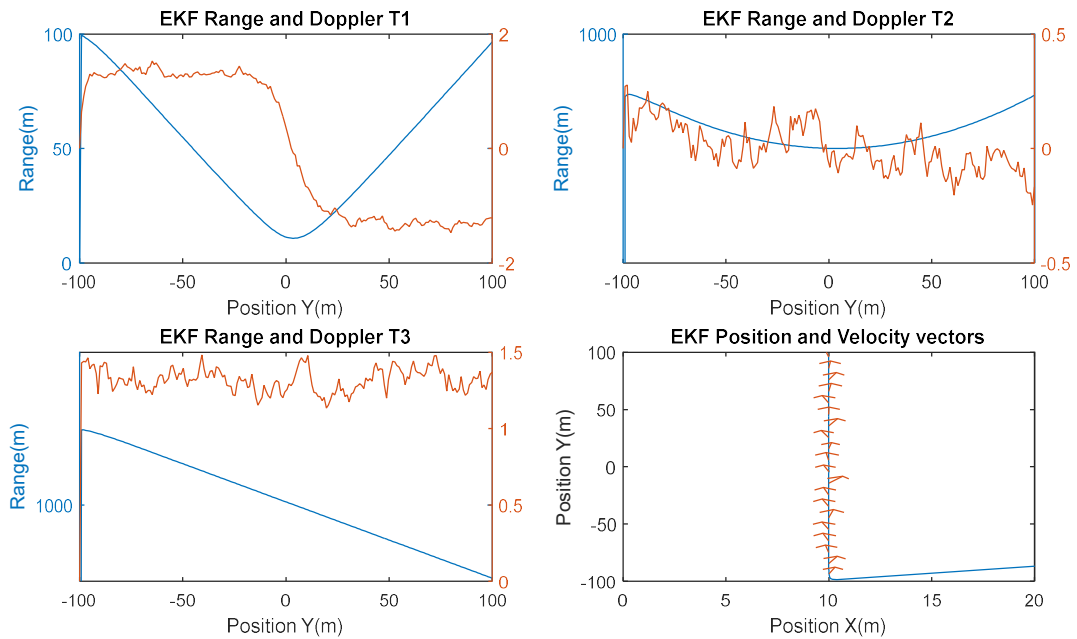


Figure 3.6.3- Range and Doppler signals with Position and Velocity reconstruction and filtered by Extended Kalman Filter from noisy signal with noise in range $\sigma_{T2W}^2 = 5.011 \cdot 10^{-4} \text{ ns}^2$ and Doppler $\sigma_{T2W}^2 = 4.55 \cdot 10^{-8} \text{ ns}^2$. Measured at $f_{IF}=1M \text{ KHz}$.

As it can be appreciated, the Position and velocity vectors are determined with much less error than in their original versions (3.5.6.a and 3.5.7.a respectively), therefore it means that Kalman filtering can compensate the accumulated noise in the system under consideration.

3.7. Summary.

For the RF positioning system architecture trade-off, both One-Way and Two-Ways methods have been proposed and analyzed in detail in terms of long term frequency stability, due to thermal drift and ageing effects, and phase noise, which is of relevant importance for both the Doppler frequency and Time-Of-Flight measurement for range and velocity determination respectively.

The main conclusions are that One-Way operation mode is feasible if the system can afford a high-stability oscillator (i.e. OCXO) in the Tracking Station, together with precise synchronization with the Mobile Node oscillator if Time-Of-Arrival measurement is also implemented. Nevertheless, such possibility becomes difficult to implement due to the strict synchronization process as well as the high power demand of high stability oscillators (OCXOs, see appendix 3 Table A.3.4 for power consumption information). OCXOs, have to be being placed in a very stable thermal environment which typically requires high power (above 1W) in a continuous regime, which makes its utilization in space exploration missions very challenging.

The Two-Ways option has been considered in a configuration based in the reception, measurement of incoming frequency and retransmission of the pulse signal. It has been demonstrated that this option is more appropriate for an application involving a system of exploration robots (defined along the analysis as Mobile nodes or Mobile Rovers) from the measurement performance point of view since it is more robust against drift effects due to thermal shift and aging, as well as influence of phase noise due to jitter effects.

Chapter 4.- Implementation Case Analysis.

4.1. Introduction.

As explained in Chapter 3, the Two-Ways implementation mode for range and Doppler Frequency shift determination (see Figure 3.1.1) is the most reliable option, in terms of both sensitivity, since it is doubled compared with One-Way approach, and total bias error mainly due to the fact that the mobile node transmission frequency drift, due to aging and thermal influences, is compensated by the differential nature of the Time-Of-Arrival measurement in this mode. All these advantages are however achieved at the expense of a more complex mobile node implementation and a higher phase noise due to the accumulation of modulation and demodulation operations, necessary for measurement and generation of RF signals associated with the location messages frames. However, it was demonstrated that the Two-Modes phase noise associated with the oscillators instabilities, the extraction of position and velocity information is still possible via Kalman filtering.

On the other hand, the One-Way operation mode is only feasible if the system can include a high-stability oscillator (i.e. OCXO) and a strong synchronization between the oscillator at mobile node and tracking station, which will greatly impact the mobile node power budget. Therefore, and considering power budgets involved, the Two-Ways operation mode seems more advantageous balancing the advantage of a differential Time-Of-Arrival measurement with the associated phase noise.

Figure 3.3.6 in chapter 3 shows the implementation approach proposed according to, as explained in Section 2.3, a Two-Ways operation mode premise.

This chapter will explain the implementation approach proposed for the Two-Ways system architecture defined in Chapter 3. Decisions about the specific parts selected and sub-systems topology will be analyzed, evaluated and justified, as well as assessing the impact of the resulting power and mass budgets on the higher level hardware assuming a spaceflight hardware implementation.

Finally, the experimental set-up implemented for laboratory analysis and validation, aimed as a representative prototype of the range determination sensor, is described.

4.2. Implementation Approach Description.

In order to define the distribution of the different sub-systems and RF stages into a suitable architecture for the radiofrequency electronics of both Main Station and Mobile node systems, several criteria were considered. In first place, the different architectural units or subsystems configured as integrating parts of the architecture must allow reusability and a certain degree of flexibility in their adaptation to Tracking Station and Mobile Node. The objective of this criterion is to minimize the design efforts for the complete system.

Second, the architecture defined must enable the possibility of implementing redundancy with minimum design changes, this design premise is of key importance to orient the design to a future real spaceborne hardware version. In addition, the architecture must allow the system to be implemented in a modular and scalable fashion. In order to permit the substitution of critical sub-systems whilst allowing the re-utilization of the rest (or the most part) of the remaining sub-systems or enhancing the functionality adding new or improved modules. Finally, and assuming all the above requirements, the architecture must allow the implementation of both Tracking Station and Mobile Node systems with minimum mass and volume budget.

Following these criteria, the RF electronics corresponding to both Tracking Station and Mobile Node systems are divided in the following sub-systems. **The Control Unit** allocates the Logic components (FPGA/microprocessor) the oscillator device (OCXO or TCXO), the power subsystem and the I/F elements. It is the master logic unit controlling all the other sub-systems, also implementing the interface to the outer systems such as the robotic platform On-board Computer. **The RF Board** includes all the RF generation components such as PLLs and mixers while the **Amplifiers Board** includes both the Rx and Tx amplifiers. Finally, the **Switch Matrix Board** accommodates all the switching elements that configure the operation mode (Tx or Rx) and selects which of the two subsystem is connected to the antenna at any moment in time.

The criteria of grouping the different electronic components in this way, is aligned with the electronic design requirements involving signal integrity and electromagnetic compatibility. The logic elements must be placed in the same PCB thus sharing a common digital ground plane. The power sub-system is included in this board in order to allow the logic control element (FPGA) to directly control the power distribution to the rest of the subsystems. The RF board includes the components that process the RF signal (Up and Down conversion, mixers, filters and IF amplification); therefore, the design of this PCB will prioritize the RF signal quality (phase noise and SNR). The amplifiers board accommodates the components that will require special thermal consideration, such as the RF Power Amplifier and LNA, therefore the design of the associated PCB will take into consideration thermal issues and mechanical aspects related to thermal energy dissipation. Finally, the switch matrix board includes all the RF switches that will configure the connection paths between the rest of the subsystems and the antennas. This board implements, in the last instance, the redundancy scheme.

Figures 4.2.1 and 4.2.2 present the architecture layout of the Main Station and Mobile Node radiofrequency electronic systems respectively.

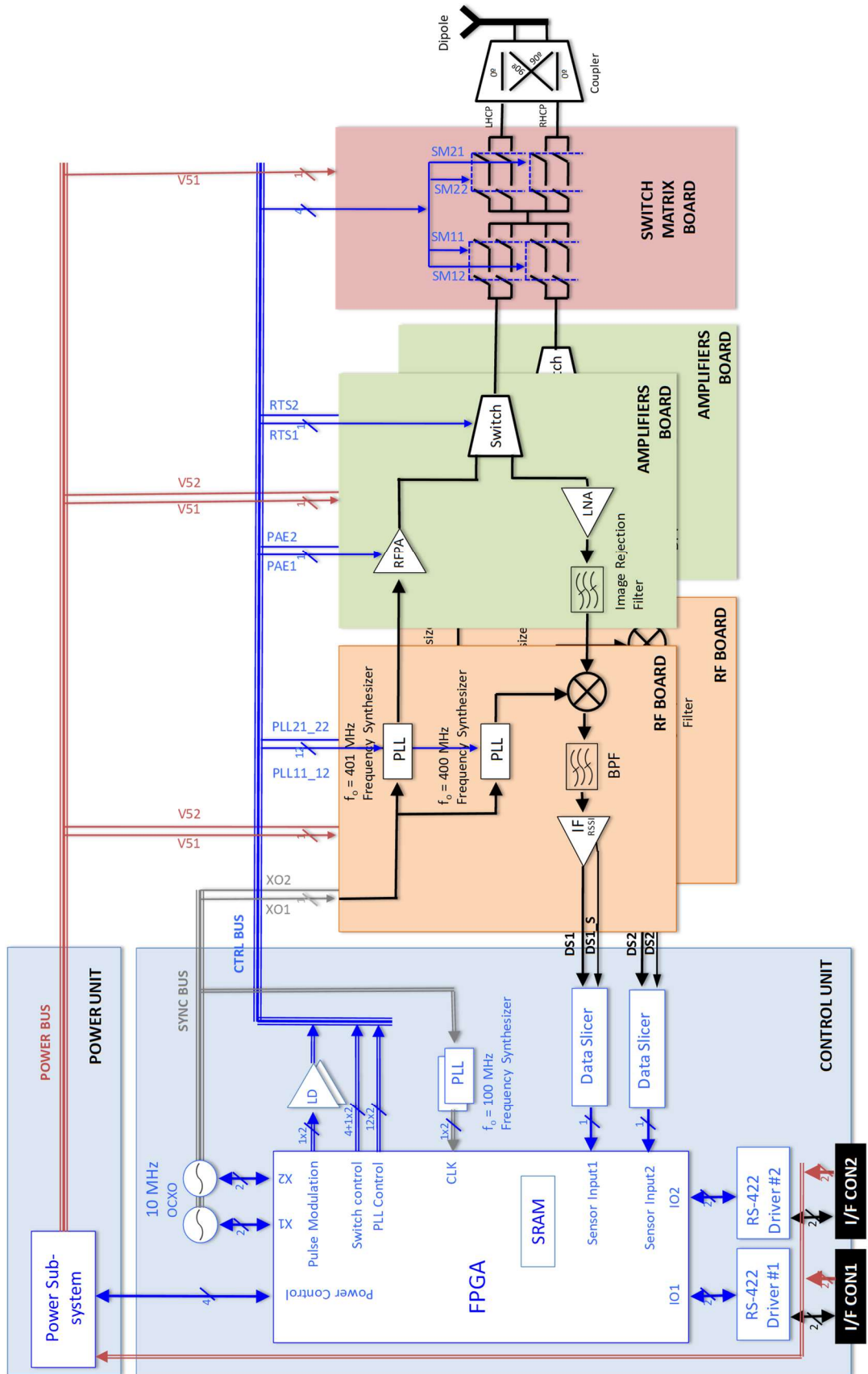


Figure 4.2.1.- Tracking Station RF system layout

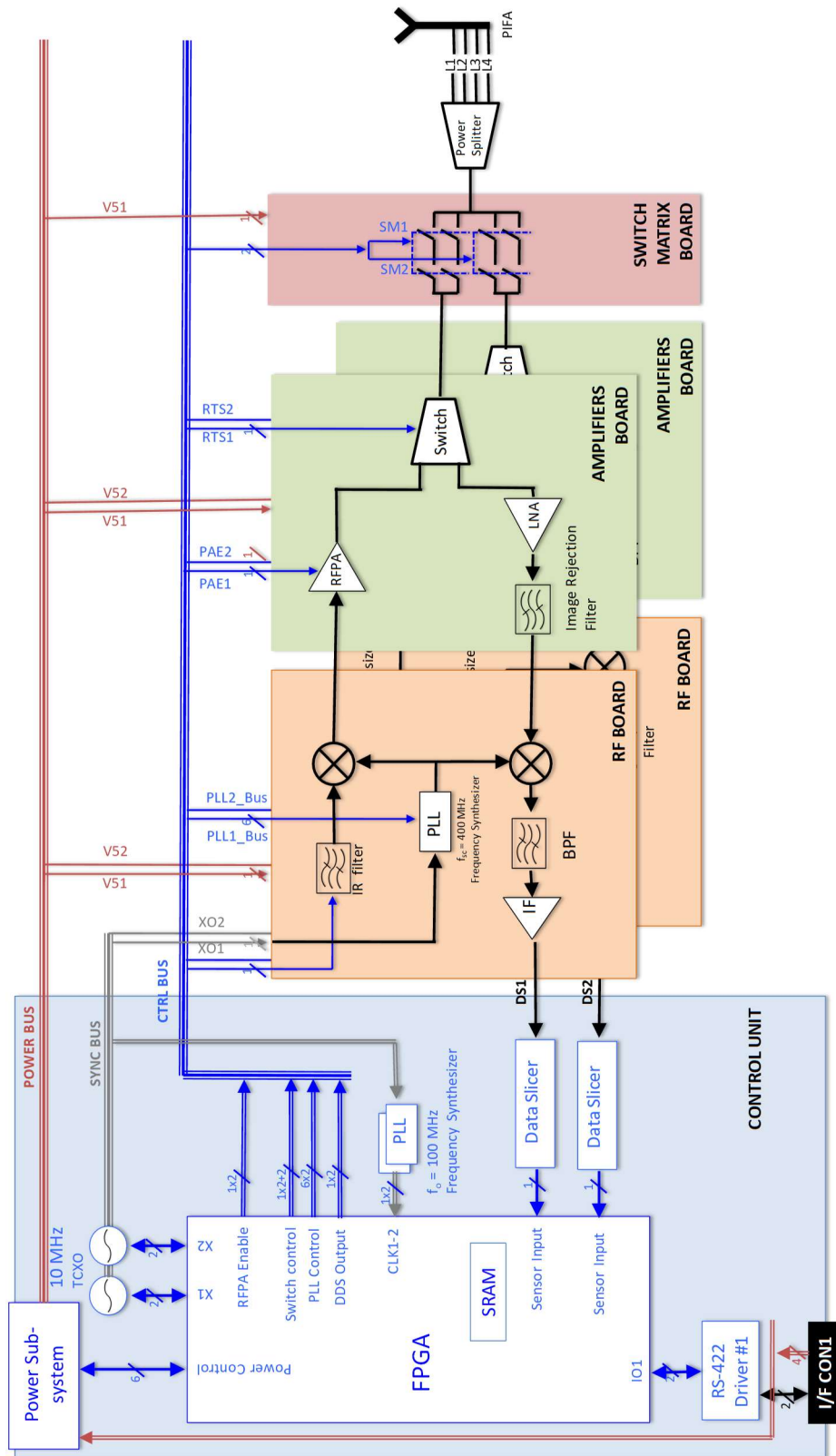


Figure 4.2.2.- Mobile Node RF system layout

The architectures proposed, guarantee the operation of the RF localization system due to a scheme of cold redundancy. The redundancy approach is based in a compromise between reliability and total number of parts included. When a system is designed in redundancy for

high reliability applications, the redundant use of components can imply an increment in complexity of the system, which could lead to a decrement of overall reliability due to the high number of components involved, each with its own failure rate. The alternative to the redundancy at subsystem level presented in Figure 4.2.1 and 4.2.2 could be to redundate at component level, which would lead to an increment in complexity in the routing of each component due to the incorporation of switches used to select the path across nominal and redundant versions.

In the Figure 4.2.1, a balance for the switches required for redundancy at component level for each subsystem is presented.

Critical Component	Number	Number of Switches (2 SPST = 1 SPDT)
RF BOARD - MOBILE NODE		
Mixer (3 lines x 2 SPST/line)	2	12
Filters (2 lines x 2 SPST/line)	2	8
PLL (2 RF lines x 2 SPST/line)	1	4
AMPLIFIERS BOARD – MOBILE NODE		
RFPA (2 lines x 2 SPST/line)	1	4
LNA (2 lines x 2 SPST/line)	1	4
RF antenna Switch (4 SPST/switch)	1	4
Filters (2 lines x 2 SPST/line)	1	4
TOTAL NUMBER OF SWITCHES:		40
TOTAL NUMBER OF COMMAND LINES:		40
RF BOARD – TRACKING STATION		
Mixer (3 lines x 2 SPST/line)	1	6
Filters (2 lines x 2 SPST/line)	1	4
PLL (2 RF lines x 2 SPST/line)	2	8
AMPLIFIERS BOARD – TRACKING STATION		
RFPA (2 lines x 2 SPST/line)	1	4
LNA (2 lines x 2 SPST/line)	1	4
RF antenna Switch (4 SPST/switch)	1	4
Filters (2 lines x 2 SPST/line)	1	4
TOTAL NUMBER OF SWITCHES:		34
TOTAL NUMBER OF COMMAND LINES:		34

Table 4.2.1.- Number of switches related with redundant configuration of RF subsystems.

As it can be noted, the number of switches involved in the redundancy at component level is much higher than the redundancy at subsystem level presented in Figures 4.2.1 and 4.2.2, being 16 switches grouped in a commutation matrix with only 4 control lines, therefore the redundancy at subsystem level introduces less elements prone to failure and a reduced number of control lines. Furthermore, the impact of such switches in the RF circuit is not negligible since the losses associated to the switches circuits may require the implementation of additional gain blocks that would increment the complexity of the whole system.

The logic controller should implement the redundancy as a part of the logic design, duplicating logic blocks within the Field Programmable Gate Array (FPGA) or implementing logic design techniques aiming towards a high fault tolerance such as majority voters, Error Detection and Correction (EDAC) systems for memory access, etc. The logic element selected for the implementation of the control functions is a FPGA rather than a processor-based component such as a microprocessor or microcontroller, due to the capability of the FPGA to implement inherent parallelism, thus simplifying the design of fault-tolerant logic schemes.

As it can be appreciated, in the case of the Tracking Station the power sub-system is separated from the control unit to a separated PCB, although it still belongs to the same functional unit. This decision is motivated by the expected size of the power system in the Tracking Station side, for an optimum phase noise characteristic the analysis in the Chapter 3 demonstrate that a highly stable oscillator is necessary at the Tracking Station, whilst the reference oscillator at the Mobile node can have lower performance, requiring less power for its conditioning.

The RF electronics are powered from the (Mobile or Tracking) Station platform bus (24V is the typical voltage for space rated batteries), therefore the requirements of voltage regulation are more demanding than those related with the lower voltages coming from in the solar arrays on the Mobile Node. In order to apply to the total envelope a minimum impact, a fifth PCB for power management is added which slightly increases the expected volume of the electronics. The power requirements for the Mobile node are less demanding, and mainly determined by the required transmission power since the clock reference does not have special stability requirements (as is the case for OCXOs) and thus being possible to use less power hungry TCXOs on that side (see Appendix 3 table A.3.4 for power consumption information associated to OCXOs and TCXOs analysed)..

For this study, the supply is assumed as based on a common compact regulator topology generating all the power voltages required by the different electronic components. The use of a 24V direct current supply for the Main Station platform assumes a non-regulated platform power bus implemented with a combination battery cells (Li-Ion for instance as this technology is mature already in past space exploration missions). This provides the possibility of a voltage variation while the system is in operation that justifies the existence of the proposed DC-DC pre-regulator.

In any case, and despite of the reusability and scalability criteria, some of the sub-systems described above could be grouped and combined in a single unit in order to address strict volume constraints, though with some limitations. Specifically, RF boards electronics could be integrated within the Control Unit provided that specific PCB routing criteria are used considering the separation of RF and digital ground connections. On the other hand, RF switches from the Switch Matrix Board could be incorporated within the Amplifiers board, provided that specific thermal conditioning techniques are used to separate the switching stage from the amplifiers area, in order to avoid yielding the Solid-State switches to the high temperatures produced by amplifiers heat dissipation effects. In any case, this would suppose an increment of the printed circuit boards' surface. This option will be considered when assessing the distribution of elements inside the Mobile Node robotic platform.

It can be noted that in the Tracking Station RF system (Figure 4.2.1) there is an additional (digital) output signal on the IF amplifier, named DSx_S (where x is either 1 or 2). This signal is intended to notify the control logic about of the RF signal power (i.e. RF signal strength) associated with the incoming RF pulse. If DSx_S is in high state, it means that the RF power is enough for frequency detection, otherwise if the signal is in low state; it means that the RF pulse transmitted by Mobile Node is being received under the power threshold, and therefore the measurement would be not valid. The RF signal strength measurement will be implemented as part of IF amplifier, detecting the envelope of the IF signal (i.e. AM demodulation) and measuring the resulting envelope level in order to determine the power associated with the incoming signal.

For the Tracking Station RF system, the transmission / reception antenna is connected to the switch Matrix Board. In this case, the selection of the appropriate antenna depends on aspects like gain, directivity, mechanical constraints, etc. The selection of a four elements PIFA

linear antenna allows the implementation of a compact antenna around the Mobile Node avoiding the deployment of a monopole, which simplifies the mechanics of the antenna deployment and the stowage of the Mobile Nodes during transport.

Concerning the aforementioned type of antenna, for instance [Navarro-2015] describes PIFA based multi-element antenna intended for drones and other autonomous vehicles, designed for circular polarization with a quasi omnidirectional radiation pattern (nulls at +Z,-Z axis). This sort of antennas could be used in mobile nodes since the hardware signature is very small, allowing the implementation of the mobile node in a compact formfactor that would make possible a very efficient storage.

The patch antenna elements present a very low profile compared with monopoles and turnstile antennas, enabling its integration in an autonomous rover seamlessly. The linear polarization of the antenna is a clear disadvantage, since circular polarization cancels multipath interference effects, however, as it was justified in Chapter 3, the effect of multipath interference is negligible for range determination and null for Doppler Frequency shift value, therefore, it is assumable to use a configuration of antenna elements to provide an omnidirectional radiation diagram in XY plane with linear polarization.

A components selection process has been performed for both Tracking Station and Mobile node RF range sensor systems. Key metrics for the selection process including component availability, thermal operational range, (compliance with -40°C to +80°C) and mass tables 4.2.2 and 4.2.3 show the outcome of this process.

Quantity	Description	Package	Mass (g)	Total Mass (g)	Availability of Space Grade Components	Availability of Industrial/Commercial grade electronics
2	CAPACITOR, big	Chip-C0402	0,009	0,018	Available VISHAY(Europe)	Available
44	CAPACITOR, small	0603	0,016	0,704	Available VISHAY (Europe)	Available
2	COMPARATOR, LM139AD	SO-14	0,148	0,296	Available Texas Instruments (USA)	Available in industrial versions, and others similar from different vendors
1	FPGA, ProAsicA3P600	PQFP-208	3,2	3,2	Available MICROSEMI (USA)	Compatible with other PROASIC3 based Microsemi's FPGAs
2	GENERIC, DSUB9F	DB9F	5	10	Available AXON (France)	Available
3	GENERIC, HDR2X25	HDR2X25	4,2	12,6	Available HYPERTAC (UK)	Available
1	SN74LVC125APW	IPC-7351\TSSOP-14	0,09	0,09	Available Texas Instruments (USA)	Available
4	Mixer, DBM177	DIL-8	0,12	0,48	Available SIRENZA (USA)	ADL5350 Analog Devices
6	OPAMP, AD8041AR	SOIC-R-8	0,074	0,444	Available Analog Dev.(USA)	Available
6	PLL SKY72310	QFN-24(RHF)	3,5	21	Available SKYWORKS (USA)	AD4108S Analog Devices, PE33241 Peregrine Semiconductor
2	Oscillators,HT-700 TCXO	TO39	3,2	6,4	Available RAKON (USA)	FOX-924B-10.000
26	RESISTORS	Chip-R0402	0,09	2,34	Available VISHAY (Europe)	Available
2	IF Gain block NBB-302	PBGA7X7	2,5	5	Available RFMD (USA)	ADL5541, TQP3M9007 Analog Devices
2	LNA, SGL-06SMT2	AVANTEK84	2	4	Available RFMD (USA)	Available
2	RF Amp, TGA2540FL	(D2PAK)	1,5	3	Available RFMD (USA)	MW71C008NT1 commercial version
2	RFOsc, VX-189 (VCXO)	DIP24L(SMT)	0,35	0,7	Available VECTRON (USA)	VX-501 commercial version
2	SPECIAL_FUNCTION, LMH6559MF	(MF05A)	0,75	1,5	Available Texas Instruments (USA)	Available
5	SW_RF, PE9354	SO-8(S8)	0,074	0,37	Available PEREGRINE (USA)	PE4259-63 Industrial version Peregrine Semiconductor
7	PCB Cards	80 x 80	18	126	Available PRIMCA (Europe)	Available
2	Transceivers, DS16F95QML	LCC-20(E20A)	1	2	Available Texas Instruments (USA)	Available substitutes from different providers
2	ZENER, BZV55-B2V4	SOD-80C	0,08	0,16	Available VISHAY(Europe)	Available
125			Total:	200,302		

Table 4.2.2.- Tracking Station RF system parts selection with mass budget estimation

Quantity	Description	Package	Mass (g)	Total Mass (g)	Availability of Space Grade Components	Availability of Industrial/Commercial grade electronics
2	CAPACITOR, big	Chip-C0402	0,009	0,018	Available VISHAY (USA)	Available
44	CAPACITOR, small	0603	0,016	0,704	Available VISHAY (USA)	Available
2	COMPARATOR, LM139AD	SO-14	0,148	0,296	Available Texas Instruments (USA)	Available in industrial versions, and others similar from different vendors
1	FPGA, ProAsicA3P600	PQFP-208	3,2	3,2	Available MICROSEMI (USA)	Compatible with other PROASIC3 based Microsemi's FPGAs
1	GENERIC, DSUB9F	DB9F	5	5	Available AXON (France)	Available
3	GENERIC, HDR2X25	HDR2X25	4,2	12,6	Available HYPERTAC (UK)	Available
1	SN74LVC125APW	IPC-7351\TSSOP-14	0,09	0,09	Available Texas Instruments (USA)	Available
4	Mixer, DBM177	DIL-8	0,12	0,48	Available SIRENZA (USA)	ADL5350 Anaog Devices
6	OPAMP, AD8041AR	SOIC-R-8	0,074	0,444	Available Analog Dev.(USA)	Available Analog Devices
2	PLL SKY72310	QFN-24(RHF)	3,5	7	Available SKYWORKS (USA)	AD4108S Analog Devices, PE33241 Peregrine Semiconductor
2	Oscillators,HT-700 TCXO	TO39	3,2	6,4	Available RAKON (USA)	FOX-924B-10.000
26	RESISTORS	Chip-R0402	0,09	2,34	Available VISHAY (USA)	Available
2	IF Gain block NBB-302	PBGA7X7	2,5	5	Available RFMD (USA)	ADL5541, TQP3M9007 Analog Devices
2	LNA, SGL-06SMT2	AVANTEK84	2	4	Available RFMD (USA)	Available
2	RFAMP, TGA2540FL	(D2PAK)	1,5	3	Available RFMD (USA)	MW7IC008NT1 RFMD commercial version
2	RFOsc, VX-189 (VCXO)	DIP24L(SMT)	0,35	0,7	Available VECTRON (USA)	VX-501 commercial version
2	SPECIAL_FUNCTION, LMH6559MF	(MF05A)	0,75	1,5	Available Texas Instruments (USA)	Available Texas Instruments
5	SW_RF, PE9354	SO-8(S8)	0,074	0,37	Available PEREGRINE (USA)	PE4259-63 Industrial version
6	PCB Cards	80 x 80	18	108	Available PRIMCA (USA)	Available
1	Transceivers, DS16F95QML	LCC-20(E20A)	1	1	Available Texas Instruments (USA)	Available substitutes from different providers
2	ZENER, BZV55-B2V4	SOD-80C	0,08	0,16	Available VISHAY (USA)	Available
118			Total:	162,302		

Table 4.2.3. Mobile Node RF system parts selection with mass budget estimation

In the table A.1.1(Appendix 1) the different signals included in the Mobile Node interface bus, as seen from the Mobile Node Control Unit connector, are listed and described, and in the table A.1.2 (Appendix 1), the different signals included in the Main Station interface bus, as seen from the Tracking Station Control Unit connector, are listed and described.

The rest of the Control Unit signals that do not appear at the interface bus are those included in the FPGA internal buses: Power Control, X1, X2, IO1 and IO2. The table A.1.3 (Appendix 1) lists the signals included in such buses. Table A.1.3 (Appendix 1) lists the signals of each interface connector at Tracking Station and Mobile node:

Concerning the overall architecture, a few points on the distribution of signals along the architecture are worthwhile mentioning.

The signal buses included in the tables correspond (in name and color) with the signal buses labeled in the architecture layouts, presented in Figures 4.2.1 and 4.2.2. The PLL signal buses are labeled to correspond to the control sub-bus for each PLL both in Tracking station and Mobile Node, where PLLx1_x2 refers to the PLL control bus for RF Board x (x=1,2), and PLLx_Bus to the PLL control signals at RF Board x respectively.

In both I/F signals list, (see Appendix 1 for I/F tables), the power coming from the two possible batteries (it is possible to implement a redundant battery bus) is distributed in one or two connectors depending on the need of an additional one for redundancy reasons. In the case of Mobile Node, the system is expected to be autonomous, barely dependent on OBC (it even could implement the OBC in its logical hardware assuming a simple computer in the mobile robotic agents), therefore the RS422 interface is more intended for tests and integration procedures than for external control. Oppositely, in the Tracking Station RF unit,

the RS422 serial interface is intended as an interface port for the platform OBC, which will command the unit by means of data messages through the serial port. In this case the I/F stage becomes critical and, thus, a redundant I/F CON2, with its RS-422 driver and logic signals, is proposed.

As it is supposed to operate in an autonomous robotic platform (Tracking Stations could be static or rmobile, in the exploration scenario proposed in Chapter 2) the system is expected to be powered from two independent batteries for both Tracking station and mobile node for redundancy reasons. The positive and negative leads of both batteries are routed to separate I/F connector pins in a way that the ground connection is performed in the power-subsystem circuit.

A difference in the Power Control Bus at both systems for the signals related to battery selection (CBAT1 and CBAT 2 at OS) can be seen. In the Mobile Node, the selection of which battery is powering the system is made in the RF power sub-system and controlled by the logic unit, achieving a more autonomous operation. In the case of Tracking Station, these signals do not exist as it is assumed that the selection of the battery powering the system will be done externally, by the station platform OBC.

4.3. Functional Description.

The operation of the RF range measurement sensor is defined by the logic system implemented in the programmable logic device (FPGA). The logic implemented in the control unit is based on three different IP blocks.

First, the **Control Block** is the master control unit, which runs the activation sequence, interprets the commands sent by the OBC and executes the necessary control tasks over the DSP block in order to perform the RF frequency pulse transmission / received frequency measurement cycle. It interfaces with the two DSP blocks (corresponding with each RF chain) to carry out a redundant operation over both sub-system blocks and with the Protocol Engine, in order to interface with outer control systems through it.

The **DSP Block** is the logic block in charge of the management of the RF components (PLL, Rx/Tx switching and RF Power amplifier modulation). It autonomously generates the RF carrier and measures the incoming signal's frequency, storing the incoming frequency samples in the SRAM and performing the necessary calculations (moving average in its simpler version or a Kalman Filter as described in Chapter 3 Section 2.6) to get the duty cycle frequency readouts. It interfaces via a 32 bits data bus with the control block to provide the frequency values, and (in case of Mobile Node DSP block) a 32 bits input bus to receive the target frequency to be generated by the DDS (Direct Digital Synthesis) RF signal generator included in the block.

Finally, the **Protocol Engine** carries out the protocol frame coding/decoding operations, checks the frame integrity and identifies the frame type in order to transmit the received commands to the control unit free of reception errors.

Figure 4.3.1 shows the logic architecture of the Main Station control unit, as a combination of the aforementioned blocks, whilst Figure 4.3.2 presents the logic architecture of the Mobile Node control unit.

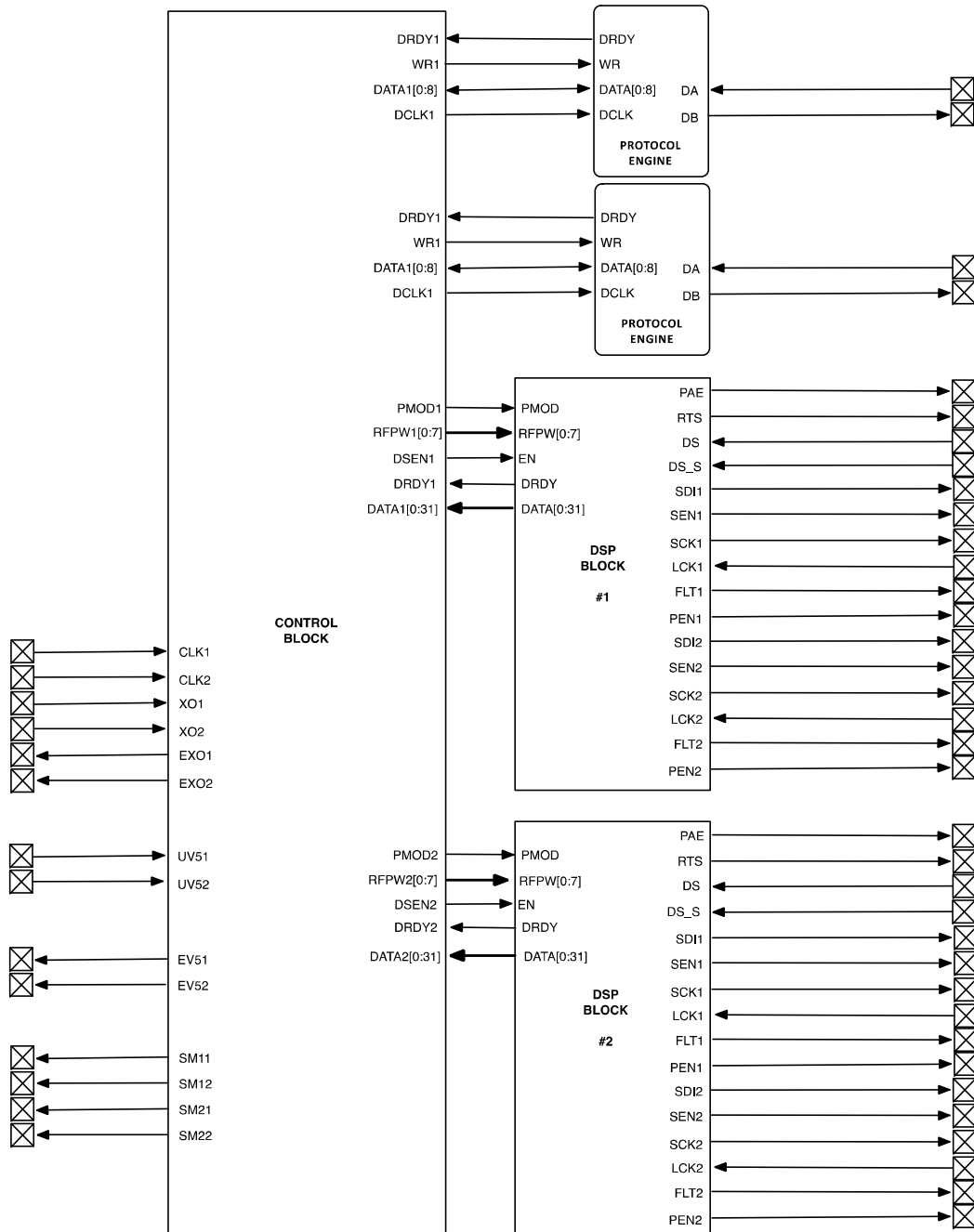


Figure 4.3.1.- Main Station Control Unit logic architecture

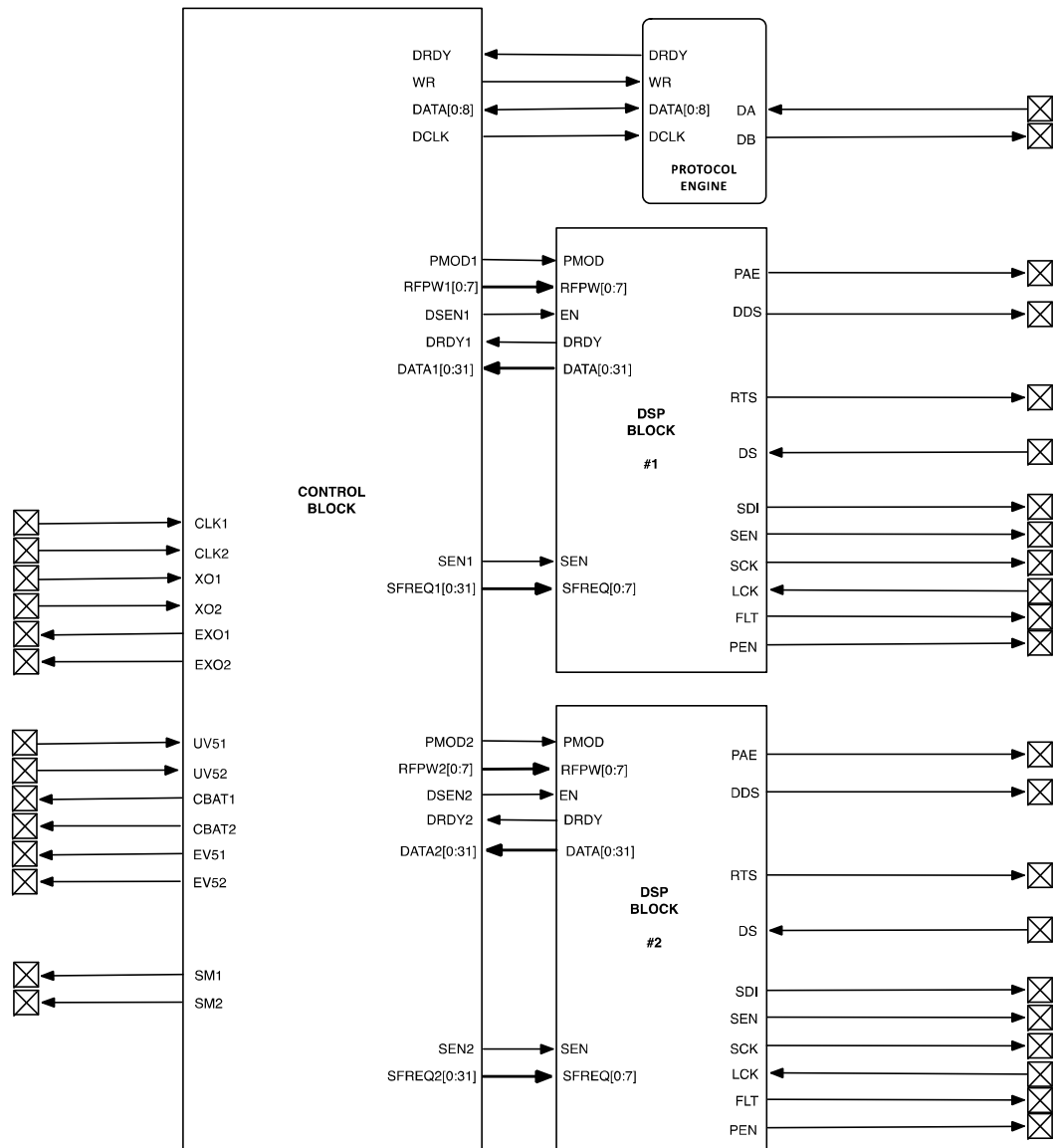


Figure 4.3.2.- Mobile Node Control Unit logic architecture

As mentioned above, the control over the RF chains leading to the generation of the RF pulses, its reception, retransmission (in case of Mobile Node) and frequency measurement is implemented entirely over the DSP blocks, in such a way that the operations over RF components are autonomous and fully (cold) redundant for increased reliability. The switch between RF chains (and thus between DSP Blocks) is commanded either externally (Tracking Station) or decided at the Control Block (OS) level. In this sense, it is relevant to recall that, the Mobile Node is equipped with more control features in order to make its implementation more autonomous for the final proposed Mobile Node platform hardware. For these reasons, the Mobile Node control units receive the under-voltage signals UV51 and UV52, in order to have the capability to disconnect any of the two battery buses as well as manage which when the RF chains is operative. In the Tracking Station this action is intended to be performed under external control via commands sent by the platform OBC. Due to this the dependency of the communication interface in the Tracking Station, serial interface with their respective protocol engines IP, are replicated in cold redundancy,

The control block, is intended to be synthesized using directives of fail-safety redundancy rules in the VHDL synthesiser (Libero from Microsemi corp.). This approach leads to a lower use of system gates, which results in lower FPGA power consumption.

Other options, aiming to implement redundancy in the control unit, were considered at this stage:

A **Control Units in cold redundancy** approach makes use of fully redundant hardware, adding a second Control Unit board to the existing arrangement. Each Control Unit should control only one of the RF chains, since the cross-connection to enable any control path would require additional hardware to ensure sufficient system reliability. The control units and their respective RF chains (RF board and Amplifiers board) would operate as separate RF systems, controlled through different communication ports in the Main Station or through a Token-Pass method in the Mobile Node. This method would increase reliability but at the cost of adding one more Control PCB, however, the present redundancy elements (PLLs and OCXOs/TCXOs) could be distributed over the two control units, thus reducing the overall mass, volume and cost requirements. Furthermore, the time needed to switch between cold redundant units should have to be determined for range measurement since it would add a significant error in the Time-of-Arrival. The redundant units switch method must consider the requirement of avoiding extra uncertainty in the range determination, for example, rejecting the Time-of-Arrival measurement during units switching.

On the other hand, including **Redundant FPGAs in the Control Unit** implies that redundant logic functionality in redundant FPGA ICs to be implemented in the same Control Unit. To ensure that each FPGA could control any of the RF chains would require a complex bus multiplex logic that would necessitate considerable volume to allow the implementation of a redundant fail-safe topology. In summary, this functionality would require an additional logic element (FPGA or CPLD), which makes the implementation of such system in the present Control Unit PCB substantially more complex. The alternative is to implement one control logic per RF chain, in two separated FPGAs within a unique Control Unit PCB, thus implementing a similar approach to the approach above but using only one PCB. Preliminary considerations about routing requirements indicate that this possibility is feasible whilst reaching a denser PCB. As in the paragraph above, the time required for switching between logic elements must be consider, being consistent with the range determination.

As a general conclusion, this second possibility would be the alternative in the case that a higher reliability degree is desired. An additional advantage is that the communications could be implemented with the same transceivers and the arbitration signals would be routed across the two FPGAs in the same PCB, simplifying the harnessing compared with the first option. In any case, the total system gates used will be incremented with any of these last options, influencing the design through a higher power consumption in the FPGA.

Regarding the logical operation of the system, the next figure presents the flow diagram of the operations performed by the logic control block (Figure 4.3.3) and DSP block (Figure 4.3.4) respectively.

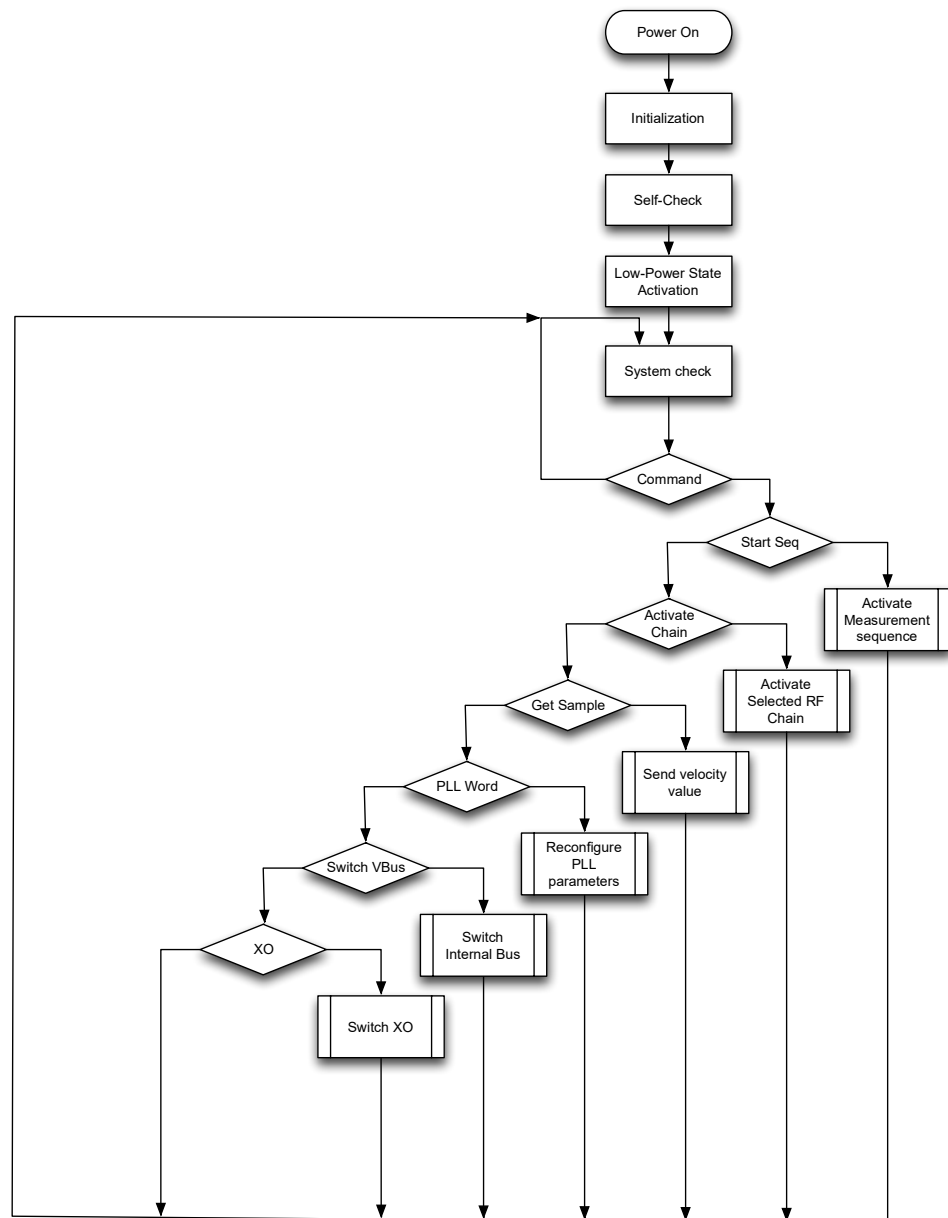


Figure 4.3.3.- Tracking Station Block logic flow diagram

As it can be seen in Figure 4.3.3, the logic structure of the Tracking Station control block is compact and straightforward, based on a command polling philosophy: the system starts the initialization process and the self-test (activating the different RF chains and checking that no under-voltage flag is activated), and then entering a low power stage until a command is received.

While this happens, the control block checks the internal signals, such as UV1 and UV2, and when, a command arrives (DRDY Data Ready signal) the parser starts the detection of the arriving command. If it is a valid command, it will find the path to the execution of the actions related to such command, and the program flow returns finally to the command detection loop. The main command loop starts with a Check phase in order to check internal failure flags before any command execution. This check phase allows responding to internal events in a time deterministic manner.

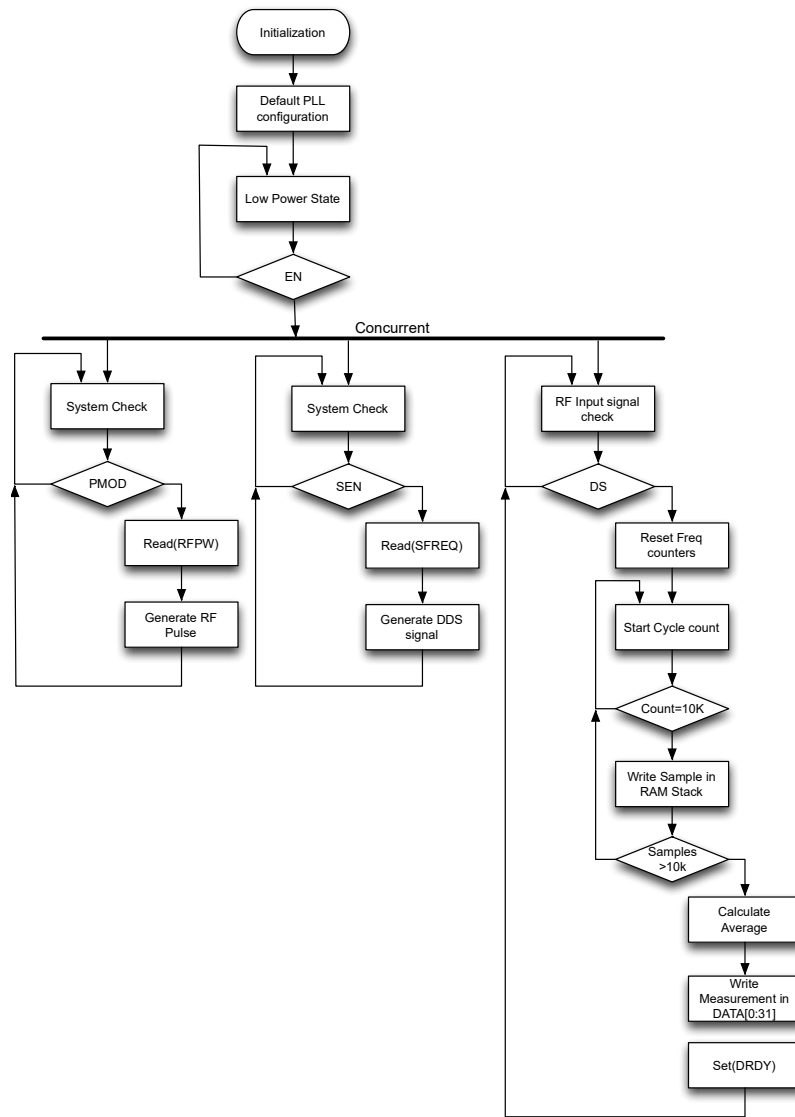


Figure 4.3.4.- DSP Logic block diagram.

On the other hand, the logical processes at the DSP block (Figure 4.3.4) are more complex and parallel data flow sequences have to be implemented. The initialization is performed after the power on and, after that, the DSP block enters a low power stage, whilst awaiting the activation signal (EN). Once the system is enabled, three concurrent process start: the process that takes care of the generation of the RF pulse signal modulating the RF power amplifier, the process that generates the RF signal by Direct Digital Synthesis (DDS) for the pulse re-transmission (only at Mobile Node side) and the process that takes care of the measurement of the incoming RF frequency.

After detecting the presence of an effective RF signal in the sensor input (DS), confirming the input RF power level through the signal DSx_S (RF signal strength digital input, which high state indicates signal level enough for frequency measurement) follows on counting the incoming RF pulses and the time-base signal cycles along a specific number of RF cycles (10.000 by default), as explained in Chapter 3. Once this process concludes, the number of cycles is stored in a data stack in the RAM in order to proceed to the next stage.

After a number of samples (100.000 by default), the samples stored in the RAM stack are averaged and stored in a second stack, making this available to the control block as well writing the last calculated measurement at the output port DATA [0:31].

Figure 4.3.5 shows the concept behind the measurement process, as it was described in chapter 3. The IF incoming signal cycles are counted in parallel with a higher frequency reference timing signal, once 10.000 cycles of IF signal are detected (for an $f_{IF} = 100\text{KHz}$), the frequency is calculated in relation of the number of cycles detected from the reference signal, since its clock frequency is known and stable. Such samples are stored in memory and further averaged to obtain an accurate measurement of the incoming pulse frequency.

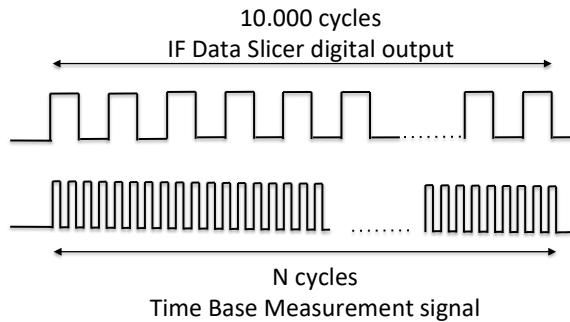


Figure 4.3.5.- Frequency measurement of the IF reception signal

In the case of the Mobile Node control logic, the operation mode is different since the system is intended to be autonomous. In the Figure 4.3.6, the logic flow diagram is presented.

As can be seen, the system after activation enters into low power mode, starting a period in Stand-By that will finish once the Mobile Node robot is deployed. After such timing process, the Mobile Node control logic quits the low power mode and enters a cycle awaiting for incoming RF pulses in a way that, once the pulse is received, the measurement sequence is activated and the outgoing pulse is transmitted afterwards. If the Mobile Node covers a timeout period without incoming pulses, it enters in a Beacon emergency mode in a way that periodic RF pulses are transmitted in order to allow the Main Station sensing the Mobile Node in an emergency One-Way mode. This state is deactivated once any incoming pulse is received.

As it can be noted in the Figure 4.3.6, there are two check steps, the Self-Check after initialization and the System check at the beginning of the logic main loop. The Self-Check, as with the Tracking Station case, includes a check of each logic module and hardware subsystem in order to verify the operational status of the whole system. The System Check in the main loop consists in checking the internal error flags in order to detect whether some failure or warning event has been generated during the execution of the main loop.

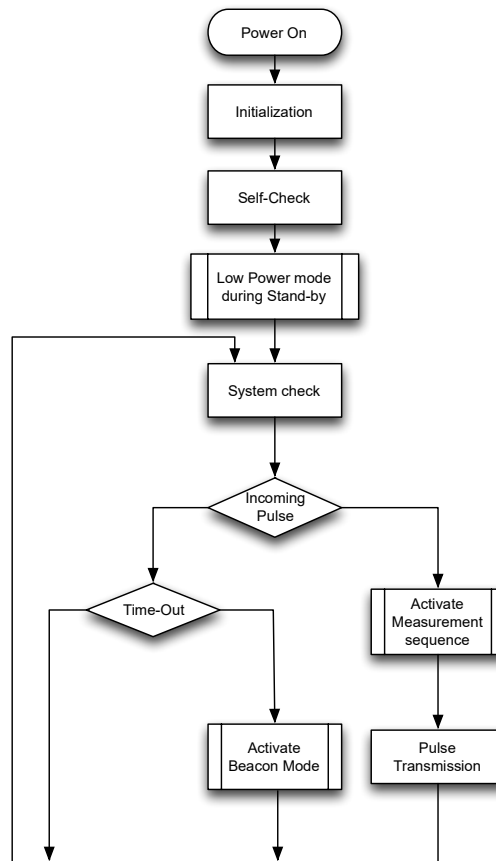


Figure 4.3.6.- Mobile Node Control Block Logic Flow Diagram.

4.4. Summary.

This chapter has presented a discussion of the proposed implementation for the architecture defined in Chapter 3. The implementation analysis has been performed on the assumption of a possible implementation of the module as a part of a real space system, therefore, with the premise of the need of space qualified components for each stage and the use of redundancies in critical sub-systems.

Once accomplished, a simplified implementation has been proposed as a prototype for experimental analysis. Those parts of the proposed implementation related with the redundancy aspects are removed from the experimental prototype because they are not necessary for characterization purposes.

In the next chapter, an analysis of the experimental setup and results obtained will be performed and relevant conclusions will be developed.

Chapter 5.- Experimental Methods and Results.

5.1. Introduction.

As described in Chapter 4, a complete experimental set-up was arranged in order to test the performance of the system in the measurement of the Doppler component in order to characterize the performance of the measurement system in the determination of Doppler frequency shift despite of the phase noise. The experimental campaign will focus on this aspect since there are many references in literature reporting previous works dealing with the characterization of Time-Of-Arrival based range determination procedures for Multilateration applications. The use of Doppler component for radial velocity determination can yield values in the range of cm/s in bands starting from S (see Figure 3.2.2 in Chapter 3), with a modest 0.1Hz resolution in frequency measurement (16.01 Hz/(m/s) for S band up to 66,71 Hz/(m/s) in X Band at 10GHz).

In Figure 5.1.1, the architecture scheme for the implementation of the Tracking Station prototype model is presented. In this architecture diagram, the redundancy scheme has been removed and the layout simplified, since the purpose of the prototype is simply to demonstrate the frequency measurement concept and not to perform a tested from the reliability point of view.

As mentioned in Section 4.2, the proposed architectures can be implemented with space quality electronic components, and the proposed breadboards can be implemented with Rad-Hard components, but for this implementation, Commercial Off-the-Shelf (COTS) components will be used since the purpose of the investigation is to demonstrate the operation and performance of the system.

A Microsemi ProASIC3 FPGA will be used as the logic element, and this can either both Space Grade (A3P600) and commercial versions.

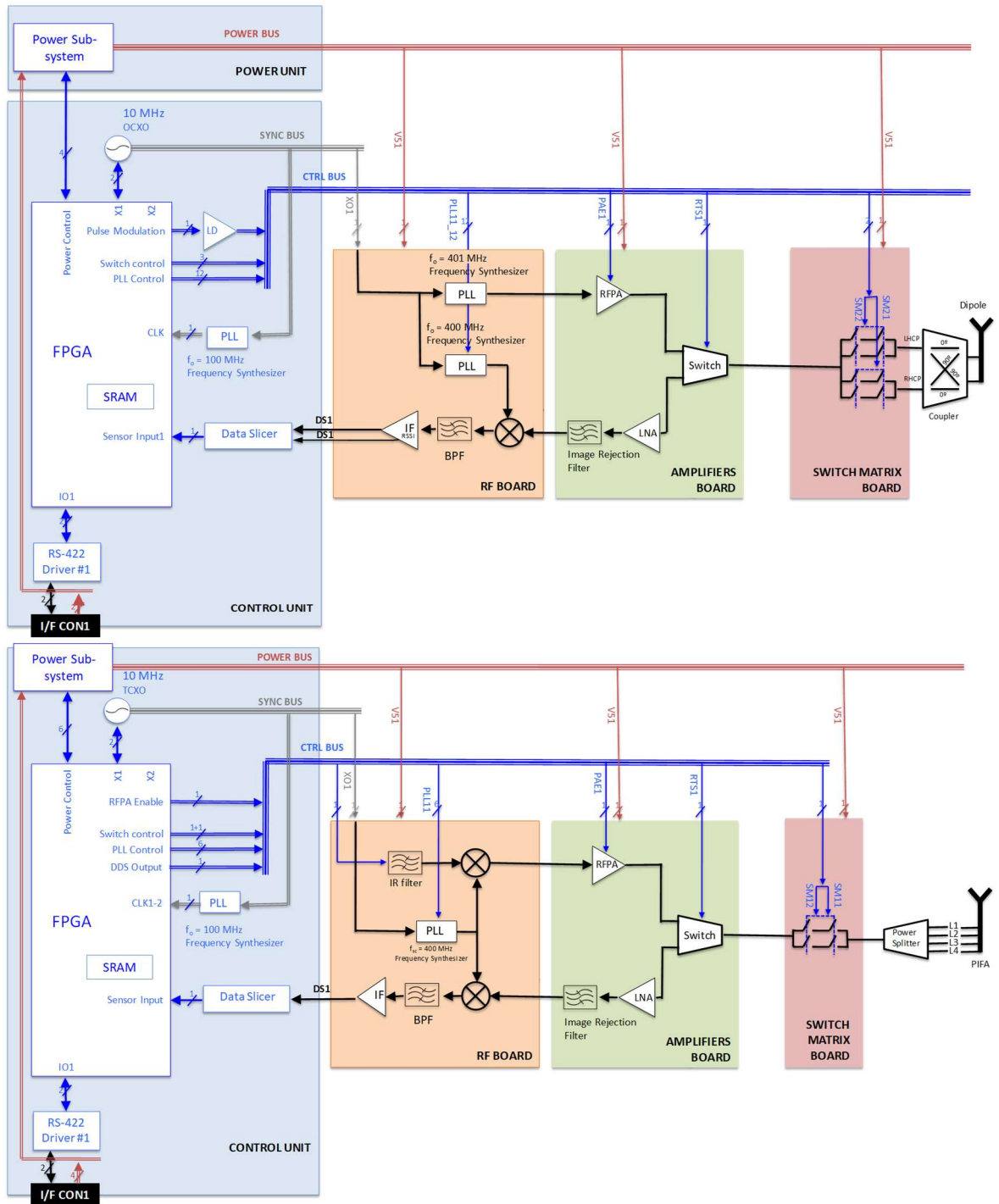


Figure 5.1.1.- Tracking Station (Top) and Mobile Node (Bottom) RF System architecture corresponding to the Breadboard implementation.

Figure 5.1.2 depicts the experimental layout proposed for the experimental tests. Both electronic systems are controlled from a computer by serial port commands.

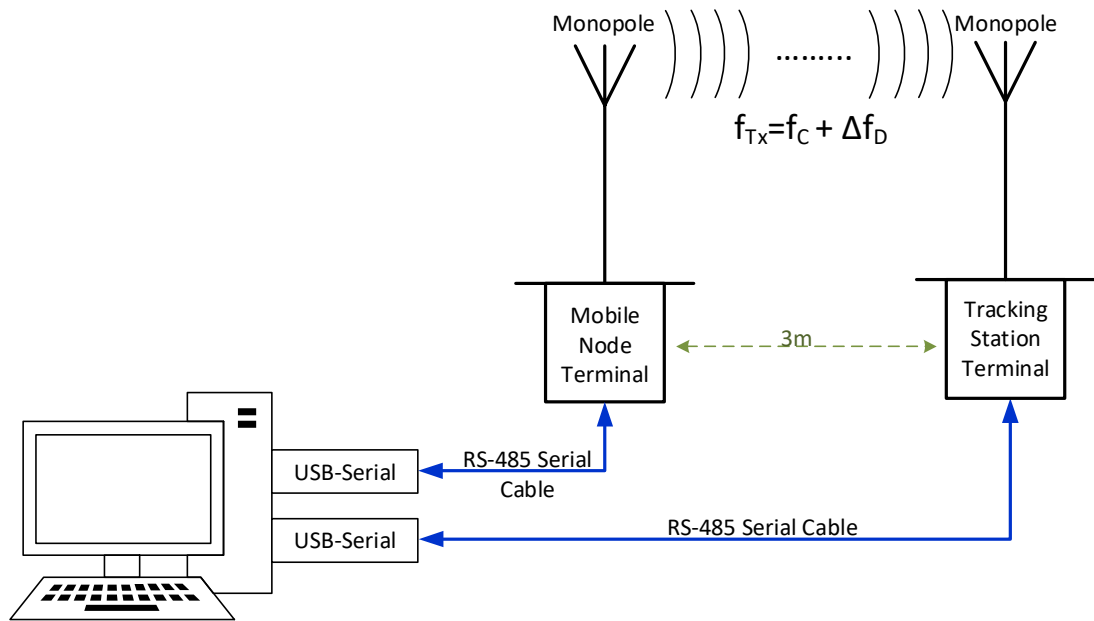


Figure 5.1.2.- Experimental Set-Up layout.

The prototypes implemented are connected and controlled from a PC computer running the software application developed on Visual Studio C# to control the experiment. The software application is designed to emulate the operation of the OBCs on each side, therefore it is able to send commands and to retrieve the data sent by the Mobile Node and Tracking Station prototype units. Specifically, the software is able to send the frequency of operation both to the Mobile Node and Tracking Station prototypes, as well as the other commands used to configure the different components. The capability of modulating the desired operation frequency will be used for experimental purposes, as it will be explained later.

For the RF connection, both monopole antennas and direct cable connection with attenuation (-20dB) has been used. The units are placed in a laboratory environment and separated 3m.

This chapter focuses on the specific experiments performed as well as detailing the components and methodologies used. Once the experiments are described, the results obtained are discussed and a critical analysis is performed.

5.2. Components and Methodologies.

The two prototypes are implemented in a stack of PCBs as described in Chapter 4, in order to represent both Mobile node and Tracking Station hardware models. The systems are powered by a laboratory power supply ISO-TECH reference IPS-3303. To generate external frequency signals, a laboratory signal generator ISO-TECH model GFG2110 was used for the digital clock signals and an AGILENT model PSG-E8257D for the analog signals.

PTFE coaxial cables ending in SMA connectors were used to harness the different stages of the breadboards, as shown in Figure 5.2.1.

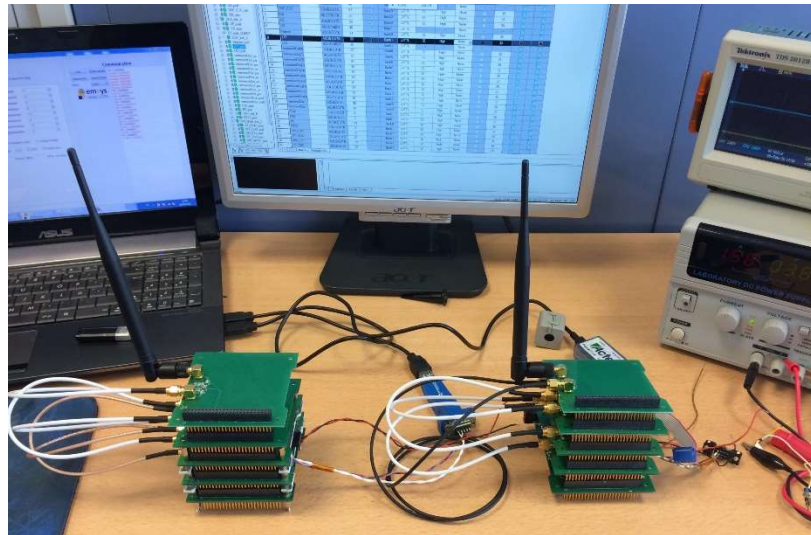


Figure 5.2.1.- Experimental Laboratory Set-Up implemented for performance analysis.

In order to test and run the Tracking Station and Mobile node Prototypes, the control computer sends commands and receives information through RS485 protocol to both systems. An US-324 UART to USB adaptor from Brainboxes™ is used as a USB-to-Serial adaptor (see Figure 5.1.1) in order to establish the communication with the UART configuration as represented in the frame structure of Table 5.2.1 (Top).

Depending on the target equipment, Tracking Station or Mobile Node unit, the Control Board might include just one or two SKY73210 Skyworks PLLs. The PLL has 10 configurable registers that can be programmed from the experiment control software independently to generate the desired RF carrier. In addition, the control software calculates the register values. Table 5.2.1 describes the configuration registers.

56,7Kbaud/sec	8 bit frame	No parity	1 bit stop
---------------	-------------	-----------	------------

Address	Name	Description
0	Divider Register	Synthesizer Divider Register
1	Divided MSB Register	Synthesizer Dividend MSB Register
2	Divided LSB Register	Synthesizer Dividend LSB Register
5	Reference Frequency Dividers Register	Reference Frequency Divider Index
6	Phase Detector/charge Pump Control Register	Phase detector Gain and Power Steering/Lock detected Enable
7	Power Down/Multiplexer Output Select Control Register	<ul style="list-style-type: none"> · Full Power Down · Synthesizer Power Down · Synthesizer Mode · Synthesizer Σ/Δ fractionality · Multiplexer Output Selection · Mux-out-pin Three-State Enable
8	Modulation Control Register	Not required
9	Modulation Data Register	

Table 5.2.1.- (Top) Data structure of the Configuration Message frame. (Bottom) The control registers of the PLL.

The software allows the configuration of such parameters and the transmission of a number of commands related with the operation of the prototype as mentioned above. Table 5.2.2 below summarizes such commands set.

Code	Command	Description
000	Reset	Sets the FPGA to initial state.
001	StartSeq	This commands controls the DSP block. It enables the measure procedure or sets PAE signal to high state a period of time depending on RFPW register.
010	Getsample	Transmission of a measured frequency sample.
011	PPL Configuration	Starts the PLL configuration. This command provides to the FPGA the number of bytes that will be sent with the configuration and which PLL should be configured.
100	PLL Word Configuration	PLL configuration words. These bytes will be sent to the PLL through the SPI.
101	SetRFPW	This command sets the RFPW register. This register contains the value that should be reach in the Power Amplifier Enable (PAE) counter while that signal remains in high state.
110	Power Control	Power amplifiers with 5.0 volts.
111	DDS Control	For DDS configuration and activation.

Table 5.2.2.- The command data for the experimental control application and FPGA IP cores running within the Mobile Node and Tracking Station.

As explained previously, the Mobile Node is able to synthesize the baseband sinusoidal carrier once the frequency measured of the incoming pulse is determined. The Mobile Node DSP block implements a Direct Digital Synthesis (DDS) procedure able to generate the desired carrier with a theoretical accuracy of the order of 0.1 Hz by means of a sinusoidal signal generation algorithm (CORDIC, also called Volder's Algorithm) and a DDS method for frequency synthesis [AD-1999] based on a phase interleave samples wheel, in a way that the number of samples skipped from the signal cycle is directly translated in a frequency increment.

Figure 5.2.2 shows the phase samples wheel as it is conceived for a DDS algorithm. As presented in the figure, and assuming that the samples presented as dots around the circumference represent the different signal values in a cycle (thus the cycle is repeated with successive turns over the samples wheel) the output frequency depends directly on the main frequency clock (i.e. the clock used to update each sample on the analog output channel), the total number of samples introduced here in an expression depending on the sample data word resolution (2^n) and the number of samples that are skipped on each cycle once the frequency must grow. Therefore, the longer the sample skip interval is, the higher the output frequency becomes. The cyclic character of the samples removed on each cycle, maintains the spectrum quality, since each time, a different subset of samples are removed, along successive cycles, all the samples are presented in the output channel.

Unfortunately, it is very complex to implement a real set-up being representative of the exploration scenario used in this thesis, which involves a mobile node travelling across an area of 1 km² with tracking stations at 1000 m distance to the origin (T_1) and more with speed resolutions in the order of cm/s. Therefore, we must use our current set-up in order to implement a solution characterize its performance in Doppler frequency measurement.

The experimental method used in this thesis is based in the fact that Doppler frequency shift in a RF signal is a physical fact that can be assumed as real. This means that the sequence of Doppler frequency shift values can be sent by the computer to the Mobile Node unit and, then, generated by the Mobile Node DDS engine to simulate the frequency shift profile and,

thus, the movement of the Mobile Node at a given velocity along a given trajectory. This way, we can simulate the travelling of the Mobile Node without the need of a very complex experimental set-up, since to implement in real life the travelling of a robot across such distances will force the need of an external position and speed determination of the robot to analyze experimental results by comparison.

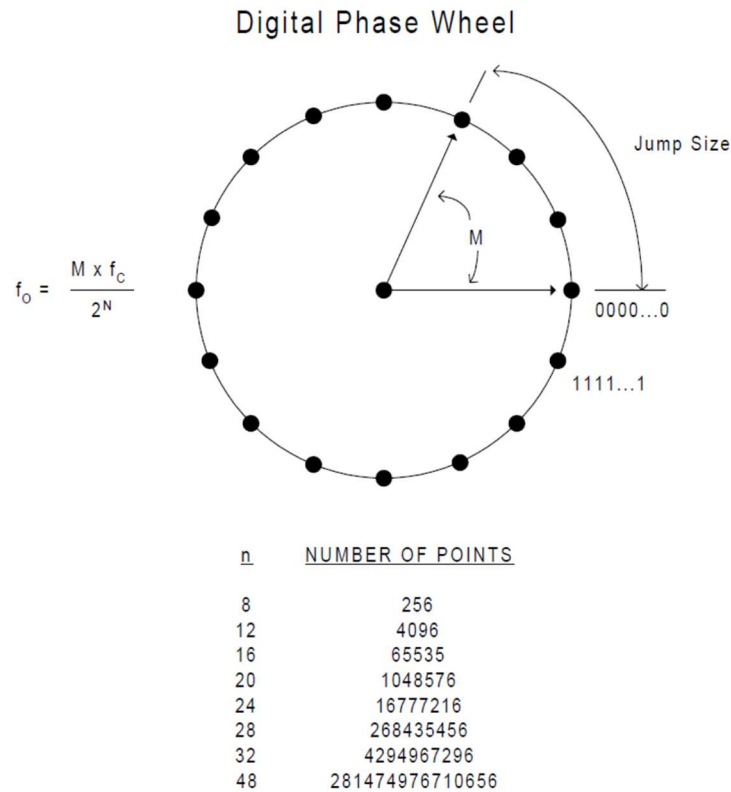


Figure 5.2.2.- Phase samples wheel for a Direct Digital Synthesis-based (DDS) frequency modulation procedure.

Following the abovementioned example, Figure 5.2.3 represents the frequency shift profile to be applied to the central frequency f_c by the mobile node.

The sequence of frequency shift values applied correspond to the theoretical model of the Doppler frequency shift observed at Tracking Station T_1 in our exploration scenario, with a central frequency $f_c = 400$ MHz.

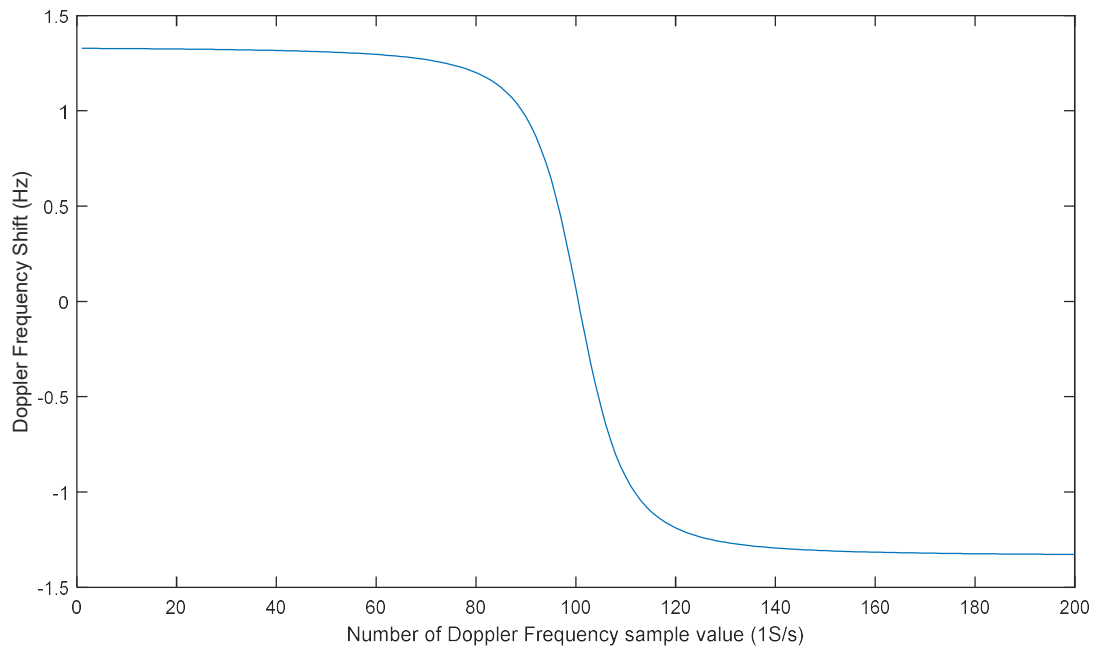


Figure 5.2.3.- Frequency shift measurement signal.

As it can be appreciated, the Tracking Station generates a 400,000 MHz carrier that is transmitted to the Mobile Node reception stage. Once the carrier reaches the Mobile Node, it reads the baseband frequency (at stationary conditions centered at 100 KHz) in order to use as the central frequency to be injected in the up-converter mixer stage.

In order to include the information of the Doppler frequency, since as it was explained above it is not efficient to implement a full scale real set-up to emulate the movement of the Mobile Node robot with enough position and velocity determination precision, the approach used for this experimental set-up is to implement the Doppler increments as pre-programmed values in the Mobile node.

Such pre-configured values of frequency are sent to the Mobile Node by the Control Computer via serial communications following the sequence of values presented in Figure 5.2.3, with an update rate of 1 Sample/s. This will provide the flexibility to implement specific radial velocity patterns and sequences to model real movement conditions, even towards different tracking stations.

Once modulated in frequency, the signal will be transmitted back to the Tracking Station where it will be demodulated (i.e. down converted) to 400,100 MHz in order to shift down in frequency the information (i.e. Doppler Shift) to the baseband IF at 100 KHz, and its frequency measured again.

Comparing the frequency shift produced with respect to the original signal transmitted from Tracking Station and with the theoretical Doppler sequence of values, the performance in the total Doppler component measurement will be obtained and, from it, the quality for the determination of radial velocity determined. The baseband is moved to 100 KHz in order to facilitate the frequency measurement since the accuracy of the frequency measurement increases at lower frequencies as explained in Chapter 3,

To assess the capability of the Mobile Node to generate different tones with a resolution in the order of 1Hz a series of sub-carrier tones were generated with a resolution of 1 Hz. Figure 5.2.4 shows the generation of a sequence of modulated sub-carriers centered on frequencies that increase at a rate of 1 Hz with an estimated error of 0.2Hz.

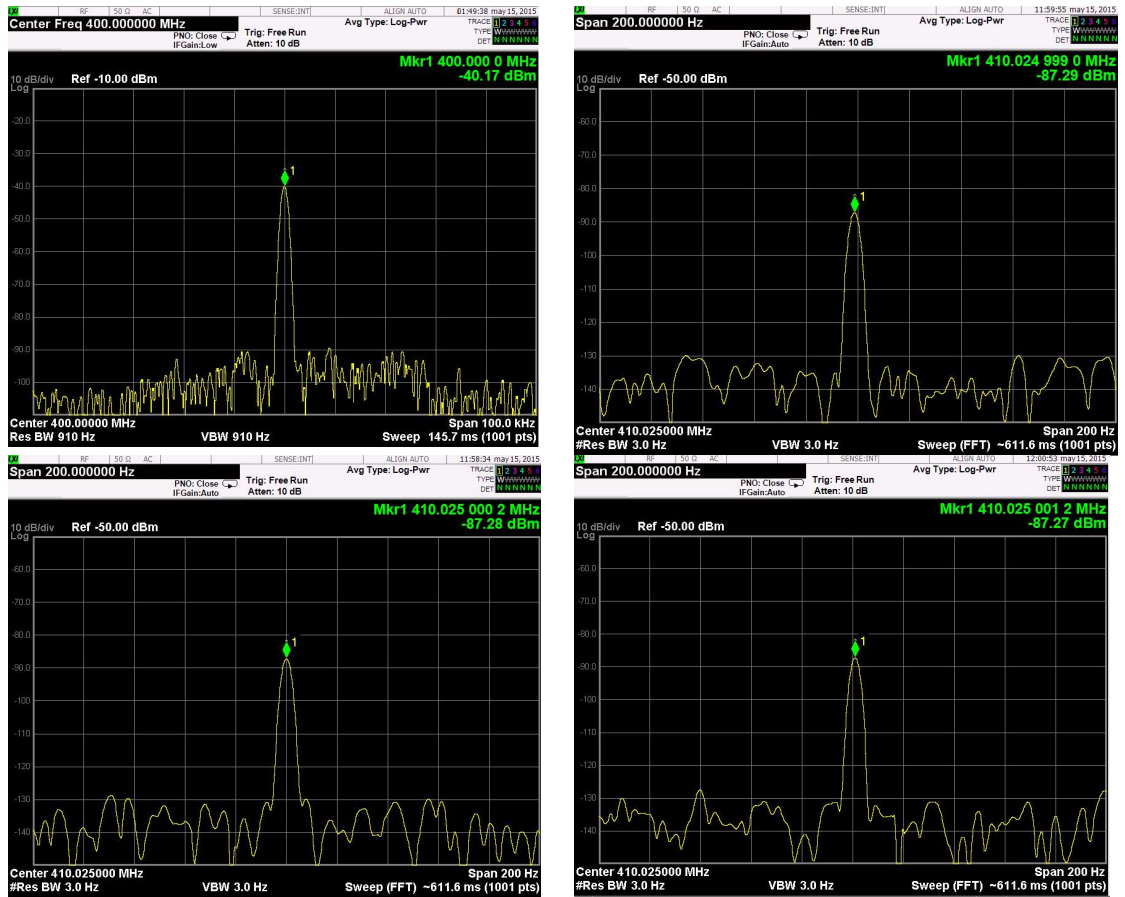


Figure 5.2.4.- DDS modulated tone over 400MHz main carrier, the detail is of the sub-carrier only, main carrier and image do not appear in the plots. The captures show the DDS sub-carrier tone centered at: (Top-Right) 24,999 KHz, (Bottom-Left) 25,000 KHz and (Bottom-Right) 25,001 KHz. The Top-Left plot corresponds to a detail of the main 400MHz carrier generated by the SKY72310 PLL.

The next figure shows an experimental campaign for the sequence of Doppler Frequency shift values shown in Figure 5.2.3 to, as mentioned above, simulate the couple Mobile Node-Tracking Station T_1 . For all measurements, the default bandwidth for the IF measurement was 5 KHz.

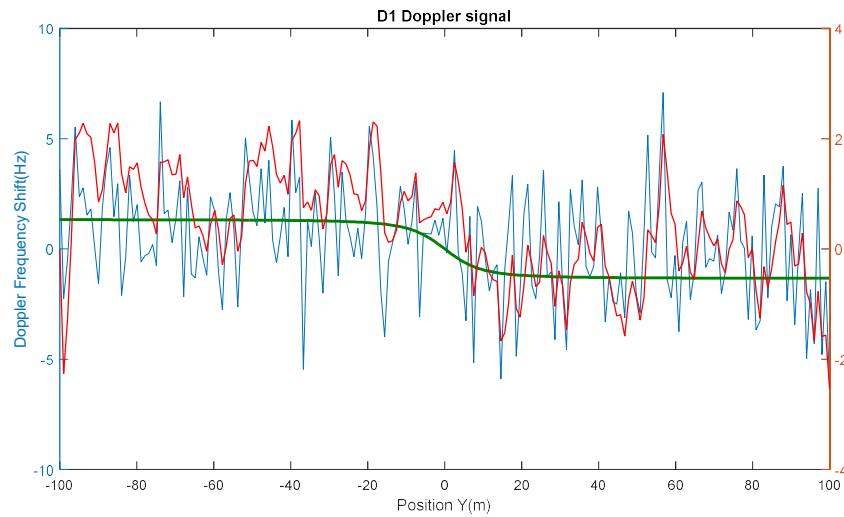


Figure 5.2.5.- D1 (Doppler signal at T₁ Station) signal measured (blue), Filtered (red) vs theoretical sequence of Doppler shift values (green). IF=100kHz. Kalman Filter constant $a=1.22$

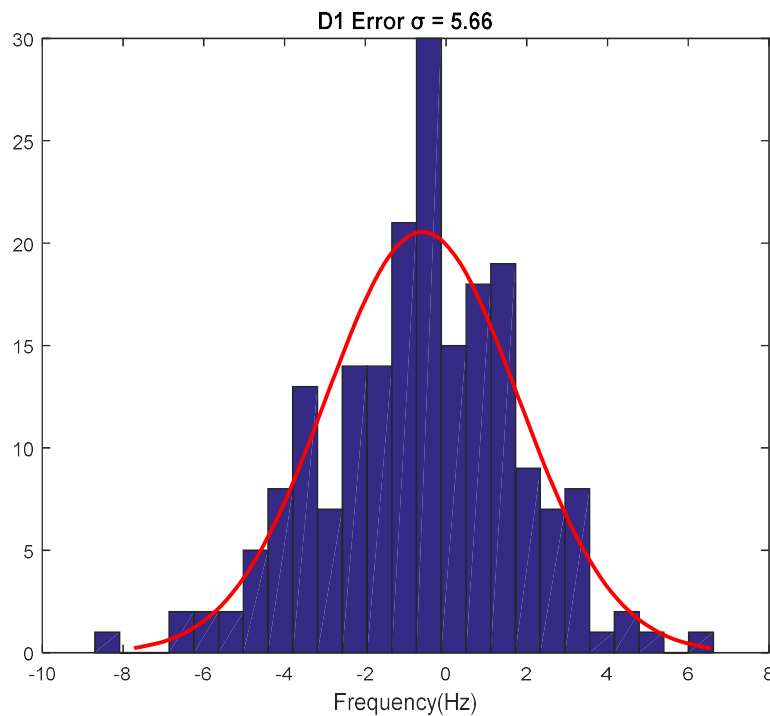


Figure 5.2.6.- D1 (Doppler signal at T₁ Station) measured error distribution (vs Theoretical sequence of values). IF=100kHz. Kalman Filter constant $a=1.22$

Nevertheless, a better response can be obtained from Kalman Filter adapting the covariance value ($a=1.04$ in *EKalman()* MATLAB function) in order to adapt to the new noise conditions, yielding the plot in Figure 5.2.7.

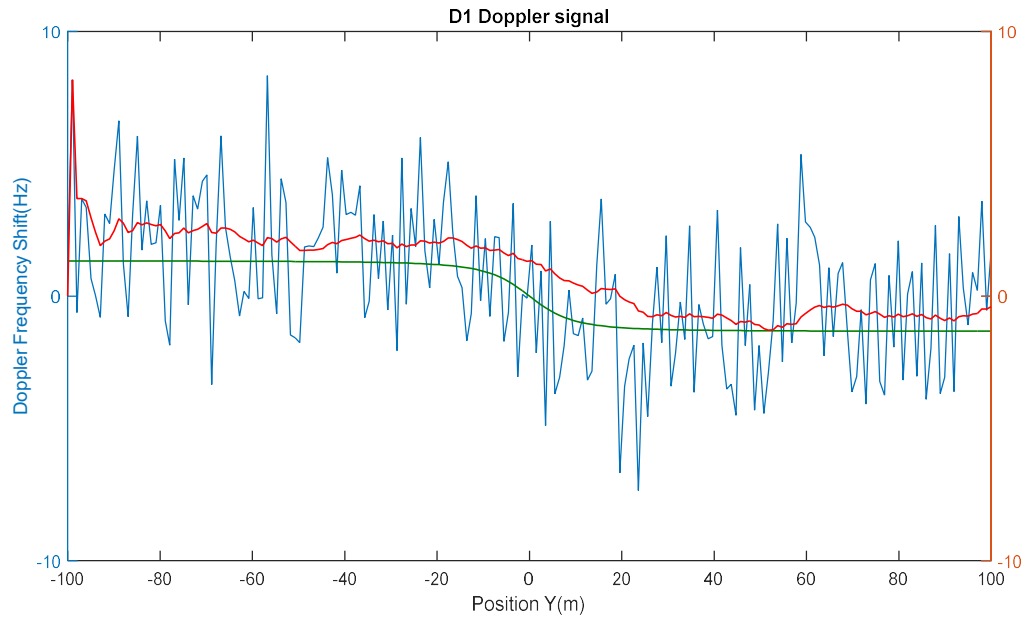


Figure 5.2.7.- D1 (Doppler signal at T_1 Station) signal measured (blue), Filtered (red) vs theoretical sequence of Doppler shift values (green). IF=100kHz, Kalman Filter constant $a=1.04$

It is appreciated a better estimation of the Doppler Frequency shift value with this new covariance value, and a clear bias in the Doppler frequency shift values, which could be the cause in the change of covariance. After an inspection of the system, it was concluded that the bias was generated at the PLL stages. The effect of new gain value (1.04) makes sense since, in Kalman filtering, higher gain values correspond to lower prediction errors, that is, when current observation values are the only information used to update the current state.

The next experimental campaign has been performed at an IF=25 kHz, in order to determine the influence of the time period duration in IF. Default bandwidth for the IF measurement keeps being 5 kHz.

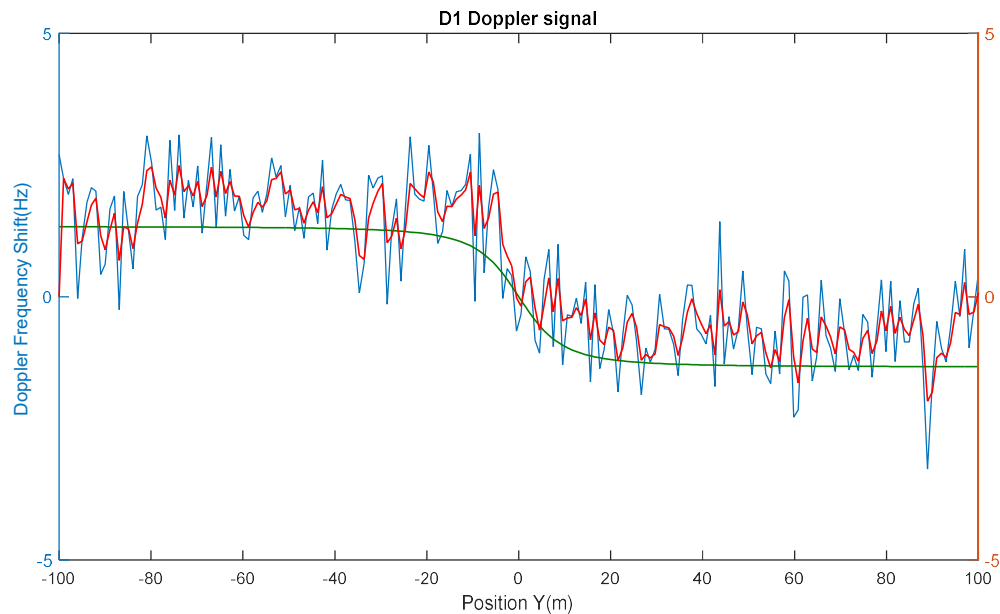


Figure 5.2.8.- D1 (Doppler signal at T_1 Station) signal measured (blue), Filtered (red) vs theoretical sequence of Doppler shift values (green). IF=25kHz, Kalman filter constant $a=1.04$

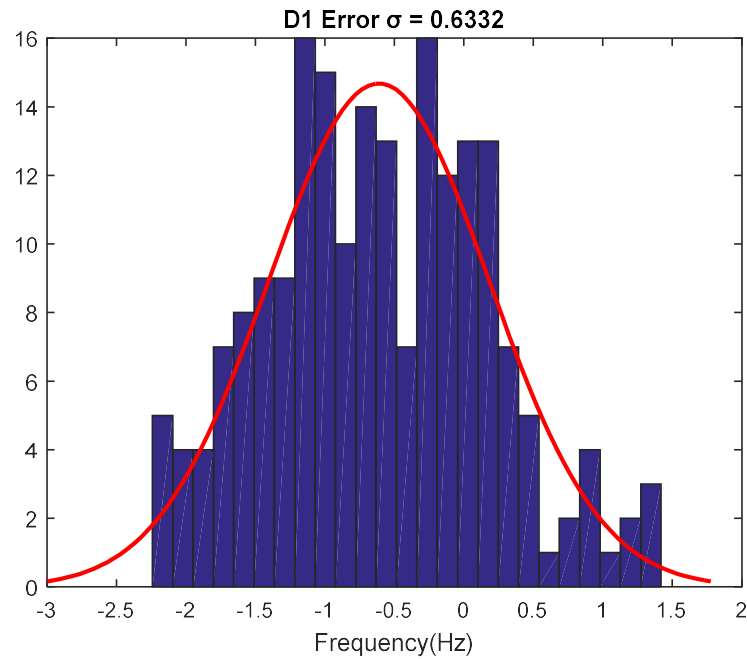


Figure 5.2.9.- D1 (Doppler signal at T₁ Station) measured error distribution (vs Theoretical sequence of values). IF=25kHz, Kalman filter constant a=1.04

As it can be appreciated, the lower IF value impacts dramatically on final error variance, passing from 5.66 to 0.63 as appreciated in Figure 5.2.9. This is consistent with the appreciation on jitter error for a given period value as explained in section 3.5.

5.3. Analysis of Results.

The experiments performed demonstrate the suitability of the proposed design for the determination of velocity that, in combination with Multilateration range determination techniques such as Time-Of-Arrival of RF location message frames, being compatible with the current system architecture, or even through the use of other external sensors, is a key parameter for the relative position determination of single mobile robots operating as autonomous mobile nodes across the defined exploration scenario, delimited by a number of Tracking stations. Some limitations have been identified, these are:

1. **Frequency deviation:** the technique used to measure the Doppler component of the incoming RF pulsed signal both in Mobile Nodes and Tracking Station consists, as explained above, in down-converting the RF signal to an IF (100kHz or 25 kHz in the above mentioned experiments) and measuring the frequency in time-domain by means of a slicer stage and a time measurement unit implemented in the main logic component (FPGA in this case). For experimental purposes, the real life behaviour of a Mobile Node travelling through the exploration scenario considered along this thesis is simulated by the generation of a sequence of RF tones with a frequency obtained by the addition of the central tone frequency f_c (400 MHz) with a sequence of Doppler shift values (Figure 5.2.3) via Direct Digital Synthesis (DDS). Two-Ways mode operation, as explained in chapter 2, introduces a compensation effect to temperature and aging frequency long-term drifts affecting the mobile node at a low implementation cost.

After the experiments performed, two disadvantages of this procedure have been detected:

- The IF is too low in up-conversion to allow the filtering of the image tone originally at 400 MHz. Once the $25\text{KHz} + f_{\text{Doppler Shift}}$ is mixed with the f_{RF} (400 MHz) RF carrier, two tones are produced by the mixing process: $f_{\text{RF}} + f_{\text{Doppler Shift}}$ and $f_{\text{RF}} - f_{\text{Doppler Shift}}$, both separated by $2 \cdot f_{\text{Doppler Shift}}$ (in the range of 50KHz). The Q factor of the filter that might suppress the image tone is too high to be implemented with discrete components ($Q > Q_{\text{min}} = f_{\text{RF}} / f_{\text{Doppler Shift}} = 16,000$); therefore, both tones are transmitted with this scheme. The main disadvantage here, though valid from the point of view of the measurement, is that transmitted power associated with the image tone is unnecessarily wasted, decreasing the power consumption efficiency of the Mobile Node.
- The Local Oscillator tone, which appears in the Mobile Node up-converter mixer output together with the direct and image tones as a consequence of the non-linear behaviour of the diode-based mixer, is very significant; which complicates its discrimination in base band once down-converted in Main Station.

In order to overcome these problems, two possible approaches have been identified:

- To perform the up-conversion in the Mobile Node at a higher modulation frequency (in the order of 1MHz – 2MHz instead the current 25KHz), either generating the DDS tone at such a higher frequency (which would not require a re-design of the current modulation scheme, further than tuning filter stages) or using a two-steps modulation scheme (two IFs consecutively, shown in Figure 5.3.1 below) in a way that the quality factor of the successive image rejection filters is low enough to be implemented with discrete components. Both approaches are feasible with the current RF architecture, providing an evolution of the current modulator design.

Concerning the costs associated to those alternatives, the double IF carrier modulation adds an additional PLL and a mixer whose conversion and driving losses must be compensated with the corresponding gain blocks, while the generation by DDS of a higher frequency base-band tone requires a faster logic that impacts on the power required by the FPGA.

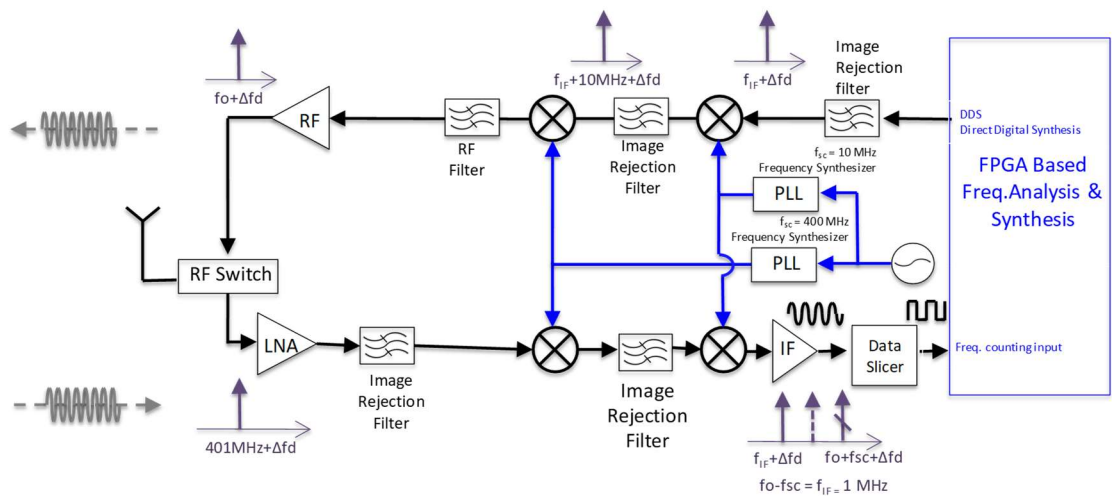


Figure 5.3.1.- Mobile Node RF architecture with double IF carrier modulation up-converter scheme to reject image tone in transmitted pulse.

Furthermore, the cost of having the IF at such high frequency in terms of SNR in time domain has been studied in chapter 3. As explained, the phase noise generated at RF frequency is more significant compared with a period of $1\mu\text{s}$ for $\text{IF}=1\text{ MHz}$ than with a period of $10\mu\text{s}$ corresponding with a $\text{IF}=100\text{KHz}$. As it was demonstrated, to operate at a low IF improves dramatically the SNR for the discrimination of the Doppler frequency shift.

- b. To implement a different modulation scheme to generate the Mobile Node transmitted RF signals that does not require image rejection filtering, specifically I/Q modulation. I/Q modulation consists of generating two modulated tones from the same modulating signal (IF) with two LO carriers, at the same frequency but with a difference of phase of 90° . The combination (i.e. addition) of both components after the mix, results in the cancellation of the image component. Therefore, in order to achieve the elimination of the image, it is not necessary to implement a highly selective filter but an Image-Rejection mixer based in a I/Q FM modulator. Different architectures exist, like the Hartley (used in the implementation proposed in the Figure 5.3.2 below) or Weaver (similar to Harley but combining 2 phase stages at $+45^\circ$ and -45° instead only one at 90°). The Figure 5.3.2 below shows the modulation scheme.

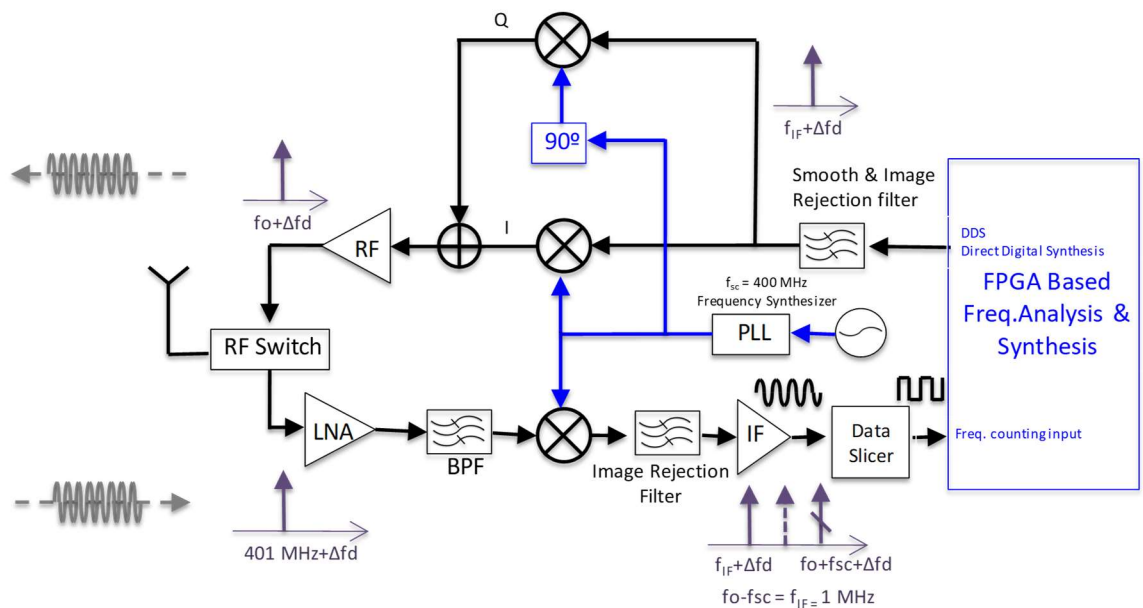


Figure 5.3.2.- Mobile node RF architecture with I/Q up-converter modulator to reject image tone in transmitted pulse. The addition of the quadrature components (I and Q) results in only one tone (Q) since the I components are cancelled by addition of conjugated phasors.

This modulation scheme allows the use of very low IF frequencies since a high Q filter is no longer needed, nevertheless, there are two important drawbacks with this design approach. First, the phase increment of 90° must be very precise in order to obtain an effective image rejection. This could be achieved with calibration algorithms or using topologies that implement phase self-compensation; and second, in order to achieve the aforementioned effective image rejection, the matching of the mixers involved (2 in case of Hartley and 4

Weaver topologies, but this number may scale up to 6 in phase self-calibration topologies) must be also very high.

In conclusion, the implementation of this modulation style is achievable only if the matching of mixers can be guaranteed and effective calibration algorithms can be implemented in the logic. Considering the characteristics of this project, the availability of logic power makes a phase self-calibration topology not necessary, reducing the design compromise to the matching of 2 mixers in case of Hartley topology (shown in Figure 5.3.2). However, if the possibility to integrate the system in an ASIC is available, more sophisticated quadrature mixers can be implemented guaranteeing a minimum mismatch between stages.

2. **Mixer sensitivity and conversion losses:** mixers are a key element in heterodyne and super-heterodyne RF stages since they allow the up and down conversion of frequency tones via FM modulation. This technique is used in both Tracking Station and Mobile node RF signal processing stages in order to generate the carrier tone in the Mobile Node and to measure the frequency of incoming carrier signals on both sides. Nevertheless, the sensitivity (meaning the minimum input power required to operate the mixer port) and insertion losses associated with the mixers introduce a need for additional signal power in order to operate within the signal quality range required by this application. This fact results in the necessity to include gain blocks in each mixer input that should compensate the sensitivity and insertion losses but will introduce an extra power consumption, more in the case of the down-converting stage in Main Station and Mobile Node since the mixer is fed with the received RF pulse. Therefore, the foreseen LNA stage must compensate the total losses.

Nevertheless, an alternative way to overcome this increment in signal power level would consist in substituting the current mixers, based on a traditional diode bridge topology with an active mixer topology based on transistors. This kind of mixers exhibit a higher sensitivity and lower insertion losses. For instance, whilst the nominal input power requirement in a diode-based mixer like the DBM-177 from Sirenza Microdevices (available in Space Grade version) is +7dBm with conversion loss of 7dB, an active mixer like the AD8343 from Analog devices (based on bipolar transistors) exhibit an input drive power as low as -10dBm.

The unavailability of this kind of technology in mixers designed for space missions in the UHF bands dissuaded us to choose this kind of components for the implementation of the breadboard, considering that a translation of the concept to a space-grade version would not be trivial. However, this possibility cannot be discarded at this point, assuming that the use of this kind of components might result in a dramatic increment of the performance.

Regarding this, two possibilities are identified:

- To qualify an existing active mixer for space applications.
- To implement the RF processing stage excluding the PLLs (mixer, filters and LNA in Main Station and two mixers coupled plus filters and LNA in Mobile Node) in a custom-made ASIC. This would guarantee both the performance associated with minimum driving and conversion losses, as well as the matching between both mixers in Mobile node, which will impact on the signal quality minimizing phase error between the down and up-conversion sides. Space Grade microelectronics technologies RF-CMOS 0,18 μm and SiGe/BiCMOS 0,35/0,18 μm from ATMEL have been identified as potential candidate processes for this approach.

5.4. Summary.

The tests performed have demonstrated that the measurement of frequency with enough resolution to extract the Doppler frequency shift component is possible with the architecture proposed, which was specifically designed for small robotic platforms.

Despite of the high levels of noise present in the experiment, since the noise is Gaussian and with known variance, Kalman filtering techniques can be used to significantly improve the SNR of the Doppler signal. As expected from theoretical studies and models analysed by simulation, as presented in Chapter 3, the noise present in the Doppler frequency signal improves at lower IF frequencies, although this poses a higher complexity at hardware level that is, as explained, feasible with a different modulation scheme.

Alongside this, the spectral bandwidth of the generated tone is very narrow, in the order of a few Hz as measured during the tests. This allows us to conclude that it is possible to synthesize a RF carrier tone with spectral purity and stability (i.e. in central frequency) enough to modulate the Doppler shift information with the RF signal generation topology.

Although important limitations have been found, the analysis presented in this section demonstrate that the lines to overcome them are clearly defined and, moreover, are both feasible and affordable in the scope of a future continuation activity.

Chapter 6.- Conclusions.

6.1. Introduction.

This final chapter presents a summary of the research performed during the development of this thesis, as well as a critical review of the results obtained, which are described and compared with the reference literature and the current state-of-the-art. Likewise, the limitations and issues encountered throughout the work are described and analyzed.

Finally, the chapter concludes with suggestions about future work directions along which the work developed here could be extended and enhanced.

6.2. Conclusions Overview.

This thesis is founded on the idea a novel robotic exploration paradigm based in an heterogeneous robotic distributed system, composed by a community of small exploration rovers and a number of stations that provide the necessary infrastructure to provide communication and localization services to the exploration robots. The concept has been justified from the engineering point of view, with a clear focus in the localization problem, by contextualizing it with a thorough review of the state-of-the-art, by developing the analysis of a specific implementation case and by evaluating the results obtained from a series of experiments performed on a breadboard specifically developed and built to validate this work.

Throughout the thesis, the importance of range measurement technologies has been highlighted as a key instrumental resource for robotic navigation. Undoubtedly, robotic systems will continue to play a leading role in space exploration as argued along Chapter 1 and, specifically of any orbiting body, not only planets or moons, but also comets and asteroids. To build a strategy of enhanced exploration in locations of great scientific interest is a natural evolution of the current approach in which space missions are often built upon a series of consecutive independent missions, without reuse of previous resources. The thesis proposes cooperative robotic systems as a more efficient paradigm that not only increases the reliability and performance over a single robot missions, but also allows the implementation of scalable robotic exploration infrastructure by reusing previous robots and stationary facilities.

It is clear that the information related to self-localization is crucial both at individual (for navigation and map construction) and at system levels, making possible an efficient distribution of research instrumental resources across the exploration area. Knowledge about the local environment is of critical importance to perform the mission, suitably designing and planning the paths to follow, developing navigation strategies and identifying the most interesting scientific targets and objects within the exploration area.

Initially an analysis that demonstrates the potential of distributed robotic systems for surface exploration has been performed. The inherent limitations of small platforms can be

compensated by an infrastructure formed for fixed or mobile stations acting as communication base stations and power production nodes (here called Tracking Stations).

Chapter two shows that this approach has intrinsic benefits when the distribution of precision clock sources is considered, thus making the hardware of the mobile robotic agents that form the distributed system simpler and less demanding in terms of stability and phase noise, factors that impact directly on the accuracy and precision of the location determination.

Along this chapter, a complete analysis of the mathematical foundations for the determination of position and velocity from range and Doppler frequency shift values has been developed both in general and specifically for the case under study. This analysis yielded relevant conclusions about which of the numerical processes involved in the determination of position and velocity vector of a Mobile Node travelling across the exploration scenario will require more computational power and the logic sequence of the different algorithms in order to make a complete simulation of the exploration scenario. In this sense, the works involved in Chapter 2 resulted in a mathematical model of the exploration scenario, a very useful tool that will make possible to understand the behavior of the different signals related with range and Doppler frequency shift related with the case under consideration.

Chapter 3 covered aspects related with the analysis of a practical implementation of the Mobile Node and Tracking Station RF systems. The research performed on the State-Of-The-Art concluded in a Two-Ways implementation due to its clear advantages in what concerns to bias and long term drift compensation despite of a higher hardware complexity and larger short term instability (i.e. phase noise). In this sense, an exhaustive analysis of the different noise sources was performed, both from the theoretical and experimental point of view, considering for this last aspect information about existing commercial oscillators through a critical review of the key parameters involved in the frequency stability. Finally, a complete model of the noise involved in both One-Way and Two-Ways has been developed and analyzed considering different parametric configurations. The possibility to compensate the error introduced in the range and Doppler frequency shift signals with Kalman filtering has been considered, and an implementation of Kalman filter has been implemented in MATLAB and tested obtaining positive results. The influence of the different noise sources, and their relevance in the final noise, as well as the impact of other parameter such as the IF value in the total SNR has been also analyzed.

Chapter 4 described the implementation of a prototype for both Mobile Node and Tracking stations RF systems, following the architecture topology defined in Chapter 3. Different aspects concerning the reliability and mass budget have been considered to obtain a hardware implementation that was compatible with a potential Space-Grade version.

Chapter 5 describes the different experiments performed, as well as their results. The results obtained reveal the suitability of the system to obtain position and velocity information in the application under consideration, and their further analysis resulted in a set of possibilities and ways to improve the performance accomplished.

The contributions of this thesis are of relevance to research topics addressing control theory of multi-agent robotic systems and robot navigation techniques. The application of the proposed methods for achieving a robust and efficient self-location method would positively impact the reliability and performance of distributed robotic systems, which combined with modern robotic agent control technologies, would provide an increase in, both efficiency and reliability, during the operation of surface exploration systems as well as in the definition of future robotic exploration mission.

The models contributed by this thesis could suppose a powerful tool in the simulation of other robotic systems in different exploration scenarios, involving a higher number of Tracking Stations, Mobile Nodes, different frequency bands in use, different noise contributions etc. making possible to test proposed systems and architectures as well as the measures to counteract noise in order to obtain precise location and velocity.

Furthermore, a novel approach for space exploration missions underlies here. This paradigm, as introduced in Chapter 1, is based on the scalability of distributed heterogeneous multi-robot systems, which would imply a more effective use of financial and technical resources, incrementally improving the affordability of future exploration missions and, consequently, helping to facilitate the future progress of space exploration.

6.3.Future Lines of Work

This thesis is comprehensive in terms of concept analysis and experimental validation, however, different research avenues could be explored to continue the work developed here.

A more in-depth analysis of the communication layers in order to allow a combination of communication capabilities with range determination could be developed as an independent line of work. This would lead to a more practical case of implementation of the range determination system in a real Software Defined Radio transceiver scheme in the line of Two-Tier or Three-Tier communication systems as presented in Chapter 2 Section 2.3.

In this sense, an analysis of the communication network topology for the mobile robotic agents is of huge interest in order to analyze the deployment of a distributed robotic system over the lunar surface, addressing aspects like radiofrequency detection range, BER achieved, communication protocols or use of this localization techniques in compatibility with existing communication standards like WiFi, UWB, Bluetooth, etc.

The radiofrequency signal proposed in this thesis for ranging and Doppler shift measurement is a simplified case but appropriate for a minimalist implementation case. Nevertheless, a more advanced analysis considering sophisticated modulation methods that allow the implementation of both range and Doppler shift with a better usage of the frequency spectrum resources, at a higher frequency band, could be performed.

The possibility to study more elaborated radiofrequency pulse configurations (methods involving time-modulation technologies like Impulse-Radio UWB, Gaussian pulses, etc.) or frequency-phase modulations to combine communications, ranging and Doppler measurement in single frames should provide interesting lines of work for other thesis projects.

Furthermore, extending the analysis case for the deployment of such a scalable robotic infrastructure to other exploration environments such as Mars or even orbital systems such as fractionated satellite systems could give rise to interesting results. The proposed paradigm would find an interesting application case in the design of distributed orbital instruments. This paradigm shares some of the advantages of the proposed distributed exploration systems in terms of reliability, efficiency, scalability etc. and, furthermore, the deployment of large scale distributed systems in space would yield sophisticated and highly sensitive

instruments supported by sensor fusion techniques. Currently, this kind of instrument arrangements are implemented by means of large deployable mechanical structures, which are technologically complex and bulky and often subject to single point failures.

The deployment of separated independent satellites incorporating single subsystems or components, organized in an array with a central node that concentrates and processes the information gathered by all the units is the central idea behind “Fractionated Space Systems”. For this to succeed, a precise control on the location and attitude of each of the satellites inside comprising the network is of key importance since the spatial organization is a critical parameter in applications such as interferometry. The methods described in this thesis could become a key asset for future fractionated system implementation, considering the advantage in terms of flexibility and robustness of radio communications, against optical based alternatives, which makes its very suitable for fractionated systems based in small satellite platforms.

In a similar line, the characteristics of the methods studied in this thesis are compatible with applications of navigation and orbit control in NEO proximity exploration missions. The low orbital velocities involved in the exploration of NEOs, like comets or asteroids, require precise navigation and orbit control instrumentation. The temperature profiles involved in this kind of mission make the application of optical instruments technically challenging, therefore, the use of RF instrumentation is usually considered.

Finally, evaluating the implementation of specific components such as the direct digital synthesis stage or frequency counter (that is, the base band electronics for carrier generation and Doppler shift measurement) or the high frequency side (modulation and demodulation stages) in specific technologies like RF CMOS that could achieve a more efficient implementation in terms of phase noise and power consumption has the potential to deliver a significant leap towards the possible use of this paradigm in a real mission scenario.

List of References

- [Crawford,I.-2012] Crawford, J. (2012). Dispelling the myth of robotic efficiency: why human space exploration. *Astronomy and Geophysics*, 53, pp.2.22-2.26.
- [White,R.J.-2001] White, R. and Averner, M. (2001). Humans in Space. *Nature*, February 409(22).
- [Osborne,J.R.-2012] Osborne, J., Brunskill, C., Jaguste, R., Johnson, C., Sharif, H., Silversides, I., Trey, B. and Vlasea, M. (2012). An interdisciplinary Approach to Human-Robot cooperation in Near-Term Exploration Scenarios. In: *Global Space Exploration Conference*. Washington D.C.: IAF.
- [Pedersen,L.-2003] Pedersen, L., Kortenkamp, D., Wettergreen, D. and Nourbakhsh, I. (2003). A Survey of Space Robotics. In: *7th International Symposium of Artificial Intelligence, Robotics and Automation in Space (i-SAIRAS)*.
- [Nechyba,M.C.-1995] Nechyba, M. and Xu, Y. (1995). Human-Robot Cooperation in Space: SM2 for New Space Station Structure. *IEEE Robotics and Automation Magazine*, 1(December).
- [Schenker,P.-2003] Schenker, P., Huntsberger, T., Pirjanian, P. and Baumgartner, E. (2003). Planetary Rover Developments Supporting Mars Exploration, Sample Return and Future Human-Robotic Colonization. *Autonomous Robots (Kluwer Academic)*, 14(1), pp.103-126.
- [Dudek,G.-1997] Dudek, G., Jenkin, M., Milios, E. and Wilkes, D. (1996). A Taxonomy for Multi-Agent Robotics. *Autonomous Robots (Springer)*, 3(4), pp.375–397.
- [Arai,T.-2002] Arai, T., Pagello, E. and Parker, E. (2002). Editorial: Advances in Multi-Robot Systems. *IEEE Transactions on Robotics and Automation*, 18(5).
- [Premvuti,S.-1996] Premvuti, S. and Wang, J. (1996). Relative position localizing system for multiple autonomous mobile robots in distributed robotic system: System design and simulation. *Robotics and Autonomous Systems (Ed. Elsevier)*, 18, pp.319-326.
- [Oliveira,S.-2016] Oliveira da Sa, A., Nedjah, N. and Mourelle, L. (2016). Distributed efficient localization in swarm robotics using Min-Max and Particle Swarm Optimization. *Expert Systems with Applications (Ed.Elsevier)*, 50, pp.55-65.
- [García,C.-2011] Garcia, C., Cardenas, P., Puglisi, L. and Saltaren, R. (2011). Design and Modelling of the multi-agent robotic system: SMART. *Robotics and Autonomous Systems (Ed. Elsevier)*, 60, pp.143-153.
- [Wang,L.-2016] Wang, L., Zhang, T. and Gao, F. (2016). Distributed cooperative localization with lower communication path Requirements. *Robotics and Autonomous Systems (Ed. Elsevier)*, 79, pp.26-39.
- [Maurette,M.-1999] Maurette, M. (1999). Robots for Lunar Exploration: Present and Future. *Adv. Space Res. COSPAR 1999.*, 23, pp.1849-1855.

- [Roumeliotis,I.-2002] Roumeliotis, S. and Bekey, G. (2002). Distributed Multirobot Localization. *IEEE Transactions on Robotics and Automation*, 18(5).
- [Franchi,A.-2009] Franchi, A., Oriolo, G. and Stegagno, P. (2009). Mutual Localization in a Multi-Robot System with Anonymous relative Position Measures. In: *IEEE/RSJ International Conference on Intelligent Robots and Systems*. St.Louis (USA).
- [NASA RP-1036] NASA (1980). ALSEP Termination Report. NASA Reference Publication 1036.
- [Bengtsson,O.-2003] Bengtsson, O. and Baerveldt, A. (2003). Robot localization based on scan-matching estimating the covariance matrix for the IDC algorithm. *Robotics and Autonomous Systems*, 44(1), pp.29-40.
- [Loevsky,I.-2010] Loevsky, I. and Shimshoni, I. (2010). Reliable and efficient landmark-based localization for mobile robots. *Robotics and Autonomous Systems*, 58, pp.520-528.
- [Indelman, V.-2014] Indelman, V., Nelson, E., Michael, N. and Dellaert, D. (2018). Multi-Robot Pose Graph Localization and Data Association from Unknown Initial Relative Poses via Expectation Maximization. In: *IEEE International Conference on Robotics & Automation (ICRA)*. Hong Kong.
- [Fox,D.-2000] Fox, D., Burgard, W., Kruppa, H. and Thrun, S. (2000). A Probabilistic Approach to Collaborative Multi-Robot Localization. *Autonomous Robots (Kluwer Academic)*, 8(1), pp.325-344.
- [ZAA-2013] ZA Architects. (2013). Mars colonization architecture study. [online] Available at: <http://www.zaarchitects.com/en/other/103-mars-colonization.html> [Accessed 3 Apr. 2018].
- [NASA-SP-2009-566] NASA (2009). Human Exploration of Mars. Design Reference Architecture 5.0. Nasa Reports.
- [GER-2013] ISECG International Space Exploration Coordination Group (2013). The Global Exploration Roadmap.
- [Nagatani,K.-2007] Nagatani, K., Yoshida, K., Kiyokawa, K., Yagi, Y., Adachi, T., Saitoh, H., Suzuki, T. and Takizawa, O. (2007). Development of a Networked Robotic system for Disaster Mitigation. In: *6th International Conference on Field and Service Robotics*.
- [Bayindir,L.-2007] Bayindir, L. and Sahin, E. (2007). A Review of Studies in Swarm Robotics. *Turk Journal of Electronic Engineering*, 15(2).
- [Kube,C.-2000] Kube, C. and Bonabeau, E. (2000). Cooperative Transport by Ants and Robots. *Robotics and Autonomous Systems*, 30, pp.85-101.
- [Schmajuk,N.A.-1999] Schmajuk, N., Weaver, E. and Szymanski, W. (1999). Adaptive Communication in Animals and Robots. *Signal Processing (Ed. Elsevier)*, 74, pp.71-87.
- [Carroll,P.-2012] Carroll, P., Zhou, S., Xu, X., Cui, J. and Willett, P. (2012). Underwater Localization and Tracking of Physical Systems, Article Id. 683919. *Journal of Electrical and Computer Engineering*, 2012.

- [Carroll,P.-2016] Carroll, P., Domrese, K., Zhou, H. and Zhou, S. (2016). Doppler-Aided localization of mobile nodes in an underwater distributed antenna system. *Physical Communication* (Ed. Elsevier), 18, pp.49-59.
- [Xiaorui,Z.-2017] Xiaorui, Z., Youngshik, K., Minor, M. and Chunxin, Q. (2017). *Autonomous Mobile Robots in Unknown Outdoor Environment*. 1st ed. CRC Press.
- [Parker L.-2007] Parker, L. (2007). Distributed Intelligence: Overview of the Field and its Application in Multi-Robot Systems. In: *AAAI Fall Symposium on Regarding the intelligence in distributed Intelligent Systems*.
- [Gouveia,B.D.-2015] Gouveia, B., Portugal, D. and Silva, D. (2015). Computational Sharing in distributed Robotic Systems: A Case Study on SLAM. *IEEE Transactions on Automation Science and Engineering*, 12(2).
- [Ahmad,A.-2013] Ahmad, A., Tipaldi, G., Lima, P. and Burgard, W. (2013). Cooperative robot localization and target tracking based on least squares minimization. In: *2013 IEEE International Conference on Robotics and Automation*. IEEE.
- [Burgard,W.-2005] Burgard, W., Moors, M., Stachniss, C. and Schneider, F. (2005). Coordinated Multi-Robot Exploration. *IEEE Transactions on Robotics*, 21(3), pp.376-386.
- [Marjovi,A.-2012] Marjovi, A., Chobdar, S. and Marques, L. (2012). Robotic Clusters: Multi-Robot systems as Computer Clusters. A Topological Map Merging Demonstration. *Robotics and Autonomous Systems* (Ed. Elsevier), 60(9), pp.1191-1204.
- [Schilling,K.-1996] Schilling, K. and Jungius, C. (1996). Mobile Robots for Planetary Exploration. *Control Engineering Practice*, 4(4), pp.513-524.
- [Khan-Mayberry,N.-2008] Khan-Mayberry, N. (2008). The lunar environment: Determining the health effects of exposure to moon dusts. *Acta Astronautica*, 63(7), pp.1006-1014..
- [Sanz,D.-2013] Sanz, D. (2013). Wireless sensors networks for planetary exploration: Experimental assessment of communication and deployment. *Advances in Space Research*, 52(6), pp.1029-1046.
- [Seedhouse,E.-2008] Seedhouse, E. (2008). *The Lunar Outpost. The Challenges of Establishing a Human Settlement on the Moon*. ISBN-13: 978-0387097466. 1st ed. Springer Praxis Books.
- [Stubbs,T.J.-2005] Stubbs, T., Vondrak, R. and Farrell, W. (2018). Impact of Lunar Dust on the Exploration Initiative. In: *36th LPSC Lunar and Planetary Science Conference*.
- [Vladimorova,T.-2007] Vladimorova, T., Bridges, P., Prasinos, G., Wu, X., Sidibeh, K., Barnhart, D., Jallad, A., Paul, J., Lapas, V., Baker, A., Maynard, K. and Magness, R. (2007). Characterizing Wireless Sensor Motes for Space Applications. In: *the 2nd NASA Conference on Adaptive Hardware and Systems (AHS 2007)*.
- [Thorbjornsen,N.-2010] Thorbjornsen, N., White, N., Brown, A. and Reeve, J. (2010). Radio Frequency (RF) Time-of-Flight Ranging for Wireless Sensor Networks. *Measurement Science and Technology*, 21(3).

- [Doberstein,D.-2012] Doberstein, D. (2012). Fundamentals of GPS receivers ISBN 978-1-4614-0408-8. New York, NY: Springer.
- [Allan,D.W.-1966] Allan, D. (1966). Statistics of atomic frequency standards. Proceedings of the IEEE, 54(2), pp.221-230.
- [Leeson,D.B.-1966] Leeson, D. (1966). A simple model of feedback oscillator noise spectrum. Proceedings of the IEEE, 54(2), pp.329-330.
- [Barnes,J.A.-1971] Barnes, J., Chi, A., Cutler, L., Healey, D., Leeson, D., McGunigal, T., Mullen, J., Smith, W., Sydnor, R., Vessot, R. and Winkler, G. (1971). Characterization of the Frequency Stability. IEEE Transactions of Instrumentation and Measurement, IM-20(2).
- [Demir.A-2000] Demir, A., Mehrotra, A. and Roychowdhury, J. (2000). Phase noise in oscillators: a unifying theory and numerical methods for characterization. IEEE Transactions on Circuits and Systems I: Fundamental Theory and Applications, 47(5), pp.655-674.
- [Shinde.S.-2014] Shinde, S. (2014). Review of Oscillator Phase Noise Models. In: International Multi-Conference of Engineers and Computer Scientists IMECS 2014.
- [Howe,D.A.-2003] Howe, D. and Tasset, T. (2003). Clock Jitter Estimation based on PM Noise Measurements. In: IEEE International Frequency Control Symposium and PDA Exhibition Jointly with the 17th European Frequency and Time Forum.
- [Kester.W-2009] Analog Devices (2009). MT-008 Tutorial: Converting Oscillator Phase Noise to Time Jitter. Analog Devices Technical Documentation.
- [Zhou,H.-2008] Carleton University, Systems and computer Engineering (2008). SCE-08-12: Frequency Accuracy & Stability Dependencies of Crystal Oscillators. Technical Report.
- [Baran,O.-2010] Baran, O. (2010). Modelling of the Phase noise in Space Communications Systems. Radioengineering, 19(1).
- [Amundson,I.-2009] Amundson, I. and Koutsoukos, X. (2009). A Survey on Localization for Mobile Wireless Sensor Networks. Mobile Entity Localization and Tracking in GPS-less Environments; Lecture Notes in Computer Science (Springer Verlag), 5801.
- [Munir,S.A.-2007] Munir, S., Ren, B., Jiao, W., Wang, B., Xie, D. and Ma, J. (2007). Mobile wireless sensor network: Architecture and enabling technologies for ubiquitous computing. In: International Conference on Advanced Information Networking and Applications Workshop. pp.Vol.2,113-120.
- [Amar,A.-2008] Amar, A. and Weiss, A. (2008). Localization of Narrowband Radio Emitters Based on Doppler Frequency Shifts. IEEE TRANSACTIONS ON SIGNAL PROCESSING, 56(11), pp.5500-5508.
- [Sha'ameri, A.-2017] Sha'ameri, A., Shehu, Y. and Amjad, F. (2017). Performance Comparison of Emitter Locating System for Low Level Airborne Targets. Defence Science and Technology Technical Bulletin, 10, pp.199-217.
- [Lanzisera-2006] Lanzisera, S., Lin, D. and Pister, K. (2006). RF Time of Flight Ranging for Wireless Sensor Network Localization. Proceedings of Fourth Workshop on Intelligent Solutions in Embedded Systems (WISES'06), June 2006, Austria.

- [Shuzhi,S.-2006] Shuzhi, S. and Lewis, F. (2006). *Autonomous Mobile Robots: Sensing, Control, Decision, Making and Applications*. 1st ed. Boca Ratón, FL: CRC Press.
- [Ollero-2005] Ollero Baturone, A. (2005). *Robótica: Manipuladores y Robots Móviles*. 1st ed. Marcombo Ed.
- [Ho,K.-1997] Ho, K. and Chan, Y. (1997). Geolocation of a Known Altitude Object From TDOA and FDOA Measurements. *IEEE Transactions on Aerospace and Electronic Systems*, 33(3), pp.770-783.
- [Seco,F.-2009] Seco, F., Jiménez, A., Prieto, C., Roa, J. and Koutsou, K. (2009). A Survey of Mathematical Methods for Indoor Localization. In: 6th IEEE International Symposium on Intelligent Signal Processing. IEEE.
- [Kusy,B.-2010] Kusy, B., Amundson, I., Sallai, J., Völgyesi, P., Lédeczi, A. and Koutsoukos, X. (2010). RF Doppler Shift-Based Mobile Sensor Tracking and Navigation. *ACM Transactions on Sensor Networks*, 7(1).
- [Fang,B.-2018] Fang, B. (2018). Simple Solutions for Hyperbolic and Related Position Fixes. *IEEE Transactions on Aerospace and Electronic Systems*, 26(5), pp.748-753.
- [Dongkyun,K.-2011] Dongkyun, K. (2011). Adaptive Extended Kalman Filter Based Geolocation Using TDOA/FDOA. *International Journal of Control and Automation*, 4(2), pp.49-58.
- [Deng,B.-2016] Deng, B., Yang, L., Sun, Z. and Peng, H. (2016). Geolocation of a Known Altitude Target Using TDOA and GROA in the Presence of Receiver Location Uncertainty. *International Journal of Antennas and Propagation*, 2016(1).
- [Anton,H.-2010] Anton, H. and Rorres, C. (2010). *Elementary Linear Algebra*. 10th ed. John Wiley & Sons.
- [Tate,K.-2015] Tate, K. (2015). Distances Driven in another Worlds. [online] www.space.com. Available at: <https://www.space.com/79-distances-driven-on-other-worlds.html> [Accessed 15 Apr. 2018].
- [MER-2016] Mars Exploration Rovers. (2016). NASA Jet Propulsion Laboratory. [online] Available at: <https://mars.nasa.gov/mer/mission/spacecraft.html> [Accessed 13 Apr. 2018].
- [MSL-2016] NASA Jet Propulsion Laboratory. (2016). Mars Science Laboratory. [online] Available at: <https://mars.nasa.gov/msl/mission/rover/> [Accessed 12 Apr. 2018].
- [Lei,Z.-2013] Lei, Z. (2013). Most Chang'e-3 science tools activated. [online] English China News. Available at: https://web.archive.org/web/20131218121731/http://news.xinhuanet.com/english/china/2013-12/18/c_132977079.htm [Accessed 12 Apr. 2018].
- [LRO-2015] Lunar Reconnaissance Orbiter. (2015). Soviet Union Lunar Rovers. [online] Available at: https://www.nasa.gov/mission_pages/LRO/multimedia/lroimages/lroc-20100318.html [Accessed 13 Apr. 2018].

- [MSL-2018] Mars Science Laboratory. Curiosity Rover. (2018). Where is Curiosity?. [online] Available at: <https://mars.nasa.gov/msl/mission/whereistherovernow/> [Accessed 22 Apr. 2018].
- [MER-2018] Mars Exploration Rovers. (2018). Opportunity Updates. [online] Available at: https://mars.nasa.gov/mer/mission/status_opportunityAll.html [Accessed 1 May 2018].
- [MER-2017] Mars Exploration Rovers. (2017). Mission Timeline: Surface Operations. [online] Available at: https://mars.nasa.gov/mer/mission/tl_surface_nav.html [Accessed 29 Apr. 2018].
- [GSF-2018] Moon Bulk Parameters. (n.d.). Moon-Earth Comparison. [online] Available at: <https://nssdc.gsfc.nasa.gov/planetary/factsheet/moonfact.html> [Accessed 2 May 2018].
- [Dogandzic, A.-2001] Dogandzic, A. and Nehorai, A. (2001). Cramér–Rao Bounds for Estimating Range, Velocity, and Direction with an Active Array. *IEEE Transactions on Signal Processing*, 49(6), pp.1122-1137.
- [Bamler, R.-1991] Bamler, R. (1991). Doppler Frequency Estimation and the Cramer-Rao Bound. *IEEE Transactions on Geoscience and Remote Sensing*, 29(3), pp.385-390.
- [Lie Ching Cheong, P.-1993] Lie Ching Cheong, P. (1993). Estimation of Doppler Frequency in the Presence of Noise. 1st ed. Ottawa: Defence Research Establishment Ottawa, pp.7-10.
- [McClanning, K.-2011] McClanning, K. (2011). *Wireless Receiver Design for Digital Communications*. 2nd ed. Scitech.
- [ITU-1990] ITU Report 1008-1. Reflection from the Surface of the Earth. (1990). 1st ed. ITU, pp.75-82.
- [Santina,M.-1996] Santina, M., Stubberud, A. and Hostetter, G. (1996). Quantization Effects. In: W. Levine, ed., *The Control Handbook*, 1st ed. CRC Press-IEEE Press, pp.301-311.
- [Kumar,A.-2016] Kumar, A., Shaik, F., Rahim, B.A., Kumar, D.S., n.d. *Signal and Image Processing in Medical Applications*, 2016th ed, Springer Briefs in Forensic and Medical Bioinformatics.
- [Saderzadeh,A.-2009] Saderzadeh, A., Sanaatiyan, M.M., Habbibnejad, K., Shahri, A., Momeni, H.R., 2009. Mobile Robot Navigation Error Handling Using an Extended Kalman Filter. *Journal of Computer Engineering* 1, 61–75.
- [Leśniak, A.-2009] Leśniak, A., Danek, T. and Wojdyła, M. (2009). Application of Kalman Filter to Noise Reduction in Multichannel Data. *Schedae Informaticae*, 1718(1), pp.63-73.
- [Oppenheim, A.-2014] Oppenheim, A. and Schaffer, R. (2014). *Discrete-Time Signal Processing*. 3rd ed. Pearson.
- [Henzler,S.-2010] Henzler, S. (2010). *Time-to-Digital Converters*. 1st ed. Springer Series in Advanced Microelectronics, pp.5-18.

- [Norton,J.-1994] Norton, J. and Cloeren, J. (1994). Precision Quartz Oscillators and Their Use Aboard Satellites. Johns Hopkins APL Technical Digest, 15(1), pp.30-37.
- [GIT-1963] Georgia Institute of Technology (1963). Quartz Crystal Aging Effects. Georgia Tech. Project No. A-680 (Unclassified). Alexandria, VA: Defense Documentation Centre for Scientific and Technical Information.
- [MML-1991] Martin Marietta Laboratories (1991). Radiation Sensitivity of Quartz Crystal Oscillators Experiment for the Long Duration Exposure Facility (LDEF). Baltimore, MD 21227: NASA Astrophysics Data System, pp.1523-1531.
- [TAC-1998] The Aerospace Corporation (1998). Low Dose Rate Proton Irradiation of Quartz Crystal Resonators. Aerospace Reports. Los Angeles, CA 90245: Space and Missiles System Center. Air Force Materiel Command.
- [Euler,F.-1980] Euler, F., Lipson, H. and Ligor, P. (1980). Radiation Effects in Quartz Oscillators, Resonators and Materials. In: 34th Annual Symposium on Frequency Control. IEEE.
- [Reitz,G.-2012] Reitz, G., Berger, T. and Matthiae, D. (2012). Radiation exposure in the moon environment. Planetary and Space Science, 74(1), pp.78-83.
- [Fang,Y.-2012] Fang, Y. and Chen, X. (2012). Design of Equal Precision Frequency Meter Based on FPGA. Engineering (Scientific Research SciREs), 4(1), pp.696-700.
- [Liu,Y.-2011] Liu, Y., Li, X. and Wang, W. (2011). High-Precision Frequency Measurement Using Digital Signal Processing. In: C. Cuadrado-Laborde, ed., Applications of Digital Signal Processing, 1st ed. InTech.
- [Hernandez,D.-2008] Hernandez-Balbuena, D., Sergiyenko, O., Tyrsa, V. and Burtseva, L. (2008). Method for fast and accurate frequency measurement. In: 16th IMEKO TC4 Symposium on Exploring New Frontiers of Instrumentation and Methods for Electrical Measurements. Torino, pp.367-373.
- [AD-1999] "A Technical Tutorial on Digital Signal Synthesis"; Analog Devices, 1999.
- [Navarro-2015] Navarro, D., Hon Ching, M., Carrera, L., Ferrando, M. and Baquero, M. (2015). Antenna Arrays for Unmanned Aerial Vehicle. Proceedings on Antennas and Propagation Conference (EuCAP) 2015, 1(1).
- [Kubota,T.-2003] Kubota, T., Kuroda, Y., Kunii, Y. and Nakatani, I. (2003). Small, light-weight rover "Micro5" for lunar exploration. Acta Astronautica, 52(2-6), pp.447-453.
- [Novara,M.-1998] Novara, M., Putz, P., Maréchal, L. and Losito, S. (1998). Robotics for lunar surface exploration. Robotics and Autonomous Systems, 23(1-2), pp.53-63.
- [Clark,J.-2007] Clark, J. and Fierro, R. (2007). Mobile robotic sensors for perimeter detection and tracking. ISA Transactions, 46(1), pp.3-13. Clark, J. and Fierro, R. (2007). Mobile robotic sensors for perimeter detection and tracking. ISA Transactions, 46(1), pp.3-13.

[Alibay,F.-2014] Alibay, F., Desaraju, V., Duda, J. and Hoffman, J. (2014). Fractionated robotic architectures for planetary surface mobility systems. *Acta Astronautica*, 95, pp.15-29.

[Olhoeft,G.-1974] Olhoeft, G., Frisillo, A. and Strangway, D. (1974). Electrical properties of lunar soil sample 15301,38. *Journal of Geophysical Research*, 79(11), pp.1599-1604.

[Anderson,R.-2005] Anderson, R., Buehler, M., Seshadri, S., Kuhlman, G. and Schaap, M. (2005). Dielectric Constant Measurements for Characterizing Lunar Soils. *Lunar and Planetary Science XXXVI*, 1(1).

[Hörz, F.-1991] Hörz, F., Grieve, R., Heiken, G., Spudis, P. and Binder, A. (1991). *Lunar Surface Processes (Lunar Sourcebook)*. 1st ed. Cambridge: Cambridge University Press.

[Kring,D.-2006] Kring, D. (2006). Parameters of Lunar Soils. In: *Lunar Exploration Initiative Workshop*.

Bibliography

Carlson, B. (1986). *Communication Systems: An Introduction to Signals and Noise in Electrical Communications*. 2nd ed. New York: McGraw-Hill.

Ge, S. and Lewis, F. (2006). *Autonomous Mobile Robots: Sensing, Control, Decision-making, and Applications*. 1st ed. Boca Ratón-FL: CRC/Taylor & Francis.

Pirsch, P. *Architectures for Digital Signal Processing*. Chichester: Wiley, 1998. Print.

Pedroni, V. (2010). *Circuit design and simulation with VHDL*. Cambridge [EE. UU.]: The MIT Press.

Griffin, M. and French, J. (1991). *Space Vehicle Design*. 1st ed. Washington D.C.: American Institute of Aeronautics and Astronautics.

Appendix 1. - Electric Diagrams and Interface Description.

Name	Type	Description
POWER BUS		
V51	PWR	+5 Volts Bus 1
V52	PWR	+5 Volts Bus 2
V33	PWR	+3,3 Volts Bus
V18	PWR	+1,8 Volts Bus
GND	GND	Ground
SYNC BUS		
XO1	CLK	Oscillator 1 CLK Output
XO2	CLK	Oscillator 2 CLK Output
CONTROL BUS		
PAE1	DO	RF Power Amplifier 1 Enable
PAE2	DO	RF Power Amplifier 2 Enable
RTS1	DO	Rx/Tx Amplifiers Board 1 Switch Control
RTS2	DO	Rx/Tx Amplifiers Board 2 Switch Control
SM1	DO	Switch Matrix Chain 1
SM2	DO	Switch Matrix Chain 2
SDI11	DO	PLL / RF Board 1 Serial configuration Input
SEN11	DO	PLL / RF Board 1 Configuration Enable
SCK11	DO	PLL / RF Board 1 Serial Configuration Clock
LCK11	DI	PLL / RF Board 1 Lock
FLT11	DO	PLL / RF Board 1 Filter selection
PEN11	DO	PLL / RF Board 1 Enable
SDI12	DO	PLL / RF Board 2 Serial configuration Input
SEN12	DO	PLL / RF Board 2 Configuration Enable
SCK12	DO	PLL / RF Board 2 Serial Configuration Clock
LCK12	DI	PLL / RF Board 2 Lock
FLT12	DO	PLL / RF Board 2 Filter selection
PEN12	DO	PLL / RF Board 2 Enable
DDS1	DO	Direct Digital Synthesis Output 1
DDS2	DO	Direct Digital Synthesis Output 2
DS1	DI	Doppler Input 1 (IF signal carrying the Doppler component from chain 1)
DS2	DI	Doppler Input 2 (IF signal carrying the Doppler component from chain 2)

Table A.1.1.- Mobile Node Control Unit Interface Bus signals list.

Name	Type	Description
POWER BUS		
V51	PWR	+5 Volts Bus 1
V52	PWR	+5 Volts Bus 2
V33	PWR	+3,3 Volts Bus
V18	PWR	+1,8 Volts Bus
GND	GND	Ground
SYNC BUS		
XO1	CLK	Oscillator 1 CLK Output
XO2	CLK	Oscillator 2 CLK Output
CONTROL BUS		
PAE1	DO	RF Power Amplifier 1 Enable
PAE2	DO	RF Power Amplifier 2 Enable
RTS1	DO	Rx/Tx Amplifiers Board 1 Switch Control
RTS2	DO	Rx/Tx Amplifiers Board 2 Switch Control
SM11	DO	Switch Matrix Chain 1
SM12	DO	Switch Matrix Chain 2
SM21	DO	Switch Matrix RHCP Antenna
SM22	DO	Switch Matrix LHCP Antenna
SDI11	DO	PLL1 / RF Board 1 Serial configuration Input
SEN11	DO	PLL1 / RF Board 1 Configuration Enable
SCK11	DO	PLL1 / RF Board 1 Serial Configuration Clock
LCK11	DI	PLL1 / RF Board 1 Lock
FLT11	DO	PLL1 / RF Board 1 Filter selection
PEN11	DO	PLL1 / RF Board 1 Enable
SDI21	DO	PLL2 / RF Board 1 Serial configuration Input
SEN21	DO	PLL2 / RF Board 1 Configuration Enable
SCK21	DO	PLL2 / RF Board 1 Serial Configuration Clock
LCK21	DI	PLL2 / RF Board 1 Lock
FLT21	DO	PLL2 / RF Board 1 Filter selection
PEN21	DO	PLL2 / RF Board 1 Enable
SDI12	DO	PLL1 / RF Board 2 Serial configuration Input
SEN12	DO	PLL1 / RF Board 2 Configuration Enable
SCK12	DO	PLL1 / RF Board 2 Serial Configuration Clock
LCK12	DI	PLL1 / RF Board 2 Lock
FLT12	DO	PLL1 / RF Board 2 Filter selection
PEN12	DO	PLL1 / RF Board 2 Enable
SDI22	DO	PLL2 / RF Board 2 Serial configuration Input
SEN22	DO	PLL2 / RF Board 2 Configuration Enable
SCK22	DO	PLL2 / RF Board 2 Serial Configuration Clock
LCK22	DI	PLL2 / RF Board 2 Lock
FLT22	DO	PLL2 / RF Board 2 Filter selection
PEN22	DO	PLL2 / RF Board 2 Enable
DS1	DI	Doppler Input 1 (IF signal carrying the Doppler component from chain 1)
DS1_S	DI	Doppler Input 1 Strength (0 if no valid signal, 1 if valid)
DS2	DI	Doppler Input 2 (IF signal carrying the Doppler component from chain 2)
DS2_S	DI	Doppler Input 2 Strength (0 if no valid signal, 1 if valid)

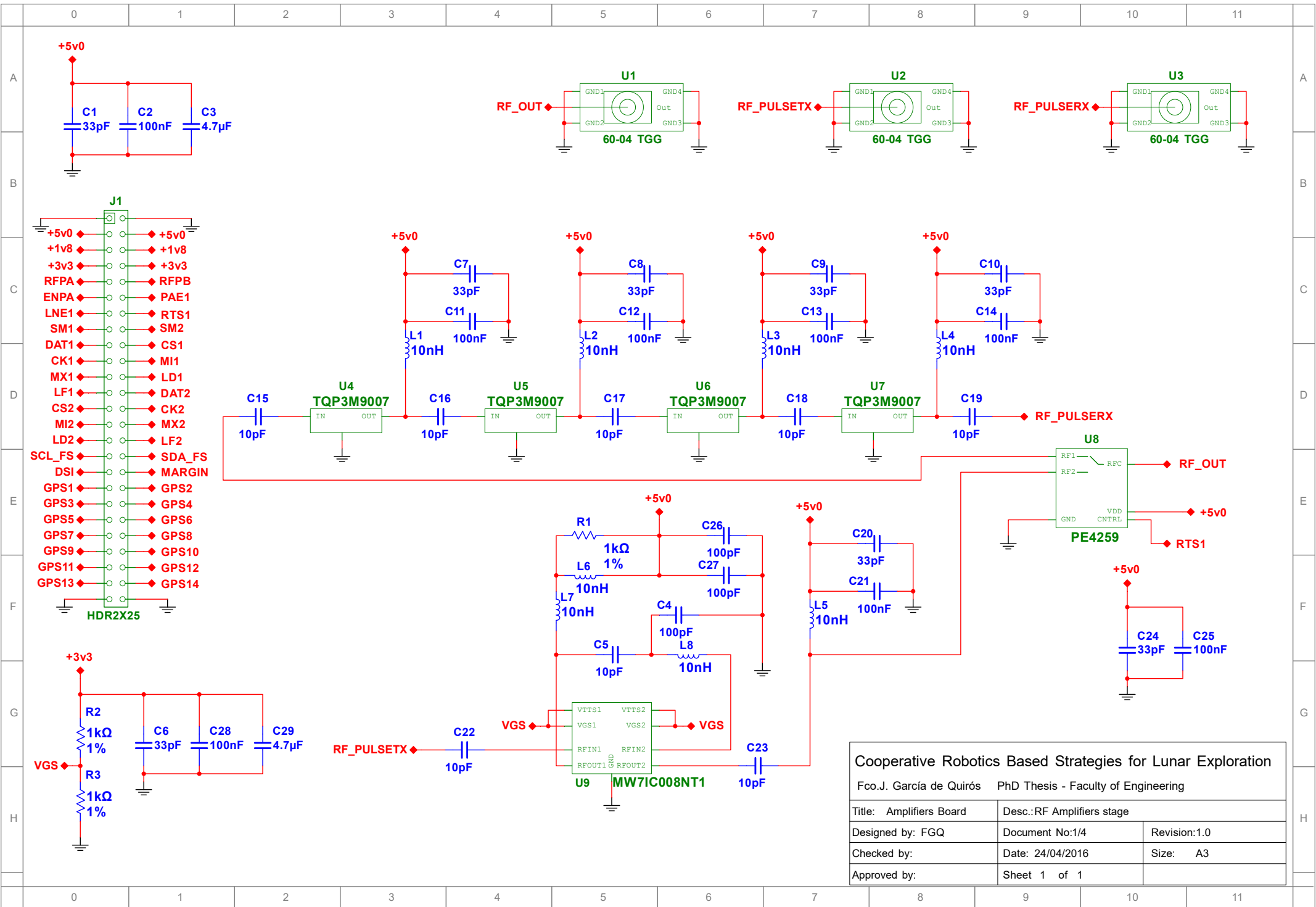
Table A.1.2.- Tracking Station Control Unit Interface Bus signals list.

Name	Type	Description
POWER CONTROL		
UV51	DI	+5 Volts Bus 1 Undervoltage
UV52	DI	+5 Volts Bus 2 Undervoltage
EV51	DO	Enable +5V Bus 1
EV51	DO	Enable +5V Bus 2
CBAT1 ¹	DO	Battery 1 connected
CBAT2 ¹	DO	Battery 2 connected
X1 & X2		
XO1	CLK	Oscillator 1 CLK Output
XO2	CLK	Oscillator 2 CLK Output
EXO1	DO	Enable Oscillator 1
EXO2	DO	Enable Oscillator 2
IO1 & IO2		
DA1	DIO	Line A RS422 (IO1)
DB1	DIO	Line B RS422 (IO1)
DA2 ²	DIO	Line A RS422 (IO2)
DB2 ²	DIO	Line B RS422 (IO2)

Table A.1.3.- Tracking Station and Mobile Node Control Unit internal buses signals list.
(Notes: ¹ Signal only in Mobile Node, ² Signal only in Tracking Station).

Name	Type	Description
I/F CONNECTOR 1		
DA1	DIO	Line A RS422 RS-422 Digital (+5, -5 V)
DB1	DIO	Line B RS422 RS-422 Digital (+5, -5 V)
BAT1+	PWR	Battery 1 Terminal + POWER +4,2V, 10A Imax
BAT1-	PWR	Battery 1 Terminal - POWER GND, 10A Imax
BAT2+ ¹	PWR	Battery 2 Terminal + POWER +4,2V, 10A Imax
BAT2- ¹	PWR	Battery 2 Terminal - POWER GND, 10A Imax
I/F CONNECTOR 2 ²		
DA2 ²	DIO	Line A RS422 (IO2) RS-422 Digital (+5, -5 V)
DB2 ²	DIO	Line B RS422 (IO2) RS-422 Digital (+5, -5 V)
BAT2+	PWR	Battery 2 Terminal + POWER +4,2V, 10A Imax
BAT2-	PWR	Battery 2 Terminal - POWER GND, 10A Imax

Table A.1.4.- I/F connectors signals list.(Notes: ¹ Only in Mobile Node, ² Only in Tracking Station)

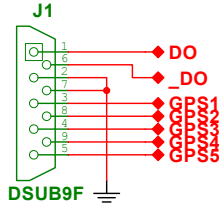
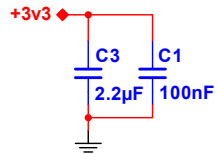
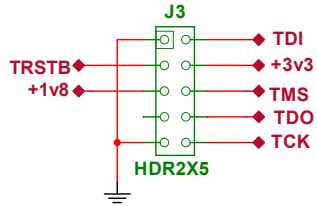


Cooperative Robotics Based Strategies for Lunar Exploration

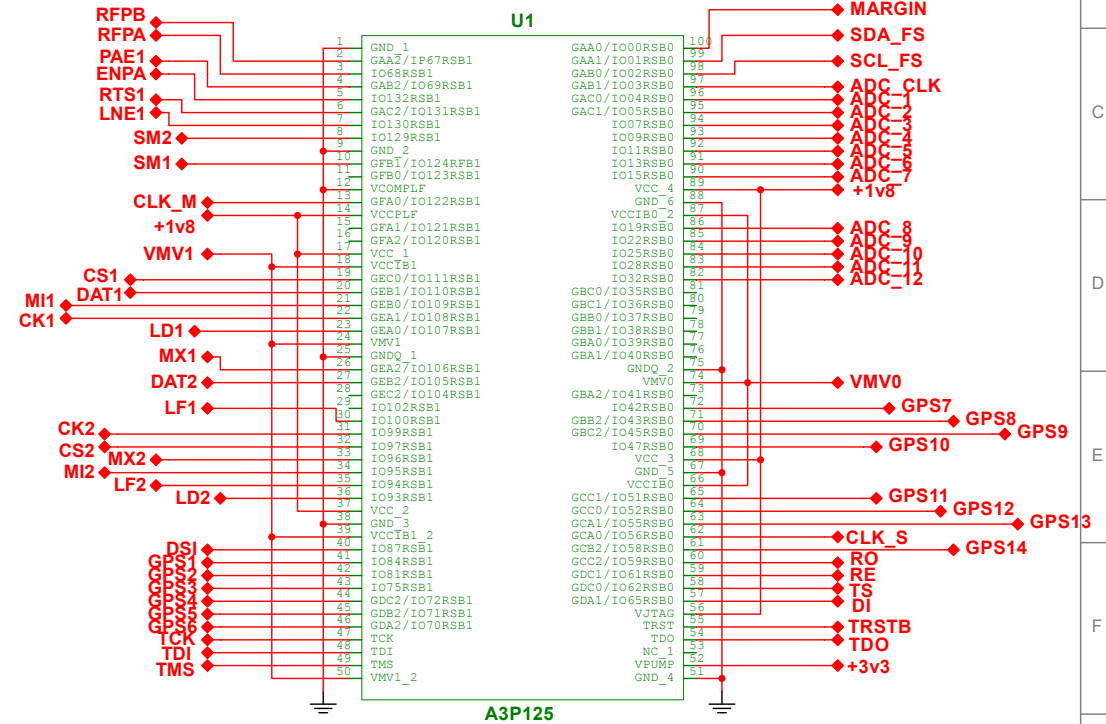
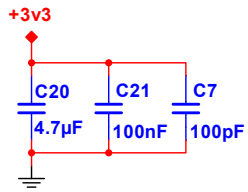
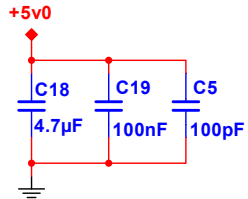
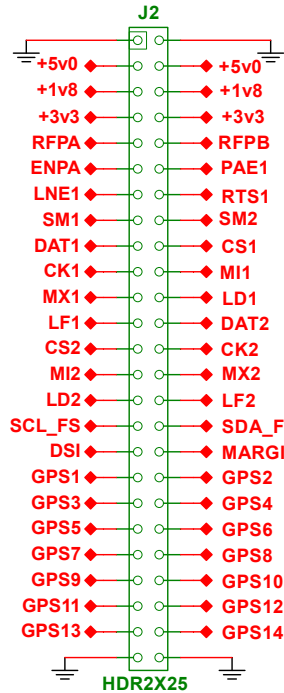
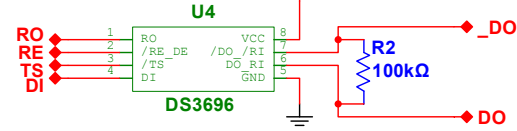
Fco.J. García de Quirós PhD Thesis - Faculty of Engineering

Title: Amplifiers Board		Desc.: RF Amplifiers stage	
Designed by: FGQ	Document No:1/4	Revision:1.0	
Checked by:	Date: 24/04/2016	Size: A3	
Approved by:	Sheet 1 of 1		

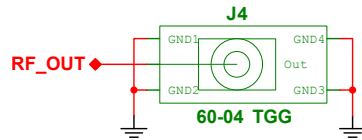
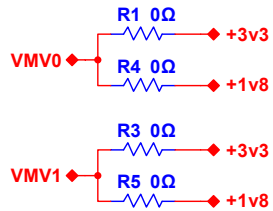
FPGA Programmer Connector



RS485 Driver +5v0



Interface Bus Connector

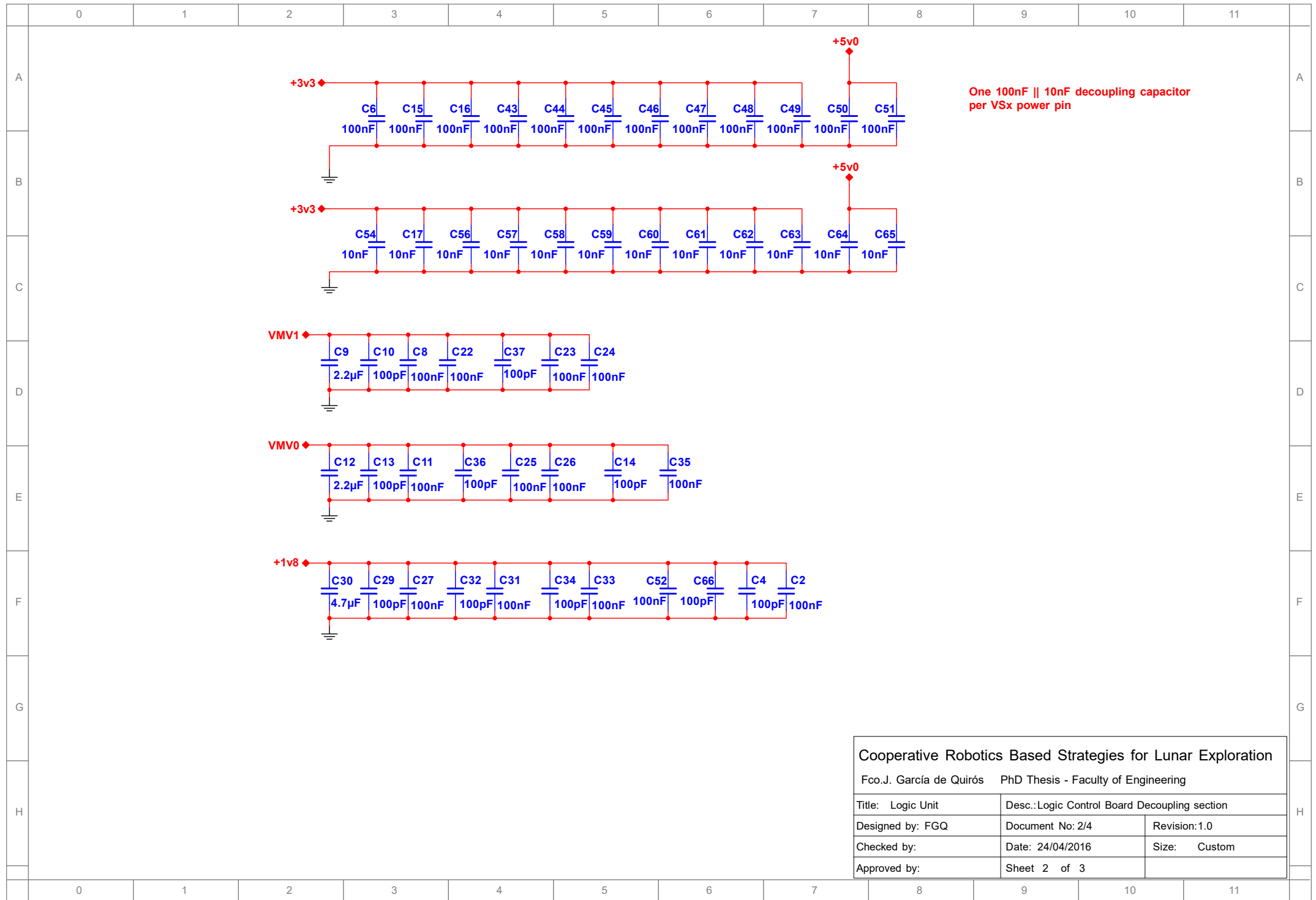


RF Output Connectors

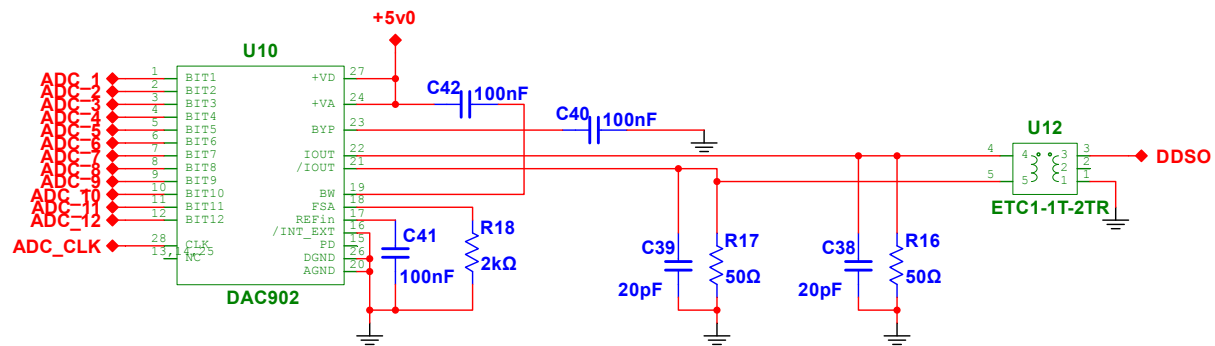
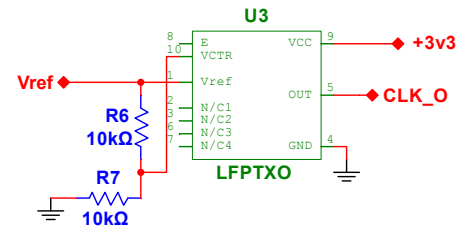
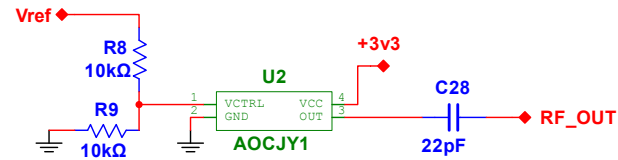
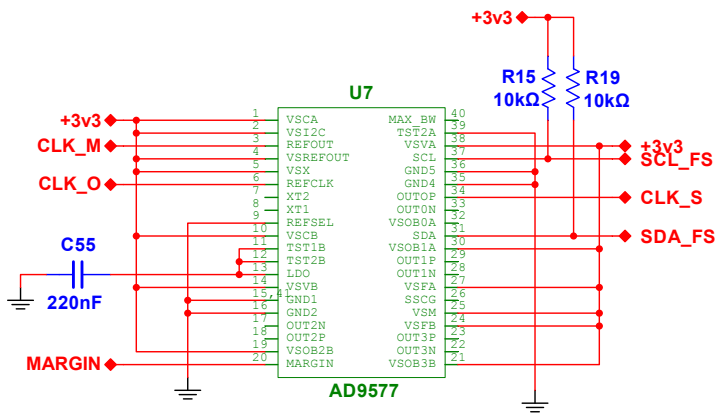
Cooperative Robotics Based Strategies for Lunar Exploration

Fco.J. García de Quirós PhD Thesis - Faculty of Engineering

Title: Logic Unit		Desc.: Logic Interface Control Board	
Designed by: FGQ	Document No: 2/4	Revision: 1.0	
Checked by:	Date: 24/04/2016	Size: A3	
Approved by:	Sheet 1 of 3		



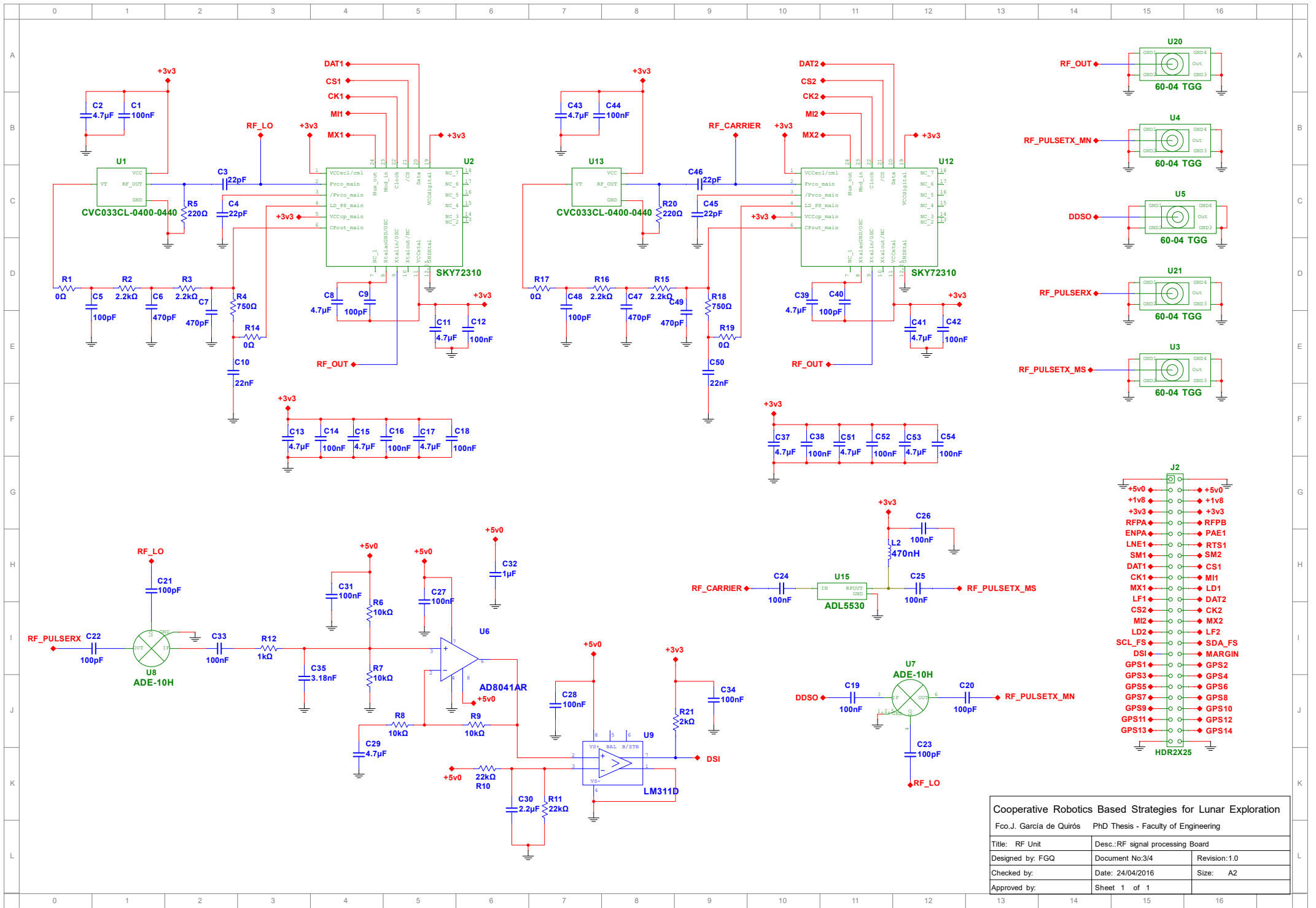
Cooperative Robotics Based Strategies for Lunar Exploration		
Fco.J. García de Quirós PhD Thesis - Faculty of Engineering		
Title: Logic Unit	Desc.: Logic Control Board Decoupling section	
Designed by: FGQ	Document No: 2/4	Revision: 1.0
Checked by:	Date: 24/04/2016	Size: Custom
Approved by:	Sheet 2 of 3	



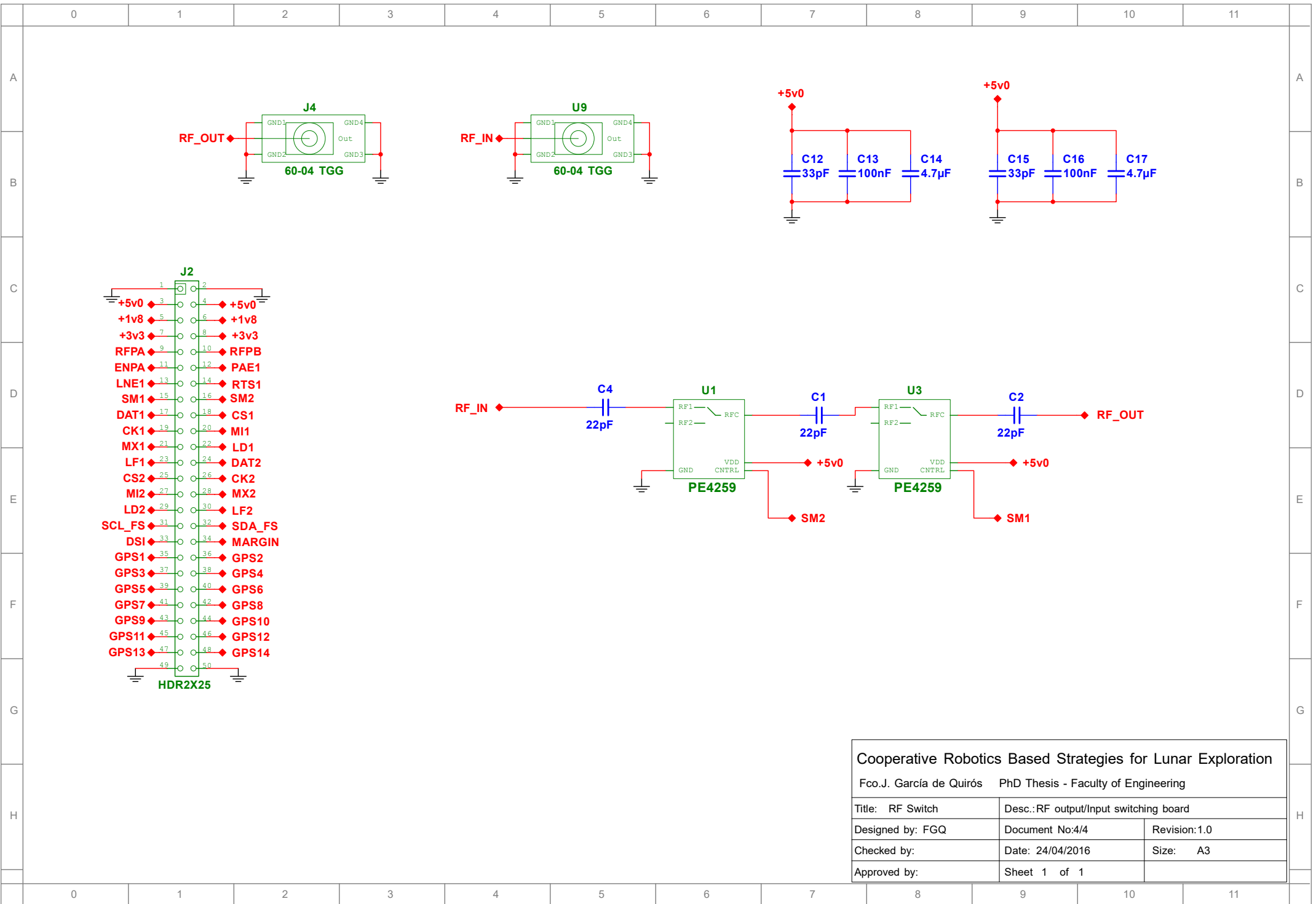
Cooperative Robotics Based Strategies for Lunar Exploration

Fco.J. García de Quirós PhD Thesis - Faculty of Engineering

Title: Logic Unit	Desc.: Signal synthesis section	
Designed by: FGQ	Document No:2/4	Revision:1.0
Checked by:	Date: 24/04/2016	Size: A3
Approved by:	Sheet 3 of 3	



Cooperative Robotics Based Strategies for Lunar Exploration		
Fco.J. García de Quirós PhD Thesis - Faculty of Engineering		
Title: RF Unit	Desc.: RF signal processing Board	
Designed by: FGQ	Document No:3/4	Revision:1.0
Checked by:	Date: 24/04/2016	Size: A2
Approved by:	Sheet 1 of 1	



Cooperative Robotics Based Strategies for Lunar Exploration		
Fco.J. García de Quirós PhD Thesis - Faculty of Engineering		
Title: RF Switch	Desc.: RF output/Input switching board	
Designed by: FGQ	Document No:4/4	Revision:1.0
Checked by:	Date: 24/04/2016	Size: A3
Approved by:	Sheet 1 of 1	

Appendix 2. – MATLAB Functions Code.

FUNCTION: *DopplerCalc_VN()*

```
function [D,R]=DopplerCalc_VN(fc,V1,X0,Y0,t0,tf,n)
% Doppler frequency increment for a mobile node moving at:
% - Constant velocity.
% - Trajectory: linear x=X0
% OUTPUT:
% D: Doppler frequency shift (Hz) vector (n) at origin
% R: Distance from mobile node to tracking station at origin vector (n)
% INPUT:
% fc: Transmitted RF signal frequency (Hz)
% V1: mobile node velocity (m/s)
% X0: X0 coordinate (m)
% Y0: Initial y value (m)
% to: initial time (s)
% tf: final time (s)
% n: number of samples (integer)
% Example: DopplerCalc_VN(400e6,2,80,-100,0,100,200);
% fc=400MHz,v=2m/s,X0=80m,Y0=-100m,t0=0s,tf=100s,n=200values

c=299792458; % Speed of light in vacuum (m/s)
D=zeros(1,n);
R=zeros(1,n);
t=linspace(t0,tf,n);
for i=1:n
    P1=sqrt((X0^2)+(Y0^2)+((V1^2)*(t(1,i)^2))+(2*Y0*V1*t(1,i)));
    D(1,i)=-((fc*V1)/(c*P1))*(Y0+(V1*t(1,i)));
    R(1,i)=P1;
end
end
```

FUNCTION: *RangeCalc_VN()*

```

function [D1,D21,D31,R1,R21,R31]=RangeCalc_VN(fc,V1,X0,Y0,T2x,T3y,t0,tf,n)
% Distance and Doppler frequency shift from Mobile node to
% the tracking stations Ti i=1 to 3
% with a trajectory:
% - Constant velocity V1
% - Trajectory: linear x=X0
% OUTPUT:
% D1: Doppler frequency shift (Hz) vector (n) at T1
% D21: Doppler frequency shift (Hz) vector (n) at T2
% D31: Doppler frequency shift (Hz) vector (n) at T3
% R1: Distance from mobile node to tracking station (m) vector (n) at T1
% R21: Distance from mobile node to tracking station (m) vector (n) at T2
% R31: Distance from mobile node to tracking station (m) vector (n) at T3
% INPUT:
% fc: Transmitted RF signal frequency (Hz)
% V1: mobile node velocity (m/s)
% X0: X0 coordinate of mobile node (m)
% Y0: Initial y value of mobile node (m)
% T2x: X coordinate of Tracking Station T2 (T2y=0)
% T3y: Y coordinate of tracking Station T3 (T3x=0)
% to: initial time (s)
% tf: final time (s)
% n: number of samples (integer)
% Example: DopplerCalc_VN(400e6,2,80,-100,0,100,200);
% fc=400MHz,v=2m/s,X0=80m,Y0=-100m,t0=0s,tf=100s,n=200values

c=299792458; % Speed of light in vacuum (m/s)
R1=zeros(1,n);
R21=zeros(1,n);
R31=zeros(1,n);
t=linspace(t0,tf,n);
for i=1:n
    R1(1,i)=sqrt((X0^2)+(Y0^2)+((V1^2)*(t(1,i)^2))+(2*Y0*V1*t(1,i)));
    R21(1,i)=sqrt((X0^2)+(T2x^2)-
(2*X0*T2x)+(Y0^2)+((V1^2)*(t(1,i)^2))+(2*Y0*V1*t(1,i)));
    R31(1,i)=sqrt((X0^2)+((Y0-T3y)^2)+((V1^2)*(t(1,i)^2))+(2*(Y0-T3y)*V1*t(1,i)));
    D1(1,i)=-((fc*V1)/(c*R1(1,i)))*(Y0+(V1*t(1,i)));
    D21(1,i)=-((fc*V1)/(c*R21(1,i)))*(Y0+(V1*t(1,i)));
    D31(1,i)=-((fc*V1)/(c*R31(1,i)))*(Y0-T3y+(V1*t(1,i)));
end
end

```

FUNCTION: *PositionCalc()*

```

function [Px,Py]=PositionCalc(R1,R21,R31,T2x,T3y)
% Determination of Position vector from distances and tracking station
% ` position informaion Ti i=1 to 3
%
% OUTPUT:
% Px: Position X coordinates vector
% Py: Position Y coordinates vector
% INPUT:
% R1: Distance from mobile node to T1
% R21: Distance from mobile node to T2
% R31: Distance from mobile node to T3
% T2x: X coordinate of Tracking Station T2 (T2y=0)
% T3y: Y coordinate of tracking Station T3 (T3x=0)
%
% Example: [Px,Py]=PositionCalc(R1,R21,R31,1000,1000);
% T2x=1000m,T3y=1000m

n=length(R1); % All input vectors must be of the same length
Px=zeros(1,n);
Py=zeros(1,n);
P=[0;0];
A=[T2x,0;0,T3y];

for i=1:n

    Bx=0.5*(R1(i)^2-R21(i)^2)+0.5*(T2x^2);
    By=0.5*(R1(i)^2-R31(i)^2)+0.5*(T3y^2);
    B=[Bx;By];
    P=((A'*A)\(A')*B; % Least Squares \ operator
    Px(i)=P(1,1);
    Py(i)=P(2,1);

end
end

```

FUNCTION: *VelocityCalc()*

```

function [Vx,Vy]=VelocityCalc(fc,T2x,T3y,Px,Py,D1,D21,D31)

% Determination of velocity vector from Doppler shift and
% ` position informaion for Ti i=1 to 3
%
% OUTPUT:
% Vx: Velocity component X vector
% Vy: Velocity component Y vector
% INPUT:
% fc: Transmitted RF signal frequency (Hz)
% T2x: X coordinate of Tracking Station T2 (T2y=0)
% T3y: Y coordinate of tracking Station T3 (T3x=0)
% Px: Position X coordinates vector
% Py: Position Y coordinates vector
% D1: Doppler frequency shift (Hz) vector (n) at T1
% D21: Doppler frequency shift (Hz) vector (n) at T2
% D31: Doppler frequency shift (Hz) vector (n) at T3
%
% Example: [Vx,Vy]=VelocityCalc(400e6,1000,1000,Px,Py,D1,D21,D31);
% fc=400MHz,T2x=1000m,T3y=1000m

c=299792458; % Speed of light in vacuum (m/s)
n=length(Px); % All input vectors must be of the same length
Vx=zeros(1,n);
Vy=zeros(1,n);
V=[0;0];
A=[0,0;0,0;0,0];
B=[0;0;0];

for i=1:n

    A= [Px(i),Py(i);(Px(i)-T2x),Py(i);Px(i),(Py(i)-T3y)];

    B(1,1)=-(c*D1(i)*(sqrt(A(1,1)^2+A(1,2)^2)))/fc;
    B(2,1)=-(c*D21(i)*(sqrt(A(2,1)^2+A(2,2)^2)))/fc;
    B(3,1)=-(c*D31(i)*(sqrt(A(3,1)^2+A(3,2)^2)))/fc;

    V=((A')*A)\(A')*B; % Least Squares \ operator
    Vx(i)=V(1,1);
    Vy(i)=V(2,1);

end
end

```

FUNCTION: *RangeNoise()*

```

function [R1n,R21n,R31n]=RangeNoise(R1,R21,R31,Var,M,W)
% Addition of White noise in time to Range arrays R1, R21 and R31
% White noise introduced in time after Multilateration determination
% R1, R21 and R31 MUST HAVE the same length
%
% OUTPUT:
% R1n: Distance from mobile node to T1 with noise
% R21n: Distance from mobile node to T2 with noise
% R31n: Distance from mobile node to T3 with noise
% INPUT:
% R1: Distance from mobile node to T1
% R21: Distance from mobile node to T2
% R31: Distance from mobile node to T3
% Var: Gaussian noise Variance (ns^2)
% M: Gaussian noise Mean (ns)
% W: One-Way (1) or Two-Ways (2)

c=299792458; %Speed of light in vacuum (m/s)
n=length(R1); % All input vectors must be of the same length

R1n=zeros(1,n);
R21n=zeros(1,n);
R31n=zeros(1,n);

T1=zeros(1,n); % Time-Of-Arrival from MN to Ri1
T21=zeros(1,n);
T31=zeros(1,n);

noise1=M+(sqrt(Var)*randn(1,n)); %Var in ns^2, M in ns
noise21=M+(sqrt(Var)*randn(1,n));
noise31=M+(sqrt(Var)*randn(1,n));

T1=(1e9*W/c)*R1; %TOA in ns
T21=(1e9*W/c)*R21;
T31=(1e9*W/c)*R31;

T1n=T1+noise1;
T21n=T21+noise21;
T31n=T31+noise31;

R1n=(1e-9*c/W)*T1n;
R21n=(1e-9*c/W)*T21n;
R31n=(1e-9*c/W)*T31n;

End

```

FUNCTION: *DopplerNoise()*

```

function [D1n,D21n,D31n]=DopplerNoise(D1,D21,D31,fc,Var,M)
% Addition of Gaussian noise in time to Doppler Frequency shift arrays
% D1, D21 and D31
% Gaussian noise introduced in time after Doppler shift determination
% D1, D21 and D31 MUST HAVE the same length
%
% OUTPUT:
% D1n: Doppler shift received at T1 with noise
% D21n: DDoppler shift received at T21 with noise
% D31n: Doppler shift received at T31 with noise
% INPUT:
% D1: DDoppler shift received at T1
% D21: Doppler shift received at T21
% D31: Doppler shift received at T31
% fc: IF baseband measurement frequency (MHz)
% Var: Gaussian noise time Variance (ns^2)
% M: Gaussian noise Mean (ns)
% W: One-Way (1) or Two-Ways (2)

c=299792458; %Speed of light in vacuum (m/s)
Fc=fc*1e6; %Frequency in Hz
n=length(D1); % All input vectors must be of the same length

D1n=zeros(1,n);% Doppler Freq shift Inc(fD) in Hz
D21n=zeros(1,n);
D31n=zeros(1,n);

T1m=zeros(1,n); % Measured period of Fc+Inc(fD)in ns
T21m=zeros(1,n);
T31m=zeros(1,n);

noise1=M+sqrt(Var)*randn(1,n); %Var in ns^2, M in ns
noise21=M+sqrt(Var)*randn(1,n);
noise31=M+sqrt(Var)*randn(1,n);

for i=1:n

    T1m(i)=(1/(Fc+D1(i)))+((1e-9)*noise1(i)); %Time1 in s with noise
    D1n(i)=(1/T1m(i))-Fc;

    T21m(i)=(1/(Fc+D21(i)))+((1e-9)*noise21(i)); %Time1 in s with noise
    D21n(i)=(1/T21m(i))-Fc;

    T31m(i)=(1/(Fc+D31(i)))+((1e-9)*noise31(i)); %Time1 in s with noise
    D31n(i)=(1/T31m(i))-Fc;

end

end
end

```

FUNCTION: *EKalman()*

```

function [Ex]=EKalman(X,r,a)
% Kalman filtering of array X with system gain and noise variance
%
% OUTPUT:
% Ex: Filtered X signal
% INPUT:
% X: Noisy signal
% r: Additive Gaussian noise variance
% a: Covariance of samples

n=length(X);
Ex=zeros(1,n);

K=0;
P=1; %Initial default value

% Default covariance a=1+0.1*r;

for i=2:n
    P=P*(a^2);
    K=P/(P+r);
    Ex(i)=K*X(i)+((1-K)*Ex(i-1));
    P=(1-K)*P;
end
end

```

SCRIPT: *NoiseModel_script*

```

% NoiseModel_script,m
%
% Noise Model simulation script
y=linspace(-100,100,200);
% application of noise normal distributio to ranges R1en
% Range noise Variance in ns^2

VarianceR=5.011e-4;

% [R1n,R21n,R31n]=RangeNoise(R1,R21,R31,Var,M,W)
[R1en,R21en,R31en]=RangeNoise(R1e,R21e,R31e,VarianceR,0,1);

KR1en=EKalman(R1en,VarianceR,1.12);
KR21en=EKalman(R21en,VarianceR,1.12);
KR31en=EKalman(R31en,VarianceR,1.12);

% Application of noise normal distribution to Doppler shifts Di1en
% Doppler Frequency noise Variance in ns^2

```

```

VarianceD=4.55e-8;

% [D1n,D21n,D31n]=DopplerNoise(D1,D21,D31,fc,Var,M)
[D1en,D21en,D31en]=DopplerNoise(D1e,D21e,D31e,1,VarianceD,0);

KD1en=EKalman(D1en,std(D1en)^2,1.12);
KD21en=EKalman(D21en,std(D21en)^2,1.12);
KD31en=EKalman(D31en,std(D31en)^2,1.12);

%Error in Doppler Frequency

Ed1=D1e-D1en;
Ed21=D21e-D21en;
Ed31=D31e-D31en;

%Error in Range measurement

Er1= R1e-R1en;
Er21= R21e-R21en;
Er31= R31e-R31en;

% Reconstruction of Positions WITH NOISE...

[Pxen,Pyen]=PositionCalc(R1en,R21en,R31en,1000,1000);

% ...and FILTERED by EKF

[KPxen,KPyen]=PositionCalc(KR1en,KR21en,KR31en,1000,1000);

% ...And velocity vectors from noisy ranges Ri1en and Doppler shift Di1en

[Vx2en,Vy2en]=VelocityCalc(400e6,1000,1000,Pxen,Pyen,D1en,D21en,D31en);

% ... and obtained from FILTERED Ranges and Doppler values

[KVx2en,KVy2en]=VelocityCalc(400e6,1000,1000,KPxen,KPyen,KD1en,KD21en,KD31en);

% Plot Doppler and ranges, and positions with sampled velocity vectors

[Pxens,Pyens,Vx2ens,Vy2ens]=SamplePosVel(Pxen,Pyen,Vx2en,Vy2en,10);

[KPxens,KPyens,KVx2ens,KVy2ens]=SamplePosVel(KPxen,KPyen,KVx2en,KVy2en,10);

f1=figure('Name','P and V');
f2=figure('Name','D and R Error Distributions');
f3=figure('Name','EKF P and V');

figure(f1);

subplot(2,2,1)

```

```

hold on
plotyy(y,R1en,y,D1en);
title('Range and Doppler T1');
xlabel('Position Y(m)');
ylabel('Range(m)');
hold on
subplot(2,2,2)
plotyy(y,R21en,y,D21en);
title('Range and Doppler T2');
xlabel('Position Y(m)');
ylabel('Range(m)');
hold on
subplot(2,2,3)
plotyy(y,R31en,y,D31en);
title('Range and Doppler T3');
xlabel('Position Y(m)');
ylabel('Range(m)');

hold on
subplot(2,2,4)
plot(Pxen,Pyen);
title('Position and Velocity vectors');
xlabel('Position X(m)');
ylabel('Position Y(m)');

hold on
quiver(Pxens,Pyens,Vx2ens,Vy2ens); %sampled position and Velocity values
hold off

figure(f2);

subplot(2,3,1);
hold on;
histfit(Er1,25);
Label=['R1 Error ',char(963),' = ',num2str(std(Er1)^2,4)];
title(Label);
xlabel('Range(m)');
hold on;
subplot(2,3,2);
hold on;
histfit(Er21,25);
Label=['R21 Error ',char(963),' = ',num2str(std(Er21)^2,4)];
title(Label);
xlabel('Range(m)');
hold on;
subplot(2,3,3);
hold on;
histfit(Er31,25);
Label=['R31 Error ',char(963),' = ',num2str(std(Er31)^2,4)];
title(Label);
xlabel('Range(m)');
hold on;
subplot(2,3,4);

```

```

hold on;
histfit(Ed1,25);
Label=['D1 Error ',char(963),' = ',num2str(std(Ed1)^2,4)];
title(Label);
xlabel('Frequency(Hz)');
hold on;
subplot(2,3,5);
hold on;
histfit(Ed21,25);
Label=['D21 Error ',char(963),' = ',num2str(std(Ed21)^2,4)];
title(Label);
xlabel('Frequency(Hz)');
hold on;
subplot(2,3,6);
hold on;
histfit(Ed31,25);
Label=['D31 Error ',char(963),' = ',num2str(std(Ed31),4)];
title(Label);
xlabel('Frequency(Hz)');
hold on;

figure(f3);

subplot(2,2,1)
hold on
plotyy(y,KR1en,y,KD1en);
title('EKF Range and Doppler T1');
xlabel('Position Y(m)');
ylabel('Range(m)');
hold on
subplot(2,2,2)
plotyy(y,KR21en,y,KD21en);
title('EKF Range and Doppler T2');
xlabel('Position Y(m)');
ylabel('Range(m)');
hold on
subplot(2,2,3)
plotyy(y,KR31en,y,KD31en);
title('EKF Range and Doppler T3');
xlabel('Position Y(m)');
ylabel('Range(m)');

hold on
subplot(2,2,4)
plot(KPxen,KPyen);
title('EKF Position and Velocity vectors');
xlabel('Position X(m)');
ylabel('Position Y(m)');

hold on
quiver(KPxens,KPyens,KVx2ens,KVy2ens); %sampled position and Velocity values
hold off

```

FUNCTION: *PDS()*

```

function [PS] =PDS(x,Fs,Note)
% Power Density spectrum of a signal x
%
% OUTPUT:
% PS: Power Spectrum in dB/Hz
% INPUT:
% x: Signal in time-domain
% Fs: Sampling frequency for input signal x
% Note: text for title of Power spectrum plot

N = length(x);
xdft = fft(x);
xdft = xdft(1:floor(N/2+1));

psdx = (1/(Fs*N)) * abs(xdft).^2;
psdx(2:end-1) = 2*psdx(2:end-1);
freq = 0:Fs/length(x):Fs/2;
PS=psdx;

plot(freq,10*log10(psdx))

% grid on;
title(Note);
xlabel('Frequency (Hz)');
ylabel('Power Spectrum Density (dB/Hz)');

end

```

FUNCTION: *Reflectance()*

```

function [Ro,Ro2]=Reflectance(theta, Dielec,Cond,f)
% RF Reflectance or Reflection coefficient for a surface
%
% OUTPUT:
% Ro: Ro Reflection coefficient for Vertical Polarization
% R02: Ro Reflection coefficient for Horizontal polarization
% INPUT:
% f: Transmitted RF signal frequency (Hz)
% theta: Incidence angle (in °)
% Cond: Electrical conductivity of the surface (Siemens, Mhos))
% Dielec: relative permittivity of the surface (Er)

thetad=2*pi()*(theta/360);
% Alternative expression for Ro Horizontal polarization:
% Ro=(sin(thetad)-sqrt(Dielec-i*(Cond/(2*pi()*f))-(cos(thetad)^2)))/

```

```

% (sin(thetad)+sqrt(Dielec-i*(Cond/(2*pi()*f))-(cos(thetad)^2)));
n=Dielec-i*60*(299792458/f);
C=(n-(cos(thetad)^2))/(n^2);
Ro=(sin(thetad)-sqrt(C))/(sin(thetad)+sqrt(C));
C=n-(cos(thetad)^2);
Ro2=(sin(thetad)-sqrt(C))/(sin(thetad)+sqrt(C));

end

```

SCRIPT: *Reflectance_Script*

```

% Reflectande_Script.m
% RF Reflectance or Reflection coefficient for a surface with
% Conductivity (Cond) and Permittivity (Dielec(
% for Theta angle=1° to 120°

Ro=zeros(1,120);
Ro2=zeros(1,120);
MRo=zeros(1,120);
MRo2=zeros(1,120);
Dielec= 2; % 2 to 4 for Lunar soil
Cond=1e-3; %1e-3 to 1e-11for lunar soil
f=401e6;

for Angle=1:120

[Ro(1,Angle),Ro2(1,Angle)]=Reflectance(Angle, Dielec,Cond,f);
MRo(1,Angle)=norm(Ro(Angle)); %Ro for Vertical Polarization
MRo2(1,Angle)=norm(Ro2(Angle)); %Ro for Horizontal Polarization

end

plot(MRo); % plot vertical polarization

```

FUNCTION: *SamplePosVel()*

```

function [Pxs,Pys,Vxs,Vys]=SamplePosVel(Px,Py,Vx,Vy,n)
% Sample Position and Velocity Vectors for clear representation
% of Veclocity vectors in vector chart
% OUTPUT:
% Pxs, Pys: Sampled Position vector (Px, Py)
% Vx, Vys: Sampled Velocity vector (Vx, Vy)
% INPUT:
% Px, Py: Original Position vector (Px, Py)
% Vx, Vy: Original Velocity vector (Vx, Vy)
% n: Sampling period (1 sample OUTPUT each n samples in INPUT Vectors

N= floor(length(Px)/n);

```

```

Pxs=zeros(1,N);
Pys=zeros(1,N);
Vxs=zeros(1,N);
Vys=zeros(1,N);

for i=1:N
    Pxs(1,i)=Px(1,(i*n));
    Pys(1,i)=Py(1,(i*n));
    Vxs(1,i)=Vx(1,(i*n));
    Vys(1,i)=Vy(1,(i*n));
end
end

```

SCRIPT: *DopplerCalc_V_Script()*

```

% Generation of Data and Plots for Range and Doppler model simulations
% Reconstruction of Position and Velocity vectors from Range and Doppler
% information generated by the model.

t=linspace(0,200,200); % time (s)
y=linspace(-100,100,200); %Y location (m)

% Generation of Distances and Doppler values on T1 to T3

[D1,D21,D31,R1,R21,R31]=RangeCalc_VN(400e6,1,10,-100,1000,1000,0,200,200);

% Estimation of distances from distances to the Tracking stations and
% Tracking station positions.

[Px,Py]=PositionCalc(R1,R21,R31,1000,1000);

% Estimation of velocity vectors from positions and Doppler shift

[Vx,Vy]=VelocityCalc(400e6,1000,1000,Px,Py,D1,D21,D31);

%Sampling of Position and vector values (N=10 samples) to
% Represent the velocity vector in a graphical view.

[Pxs,Pys,Vxs,Vys]=SamplePosVel(Px,Py,Vx,Vy,10);

% Representation of Range and Doppler values for T1, T2 and T3 in
% in rectilinear trajectory, and the reconstructed position and
% velocity vectors (these last sampled for a more clear representation)

subplot(2,2,1)
hold on
plotyy(y,R1,y,D1);
title('Range and Doppler T1');
xlabel('Position Y(m)');

```

```
ylabel('Range(m)');  
hold on  
  
subplot(2,2,2)  
plotyy(y,R21,y,D21);  
title('Range and Doppler T2');  
xlabel('Position Y(m)');  
ylabel('Range(m)');  
hold on  
  
subplot(2,2,3)  
plotyy(y,R31,y,D31);  
title('Range and Doppler T3');  
xlabel('Position Y(m)');  
ylabel('Range(m)');  
hold on  
  
subplot(2,2,4)  
plot(Px,Py);  
title('Position and Velocity vectors');  
xlabel('Position X(m)');  
ylabel('Position Y(m)');  
hold on  
  
quiver(Pxs,Pys,Vxs,Vys); %sampled position and Velocity values
```

Appendix 3. – Oscillators Performance Tables.

	f Offset (Hz)	L(f) dBc/ SQRTHz	L(f)	Ai (ares)	JITTER (Rad)	JITTER (ps)	3-Sigma (ps)	Freq.Shift(Hz)	Doppler Error (m/s)	RAV (10s)
OCXO DS 9700										
Symmetricon										
Frequency (MHz):	1	-100	1E-10	3.16876E-05	0.504324308	1.5130E+00	151.2950034	56.45335948	5.00E-12	
	10	-125	3.16228E-13	4.51423E-10						
Space-Grade	100	-145	3.16228E-15	1.43726E-11						
	1000	-150	1E-15	1.87302E-12						
	10000	-155	3.16228E-16	5.92302E-12						
	100000	-155	3.16228E-16	2.84603E-11						
OCXO DS 9600QT										
Symmetricon										
Frequency (MHz):	5	-112	6.30957E-12	8.92421E-06	0.284066572	8.5220E-01	21.30490209	7.949590332	2.00E-12	
	10	-140	1E-14	2.84381E-11						
Space-Grade	100	-150	1E-15	4.95E-13						
	1000	-157	1.99526E-16	5.39787E-13						
	10000	-160	1E-16	1.34787E-12						
	100000	-160	1E-16	9E-12						
RK410 AV OCXO										
Rakon										
Frequency (MHz):	1	-110	1E-11	1.86485E-05	0.296500558	8.9040E-01	89.03937452	33.22364721	7.00E-13	
	10	-120	1E-12	4.95E-11						
Space-Grade	100	-130	1E-13	4.95E-11						
	1000	-145	3.16228E-15	4.6423E-11						
	10000	-145	3.16228E-15	2.84603E-11						
TE400 OCXO										
Rakon										
Frequency (MHz):	1	-65	3.16228E-07	0.00169638	6.749685568	2.0249E-01	32.37227041	12079.20538	5.00E-11	
	10	-95	3.16228E-10	1.42445E-06						
Space-Grade	100	-125	3.16228E-13	1.42445E-08						
	1000	-145	3.16228E-15	1.43726E-10						
	10000	-155	3.16228E-16	1.56533E-11						
LNO 100 OCXO										
Rakon										
Frequency (MHz):	10	-109.9	1.0233E-11	3.05481E-05	0.0486188	1.4586E-01	14.58542728	544.2323612	5.00E-10	
	100	-139.7	1.0715E-14	4.60964E-10						
Ht-Rel	1000	-168.1	1.5488E-17	4.82881E-12						
80 to 125 MHz	100000	-181.8	6.6069E-19	7.99369E-13						

Table A.3.1.- Phase noise performance for a selection of oscillators (RAV stands for *Root Allan Variance*, equivalent to *Allan Deviation*).

TE-300 TCXO	f Offset (Hz)	L(f) dBc/ SQRT(Hz)	L(f)	A1 (arens)	JITTER (Rad)	JITTER (ps)	3-Sigma (ps)	Freq.Shift(Hz)	Doppler Error (ms)	RAV (1s)
Rakon										
Frequency (MHz):	10	-75		3.16228E-08	0.001696577	27.0018909	8.1006E+01	8094.010662	3020.153232	1.00E-09
Space Grade no ITAR	100	-105		3.16228E-11						
	1000	-130		1E-13	1.42752E-08					
10 to 100 MHz	10000	-145		3.16228E-15	4.6423E-10					
HT700 TCXO										
Rakon										
Frequency (MHz):	1	-65		3.16228E-07	0.001696399	26.99904832	8.0997E+01	8093.159269	3019.835548	5.00E-10
	10	-95		3.16228E-10	1.42445E-06					
Hi Rel	100	-132		6.30957E-14	1.42331E-08					
10 to 60 MHz	1000	-142		6.30957E-15	3.12324E-11					
	10000	-147		1.99526E-15	3.23718E-11					
	100000	-150		1E-15	1.34787E-10					
Q1806-X TCXO										
Q-Fech										
Frequency (MHz):	1	-50		0.00001	0.009539406	151.8244952	4.5547E+02	45340.83307	16918.2213	1.00E-04
	10	-80		0.00000001	0.000045045					
Space Grade	100	-110		1E-11	4.5045E-07					
	1000	-135		3.16228E-14	4.51423E-09					
	10000	-155		3.16228E-16	1.43726E-10					
	100000	-155		3.16228E-16	2.84605E-11					
2101-2114 W TCXO										
VECTRON										
Frequency (MHz):	1	-50		0.00001	0.009539406	151.8244952	4.5547E+02	45340.83307	16918.2213	Not available
	10	-80		0.00000001	0.000045045					
Space Grade	100	-110		1E-11	4.5045E-07					
	1000	-135		3.16228E-14	4.51423E-09					
	10000	-155		3.16228E-16	1.43726E-10					
	100000	-155		3.16228E-16	2.84605E-11					
9960 TCXO										
Symmetricon										
Frequency (MHz):	1	-78		1.58489E-08	0.000380492	6.055719188	1.8167E+01	1816.385771	677.7558846	Not available
	10	-108		1.58489E-11	7.13915E-08					
Space Grade	100	-125		3.16228E-13	2.74342E-10					
	1000	-142		6.30957E-15	1.45142E-10					
	10000	-150		1E-15	3.28931E-11					
	100000	-150		1E-15	9E-11					
EX209 EMXO										
VECTRON										
Frequency (MHz):	1	-100		1E-10	0.000100049	0.796162675	2.3885E+00	955.3495738	356.4737216	Not available
	10	-125		3.16228E-13	4.51423E-09					
Hi Rel for Space Apps.	1000	-140		1.46802E-10						
10 to 40 MHz	10000	-145		3.16228E-15	5.92302E-11					
	100000	-145		3.16228E-15	2.84605E-10					

Table A.3.2.- Phase noise performance for a selection of oscillators (RAV stands for *Root Allan Variance*, equivalent to *Allan Deviation*).

OCXO DS 9700 Symmetric	Ageing (ppm/Yr)	Ageing Drift (Hz/Yr)	Doppler Aging Drift (Yr)	Temp.Min(°C)	Temp.Max(°C)	T° Drift (ppm)	T MaxOp(°C)	T MinOp(°C)	Freq.Drift (Hz)	Velocity 2-W T° Drift (m/s)
Frequency (MHz):	0.04	0.4	0.149253731	-40	65	0.004	50	-20	0.026666667	0.009950249
OCXO DS 9600QT Symmetric	Ageing (ppm/Yr)	Ageing Drift (Hz/Yr)	Doppler Aging Drift (Yr)	Temp.Min(°C)	Temp.Max(°C)	T° Drift (ppm)	T MaxOp(°C)	T MinOp(°C)	Freq.Drift (Hz)	Doppler T° Drift (m/s)
Frequency (MHz):	0.04	0.2	0.074626866	-40	65	0.005	50	-20	0.016666667	0.006218905
RRK410 AV OCXO Rakon	Ageing (ppm/Yr)	Ageing Drift (Hz/Yr)	Doppler Aging Drift (Yr)	Temp.Min(°C)	Temp.Max(°C)	T° Drift (ppm)	T MaxOp(°C)	T MinOp(°C)	Freq.Drift (Hz)	Doppler T° Drift (m/s)
Frequency (MHz):	0.01	0.1	0.037313433	-30	60	0.002	50	-20	0.001555556	0.000580431
TE400 OCXO Rakon	Ageing (ppm/Yr)	Ageing Drift (Hz/Yr)	Doppler Aging Drift (Yr)	Temp.Min(°C)	Temp.Max(°C)	T° Drift (ppm)	T MaxOp(°C)	T MinOp(°C)	Freq.Drift (Hz)	Doppler T° Drift (m/s)
Frequency (MHz):	0.3	12	4.47761194	-40	70	0.25	50	-20	6.363636364	2.37449118
LNO100 OCXO Rakon	Ageing (ppm/Yr)	Ageing Drift (Hz/Yr)	Doppler Aging Drift (Yr)	Temp.Min(°C)	Temp.Max(°C)	T° Drift (ppm)	T MaxOp(°C)	T MinOp(°C)	Freq.Drift (Hz)	Doppler T° Drift (m/s)
Frequency (MHz):	0.5	50	18.65671642	-40	85	0.5	50	-20	28	10.44776119
TE300 TCXO Rakon	Ageing (ppm/Yr)	Ageing Drift (Hz/Yr)	Doppler Aging Drift (Yr)	Temp.Min(°C)	Temp.Max(°C)	T° Drift (ppm)	T MaxOp(°C)	T MinOp(°C)	Freq.Drift (Hz)	Doppler T° Drift (m/s)
Frequency (MHz):	1	10	3.731343284	-40	85	5	50	-20	28	10.44776119
HT700 TCXO Rakon	Ageing (ppm/Yr)	Ageing Drift (Hz/Yr)	Doppler Aging Drift (Yr)	Temp.Min(°C)	Temp.Max(°C)	T° Drift (ppm)	T MaxOp(°C)	T MinOp(°C)	Freq.Drift (Hz)	Doppler T° Drift (m/s)
Frequency (MHz):	1	10	3.731343284	-40	85	0.5	50	-20	2.8	1.044776119
QF806-X TCXO Q-Tech	Ageing (ppm/Yr)	Ageing Drift (Hz/Yr)	Doppler Aging Drift (Yr)	Temp.Min(°C)	Temp.Max(°C)	T° Drift (ppm)	T MaxOp(°C)	T MinOp(°C)	Freq.Drift (Hz)	Doppler T° Drift (m/s)
Frequency (MHz):	0.5	5	1.865671642	-40	85	4	50	-20	22.4	8.358208955
2101-2114 W TCXO VECTRON	Ageing (ppm/Yr)	Ageing Drift (Hz/Yr)	Doppler Aging Drift (Yr)	Temp.Min(°C)	Temp.Max(°C)	T° Drift (ppm)	T MaxOp(°C)	T MinOp(°C)	Freq.Drift (Hz)	Doppler T° Drift (m/s)
Frequency (MHz):	1	10	3.731343284	-40	85	5	50	-20	40	14.92537313
9960 TCXO Symmetric	Ageing (ppm/Yr)	Ageing Drift (Hz/Yr)	Doppler Aging Drift (Yr)	Temp.Min(°C)	Temp.Max(°C)	T° Drift (ppm)	T MaxOp(°C)	T MinOp(°C)	Freq.Drift (Hz)	Doppler T° Drift (m/s)
Frequency (MHz):	0.5	5	1.865671642	-40	85	2	50	-20	11.2	4.179104478
EX209 EMXO VECTRON	Ageing (ppm/Yr)	Ageing Drift (Hz/Yr)	Doppler Aging Drift (Yr)	Temp.Min(°C)	Temp.Max(°C)	T° Drift (ppm)	T MaxOp(°C)	T MinOp(°C)	Freq.Drift (Hz)	Doppler T° Drift (m/s)
Frequency (MHz):	0.2	4	1.492537313	-40	85	0.1	50	-20	1.12	0.417910448
	20								8.88889E-05	3.31675E-05

Table A.3.3.- Thermal characteristics for a selection of oscillators.

OCXO DS 9700	Power (W)
Symmetricon	1,3
Frequency (MHz):	Warm-Up:
10	4 to 8
OCXO DS 9600QT	Power (W)
Symmetricon	1,5
Frequency (MHz):	Warm-Up:
5	7
RK410 AV OCXO	Power (W)
Rakon	3
Frequency (MHz):	Warm Up:
10	10
TE400 OCXO	Power (W)
Rakon	0,65
Frequency (MHz):	Warm Up:
40	2
LNO 100 OCXO	Power (W)
Rakon	2,2
Frequency (MHz):	Warm Up:
100	3,7
TE 300 TCXO	Power (W)
Rakon	0,2
Frequency (MHz):	
10	
HT700 TCXO	Power (W)
Rakon	0,055
Frequency (MHz):	
10	
QT806-X TCXO	Power (W)
Q-Tech	0,055
Frequency (MHz):	
10	
2101-2114 W TCXO	Power (W)
VECTRON	0,055
Frequency (MHz):	
10	
9960 TCXO	Power (W)
Symmetricon	0,22
Frequency (MHz):	
10	
EX209 EMXO	Power (W)
VECTRON	0,055
Frequency (MHz):	
20	

Table A.3.4.- Power consumption characteristics (Note: *Power* denotes nominal power consumption, *Warm-Up* denotes initial temperature stabilization for OCXOs. The duration of that period depends on the environmental conditions, being from seconds to several minutes)